ISTANBUL TECHNICAL UNIVERSITY ★ GRADUATE SCHOOL OF SCIENCE ENGINEERING AND TECHNOLOGY

A REVIEW AND EVALUATION OF DEVELOPMENT IN EXPLORATION, PRODUCTION, RESERVES ESTIMATION, AND RESEARCH EFFORTS FOR SHALE GAS AND OIL

M.Sc. THESIS

Osman Mohammed

Department of Petroleum and Natural Gas Engineering

Petroleum and Natural Gas Engineering Programme

February 2015

ISTANBUL TECHNICAL UNIVERSITY ★ GRADUATE SCHOOL OF SCIENCE ENGINEERING AND TECHNOLOGY

A REVIEW AND EVALUATION OF DEVELOPMENT IN EXPLORATION, PRODUCTION, RESERVES ESTIMATION, AND RESEARCH EFFORTS FOR SHALE GAS AND OIL

M.Sc. THESIS

Osman Mohammed
(505111505)

Department of Petroleum and Natural Gas Engineering

Petroleum and Natural Gas Engineering Programme

Thesis Advisor: Asst. Prof. Dr. İ. Metin Mıhçakan

February 2015

0sman Mohammed, a **M.Sc.** student of ITU **Institute of Graduate School of Science, Engineering and Technology** student ID 505111505, successfully defended the **thesis** entitled "**A Review and Evaluation of Development in Exploration, Production, Reserves Estimation, and Research Efforts for Shale Gas and Oil.**", which he prepared after fulfilling the requirements specified in the associated legislations, before the jury whose signatures are below.

Thesis Advisor :   **Asst. Prof. Dr. İ. Metin MIHÇAKAN**   ....
İstanbul Technical University

Jury Members :   **Asst. Prof. Dr. Gürşat Altun**   ....
İstanbul Technical University

Asst. Prof. Dr. Abdullah Fişne   ....
İstanbul Technical University

Date of Submission : 15 December 2014
Date of Defense : 23 January 2015

To my spouse and children,

FOREWORD

I would like to express my sincerest gratitude to Ass. Prof. Dr. Ibrahim Metin Mihcakan, who doubled as my teacher and supervisor, and my family. I have benefited inmensely from the great kindness, guidance and motivation accorded me during my studies. For this I say a heartfelt thank you. To my beloved family, I owe a deep dept of gratitude for their contributions to my life. My special thanks also goes to the Honorary consulate of Ghana in Istanbul, Mr. Unal Kabaca for his unflinchnig support and words of encouragement during the entire period of my study.

February 2015   Osman Mohammed

x

TABLE OF CONTENTS

ABBREVIATIONS

BDF	**:**	Boundary Dominated Flow
BHA	**:**	Bottom Hole Assembly
BHN	**:**	Brinell Hardness Number
CBL	**:**	Cement Bond Log
c/s/API	**:**	count per second per API
CST	**:**	Capillary Suction Time
DCA	**:**	Decine Curve Analysis
2D-EOS	**:**	2 Dimensional Equation Of State
DLS	**:**	Dog Leg Severity
DOE	**:**	Department Of Energy
ECP	**:**	External Casing Parker
EL	**:**	Extended Langmur model
EUR	**:**	Estimated Ultimate Recovery
FIB	**:**	Focused Ion Beam
FTIR	**:**	Fourier Transform Infrared Spectroscopy technique
GIP	**:**	Gas In Place
GR	**:**	Gamma Ray
GTI	**:**	Gas Technology Institute
IAS	**:**	Ideal Adsorbed Solution
ICP	**:**	Inductively Coupled Plasma
IOF	**:**	Initial Open Flow
IPS	**:**	Initial Potentials
lbs	**:**	pounds
LGR	**:**	Local Grid Refinement
LPP	**:**	Low Pressure Pycnometer
LWD	**:**	Logging While Drilling
MD	**:**	Measured Depth
MEM	**:**	Mechanical Earth Model
MHF	**:**	Massive Hydraulic Fracturing
MW	**:**	Mud Weight
NEPA	**:**	National Environmental Policy Act
NIST	**:**	National Institute of Standard and Technology

NPI   **:** Normalized Pressure Index

OPEC   **:** Organization of Petroleum Exporting Countries

PNS   : Pulse Neutrons Spectroscopy

PPF   : pound per foot

RBI   : Relative Brittleness Index

RD&D   : Research Development and Demonstrations

RNI   : Rate Normalized Index

RPM   : Revolution Per Minute

RSCT   : Rotatry Sidewall Coring Tools

RSS   : Rotary Steerable System

RTGM   : Real Time Geomechanical

SEM   : Scanning Electron Microscopy

SGPM   : Shale Gas Predictive Model

SRV   : Stimulated Reservoir Volume

TGA   : Thermo Gravimetric Analysis

TIV   : Tranverse Isotropic Vertical

TSD   : Total Stratigraphic Depth

XRD   : X-Ray Diffraction

LIST OF TABLES

LIST OF FIGURES

A REVIEW AND EVALUATION OF DEVELOPMENTS IN EXPLORATION, PRODUCTION, RESERVES Estimation, and Research Efforts for Shale Gas and Oil.

SUMMARY

Shale is a fine-grained sedimentary rock that consists of significant amount of clays, in addition to sand and silt size minerals. During the sedimentation period, depending on the aqueous sedimentation environment, some organic material in the form of the remnants of dead organisms might accumulate along with some inorganic material, such as the organic or inorganic compounds nickel, zinc, vanadium, molybdenum, selenium, etc, among the grains of shale constituents. Shale is formed as the result of compaction of its constituents under the overburden stress (pressure) of overlaying strata that are accumulated later and under the rising temperature with increasing burial depth, throughout the vast geological time periods. During the millions of years of diagenesis, the period in which the sediments go through various physical and chemical alterations and deformations, the in-situ water in between the granules provides the means for the consolidation and cementation of compacting constituents to form a somewhat firm rock of shale, while some part of the in-situ water being expelled out due to compaction.

In addition to pressure the increasing temperature and the radiation from the radioactive elements among the constituents cause shale to experience thermal maturity. Contained organic material, if there is any, in shale would eventually be decomposed into hydrocarbons, partially in the form of kerogen and partially in the form of petroleum, until thermal maturity has reached a certain level. Kerogen is the organic material with long and complex molecular chains that was not converted into petroleum. During diagenesis, oil and gas type hydrocarbons may escape out of shale into other adjacent, preferably sedimentary, formations via the pathways, such as pore networks, cracks, fractures, joints, or faults, and form conventional oil and gas reservoirs if they get hydrodynamically trapped.

Therefore, shale is a easy-splitting laminated soft rock and such feature makes it different than the rock called mudstone. Economic oil and gas accumulations in shale formations are classified as unconventional reserves, since pore size and permeability levels in such rocks are much below microscopic scale and, hence, the application of conventional production and reserve estimation techniques is invalid. In this study the interest is in the shale formations that contain unconventional reservoirs of oil and gas. A shale formation is considered to have a prospective reservoir if its organic kerogen content is between 2 to 14 percent. The hydrocarbon that can form in shale is determined by the kerogen type and thermal maturity level in shale. Kerogen, as a solid matter, might have pores with size in the range from few nanometers to few hundred nanometers.

Production of oil and gas from shale formations was started during the World War II by the U.S.A. to fuel war tanks. After the war, however, it was uneconomical to produce from the shale formations due to unfeasible technology and low price of oil and gas. The adverse effect of significant increase in oil and gas prices, due to Yom Kippur war between Egypt and Israel in 1973, has forced the U.S. to explore new technology for feasable exploitation of oil and gas in shale formations.

In the past two decades, many researchers have introduced new and various methods and techniques for classifying shale formations, estimating oil and gas reserves, and drilling, completing, and stimulating wells for producing unconventional shale plays. Substantial investment in research has led to the development and use of horizontal well drilling and hydraulic fracturing technology that has draw a massive interest in the industry and has enormously increased the shale gas and oil production in the U.S., e.g. the U.S. hydrocarbon gas reserves have increased about 35 percent in 2008. Such success has led many countries worldwide to attempt to explore unconventional oil and gas in shale formations in their sedimentary basins. While research is still continuing worldwide for futher improvement in aforementioned methods and techniques to maximize ultimate recovery from shale formations, only Russia and China other than the U.S. had some limited success in shale gas and oil play so far.

Among the shale classification methods, real-time classification is based on well logs to estimate the petrophysical, compositional, and elastic properties of shale rocks. Another technique attempts to identify hydrocarbon-bearing shale groups, based on similar compositional properties exhibited on a combination of well logs, and also to minimize the shoulder-bed effects using the inversion of log derived layer properties. Other method integrates core analysis and well log information to classifying shale in terms of porosity, capillary pressure, mineralogy, and TOC. Though, all the methods are found to yield good results, all of them have to be applied on the same formation to ascertain which method is better than the others, since each shale play is unique.

Although conventional reserve estimate methods seem not to work in unconventional shale gas and oil reservoirs, a group of researchers tried to use the usual hyperbolic decline curve analysis technique on a production rate versus time plot to estimate the recoverable reserves. They came up with a nine–equation bivariate regression model based on initial test and recovery data to estimate the reserves in the Devonian shale. A new volumetric total-gas-in-place estimation equation that incorporates Langmuir adsorption isotherm was formulated to take the pore space occupied by the sorbed phase into account. Hydrocarbon phase behavior is realized to be quite different in pores and capillaries with characteristic length less than 100 nanometers, since gas density varies under the influence of organic pore walls of kerogen.

Interest in drilling and completion of horizontal wells has increased during the last two decades to enhance productivity and ultimate recovery from shale reservoirs. The most commonly used completion method is casing and perforating the horizontal section of wells. In horizontal wells an optimized multi-stage hydraulic fracturing through perforations is the inevitable stimulation technique to create interconnected fracture network for maximizing the flow into wellbore.

Various explosive or impact methods of dynamic fracture and fragmentation data on shale rocks has showed that the interaction of transient wave with the local free surfaces in rock generates tension in some regions of rock where fracture and fragmentation is initiated. Studies has also showed that the static strength of a rock can be less than the dynamic fracture strength as much as one order of magnitude. A

researcher with the objective of intersecting as many natural fractures as possible with the hydraulic fractures has developed a rationale for stimulation design for the Devonian shale. The MHF (massive hydraulic fracturing) technique has long been used for the same purpose. It has been found that shale thickness and fracture density are important factors in determining the stimulation technology and strategy. A new hydraulic fracturing technique is CHF (channel hydraulic fracturing) that was first applied in Marcellus shale. In CHF technique; which integrates the geomechanical modeling and perforation strategy, fiber-laden fluid is pumped in a unique manner to create high-conductivity stable channels in the proppant pack placed in the created fracture. Hydrocarbon fluids flow through these high conductivity channels rather than being dependent on the permeability within the proppant pack. Appreciable increase in fracture conductivity by these flow channels has been proven in practice.

Reliable forecast of production from shale reservoirs has been another requirement in the industry. The methods of analytical simulation, numerical simulation and various decline curve analyses (DCA) have been utilized. Each method has its own particular advantages and disadvantages. Rapidity and extent of accuracy in production forecast are among the factors considered in these methods.

Another model, called the Shale Gas Predictive Model (SGPM), was developed with an alternative approach and was proposed to mitigate the challenges associated with shale gas production. Simple and easy to use model focuses essentially on the flow around individual wells while conserving overall mass. The model has the advantage of generating rapid and repetitive results, in situations where quick turnaround is required to estimate the production and reserves from a large number of wells in a single or multiple shale gas plays. Such situations arise frequently if the operating companies plan to drill hundreds of wells year by year on the millions of acres of land. The model can be run in conjunction with a fracture mechanics software for better fracture design. Production forecasting capability of the model was validated against the actual production from various shale gas plays in different regions. Thus, the model can be reliably used for both matching the past production history and the future production forecast. Oil-rich play and multi-phase flow features of the model provides insight to the condensate production. However, the inaccuracies in recovery prediction are highlighted if the presence of condensate is not considered.

When the development of Eagle Ford shale in South Texas was started in 2008, there was not any data analysis available on the production from this shale at that time. Linear dual-porosity type-curve analysis technique was employed for modelling the production behavior and for estimating the essential reservoir parameters. The type curves used were constructed based on the transient production rate at constant well pressure and closed-boundary double-porosity stimulated reservoir volume (SRV.) Two different approaches of Bello-and-Nobakht method were employed to account for apparent skin in analyzing the early-time and the late-time production data. The production from Eagle Ford shale exhibited linear flow, bilinear flow, and boundary dominated flow regimes. Based on bilinear flow analysis and the assumption of slab-type fracture model, the fracture permeability was estimated to be about 820 nano Darcy. On the other hand, the matrix permeability was estimated to be in the range of 181 to 255 nano Darcy, based on linear matrix flow analysis. The results were validated by means of numerical simulation, due to the fact that the permeability values obtained from the numerical simulation study were in the range of agreement with those obtained from the type curve analysis.

In order to carry out production forecasting for Eagle Ford shale different adsorption isotherms were used. It was deduced from the results of production forecasting that the gas desorption depends on both the reservoir pressure and adsorption isotherm. The gas desorption in early times, when the reservoir pressure is high, was found to be usually not that important. However, based on the laboratory measured adsorption isotherms, long-term production forecasting is needed for desorption to be effective.

A genesis of decline curves with the use of a simple hydrodynamic analogy was also provided. Some physical factors that are critical to well productivity were also examined, based on several studies on production decline curves. It was observed that an exponential or hyperbolic decline curve would adequately fit the production decline data for the wells producing from Devonian Shale. An attempt has also been made to characterize the production decline based on open flow, rock pressure, and specific shale production mechanisms.

An analytical tri-linear-flow solution was presented to simulate the transient pressure behavior and production behavior in fractured horizontal wells in unconventional shale reservoirs. Though the model is simple, it is versatile enough to incorporate the fundamental petrophysical characteristics including the intrinsic properties of both matrix and natural fractures of a shale reservoir. Various reservoir components in addition to the special characteristics of fluid exchange may also be considered. A practical analytical model is presented and discussed in this study for the analysis of pressure transient responses in multiple fractured horizontal wells in unconventional shale reservoirs.

Oil and gas production from unconventional shale reserves in the U.S. has become feasible both technically and economically, after the remarkable rise of oil and gas prices. Among the mature shale plays in the U.S., and in the World, Barnett shale near Forth Worth, Texas, is the one for which there is satisfactory production history. Therefore, the examination of the economics of exploitation of Barnett shale, as the field had been developed with more than 6000 producing wells, can be considered as the role model for establishing an idea of how shale plays can become commercial.

For the costs and prices during this thesis work is conducted, an ultimate recovery of about 550 to 900 million standard cubic feet of gas has to be produced to pay out for one well. In oil production from shales, for a mature field with 100 000 barrels per day oil production the minimum oil price should be at least 43 USD per barrel.

ŞEYL GAZI VE PETROLÜ IÇIN ARAMA, ÜRETIM, REZERV KESTIRIMI VE ARAŞTIRMA ÇALIŞMALARININ İNCELENMESI VE DEĞERLENDIRILMESI

ÖZET

Şeyl büyük miktarda killerden ve daha az miktarda kum ve silt boyutlu minerallerden oluşmuş, çok küçük tanecikli bir çökel kayaç türüdür. Çökelme döneminde, su içi çökelme ortamının türüne göre, ölü organizimaların kalıntıları biçimindeki organik malzemeler yanında nikel, çinko, vanadyum, molibden, selenyum, vb elementlerin organik ve/veya inorganik bileşikleri şeyli oluşturan tanecikler arasında birikebilirler. Şeyl çok uzun jeolojik zaman içinde onu oluşturan bileşenlerin, daha sonra üzerlerine yığılmış üst kayaç katmanlarının ağırlık baskısı (basıncı) ve artan gömülme derinliği ile yükselen sıcaklık altında sıkışmaları sonucunda oluşur. Milyonlarca yıl boyunca çökelen malzemenin geçirdiği fiziksel ve kimyasal dönüşümler ve yapısal değişimler olarak işleyen dijajenez sürecinde, tanecikler ve mineral parçaları arasındaki yerinde su sıkışan taneciklerin çimentolanma ve sıkılaşmaları için uygun koşulları sağlayarak şeylin oldukça katılaşmış bir kayaç olarak biçimlenmesini sağlarken, yerinde suyun bir bölümü de sıkışma etkisi altında oluşan şeyl ortamından dışarı atılır.

Basınca ek olarak, artan sıcaklık ve ışıyan (radyoaktif) element içeren bileşenlerden olan ışınım şeylin ısıl olgunlaşma geçirmesine yol açar. Isıl olgunlaşmanın belirli bir düzeye erişmesine kadar, şeyl içindeki (eğer var ise) organik malzeme bozunmaya uğrayarak, ham petrol, gaz ve kerojenden oluşan hidrokarbonlara dönüşür. Kerojen ham petrol ve gaza dönüşemeyen, uzun ve karmaşık zincir yapılı moleküllere sahip bir tür organik malzemedir. Diyajenez sürecinde şeyl içinde oluşan hidrokarbon (ham petrol ve gaz) akışkanlar gözenek ağları, kırıklar, çatlaklar, veya faylar gibi geçiş yolları boyunca şeylden dışarıya, tercihen çökel kayaç yapıları içine göç edebilirler. Göç gözenekli ve geçirgen bir kayaçta hidrodinamik bir kapan içinde birikme ile son bulur ve böylece sıradan türde bir petrol ve gaz haznesi (rezervuar) oluşur.

Oldukça yumuşak bir kayaç olan şeyl, kolay ayrılabilen ince katmanları ile, benzer bileşime sahip ve çamur taşı olarak anılan kayaçtan farklıdır. Şeyl içinde gözenek boyutu ve geçirgenlik düzeylerinin mikroskopik ölçeğin çok altında olması ve buna bağlı olarak geleneksel üretim ve rezerv kestirim uygulamalarının geçersiz kalması nedeniyle, şeyl yapıları içindeki ekonomik petrol ve gaz birikimleri "sıradışı" rezerv sınıfı içine sokulur. Bu çalışma şeyl yapılarındaki sıradışı petrol ve gaz rezervuarları ile ilgilenmektedir. Eğer bir şeyl yapısının organik kerojen içeriği yüzde 2 ile 14 arasında ise, o şeyl nurşen (umut var) bir kaynak olarak dikate alınır. Bir şeyl içinde oluşabilecek hidrokarbon, kerojen türü ve ısıl olgulaşmanın düzeyi ile belirlenir. Katı bir madde olan kerojen birkaç nanometre ile birkaç yüz nanometretre arasında değişen boyutta ve içine petrol ve gaz yerleşmiş gözeneklere sahip olabilir.

Şeylden dikkate değer miktarda petrol üretimi II. Dünya Savaşı sırasında A.B.D.'de savaş tanklarına yakıt sağlamak üzere başlatılmıştır. Savaştan sonra, düşük petrol ve gaz fiyatları ve teknolojik yetersizlik nedeni ile şeylden üretim ekonomik olmamıştır. Mısır ile İsrail arasındaki 1973 Yom Kippur savaşı nedeniyle petrol fiyatlarındaki artışının olumsuz etkisi, A.B.D.'yi şeyl yapılarından ekonomik petrol üretmeye ve bunun için gereki yeni teknolojileri keşfetmeye ve geliştirmeye zorlamıştır.

Geçen son yirmi yıllık dönemde, bir çok araştırmacı şeyl yapılarında sınıflandırma, petrol ve gaz rezerv kestirimi ve sıradışı şeyl girişimlerinde üretici kuyuları delme, tamamlama ve canlandırma için yeni yöntemler tanıtmışlardır. Araştırmaya yapılan dolgun yatırımlar A.B.D.'de şeylden petrol ve gaz üretiminde dikkate değer artışa, örneğin 2008'de A.B.D. hidrokarbon rezervlerinde yaklaşık yüzde 35 artışa, yol açan ve endüstriye som ilgi çeken yatay kuyu delme ve hidrolik çatlatma tekniklerinin geliştirilmesine ve kullanımına önderlik etmiştir. Bu başarı dünyada birçok ülkenin çökel havzalarındaki şeyl yapılarında sıradışı petrol ve gaz keşfine kalkışması için bir kılavuz olmuştur. Şeyl yapılarından üretimi en üst doruğa ulaştırmak üzere, anılan yöntemleri ve teknikleri daha da geliştirmek için araştırmalar tüm dünyada sürerken, şu ana kadar A.B.D. dışında yalnız Rusya ve Çin şeyl petrolü ve gazı girişimlerinde sınırlı bazı başarılar elde etmişlerdir.

Şeyl sınıflama yöntemlerinden biri olan gerçek zaman sınıflaması, şeyl kayaçlarının petrofizik, bileşim ve elastik özeliklerinin kuyu loglarından kestirimine dayanır. Bir diğer teknik, hidrokarbon içerikli şeyl gruplarını bunların birleşik kuyu loglarında sergiledikleri benzeri bileşim özeliklerine ve loglardan türetilen katman özeliklerinin evrilmesi ile komşu katman etkilerinin en düşük düzeye indirgenmesine dayanarak tanımlamaya çalışır. Bir başka yöntem ise, karot analizi ve kuyu logu bilgilerini birlikte değerlendirerek şeylleri gözeneklilik, kılcal basınç, mineral yapısı ve toplam organik karbon bakımından sınıflandırır. Tüm bu yöntemler iyi sonuçlar veriyor ise de, her şeyl girişimi kendine özgü biricik olduğundan, hangi yöntemle daha iyi sonuç alınacağını saptamak için yöntemlerin hepsi de aynı kayaç yapısına uygulanmalıdır.

Sıradan rezerv kestirim yöntemleri sıradışı gaz ve petrol rezervuarlarında çalışmıyor görünse de, bir öbek araştırmacı üretilebilir rezervin kestirimi için zamana bağımlı üretim debisi grafiklerinde olağan azalım eğrisi çözümleme tekniğini kullanmışlardır. Devoniyen Şeyli rezervlerini kestirmek için başlangıç test ve üretim verilerine dayalı, çift değişkenli dokuz denklemden oluşan bir regresyon modeli ortaya koymuşlardır. Langmuir adsorpsiyon izotermini de içine alan yeni bir hacimsel toplam yerinde gaz kestirim denklemi, soğurulmuş gaz fazı tarafından işgal edilmiş gözenek hacmini de dikkate alacak biçimde formüle edilmiştir. Kerojenin organik gözenek duvarlarının etkisi altında gaz yoğunluğu değişebildiğinden, hidrokarbon faz davranışının özgün uzunluğu 100 nanometreden kısa kılcal gözeneklerde çok farklı olduğu anlaşılmıştır.

Şeyl rezervuarların üretimini ve doruk kurtarımını yükseltmek için yatay kuyu delme ve tamamlamaya olan ilgi son yirmi yılda artmıştır. En yaygın kullanılan tamamlama yöntemi kuyuların yatay kesimlerine koruma borusu indirmek ve deliklemedir. Kuyu yatay kesimi deliklemelerinden çok aşamalı optimize hidrolik çatlatma yapılması, ara bağlantılı çatlak ağları yaratarak kuyuya en yüksek akışı sağlamak için zorunludur.

Çeşitli patlatma ve darbe yöntemleri ile şeyl kayaçlarda elde edilen dinamik çatlatma ve parçalama verileri, geçici dalga ile kayaç serbest yüzeyleri arasındaki etkileşimin kayaçta yöresel çatlama ve parçalanma başlatan gerilimler yarattığını göstermektedir. Bazı çalışmalara göre, kayacın statik dayanımı dinamik çatlama dayanımından onda bir (bir mertebe) daha düşüktür. Masif hidrolik çatlatma tekniği (MHF) kayacın olası

birçok doğal çatlağı ile hidrolik çatlakları kesiştirme amacıyla uzun zamandan beri kullanılmaktadır. Çatlak yoğunluğu ve şeyl kalınlığının canlandırma teknolojisi ve stratejisinin belirlenmesinde önemli unsurlar oldukları bulunmuştur. Yeni bir hidrolik çatlatma tekniği olan kanal hidrolik çatlatma (CHF) tekniği, jeomekanik modelleme ve delikleme stratejisini birleştiren özelliği ile Marcellus şeyline uygulanmıştır. CHF tekniğinde, elyaf yüklü akışkan özgün biçimde pompalanarak, yaratılan çatlağın içine yerleştirilen dayak tanecik paketlerinin içinde iletkenliği yüksek kararlı akaç (kanal) ağı oluşturulur. Hidrokarbon akışkanlar dayak tanecikleri paketlerinin geçirgenliğine bağımlı kalmayarak, iletkenliği yüksek bu akaçlarda akarlar. Çatlak iletkenliğinin bu akaçlarla önemli düzeyde arttığı uygulamada kanıtlanmıştır.

Endüstrinin bir diğer gereksinimi, şeyl rezervuar üretimlerinin öngörüsünün güvenilir biçimde yapılmasıdır. Üretim öngörülerinde her birisinin kendine özgü getirileri ve sakıncaları olan analitik andırı (simülasyon), sayısal andırı ve çeşitli azalım eğrisi çözümleme yöntemlerinden yararlanılmıştır. Bu yöntemlerde dikkate alınan unsurlar arasında öngörünün hızı ve doğruluğu önemli unsurlardır. Şeyl gazı kestirim modeli (SGPM) olarak anılan ve farklı bir yaklaşımla geliştirilmiş bir diğer model, şeyl gaz üretimindeki zorlukları azaltmak üzere önerilmiştir. Kolay kullanımlı bu basit model temelde tüm kütleyi korurken bireysel olarak her kuyu cıvarındaki akışa odaklanır. Modelin üstünlüğü, büyük sayıda kuyu bulunan tek veya çoğul şeyl girişimlerinde rezerv ve üretim kestirimi yapılırken, çabuk geridönüş gerektiren durumlarda hızlı ve yinelenebilir sonuçlar türetmesidir. Model bir çatlatma mekaniği yazılımı ile birlikte koşulabildiği için daha iyi çatlatma tasarımına olanak tanır. Modelin üretim öngörü becerisi farklı bölgelerde bulunan şeyl girişimlerinin gerçek üretimine karşı sınanmış ve kanıtlanmıştır. Bu nedenle, model hem geçmişteki üretime hem de gelecekteki öngörülen üretime güvenilir çakıştırma yapılmasında kullanılabilir. Modelin petrol ağırlıklı girişim ve çok fazlı akış vasıfları yoğuşuk üretiminin de anlaşılmasını sağlar.

Güney Teksas'taki Eagle Ford şeylinin geliştirilmesi 2008 yılında başlatıldığında, bu şeylden yapılan üretime ilişkin hiçbir veri analizi bulunmadığı için, üretim davranışı modellemesi ve temel rezervuar parametreleri kestiriminde doğrusal çift gözeneklilik tip-eğrisi çözümleme tekniği kullanılmıştır. Kullanılan tip-eğrileri, durağan kuyu basıncında geçici üretim debisi ve kapalı-sınırlı çift-gözeneklilikli canlandırılmış rezervuar hacmi (SRV) baz alınarak oluşturulmuştur. Bello-ve-Nobakht yönteminin iki farklı yaklaşımı, erken-zaman ve geç-zaman üretim verilerinin çözümlenmesinde görünür zarı dikkate almak üzere kullanılmıştır. Eagle Ford şeylinden yapılan üretim doğrusal akış, çift doğrusal akış ve sınır egemen akış rejimlerini sergilemiştir. Dilim tipi çatlak modeli varsayımı ve çift doğrusal akış çözümlemesi baz alınarak, çatlak geçirgenliği yaklaşık 820 nano Darcy olarak kestirilmiştir. Buna karşılık, doğrusal matriks akış çözümlemesi baz alınarak, matriks geçirgenliği 181 ile 255 nano Darcy arasında kestirilmiştir. Bu sonuçlar sayısal andırı (simülasyon) yardımı ile geçerli kılınmıştır. Çünki, sayısal andırı çalışmasında elde edilen geçirgenlik değerleri tip-eğrisi çözümlemesinden elde edilenler ile aynı değer aralığında çıkmışlardır. Eagle Ford şeyli için üretim öngörüsü yaparken farklı soğurulma izotermleri kullanılmıştır. Üretim öngörüsü sonuçlarından gazın geri bırakılmasının hem rezervuar basıncı hem de soğurma izotermine bağlı olduğu sonucuna varılmıştır. Erken zamanda gazın geri bırakılmasının, yüksek rezervuar basıncı nedeniyle, genelde pek de önemli olmadığı bulunmuştur. Laboratuarda ölçülmüş soğurma izotermlerine göre, gazın etkin olarak geri bırakılması için uzun erimli üretim öngörüsüne gerek vardır.

Ayrıca, basit hidrodinamik benzeşlikten yararlanılarak azalım eğrileri türetilmiştir. Çeşitli üretim azalım eğrisi çalışmaları baz alınarak, kuyu üretkenliğinde önemli bazı

fiziksel unsurlar da sınanmıştır. Eksponansiyel veya hiperbolik azalım eğrisinin Devoniyen Şeyli kuyuları üretim azalım verilerine gayet iyi uyabileceği görülmüştür. Üretim azalımının açık akışa, kayaç basıncına ve özgün şeyl üretim mekanizmalarına bağlı olarak karakterize edilmesine uğraşılmıştır.

Sıradışı şeyl rezervuarların çatlatılmış yatay kuyularında geçici basınç davranışı ile üretim davranışını modellemek üzere analitik bir üçlü doğrusal akış çözümü ortaya konulmuştur. Model basit olsa da, bir şeyl rezervuarın matriksi ve doğal çatlaklarının içsel özeliklerini de içeren temel petrofizik niteliklerini birleştirecek yeterlilikte çok yönlüdür. Modelde akışkan takasının özel özgünlüklerine ek olarak çeşitli rezervuar bileşenleri de göz önüne alınabilmektedir. Ayrıca, sıradışı şeyl rezervuarların çoğul çatlatılmış yatay kuyularındaki geçici basınç tepkilerinin çözümlemesi için pratik bir analitik model de sunulmuş ve açıklanmıştır.

Petrol ve gaz fiyatlarının dikkate değer düzeyde yükselişinden sonra, A.B.D.'deki sıradışı şeyl rezervuarlardan petrol ve gaz üretimi hem teknik hem de ekonomik olarak yapılabilir hale gelmiştir. Teksas'ta Forth Worth yakınlarındaki Barnett şeyli A.B.D.'deki ve dolayısıyla dünyadaki olgun şeyl girişimleri arasında tatmin edici üretim geçmişine sahip olanlardan bir tanesidir. Bu nedenle, 6000'den fazla üreten kuyusu ile geliştirilmiş olan Barnett şeylinin üretim ekonomisinin incelenmesi, şeyl girişimlerinin nasıl ticarî hale getirilebileceğine ilişkin fikir oluşturabilmek için örnek bir model olarak dikkate alınabilir.

Bu tez çalışmasının gerçekleştirildiği süre içindeki maliyetler ve fiyatlar esas alınırsa, bir kuyunun maliyetini karşılamak için doruk gaz üretiminin yaklaşık 550 ile 900 milyon standart feet küb arasında olması gerekir. Şeyl kayaçlardan petrol üretiminde ise, olgun bir sahadan günde 100 000 varil petrol üretebilmek için en düşük petrol fiyatı en azından varil başına 43 USD olmalıdır.

1. INTRODUCTION

Petroleum Industry has been applying the conventional methods for exploring and producing oil and gas accumulations in the structural or stratigraphic traps in subsurface formations. Conventional methods have been developed so as reservoir rocks with reasonable magnitude of porosity and permeability have been focused for oil and gas extraction. It is commonly accepted that petroleum occurs from the organic matter buried in a source rock and, as the overburden and tectonic stresses increase to compact the source rock towards a drastic decrease in porosity and permeability, migrates out into adjacent porous and permeable strata. Such migration, entitled the "primary migration," continues until petroleum encounters a trap, which would be bounded above by a sealing stratum, which is impermeable to petroleum and is called "caprock." Then, the "secondary migration" takes place, during which petroleum moves upward through the interconnected porous network and accumulates in the trap to form a reservoir.

This type of oil and/or gas trap is called a "conventional reservoir," which comprises of three layers of different rocks, or two of these layers may be of the same kind of rock. The upper and lower rocks are non-permeable with almost no porosity, while the middle rock which contains the oil and gas is very porous. In many cases, the lower part of the reservoir may be supported by water and not a rock. For hundreds of years, this was the main interest for petroleum engineers since there was no technology and convincing oil and gas prices to guarantee production from the source rock called hydrocarbon shale rock.

Shale gas and oil can be defined as natural gas and oil trapped within the fine-grain sedimentary rocks known as shale or mudstone which can be rich source rocks for natural gas and oil. In the United States, the impact of shale gas has been especially profound and it has change the energy equation around the world, even though the natural fracture and flow mechanism through these multi-porosity systems are not well understood. Countries and companies are investing huge sum of money into this shale industry so as to have better understanding of this complex system to maximize

production. There have been a lot of controversies and debates on this shale industry. For instance, there is still debate on the predominant transport mechanism such as diffusion, convection and desorption, and also flow interaction between fracture, organic matter and inorganic matter.

Many researchers are trying to modify the current equations and simulators to models this ultra-low porosity system, and this has led to changes in equations and simulators from the conventional reservoirs to this shale reservoir systems.

2. BACKGROUND INFORMATION

As far back in early 1860s deposits of opencast shale was discovered, in an area between Hayscraigs and Pyothall, Scotland. Shale mining for production of oil and gas was started by Robert Bell during his coal operations in Broxburn village, Scotland, sometime in 1861. Bell is credited with being the first man in Scotland to distil oil from shale and his shale discovery laid the foundation of the great shale oil industry [1]. Bell method of shale oil production was totally different from what we are experiencing nowadays. Bell used to dig out the shale using pig axe (mining) and distilled mineral oil out of the kerogen content in the rock. Bell was heating the rock to a high temperature to vaporize the kerogen, and this vapor condensed into slow-flowing oil, petroleum like liquid called shale oil [1]. Bell was threatened with legal action in 1870s because the streams near his oil works were being polluted with the water discharged from his shale oil field. He decided to pump this discharge up to the top of the shale waste hoping that it would evaporate. Instead, it gradually soaked right through the shale and finally oozed out from the bottom edges. To his surprise, Bell notice that the grass growing around his discharge was much more luxuriant than the grass growing further away, so he decided to analyze that liquid and found out that it contained ammonium nitrate, a very valuable fertilizer. The business grew so much that it became difficult for one individual to control, and this was one of the reasons why the Broxburn Oil Company Limited was formed in 1877 [1].

After the discovery and exploitation of most of the conventional and large scale oil and gas reservoirs in the world, the attention of petroleum industry has turned into the exploration and production of the unconventional hydrocarbon (oil and gas) resources. Among the unconventional resources coal bed methane, very tight (very low permeability) oil and gas reservoirs, shale gas, and shale oil have been the ones that drawn the most attention due to their significant quantity of hydrocarbon content. However, it has been soon realized that the exploration and exploitation of unconventional hydrocarbon resources could be achieved using the newly developed technologies and substantial amount of investments, in addition to cumbersome and persistent efforts.

Shale oil and gas technologies have been developed to produce from such source-rock reservoir over a decade and will be continuing for foreseeable future. Even though these technologies are not well understood, many shale gas fields are being produced by the main mechanism of hydrocarbon desorption and associated flow through the microscopic and/or macroscopic porosity generated within the reservoir by stimulation operations. With the hope that we can still use renewable energy for decades to sustain the growing demand for energy, shale oil and gas is gaining importance in strategic thinking for securing energy need for the future.

With the modern technology horizontal wells can be drilled into the source rock, and multiple fracturing operations can be conducted in those wells to create flow channels that increase the connection between the pores of the rock, so that oil and/or gas can be produced directly from the source rock. In early 1970s this technology was possible but the cost involved was so high that it became uneconomical to produce from the source rock. The rapid growth of human population has increased the demand for oil and gas as the sources of energy for movement from one place to another, to generate electricity, and to warm houses or to cook food. As a result, over dependence on oil and gas has led to a significant increase in oil and gas prices [1].

Even though the technology has not been fully developed, sufficient increase in oil and gas prices had made it possible for nations and organization to invest more money into research so as to provide adequate knowledge for petroleum engineers to produce directly from the source rock. Therefore, the developments in technology with the increase in petroleum prices has re-awakened the shale oil and gas business in the United States. Soon after, this business has rapidly become a zeal across the World, so that the exploration efforts were initiated in various countries that have potential shale formations in their sedimentary basins. As of today, besides the U.S. at least two or more countries have succeeded to produce oil and/or gas from shale formations that were determined to be the source rock.

Shale is a fine-grained, laminated, indurated, and fissile sedimentary rock with more than 67 % clay-sized minerals. Since fissility is not an inherent property of a rock, shale has been refered to as mudstone by many researchers. The term "mudstone" is used for a sedimentary rock that is composed of grains, of which more than 50% is in the size of less than 62.5 microns. Shale can be the source of in-situ generated hydrocarbon fluids, i.e. crude oil and natural gas. Over the past decade, the synergy

of horizontal drilling and hydraulic fracturing applications in shale formations has allowed the access to the rich accumulations of in-situ generated hydrocarbon fluids, of which the production was previously uneconomical has then become economical. Horizontal well drilling and hydraulic fracturing processes are not new technology in the industry [2]. Horizontal well drilling, as we know today, was first performed in 1930s and has become a common application in 1970s. Hydraulic fracturing was first experimented in 1947 and was accepted to be commercially viable in 1950.

2.1 Shale Gas

Shale gas resources are found in the sedimentary basins across the World. Oil and gas production from some of the shale formations in Devonian-age shale formation stack, including Marcellus shale, as shown in Figure 2.1, in the Northeast region of the U.S. is not new [2].
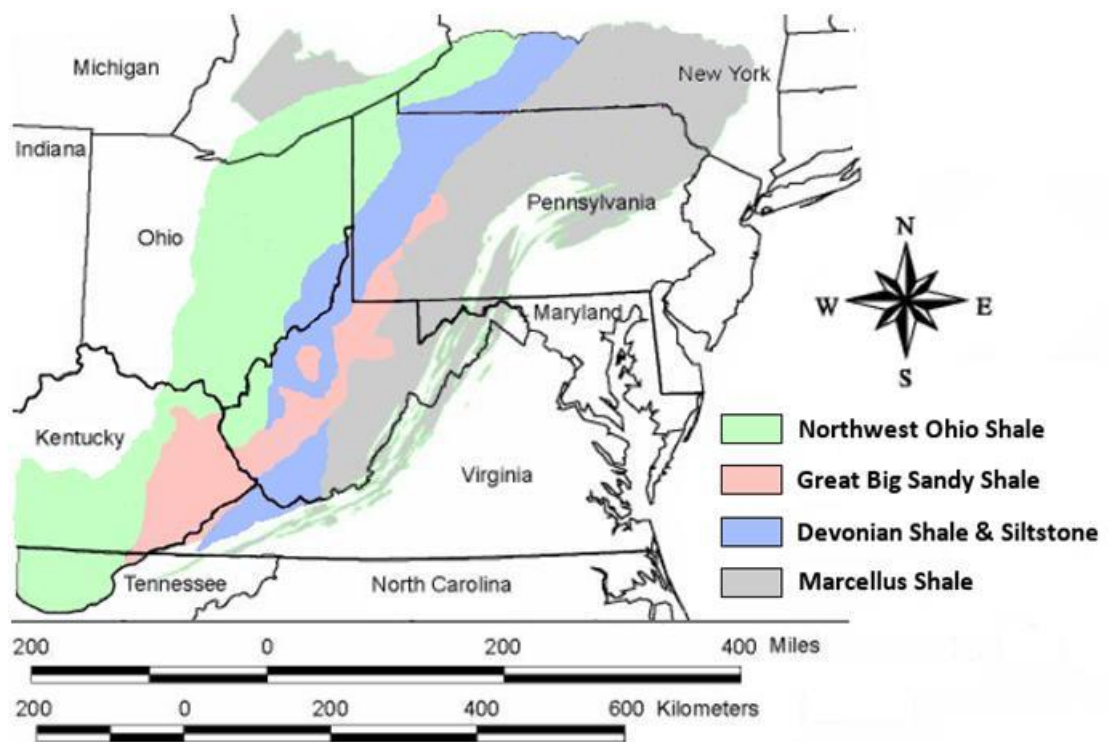
Figure 2.1: Distribution and vertical stack of Devonian-age shale formations in the Northeast region of the U.S.; modified after Reference [3].

Between the years of 1800s and 2000, over 20,000 wells have been drilled in shale formations in the United States. First oil production of 0.24 m^3/d in the Devonian Shale, a member of the Devonian-age shale formation stack, was recorded in around 1939 [4]. Shale oil and gas production increased tremendously in the U.S., between

1979 and 1999 [1]. Economical production from these ultra-tight shale formations became possible in the past decades due to the technological advancement such as horizontal drilling and hydraulic fracturing. In the year of 2007, 225 to 248 TCF of gas was estimated to be stored in Devonian and Ohio shale reservoirs of the Appalachian basin in the Northeastern United States. At the beginning of 2009 about 410 TCF and by 2012 up to 2700 TCF of gas was estimated to be contained in the Marcellus shale, located below the Devonian shale stack in the Northeastern U.S.

According to the estimates by the U.S Energy Information Administration (EIA) 6622 TCF of the World shale gas resources was technically recoverable, and about 29 % of this amount was in the U.S. About 4 TCF of gas was produced in 2000 from the U.S shale gas reserves, of which 31 and 76 TCF was declared to be technically recoverable and another 131.3 TCF of gas was estimated to be undiscovered gas [4]. In 2006, the U.S. proven shale gas reserves were increased to 92 TCF, of which 58 TCF had been produced, and the undiscovered gas reserve was estimated to be 350 TCF. Gas Technology Institute (GTI) in the U.S. claimed that approximately 5000 TCF of gas was stored in all U.S tight gas basins and about 185 TCF of this reserve was technologically recoverable [5]. As shale oil and gas has become an increasingly important source of oil and natural gas in North America, over the past decade, the use of horizontal drilling and hydraulic fracturing technology for the development of unconventional oil and gas reservoirs was pioneered in the U.S. Such breakthrough has led to a huge 35% increase in natural gas reserves in the U.S. and this result has spurred a massive interest in the industry by 2008.

2.1.1 Shale oil

Shale oil was originally considered as a reserves supply of crude oil to fuel US Naval vessels in case of emergencies. Historically the U.S. Federal government has had an interest in encouraging the development of the shale oil resources. The existance of the largest shale oil resources in the Federal land made the Federal government a complete owner of the resources. The shale-oil bearing lands initially in Wyoming and California then in Colorado and Utah were set aside for production of fuel for the Navy under the Pickett Act of 1910 [6]. The areas that contain shale oil in Colorado, Utah and Wyoming are shown in Figure 2.2.
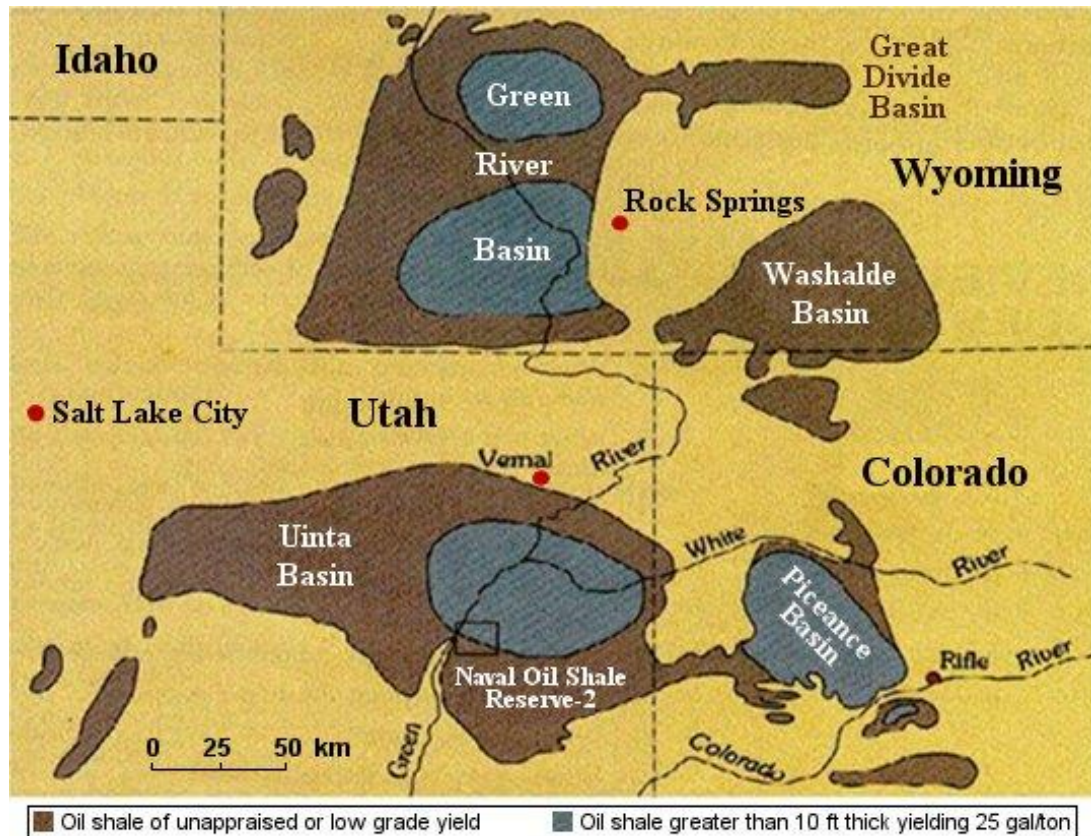
Figure 2.2: Distribution of Shale oil reserves in three basins in the states of Colorado, Utah and Wyoming [6].

Beside the shale oil reserves in Green River, Uinta, Piceance, and Washalde basins, as much as 3 billion barrels of oil, lower in grade with respect to the aforementioned, is in the Devonian-Mississippian shale that is thinner than the Green River shale and extends over 400,000 square miles. Other shale oil of interest is in the Triassic and Jurassic age Alaskan marine shale, of which the grade and reserves have not been determined. The upper Triassic shale with an oil yield of 30 gal/ton and unexplored extensions of similar grade shale are estimated to contain about 200 billions barrels of oil. Black marine shale of Northern Alaska is extensive with oil yield over 25 gal/ton and may contain 250 billions barrels of oil. Heath and Montana shales with oil yield of 10 gal/ton have the potential to produce more than 180 billion barrels of oil along with vanadium, molybdenum, selenium, nickel, and zinc [6]. The Woodruff formation in Nevada contains low-to-moderate grade shale oil with 0.8 % vanadium-pentoxide. Shale oil may also be present in the Phosphoria formation of Idaho and in the underlying strata of the Great Plains and Rocky Mountains [6].

With all these reserves potential of hydrocarbons, fuels, and raw material, previous attempts to develop shale oil industry was not successful due to one reason or the other. Savage suggests a misplaced emphasis on process engineering and a lack of attention to mining technology. Welles also suggested that the oil companies had and has a strong reluctance, if not aversion to the development of an alternate energy industry because of the fear of establishing competitors which may be subjected to different regulations and hence have unfair advantages over the well-established oil production systems [7].

In 1973, the Yom Kippur war between Egypt and Israel led to the declaration of an embargo against countries friendly to Israel by the OPEC (Organization of Petroleum Exporting Countries), which promised to reduce oil production level drastically on monthly bases until a political objectives were met. Immediately after this embargo was announced the U.S. declared its support to Israel, in the period when the U.S. was dependent on imported oil as the main source of energy. The embargo adversly affected the U.S. since the price of oil, which was less than $2 per barrel previously, was increased to $12 per barrels. When the political objectives of the OPEC was met and the embargo was lifted, the price of oil was never reduced and this condition led the U.S. to re-discover its interest in the development of the vast deposits of shale oil. Most oil companies that had been abandoned after the World War II were revived to buy coal mines to extract gas from coal and oil from shale.

But again, this situation did not last for long time until 2005, when shale oil has regained grounds due to both the development of technology and very high demand for petroleum, even with continuously increasing fuel prices, which made the oil and gas production from source rock economic. In 2005, the U.S. Congress conducted hearings on oil shale to discuss opportunities for advancing technology that would facilitate "environmentally friendly" development of shale oil and oil sand resources. The hearing addressed administrative and legislative actions that necessitated the provision of incentives for exploration concerns and industry investment [8].

In 2005, Shale Oil Task Force was established by the Bureau of Land Management (BLM) to address problems relating to the accessibility of shale oil on public lands and to the factors that could impede the development of the shale oil industry on public lands. Although the Title 30, Section 241 (a) of the Mineral Land Leasing Act restricted the individual lease size on public lands to 5,120 acres, the shale-oil

advocates claimed that this restriction would impede the economic development. The claim led to the raise of lease size to 5,760 acres and to the restriction of total lease holding to no more than 50,000 acres in any one State [8].

On September 20, 2005, the BLM announced that 19 nominations for 160 acres of public land were received and to be leased in Colorado, Utah and Wyoming for the research, development and demonstration (RD&D) of shale oil. On January 17, 2006, the BLM announced the acceptance of eight (8) proposals from six companies for the development of shale oil technologies. Of these selected companies the major ones were ExxonMobil Corp., Oil-Tech Exploration LLC., Shell Frontier Oil and Gas, Chevron Shale Oil Co., and EGL Research Inc.. The six out of 8 proposals would consider in-situ extraction to minimize surface destruction, and all proposals were subject to be scrutinized under the National Environmental Policy Act (NEPA). Apart from the 160 acres of land allocated for RD&D proposal, an area of 4,960 acres of land was reserved for preferential right to each project sponsor for future commercial lease after further BLM reviews [8].

Shale oil was also identified as a strategically important domestic resource by the Energy Policy Act and, then, DOE was directed to coordinate and speed up the development of shale oil to commercial production. Thus, the Section 369 (q) of the Act (Procurement of Unconventional Fuels by the Department of Defence) directed both Secretaries of Defence and Energy to develop shale oil production for the fuel that can meet the standard of fuel demanded by the Defence Department, which was regarded as of the national interest. This realization led to the cooperative action of the Defence Department and the Energy Secretary for the establishment of the Clean Fuel Initiative, which was intended to develop, test, and certify the use of zero-sulfur fuels that would be suitable for use in aircraft turbine engines, ground vehicles, and in fuel cells to generate electricity [9].

2.2 Global Interest in Shale Gas and Oil

The interest in unconventional shale oil and gas has also grown worldwide. With this revived interest, at least one or two countries in every continent is either producing shale oil or gas, but much is read and heard about shale gas rather than shale oil. Nevertheless, the technology initially developed to produced shale oil has a direct or indirect influence on the production of shale gas. Many countries are striving to

achieve the horizontal drilling and hydraulic fracturing technology used to develop unconventional oil and gas resources. The countries listed below have attempted to become a major shale gas and shale oil player [1].

Morocco, South African Republic, and Zaire in Africa.

Russia, Israel, Jordan, Syria, Turkey, China, Burma, and Thailand in Asia.

Italy, Poland, Germany, Austria, Bulgaria, Czechoslovakia, Luxembourg, Portugal, Spain, Serbia, Croatia, Romania, Scotland, Sweden, and Switzerland in Europe.

Canada, the United States of America, Mexico, Costa Rica, Argentina, Brazil, Chile, Paraguay, and Uruguay in the Americas.

Australia and New Zealand in the Pacific.

2.2.1 Current status

Currently about 20% of the gas produced in the United States is being supplied from shale gas, and natural gas resources in the United States can mostly be found in hydrocarbon rich shale formations. Although the shale oil and gas play is spreading across the World and huge sums of money are currently being invested to develop the sector, the productivity forecasting and the science of shale gas in general is still young. In 2005 only few hundred wells were drilled for shale gas. The longest time of production history is available for approximately six (6) years, even though about twenty thousand horizontal well have been drilled as of 2011.

An unconventional shale reservoir that has organic kerogen content equal or greater than 2% is considered as a prospective reservoir. The hydrocarbon that will form in shale is determined by the type of kerogen and the thermal maturity [6]. During the maturation of the kerogen a part of the hydrocarbon formed may escape from the source rock and move into another location to form a conventional oil and gas reservoir. A part, sometimes, charges the inorganic rock while the other parts can be found in the natural fracture within the shale. There is some evidence that indicates most of the hydrocarbon is within the pores of kerogen. The pores in kerogen may range from a very few nanometers to a very few hundred of nanometers [10].

During the early days it was mostly believed that the regional variation in reservoir quality in shale formations was relatively minor and understanding of production mechanism as well as petrophysical analysis were very poor. It was also then and

still is believed to a certain extent that well completion technology determined the primary production and economic success [11].

Many researchers across the world have published many papers and journal articles on this shale oil and gas business, but mostly on shale gas. These publications are on the modern technologies used in geological survey and the techniques of drilling, completion, reserves estimation, and production as well as in the environmental problems associated with the shale oil and gas business.

Some of the shale oil and gas bearing rock formations encountered worldwide that we come across on which publications are available worldwide are as follows;

The Devonian shale which covered over 25% of North America continent. This black and grey shale lies mostly between Mississippian shale and Middle Devonian limestone. The shale is called the Woodford shale in the Western plain states basin where it is thin, it is called the New Albany shale in the Illinois basin where it is 300-100 meters thick, the same shale which is 25-40 meters thick is called the Anthrim shale in the Michigan basin. Along the western Appalachian basin where the thickness is up to 400 meters and is called either the Ohio shale or the Chattanooga shale. In the central Appalachian portion of the basin, stratigraphic problems arises in eastward where the interbeded sands and silts of the Appalachian Catskill deltaic sequence changes facies. Large quantities of gas from the Devonian shale are been produced along the western Appalachian flank. The blank-like deposit in eastern Kentucky and in western Virginia and Ohio are the major areas of production of shale gas [12]. Four criteria (regional facies pattern, area of thick shale accumulation , the degree of thermal maturation of the organic matter in the shale and the presence of extensive fracturing or faulting) was used to indicated that southeastern Illinois was the suitable area for the production of Gas [12]. Usually shale in the Appalachian basin are from black to brownish- black in colour, laminated and organic-rich shale where the shale gas is being produced [13].

Makenzie Delta also referred to as Beaufort Basin which is not defined towards the Northern part, overlies part of a continental margin basin extending northward benearth the Arctic Coastal plain, and offshore from the northern coast of Alaska and Canada. The location of Makenzie delta is shown in the Figure 2.2 below.

Figure 2.3: Map showing location of Makenzie Delta in Northwestern Canada [14].

To the southeast, there is a complex fault that seperates the formation from a stable cratonic shelf extending to Canadian shield, the southern part borders of this basin is made of high-lands (the Richardson Mountains to the North and the British and Barn Mountains to the east) (Figure 2.3) [14].

The Northern Arabian plate which is mostly called the Gotnia basin is made of the Naokelekan formation, the Barsarin formation, the Sargelu formation and the Najmah formation. Most of these formations are been named differently in other places.

The Naokelekan formation is made of thin bedded having bituminous limestones, micritic limestones, black bituminous calcareous shale and a thin bed of fine-coarsely crystalline bituminous dolomite. The Gotnia formation composed of thick anhydrite with a thin limestone bed, has four halite units in the Southern Gotnia basin, and in South West of the Gotnia basin, the Dhruma formation which is almost the same in age as the lower portion of Sargelu formation can be found [15].

The Barsrin formation consist of intra-formational breccias alternating with laminated beds of limestones and beds of gypsum locally preserved. Sargelu formation comsist of black shale, dolomitic limestones, cherty limestones and a thin bedded bituminous limestones. The Najmah formation in which well Najmah-29 can

be found, is 340 meters thick consisting of 240 meters of limestones and 100 meters of dolomite [16]. The Najmah formation is about 450 meters thick in South West of Iraq, and this thick Najmah formation platform made of margine carbonates passes through Eastwards in Western Iraq to relatively condensed thin basin euxinic faces of the Naokelekan formation.

The term Naokelekan formation is not used in Kuwait. The Lateral equivalent of Sargelu and Najmah formation is known as the Surmeh formation in the Zagros of Iran and composed of thick platform of limestones and dolomites. Sehkaniyan formation made up of three units (the upper unit, middle unit and the lower unit) composed of dark brown weathering factid sacchariodal dolomites unit of dark brown limestones in the upper and lower portion and a pelletal fossiliferous limestones equivalent to the Alan Anhydrite and Adaiyah Anhydrite formation and the Mus limestone respectively in the middle unit. In Kuwait and Iran, these formations are equivalent to the middle and upper Marrat formation and the Neyriz formation respectively [17].

In Ecuador, the Hollin formation is divided into two (the lower and the upper). The lower is refered to as Hollin Principal and Secundario is the name given to the Upper member. The Hollin Principal is further split into three stratigraphic units(the Upper Sandstone called Marron, the interlayer shale and the Lower Sandstone called Naranja). The lenses of shale in the Upper and Lower sand areal extent is not large.

Hollin Secundario is again divided into four stratigraphic units (Verde, Azul, Radioactive and Hollin Secundario). Bermejo South field stratigraphic sections indicate that thickness variation, areal distribution, and facies changes for these stratigraphic units [18].

The Ghandames basin is an intra-cration polycyclic intracontinental basin, located within the Saharan platform and extends to more than 250,000 km^2 in the Western part of North Africa. In North Africa, huge reserves are mainly from a world-class source rock (the base Silurian Hot shale and the late Devonian Frasnian Hot shale).

The Silurian Hot shale is widely spread more than the Frasnian Hot shale which was significantly affected by the Hercynian erosion. The Silurian Hot shale is present in Southern Tunisia with a thickness of 30 meters [19]. Sud Remada formation which is located in the Northern flank of Ghadames basin, exhibits a transitional position

13

Permian basin towards the North and Paleozoic Ghadames basin towards the south. The Northern border of the Sud Ramada basin is defined by Nefusa and Telmzane arches and the Southern border is indicated by Gargaf High [20]. Figure 2.4 below shows the distribution of hot shale in North Africa.
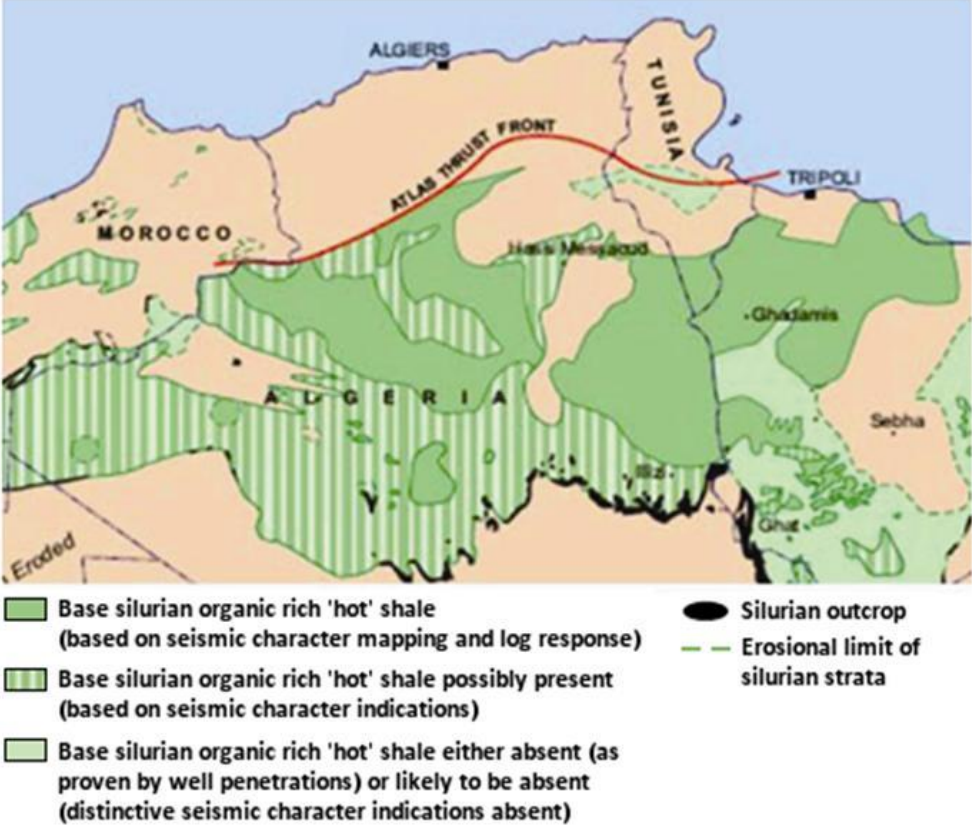
Figure 2.4: Hot shale distribution in North Africa [19].

In the United States, the Bakken formation which covers parts of Montana and North Dakota as its US share, is an oil-bearing stratum and the most important tight oil play. The Bakken formation is made up of three different layers (Upper layer, Middle layer and the lower layer) in which production started over 50 years ago. In between the black upper and lower shale is the middle layer of the Bakken formation which is very fine-to-fine grained argillaceous, dolomitic sandstone to siltstone [21]. The latest release of USGS in 2008, the Bakken formation resources in its US shale which is undiscovered was estimated to be 3.65 billion barrels of oil and the quantity of natural gas present was also attracting (relevant). The substantial increase of the new estimate was as a result of the unprecidented achievement of hydraulic fracturing and horizontal drilling in this field. The Bakken formation covers 200,000

square miles of Williston basin in the North Dakota and Montana and continued to Canada, belongs to the late Devonian and early Mississippian age [22].

Also in Turkey, two shale-gas basins were assessed and published by Advanced Resources Internation [23]. These basins are the Thrace Basin in the Western Turkey and the Southeast Anatolia Basin along the border with Iraq and Syria. These basins can be seen in Figure 2.5 below. These two basins are under active shale gas and conventional gas exploration by the Turkish Petroluem Company (TPAO) and international exploration companies. The interior Black lake and the Taurus basin as well as the onshore portion of the Black Sea Basin in Turkey may also have shale gas potential. But as the detailed reservoir data on shale formations are not readily available for these basins, the potentials of their shale gas reources are not been assessed.

Figure 2.5: Shale gas basins in Turkey [23].

3. CLASSIFICATION OF SHALE FORMATIONS

Shale is a fine-grained sedimentary rocks that contain significant amounts of clay minerals. Shale is formed as a result of clay having being compacted by pressure throughout vast geological time period. Over many millions of years, it has been laid down one stratum on top of another eventually forming hard rock such as coal or a less firm rock such as shale, depending on amongst other things including the amount of organic material contained within it. Shale is a timely-layered, soft rock, that splits easily, but not all shale contains oil. There are two different types, ordinary shale and hydrocarbon shale. Since we are more interested in shale oil and gas, much emphasis will be put on the hydrocarbon shale.

There is little information on shale rock classification or typing, nonetheless, shale rock typing is very important. It provides a better understanding of the shale reservoir which can further improve shale oil and gas production. Even in the conventional reservoir, understanding the properties of the reservoir rock allow the petroleum engineer to apply a very suitable recovery technology to enhance recovery. A reliable shale rock typing based on proper shale rock typing techniques allows the petroleum engineer to detect best production interval, gives an idea of the Total Organic Content (TOC), and the completion technique to be used in this interval to maximize recovery.

Unfortunately, there is insufficient or little information on shale rock typing technique, and this means we can still increase the productivity in shale containing oil and gas in future, since many researchers are making effort to develop shale rock classification technique that will provide better understanding of the shale rock properties within a particular locality. Even though the research is still ongoing some have finished and published their findings.

A new technique called "Real-time rock classification" based on logs and well-logs-based estimates of petrophysical, compositional and elastic properties, successfully classified the Haynesville shale gas formation [24]. Since most rock typing

techniques requires large number of core measurements to be collected for heterogeneity and different rock capturing in the formation detection, this technique minimize the core measurements to characterize heterogeneity in organic-rich shale formation vertically. The identified rock types and petrophysics estimated. Compressional and elastic properties were further cross match using thin-section core images and core measurements respectively. They started by well-log interpretation and finally cross match the results against core data. The processes involved in the well-log interpretation to estimate compositional, elastic and petrophysical properties are discussed in the following sections.

3.1 Well-Log Interpretation

Depth-by-depth petrophysical and compositional properties of the formation such as total porosity, TOC and volumetric/weight concentration of minerals and fluid constituents were estimated using joint interpretation of Photoelectric Factor (PEF), bulk density, neutron porosity, compositional-and shear-wave slowness, and Elemental capture Spectroscopy (ECS) logs. Organic-rich source rock's non-clay minerals, clay minerals, organic matter and total pore space were obtained using the Assumed petrophysical/compositional model. The mineral types input to the joint inversion were obtained from core X-ray Diffraction (XRD) measurement, and non-uniqueness of the results was reduced by the addition of constraints based on core measurement to the inversion.

3.1.1 Assessment of elastic properties

Again depth-by-depth estimates of elastic properties, bulk and shear moduli in the formation was obtained after the estimation of the volumetric concentrations of minerals/fluid constituents. A reliable assessment of effective bulk and shear moduli was calculated by using a self-consistency model. This model includes elastic properties, volumetric fractions and shape geometry of rock components (minerals and fluid-bearing pores). Grains and pores were represented as idealized shapes, like spheres and penny-cracks. The effective bulk and shear moduli was calculated using the equations given below respectively.

$$\sum_{i=1}^{N} X_i \ (K_i - K_{sc}^*)P^{*i} = 0 \qquad (3.1)$$

and

$$\sum_{i=1}^{N} X_i \ (\mu_i - \mu_{sc}^*)Q^{*i} = 0 \qquad (3.2)$$

Where i = each rock component, X_i = volumetric fraction of the rock component i, K_i and μ_i are bulk and shear moduli for the rock component i, N is the total number of inclusions, K_{sc}^* and μ_{sc}^* are the matrix effective bulk and shear moduli. The factors P^{*i} and Q^{*i} corresponds to the shape geometry of the rock component "i".

From the estimates of bulk and shear moduli, Dynamic Young's (E) modulus and Poisson's Ratio (v) were then calculated using the equations below.

$$E = \frac{9K\mu}{3K + \mu} \qquad (3.3)$$

$$v = \frac{3K - 3\mu}{2(3K + \mu)} \qquad (3.4)$$

K and μ are the matrix effective bulk and shear moduli (Birch 1961) estimated.

3.1.2 Rock classification

Based on the processes above, the shale was classified by using an unsupervised artificial neural network. Different input parameters was indexed using fuzzy clustering method and a Self-Organizing Map (SOM) known as Kohonen map to classify the shale rock. The SOM sizes corresponding to classes of numbers and nodes (10 x 10 maps represent 100 nodes) were then fed to the unsupervised artificial neural network. These inputs were either well logs or well-log-based estimates of compositional, elastic and petrophysical properties.

For the second part, the petrophysical and compositional properties of the formation was determined from well logs and core data. These properties were obtained from PEF, apparent resistivity, neutron porosity, bulk density and ECS logs from the formation. Their petrophysical model assumed components like illite, quartz, plagioclase, calcite, dolomite, kerogen and pyrite for Haynesville field case. TOC volume/weight concentration was obtained by using ΔlogR technique incorporating acoustic and resistivity well logs. From this TOC estimates, the volumetric concentration of kerogen which was included as a constraint in the joint inversion of well logs was calculated (by inverting the results again). XRD measurements

indicate a linear correlation between concentration of quartz and a plagioclase, and this was another constraint in the inverse problem to reduce uncertainty.

Depth-by-depth effective bulk and shear moduli of the matrix was estimated by using the Self-consistent approximation model, and by observing thin-section of core images and previous works on this field different shapes and mineral and fluid bearing pore ratios in the matrix were assigned. Spherical shapes were considered for stiffer rocks constituents and softer rocks constituents have been assigned by penny-crack shapes. The penny-crack or oval shape pores was assumed to contain the reservoir fluid, and more than one shape was considered for minerals such as calcite.

They identified four classes of rock by using inputs data from well logs and well-log-based estimated properties. The rocks were labelled as Rock Type M1 to M4. It was observed that the rock class M1 (yellow) was the best class for production and M4 was the worst class for production. The average physical properties, petrophysical composition, and elastic properties of each rock class where inputs to the rock classification technique were estimated from well logs and well-log-based properties respectively are shown in Figures 3.1 and 3.2.
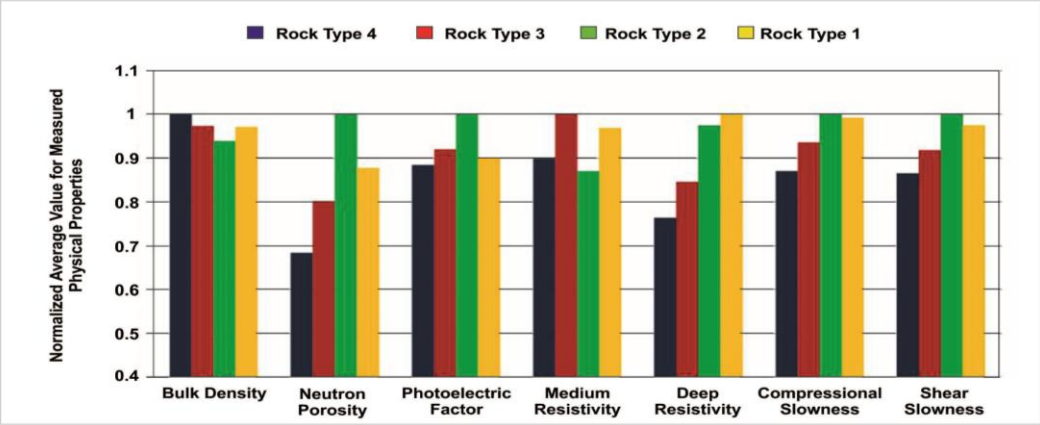
Figure 3.1: Normalized average values for measured physical properties of the four rock types when well logs are inputs to the rock classification technique [24].

Finally, they crossed match the rock classes identified at different depths by using thin-section images. The identified rocks petrophysically were in good agreement with the lithofacies defined by other researchers. Rock Types M1 and M2 classes were the laminated mudstone facies and M3 represent the Bioturbated facies with evidence of fossils, shells and sponge spicules in the core images, and the final M4

classes which has a low concentration of TOC represent the organic-poor Haynesville shale facies.
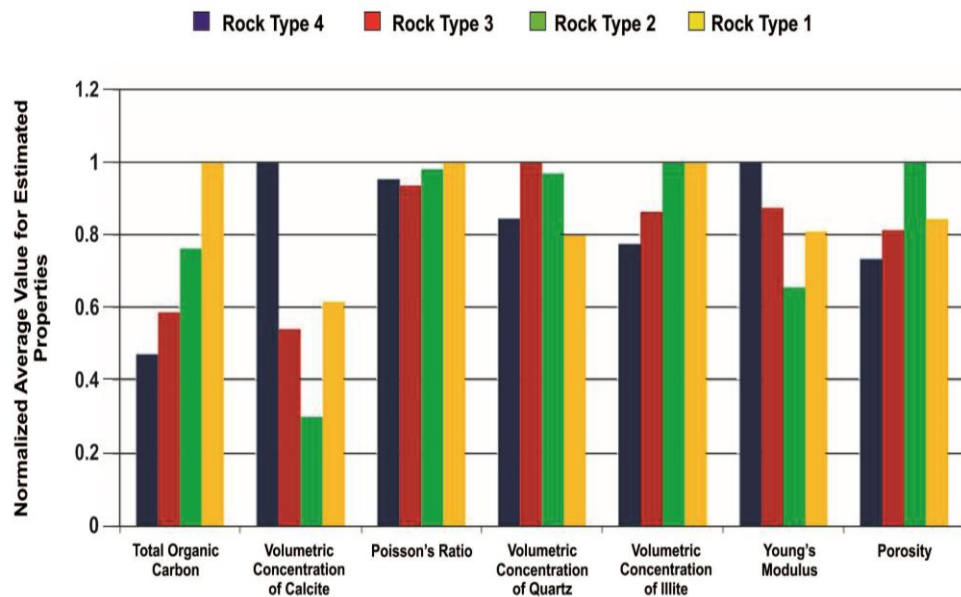
Figure 3.2: Normalized average values for petro-physical, compositional and elastic properties of the four rock types when estimated values are inputs to the rock classification technique [24].

A technique (with the assumption that a combination of well logs can identify groups of rock that shows similar compositional properties), was introduced to classify a hydrocarbon bearing-rock reservoir by using conventional well logs and core data [25]. The main objective of developing this technique was to know whether in hydrocarbon-bearing rocks, well logs can be used to determine the classes of rock and also to determine whether in classifying rocks, the inversion of layer properties gives advantage by minimizing shoulder-bed effects and vertical resolution refinement by performing log and core alignment and employing inversion of estimates of layer properties and estimates of rock compositions. This technique does not quantify reservoir parameters directly, hence cannot be used to quantify gas-in-place. Nonetheless with the conventional well log, this typing provide qualitative rock classes which can be used to compute net-to-gross, carry out well-to-well correlation, validate conventional interpretation techniques and provide facies distribution for integrated reservoir modeling in a source rock reservoir. This technique also present inversion calculation method developed for source rock reservoir applications and, assumed to be valid for mineralogy estimations from

conventional well logs. The technique is based on observation from core data obtained from the interpretation of well logs and by direct measurement of rock properties in the laboratory. With well logs and core data, statistical techniques are used to expose correlations between well logs from different wells. These statistical techniques are called K-means cluster analysis and Factor analysis. These techniques were chosen due to their ability to handle larger amount of complex data. Since shoulder-bed effects pose problems to statistical techniques in conventional well logs, one of the aim of these techniques was to establish whether inversion of layer properties provide advantages in rock typing by reducing the shoulder-bed effects.

3.1.3 Measurements procedures

Formation properties from well logs were estimated and their inverse calculated as the inverse properties are critical to the evaluation of source rock reservoir. Applying a two-step inversion technique [26], the results of the first inversion of the well logs readings were used to type source rock. The second inversion yields volumetric concentrations of the various rock components and were used for subsequent verifications of the rock types. Table 3.1 shows the properties and parameters involved in the inversion below. Core data which was obtained in the laboration was grouped according to similarities using the commercial software package of K-means clustering. The quantity or number of well logs used for cluster analysis was reduced by factor analysis. This tecnique assumed that a multivariate set of data has a relationship with controlling factor. Measurement that correlated to one is most likely to influence the same factors, since the factor analysis quantifies covariance between data measured [27]. The Factor Analysis serves two purposes; to determine the logs that should be used for the cluster analysis and also to confirm that the particular unique elements in source rock are determined by inversion process, through the use of responsive logs to such elements.

The process of inversion is known as "nonlinear" inversion in this work. Rock classification can be used as an alternative verification method of a multi-mineral solution.

K-means cluster analysis is best performed when data correlations are linearized, hence it is important to linearize resistivity and sonic logs if they are to be use in the K-means cluster analysis, because these logs mostly exhibit nonlinear correlations

with other logs. We can linearize them by taking the inverse or by taking their logarithm.

Table 3.1: Mineral, fluid and resistivity values assumed in rock-compositional inversion for the lower Barnett formation well [25].

Constituent Mineral	Source
Quartz [SiO_2], $\rho = 2.65$ g/cc	Zinsner and Pellerin (2007)
Calcite [$CaCO_3$], $\rho = 2.71$ g/cc	Zinsner and Pellerin (2007)
Pyrite [FeS_2], $\rho = 5.01$ g/cc	Zinsner and Pellerin (2007)
Illite, $\rho = 2.78$ g/cc	McKeon and Scott (1989)
Kerogen [$C_{6.5}H_{10.2}N_{0.12}S_{0.02}O_{0.32}$], $\rho = 1.3$ g/cc	Yen and Chilingarian(1976)
Contained Fluid	
Gas [methane - CH_4], $\rho = 0.2$ g/cc	Estimate from Schlumberger Chart book, Gen-8: Density and Hydrogen Index of Gas
Water [with salinity of 90,000 ppm NaCl equivalent]	Zhao et al. (2007)

Archie's Resistivity Parameters

	a	m	n
Class 1	1	2.05	2
Class 2	1	2.3	2
Class 3	1	2.1	2
Class 4	1	1.7	1.5

3.2 Rock Typing Validation With Compositional Results From Inversion

Estimates from nonlinear inversion of rock-composition gives an opportunity to examine rock classes determine from well logs and inverted estimates of bed-properties. With these estimates of composition, the cluster of log responses (rock type) were grouped together with regards to similarities in composition, especially kerogen concentration, and they can further categorized and develop rock types as core data providing a comprehensive rock classes.

A synthetic case was established to ascertain the following;
1) The overaging of bed-level properties effects on well logs and subsequent well-log-based rock types,
2) The importance of inversion for the properties resolution in well logs and mineral compositions.

3) To what entent or level of data manipulation (inversion of well logs properties ,mineral compositions and un-invented well logs) yields the best practical inputs for rock typing.

This synthetic model assume that in a formation, individual beds are homogeneous with negligible dip. The physical properties of interest in this artificial model were density, photoelectric factor (PEF), apparent deep resistivity and migration length. The numerically stimulated well logs with a sampling interval of 0.5 ft were represented by measured bulk density, neutron porosity, apperant resistivity and PEF. Volumetric concentration of the solid and fluid constituents assumed in the model are shown in Table 3.2 below.

Volumetric concentrations of all lithological components plus porosity sum to 100%. Water and methane saturations are displayed as a percentage of pore space concentration.

Table 3.2: Hypothetical solid and fluid constituents for three rock types included in the hydrocarbon-bearing shale synthetic model.

Lithological components (%)	Rock type 1 (calcite rich)	Rock type 2 (Silt rich)	Rock type 3 (organic rich)
Quartz	35.5	61	53
Calcite	35.5	3.5	3.5
Pyrite	1.5	1.5	2
Illite	24	24	24
Kerogen	1.5	5	10.5
Pore components (%)			
Porosity	2	5	7
Water saturation	80	40	20
Methane saturation	20	60	80

The hypothetical rock type were represented by parameters composition, (a calcite-rich rock type as rock type 1, a silt-rich and organic-poor rock type as rock type 2 and organic-rich rock type as rock type 3). These composition of rocks was based on observation from the lower Barnette formation core data.

Attempts were made to ascertain whether the inverted numerically stimulated logs from this synthetic case could reproduce model properties at different bed intervals (thickness). But it was established that, when bed thickness are equal or thinner than

sampling intervals, the inverted values are unreliable estimates of true bed properties, hence in thinner beds, inverting well logs results in large errors on inverted values due to bed placement and thickness. Nevertheless, the inversion shoulder-bed and vertical resolution effects were reduced significantly to emphasize that layer properties can subsequently be used for statistical grouping.

K-means cluster analysis was also carried out by considering neutron, density and resistivity measurements. With this K-means analysis, in order from most to least accurate, the model rock type properties were reproduced from the inverted properties, center-bed values and un-inverted well logs. The actual rock types in thicker beds than 0.5 ft was identified by inverted well logs values. The correct rock type values in center-beds were reproduced until 1 ft section, stimulated logs in multiple instances throughout 10 ft, 2ft, 1ft and 0.5 ft in field log produced groups which were as a result of thin bed and shoulder-bed effects.

These techniques were finally applied to the Barnette shale gas formation and the Haynesville formation, and it was found out that, in the Barnette formation, four different types of rocks identified. Rock quality ranking interms of highest to the lowest kerogen concentration as (a) rock type 1, (b) rock type 3, (c) rock type 2 and (d) rock type 4.

In the Haynesville where K-means cluster analysis was employed in connection with well-log-based, it was observed that two groups of rock can be found in this formation; rock type 1 which constitute 46.4% of the reservoir while rock type 2 constitute the remaining 53.6% of the reservoir. Also when the K-means cluster analysis was empolyed in connection of the inverted well-log properties, the same two rock types were identified but there were differences in their constitutions as compared to the well-log-based, since each rock type constitute 50% of the reservoir, and this differences can be attributed to shoulder-bed effects. But in all the two formations the results obtained were in agreement with other work done on these field interm of classification.

The Barnett shale reservoir rock was classified by integrating geological core description with porosity, TOC, mineralogy and mercury injection capillary presure technique. About 800 plugs obtained from almost 1600 ft of core, were continuously recovered from the Newark East field [28], [29]. Stratigraphic columns developed by

Singh [30] was used to assign lithofacies of these plugs. Capillary curves and microstructure obtained by ESEM was found to be different from each petrofacies.

Three goups of rocks were identified from the petrophysical measurement and were labelled '1', '2' and '3'. Cluster analysis also shows that the rereservoir rock cored can be grouped into three classes when petrophysical data obtained were used. It was then found out that, petrofacies '1' was the best reservoir rock in terms of high porosity, TOC and quartz content, but has a low calcite content. To ascertain the high quality petrofacies '1', thickness was compared with the overall gas production in two vertical wells, it was found that wells peforated in the continuous petrofacies '1' intervals where petrofacies '2' and '3' interference was minimum, produces more and better than wells perforated in the intervals where petrofacies '2' and '3' were more. Hence they concluded that petrofacies '1' was the best reservoir rock and a better gas producing rock in this particular field in terms of petrophysical sense.

Samples for their study was taken from four different wells on this field. Well 'A' and 'B' in the core production area were vertical wells, but wells 'C' and 'D' which was in the extended part of the field were horizontal. Core from the horizontal wells does not cover the lateral portion of these wells in the reservoir since it was taken from adjacent pilot wells. For the measurement of porosity and mineralogy, samples were taken within the intervals of 2 ft while samples for mercury injection measurement was taken in every 10 ft to reduce bias towards some of the lithofacies. For TOC measurements samples were taken in every 2ft in wells 'C' and 'D' but at a selected locations in wells 'A' and 'B'.

To get homogeneous samples, every single large piece of rock was broken into smaller pieces during the sampling before used for petrophysical measurements. Hellium porosity, FTIR mineralogy and Hg injecton capillary pressure measurements were conducted at the Integrated Core Characterization Center (IC^3) at the University of Oklahoma while TOC sampls were sent to commercial laboratory for measurement. A total number of data set used in petrophysical measurements was 796 for mineralogy and porosity. For TOC, 436 data set were used and 130 data set for Hg injection capillary pressure measurements.

3.3 Measurement Procedures

A technique for measuring porosity by using helium in the IC^3 laboratory was developed [31]. This technique, which removes free water without removing the organics contained in the sample, measures effective porosity based on Boyle's Law.

Thermo Gravimetric Analysis (TGA) was used to determines the maximun heating time and temperature for FTIR minerology experiment [32] This maximum heating time is a fuction of the sample minearolgy. The bulk volume of the whole sample was measured and recorded after heating and cooling down to room temperature by using Hg immersion technique. The particle sizes of the sample was measured after crushing the sample using pestle and crucible. The particle size obtained by using Laser Diffraction Particle size Analyzer on 41 samples was somewhere 400 μm. The distribution of the particle size of the crushed sample where the weight loss of sample during crushing was kept to less than 0.1 weight %, was used to measure Helium porosity by accounting for the weight lost in the sample. The crushed sample was finally heated again under the same conditions as in the first heating cycle. The grain volume of the sample after cooling down to room temperature was measured by Low Pressure Pycnometer (LPP) apparatus. Porosity was then calculated by using measured bulk and grain volumes.

Sixteen minerals were detected in the sedimentary rocks and quantified in terms of weight percentages by using Fourier Transform Infrared Spectroscopy (FTIR) technique during the mineralogy determination. About 0.3 g of potassiumbromide (KBr) was mixed with 0.0005 gm of the sample that was in a finely grinded powder form. 10 ton of load was used to pressed this mixture into a die to get a thin transparent disc. A spectrum that is proportional to the mineral concentration was then obtained after the disc was put into a sample holder and run in the FTIR machine. After inverting the spectrum produced by using inversion software developed in the laboratory, the mineralogy of the sample was obtained. The KBr which was completely transparent to mid-infra-red radiations was used due to the ionic bond betweenits atoms. Because moisture and organic carbon shows very strong peaks in mid-infra-red sections, the sample must be free of moisture and organic carbon before being pressed into the disc to mask the absorption of other minerals peak.

By using low temperature plasma Asher to oxidize the sample as low as $80^{\circ}C$, organic carbon present can be removed and vacuun pump can be used to remove CO_2 as a product organic carbon oxidation from the oxidation chamber continuously.

LECO method was used to measure the quantity of TOC (total organic carbon) in samples. The samples, which was first powdered and dried, were acidified with hydrochloric acid (HCl) to remove all associated inorganic carbon in the form of CO_2, while not affecting the organic carbon contained in the sample. The sample was combined in an environment that was rich in oxygen, and the generated CO_2 was allowed to passed through a non-dispersive infrared-detecting cell that selectively detects and quantifies the CO_2 produced. The percentage of carbon in the sample was then calculated by material balance.

The connected pore space and pore throat distribution is measured using mercury injection capillary pressure apparatus. External pressure is predefined to be between 5 to 60,000 psia. The sample is first dried and, then, put into the pycnometer of the apparatus before it is sealed in the low pressure measurement section. The pressure is reduced to 200 mm of Hg (mercury) column by vacuum pull and is maintained for one hour to remove the traces of moisture and air from the sample and the flow lines of the experimental set up. The mercury is injected into the sample and its intruded volume is measured and recorded at each pressure step, until the maximum level of injection pressure is reached.

At a pressure of 5 psia, Hg was introduced into the Penetrometer through the stem to filled the empty space in the Penetrometer and surrounds the sample contained in it. The introduced Hg then exert a proprtional hydrostatic pressure as the pressure is applied from outside onto the sample, the mercury begins to occupy the pore space in the sample. Stabilized pressure equilibrium over sixty seconds was allowed to reach at each step before adjusting to the next pressure step. Externally, the pressure was applied with Nitrogen at the low pressure sections, and during the high pressure sections of the experiment, the pressure was applied externally with mineral oil to the Autopore IV machine. The mercury length in the Penetrometer stem decreases as Hg fills the pore space. The penetrometer behaves like a capacitor when filled with mercury as the stem is made of glass and coated with metal from outside.

The dropping of mercury levels during the intrusion cycle of the experiment decreases the capacitance of the Penetrometer stem. The differences in capacitance was recorded at each pressure step. This capacitance was then converted to Hg intrusion into the sample at each pressure step. Capillary pressure curves was generated with these readings for the sample.

It was observed that, the average porosity of all the 796 samples was 5.7% with a standard deviation of 2.1%. The accuracy of the measurement was within the +/- 0.5%. The sixteen minerals was found and identified in the sedimentary rocks by the FTIR mineralogy technique. Quartz, calcite and illite had a dynamic range to be used for rock typing. Apart from calcite, the rest of the minerals did not correlate with other petrophysical parameters like TOC and porosity very well. The rock typing correlations was then generated based on the content of calcite in the samples. Singh [30] work was used as basis to assigned lithofacies to each sample. Figure 3.3 below shows the ten samples lithofacies distribution.

Some of the lithofacies was found to show almost the same petrophysical properties as can be seen in Figure 3.4 below. These lithofacies were grouped with regards to the fact that some of them contributed very little to the petrophysical properties within the inverval cored. The lithofacies grouped were unique with regards to petrophysical properties. Figure 3.3 which is the petrophysical column indicate that lithofacies 1,2, 3 and 6 were the major contributors, and Figure 3.4 shows clearly that these major contributors were different from each other in terms of perophysical properties and also suggest that there are three main groups of rock types. This suggestion was confirmed by the mercury injection measurement that shows three different capillary curves, as petrophysical parameters relating to each Hg injection curves were determined by using properties of the companion samples.

The major petrophysical parameters for these three petrofacies are shown in Tables 3.3 and 3.4.
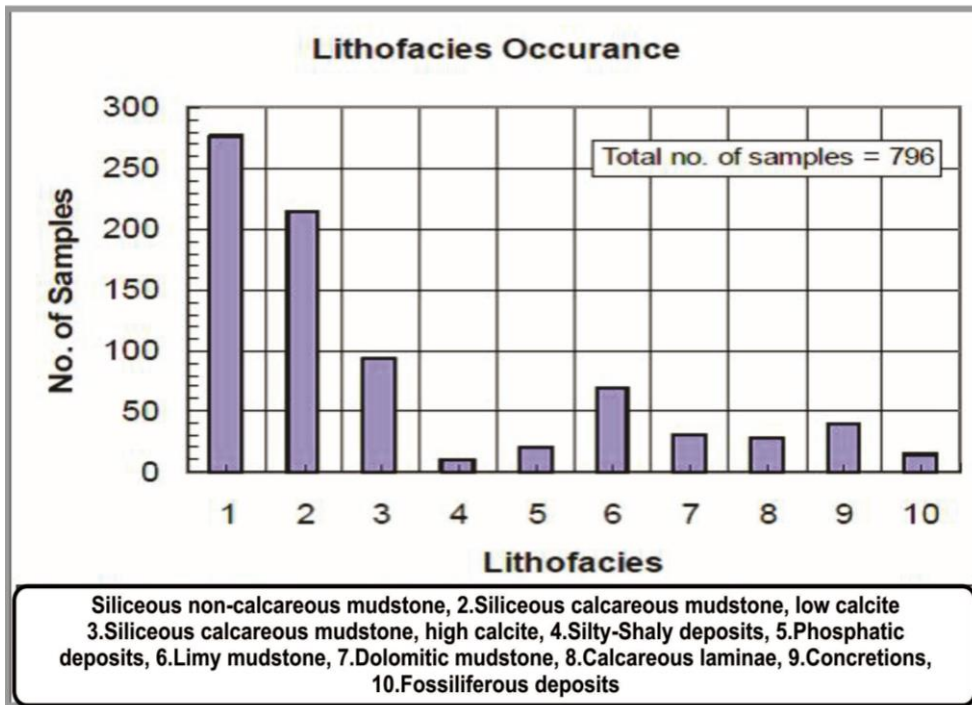
Figure 3.3: Occurence of lithofacies in the four wells obtained from 796 samples used for petrophysical measurements [28].
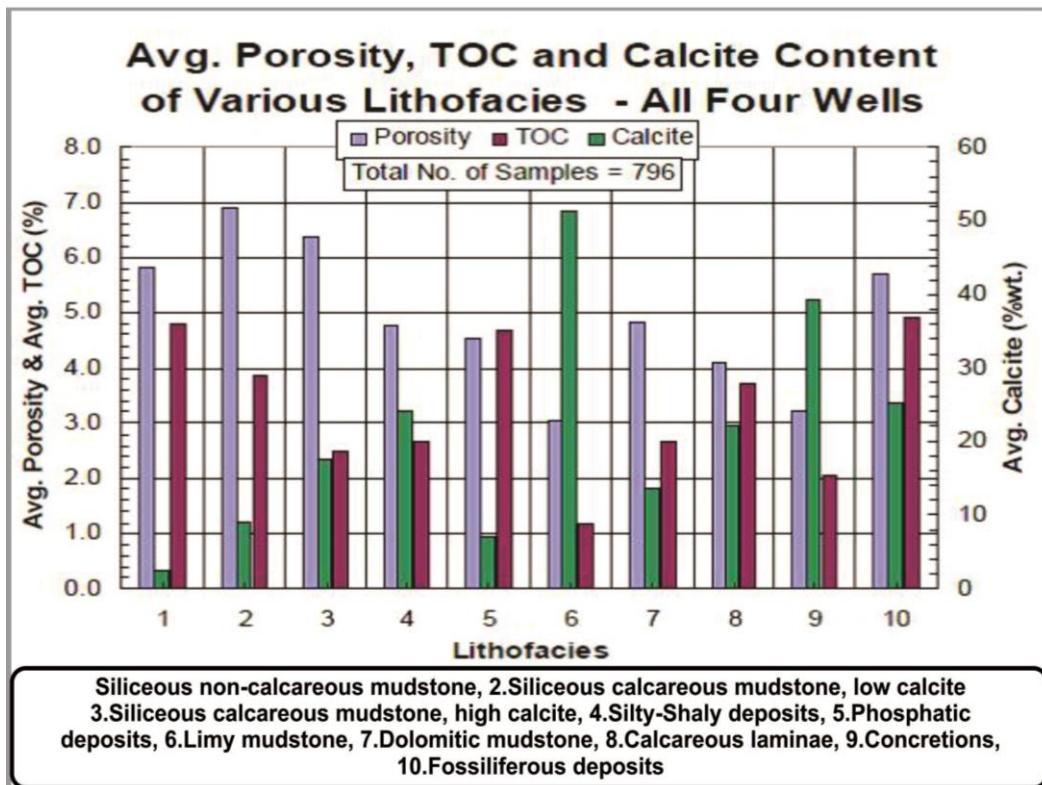
Figure 3.4: Each lithofacies average content for porosity, TOC and calcite [28].

Table 3.3: porosity and TOC data for the three petrofacies in Barnett shale along with lithofacies

Petrofacies	Helium porosity		TOC		Lithofacies
	average	95% confidence interval	average	95% confidence interval	
1	6.1	6.0-6.3	4.8	4.7-5.0	1,2,5
2	6.0	5.8-6.3	3.6	3.4-3.8	2,3,7,8
3	3.7	3.4-4.0	1.8	1.6-1.9	4,6,9

Table 3.4: Mineralogy data for the three petrofacies in Barnett shale.

Petrofacies	Quartz		Calcite		Clay	
	average	95% confidence interval	average	95% confidence interval	average	95% confidence interval
1	30	29.2-31.0	3	2.7-3.3	44	43.0-447
2	21	19.4-22.2	15	14.6-16.2	36	34.6-37.6
3	12	10.7-13.4	46	43.4-48.8	19	17.2-20.4

The petrofacies of these rocks were plotted against average porosity, average TOC and calcite content, as shown in Figure 3.5 below. The technique used here were crossed checked by using the same data set to type the rocks by applying Principal Component and Cluster Analysis. It was then observed that a fairly good equivelency exist between these two techniques.
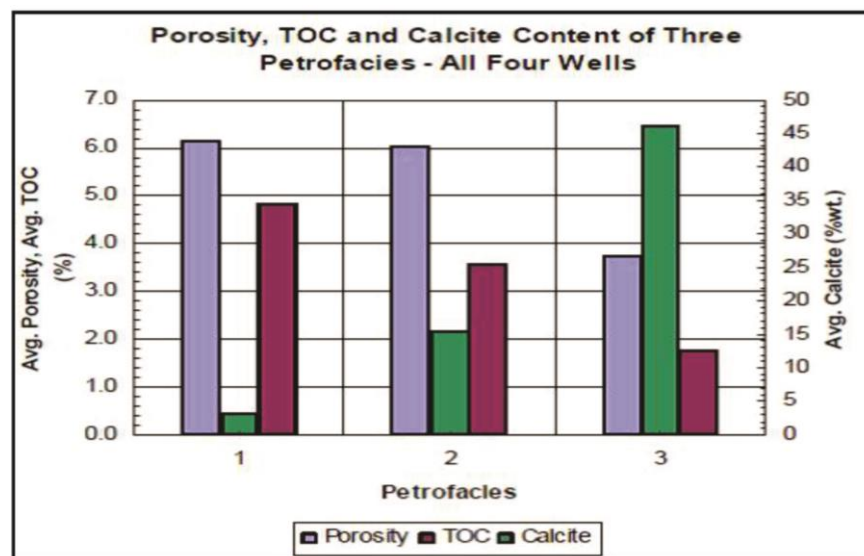
Figure 3.5: Average porosity, TOC and calcite content of three petrofacies in the Barnett shale play [28].

4. ESTIMATION OF RESERVES RESOURCE POTENTIALS

The first and foremost thing we think of when a gas well is evaluated for completion is the well payout time. This payout time depends on reserves forecasting and this reserves forecasting depends on estimating the recoverable reserves.

Usually, it is more difficult to estimate gas reserves than oil reserves. On volumetric basis, many factors affects estimations of reserves on multiples ways. Drainage area, volume factor and recovery factor are particularly difficult to obtain from an individual well; hence average area usually are replaced for actual values. Well test analysis informations is dependent on data derived from other test. Assessing reserves potential compared with other wells, preliminary reservoir data is very difficult.

Reserves estimations are then limited in the early life of the well and this is the option available so far. If the gas reservoir is tight and naturally fractured, more complications are even encountered. The Devonian shale of the Appalachian basin is an example of such reservoir systems. Gas is released in different ways in such reservoir systems. The gas is release as free gas in the open fractures, adsorbed gas on the walls of the fractures and on the matrix and absorbed gas release from the shale matrix. Mostly there are overlap of these three release mechanisms. A new well has no production history on which we can extrapolate a curve, therefore recoverable reserves estimation would be questionable. It is now left with the evaluation engineer to use the available data mostly the initial shut-in pressure and open flow rate and try to relate these to another well to draw analogy.

The production rate was used to produce a usual hyperbolic decline curve on a production rate versus time plot to estimates reservoir recoverable reserves [33]. They studied the relationship between the initial reservoir data to cumulative recovery in order to assess the reliability of using analogy to estimate reserves for the Devonian shale. Their study area represent a twenty county area along the common borders of west Virginia, Kentucky and Ohio. These areas has almost the same

geological, geochemical and reservoir engineering characteristics in light of shale attributes throughout the extensive Appalachian basin. On this area, there is adequate information and due to the promising nature of this field for future development, this area was considered for their study.

4.1 Study Procedure

Initial reservoir data was gathered from files of operators in the area and from gas Research Institute Eastern Gas Data System (EGDS). A total number of 508 non duplicated wells information was taken. But only wells that was produced continuously for twenty years history was considered in their study, since majority of these wells reserves are produced in the first twenty years, there was enough data for these wells. The 1970s and early 1980 heavy promotion affected many well to had insufficient histories and were screened off leaving 174 number of wells. Ten of which were in Ohio, eighty seven wells were in west Virginia and seventy one wells were in Kentucky.

Bivariate regression technique was used to test the dependency of recovery on test data in order to analyze the relationship between cumulative production and initial test data. A scattered diagram of initial open flow rate in thousand cubic feet of gas per day (Mcf/d) versus twenty year cumulative recovery in millions of standard cubic feet (MMcf) was generated with the 174 number of wells. The data was heavily clustered at the lower left hand side with many observed anomalous points spread to the upper right side. Without considering data manipulation, bivariate regression applied to such a diagram does not give satisfactory "goodness-of-fit. Therefore, between open flow rate and the recoverable reserves, there is no direct linear relationship.

Boundary conditions was imposed to obtained a working relationship. The data set was reduced by ten percent thereby placing the upper limit on initial open flow at 700Mcf/d ($19810m^3$/d), more compression would reduce the sample size too much to produced too limited relationship.

Also, a graph of initial rock pressure in pound per square inch (psi) versus twenty year cumulative recovery in MMcf was generated with the same 174 wells data. It was however observed that the data points did not follow a definite trend.

Again, a graph of initial open flow rate versus initial rock pressure was generated. Again the data set was scattered which suggest anomaly in the upper central portion of the graph. There was a dispersed of data points when the boundary conditions (700Mcf/d or 19810m^3/d) was imposed to facilitate a better bivariate regression.

The three graphs were generated to depict the range of data obtained before manipulation. To provide a linear relationship between the variables within the boundary condition was the main aim of the data manipulation.

Regression analysis was performed by imposing boundary condition on the data to generate the following graphs.

A) Recovery (MMcf) versus initial open flow rate (Mcf/d)
B) Recovery (MMcf) versus initial rock pressure(psi)

Considering the 700Mcf/d (19810m^3/d) level, the total number of wells was reduced to 154. In any regression analysis, statistical test need to be conducted to weigh the results and much emphasis must be placed on the confidence intervals of the equation over a range of values when working with one dependent and one independent variable at a time. The dependent variable extent is explained by the independent variable. When the dependent variable goes in line with a sequential pattern an autocorrelation is experience or we have a homoscedasticity when the dependent variable can be explained by the independent variable variation and how better the values predicted can be compared with the observed values.

For each state, the behavior of initial open flow rate versus twenty-year cumulative recovery was put in the form of a linear equation of y = a + bx by bivariate regression; in which "y" is the recovery in MMcf and "x" is the initial open flow rate in Mcf/d. Among the four regression lines generated, one was for the general regression line for the entire 154 well-data and the rest were for each state covered in the study. The statistical analysis is shown in the Table 4.1 below. A very broad confidence band have to be provided because of the scattered nature of the data points in order to get a high confidence level so that we can rely on the equations. For instance, a plot of initial open flow versus recovery for the general case requires a band of $\pm$ 250 MMcf if 90% confidence level is needed. Even though it is obvious that there was a very poor line fit, showing that there is no direct correlation.

Several measures-of-fit was employed as shown in Table 4.1, some of these were the percentage point of data beyond one standard deviation from the regression line. It was then observed that ''the further the actual point from the regression line, the more disastrous their effects on bivariate regression. The actual data lie more than three standard deviations from the regression line in some cases.

Table 4.1: Regression equations [33].

Case	Equation	A	B	C
Initial Open Flow vs. Recovery				
General (154 wells)	Y= 116.160 + 0.749x	25	33	Yes/Yes
West Virgina (74 wells)	Y = 113.392 + 0.654x	26	35	Yes/Yes
Kentucky (71 well)	Y = 128.644 + 0.839x	25	32	No/Yes
Ohio (9 wells)	Y = 32.969 + 1.058x	33	47	No/No
Initial Rock Pressure vs. Recovery				
General (154 wells)	Y = 190.593 + 0.138x	25	1.5	Yes/Yes
West Virgina (74 wells)	Y = 126.736 + 0.287x	24	6	Yes/Yes
Kentucky (71 well)	Y = 192.432 + 0.192x	17	2	Yes/Yes
Ohio (9 wells)	Y = -242.168 + 0.522x	22	28	Yes/No
Initial Rock Pressure vs. Initial Open Flow				
General (154 wells)	Y= 182.315 – 0.0047x	20	0	No/Yes

A: percent data points > 1 standard deviation.

B: percent variation explained by X.

C: Auto correlation / Heteroscedasticity.

Variations explained by the initial open flow rate (independent variable) and variation from other source such as autocorrelation in which the differences between the actual and the estimated recovery (residual) are related sequentially can be attributed to the departure from the regression line. Autocorrelation has a disastrous effect on the variations which was shown by the residual propagating along the regression line like sine wave. The extend of the error relating to this residual can be check against variation in magnitude of independence variable in order to identify the condition by which residual errors are inconsistent with changes in the independent variable (heteroscedasticity), if the error changes at the same pace with the independent variable, we have a homoscedasticity.

The four regression equations that is relating initial open flow rate to twenty years of recovery have a relevant number of observations which are beyond one standard deviation of the fitted lines as shown on Table 4.1. Only general case shows a moderate positive statistical relationship, while the individual states shows strong relationship with their various data. Even though Ohio and Kentucky shows no autocorrelation, the Ohio sample size was too small. Therefore, homoscedasticity was shown and at the same time high percentage of recovery variation was explained by the initial open flow rate for Ohio state. It was also observed that "the smaller the sample size, generally the better the regression fit and the more variation of the dependent variable is explained by the independent variable.

Also in the graph of initial rock pressure (psi) versus recovery (MMcf). It was the Ohio state that only shows a strong positive relationship and this can also be attributed to the small sample size nature. In Table 4.1, equations for the graphs, x is the initial rock pressure (psi) and y is the recovery (MMcf).

The data has a high residual as it was observed to scattered at the center of a graph, therefore had a broad band showing a poor fit. The initial rock pressure can be used to explain very little of the recovery variation. Most of the data points fall beyond one standard deviation from the fitted line but were less than two standard deviation away from the line.

All the four cases indicates autocorrelation but homoscedasticity was also shown in Ohio state alone. The small sample size of Ohio affected the regression line leading to the regression line intersecting the abscissa nearby. This can also be due to the fact that the lowest rock pressure for these samples was 605 psi (4170 kpa).

Finally, initial rock pressure versus initial open flow rate regression analysis was performed considering that the flow rate depends on the pressure. An inversed relationship between this analysis was observed, since an increased in rock pressure leads to a slightly decreased in open flow rate. Hence the equations in Table 4.1 show that the actual regression line is a horizontal line. The rock pressure could not be used to explain any of the initial open flow. Well treatment was suggested to be the factor most likely to cause this anomaly as only about 20% of data point lie within one standard deviation of the estimated recovery and residuals were auto correlated but randomly distributed.

It was realized that thermodynamics (phase behavior) of fluids in pores and capillaries having characteristics length which are less than 100nm is quite different, as gas in the small pores or capillaries having a low density is under the influence of the organic pore walls and shows a different density profile [34]. Well-meaning questions were raised with regards to gas-in-place calculations. Most of the questions were as follows;

What fraction of the pore volume of the organic material can be considered as available as free gas and what fraction is taken up by the adsorbed phase under reservoir conditions?, how accurately is the shale gas storage capacity estimated using the conventional volumetric methods?, and do average densities exist for free and adsorbed phase?.

A new a volumetric total-gas-in-place estimation equation was formulated by a combined Langmuir adsorption isotherm with volumetric equation for free gas which account for pore space taken up by sorbed phase. The sorbed phase for void volume was corrected and the density of the sorbed-phase was estimated to calculate the volume occupied by the sorbed phase. Finally, they modified the conventional method of reserves estimation to generate this new volumetric equation.

4.2 Sorbed-Phase Correction For Void Volume

Equilibrium adsorption-isotherm experiment is used to estimate the quantity of sorbed gas in the shale. Helium was used to measure the void volume in this study. The technique employed was the same as helium porosimetry technique used in grain density determination. The material balance and a given thermodynamic equation of state was used to measure the mass of sorbed gas, and estimate the void volume. An isotherm was then generated for the sorbed gas. At each pressure step in the process of constructing the isotherm, the adsorbed gas reduces void volume, therefore the initial determine void volume have to be corrected at the beginning and at the end of pressure step. It was observed that the isotherm analysis over the process for each subsequent pressure steps, the void volume was further reduced. It is therefore more convenient to determine the Gibbs isotherm in terms of number of moles of absorbed gas. Using the equation of state, the Gibbs isotherm was then converted to volume which was then adjusted for void volume with the Gibbs correction factor (ρ_f/ρ_s), where ρ_f is free-gas-phase density in g/cm^3 and ρ_s is sorbed phase density in g/cm^3.

The above mentioned void volume considerations are important since it has a significant implication on the "live" in-situ available shale pore volume for free-gas storage. Hence the effective-porosity/gas-saturation product derived from a total pore volume which is estimated under static laboratory conditions, does not reflects live-reservoir conditions. The total pore volume of the reservoir is consumed by adsorbed gas in addition to water and oil. This was the reason why it was suggested that, the calculated free-gas pore volume must be corrected for the adsorbed-gas fraction present under reservoir pressure and temperature conditions.

Also, it has been reported that most of the gas-storage capacity within the shale associated with the organic fraction of the matrix [34]. Hence the free-gas volume determined by pycnometry using non-adsorbent gas such as helium need to be corrected for adsorbed gas present within the organics.

4.2.1 Method for shale gas-in-place calculations

A new petrophysical model that is different from the previous effective porosity measurement to determine the total gas-in-place, by considering void space and sorbed gas mass estimated by adsorption experiment.

In this new methodology, it was observed that methane exist in different thermodynamics states and that estimation of gas-in-place in the shale should not be considered independently of these states, hence void space measured by porosity measurements plus sorbed mass measured by adsorption experiment minus free-gas volume taken up by sorbed gas is the best way to calculate the total gas-in-place. The new method put emphasis on two (2) different conceptual changes with regards to the old or previous model.

a) there is a dependency between the connected pore space and the organic.

b) there exist a dependency on the free pore space by the inclusion of the sorbed phase.

Focused-ion-beam (FIB)/scanning electron microgramme (SEM) images and segmentations observations shows that there are errors as a results of the assumption that the sorbed gas takes up no volume. It was then maintained that, to accurately calculate for the total and free gas-in-place, the volume that the adsorbed gas occupy should be estimated and subtracted from the free-gas calculation. It was therefore

proposed that, to calculate free-gas storage capacity in a standard way, the following equation 4.1 should be used;

$$G_f = \frac{32.0368}{B_g} \left[\frac{\phi(1 - S_w)}{\rho_b} - \frac{1.318 \times 10^{-6}\acute{M}}{\rho_s} \left(G_{sL} \frac{P}{P + P_L} \right) \right] \qquad (4.1)$$

Where G_f =free gas storage capacity, scf/ton. B_g = gas formation factor, reservoir/surface volume. Φ = porosity, fraction. S_w = water saturation, dimensionless. ρ_b = bulk rock density, g/cm3. ρ_s = sorbed phase density, g/cm3. $\acute{M}$ = apparent natural gas molecular weight, lbm/lbmole. G_{SL} = Langmuir storage capacity, scf/ton. P = pressure, psi. P_L= Langmuir pressure, psi.

The porosity of the water saturation measurements requires that the volume that is being occupied by the sorbed gas must be account for after correcting the water saturation.

4.2.2 Sorbed phase density

The density of the adsorbed gas must be known in the organic pores so that the volume occupied by the sorbed phase can be calculated. Due to the interaction between the methane and organic pore walls, methane local density is varied or expected to vary across the pores and also to differ from its average bulk density. It is very challenging to study phase transition and also tell whether the adsorbate is in the liquid or vapor form. This is due to the fact that shale gas reservoir temperature is much greater than the critical temperature of natural gas.

Many documented suggestions in physical chemistry literature had been used to estimate the density of adsorbed phase on the surface of solids. Dubinin [35] suggested that, adsorbate density is related to Van der Waals co-volume constant (b). Methane and propane density values was found experimentally to be almost the same as the Van der Waals co-volume constant (b) [36]. It was also argued that, sorbed phase density is equivalent to the liquid density [37]. The sorbed phase was considered as a superheated liquid and that the density depends on the thermal expansion of the liquid[38]. It was also suggested that the sorbed phase density is equivalent to the critical density [39]. It was also gathered all the above mention methods and compared them to Langmuir-Freudlich adsorption model, and observed that there is a temperature dependence in the sorbed-phase density, and this value approaches those suggested [35], [40].

All these studies did not indicate a clear and accurate way by which the density of the sorbed phase can be estimated in shale and therefore be used to calculate the total gas-in-place. The previous studies were carried out at low temperature and pressure values but the density of the sorbed-phase is sensitive to changes in pressure, temperature and pore size. The walls used in their studies was an organic walls [36]. Density in the first layer were in the range of 0.28-0.35 g/cc in this study, when molecular modelling and simulation was used. Methane has an adsorbed-phase density of 0.35 g/cc at 3043 psi and 176°F for pore width of 2.3nm when Langmuir single layer theoretical model was used.

The first principle of Newtonian mechanics was applied to numerical molecular-modeling approach to estimate the adsorbed-phase density. "molecular modelling and simulation is a form of computer simulation that enables us to study thermodynamics and transport properties of many particles systems, in which particles (atoms and molecules that make up the natural gas and pore walls) with initial known and instantaneously predicted position and moments are allowed to interact for a period of time, giving a view of the motion of the particles as trajectories in space and time" [34]. Newton's equation of motion numerical integration gives us the core of simulation, hence, special algorithm such as Verlet, Leap Frog or Beeman algorithm commonly used for molecular simulation studies have been developed.

In this case, they employed two sets of molecular-dynamic (MD) simulation runs to determine and analyze the density of the sorbed-phase under the conditions of reservoir temperature and pressure: a) the runs in the absence of pore walls (involving bulk-phase,) in which a constant number of methane molecules at a constant temperature and pressure was used to measure the methane-density, and b) the runs that involve methane density measurement at the same temperature but confined to a pore with organic (graphite) walls. In the latter set of runs, methane density profile deviation along the pore width was evaluated relative to the uniform bulk density, to consider the impact of the pore-wall effects.

4.3 Molecular-Dynamics (MD) Simulation Of Methane Adsorption In Organic Silt-Pores

Investigation at the molecular level, methane was considered under thermodynamic equilibrium in a 3D periodic orthorhombic pore geometry consisting of lower and upper pore walls made of carbon (graphene) layers at some supercritical conditions. Three silt-like pores with pore width (H) equal to 3.9, 2.3, and 1.1 nanometers (nm) was taken into account for comparison, since the important parameter was the pore width length scale for this study, and this is defined as the distance to the innermost graphene planes.

In the y-coordinates (L_y = 3.93 nm) the pore width length was constant but varies in the x-coordinates in order for both pores to approximately host the same number of molecules of methane (400-450) in the process of the simulation. For the small and large scale, the dimension in the x-direction were equivalent to L_x = 7.67 nm and L_x = 4.26nm respectively. The number of particles was increased from 400 to 600 within a 2.3 nm pore when the pore pressure effect was investigated. The computation time was approximately 1,500 – 3,000 seconds, but 100 to 144 cores was used during the simulation. The methane molecules was modeled by a united-atom carbon-centered by Lennard-Jones potential based on the optimized potential for liquid simulation (OPLS), OPLS-UA force field. Shown in Table 4.2 below is the distance and energy parameters that was used for solid/solid and fluid/fluid interactions [41].

Table 4.2: Lennard-Jones potential parameters for methane and carbon.

Atom	σ (nm)	ε / K_B (K)
carbon	0.34	28
methane	0.373	147.9

Lennard-Jones method was used for methane/solid and methane/methane interaction. Fluid/solid (methane and pore wall) interaction was described by Lorentz-Berthelot mixing rule, defined as [$\sigma_{ij} = (\sigma_{ii} + \sigma_{jj})/2$ and $\varepsilon_{ij} = (\varepsilon_{ii} \varepsilon_{jj})^{1/2}$]. Where σ_{ij} and ε_{ij} are the Lennard-Jones parameters accounting for interaction between a molecular site of methane species and a carbon atom of the organic wall. At 4.1 σ_{ii}, interaction of

Lennard-jones were cut off for 3.9-nm pore width, and at 3 σ_{ii}, Lennard-Jones interaction were again cut off for 1.1 and 2.3 nm pore width respectively. For all the three systems, Van der Waals interaction were cut off at 3 σ_{ii}.

The simulation was carried out by the DL-POY (version 2.20) MD simulation package [42]. Considering isotherm and isobaric conditions at a constant number of atoms, constant temperatures (176, 212, and 266°F) and at constant pressure, the bulk-density for methane was calculated using Nose-Hoover thermostat and barostat ensemble. The Nose-Hoover thermostat relaxation time was adjusted to 15 ps (pico-seconds). During the simulations of methane in carbon slit-pores, the fluid system was initially equilibrated at a constant temperature, and the canonical ensemble was also set to a constant number of atoms, volume and temperature. In the process, where there was no drift in time observed in the time-independent quantity, like the total energy of the system, the equilibrium was assumed to be achieved. For the pore width of 1.1, 2.3 and 3.9 nm, the Nose-Hoover thermostat optimized relaxation time was adjusted to 13, 15 and 20 ps respectively.

The real canonical ensemble calculations were conducted for the density calculations and the Nose-Hoover algorithm was used to control the temperature of the system. When the fluctuations in the density profile along the time were uniform, thermodynamic equilibrium was assumed to be achieved, and the average quantities within one (1) nanosecond (ns) intervals was used for the analysis. Usually, a simulation total run time was 1.5 ns with a pore and 0.003 ps time set was used.

Number of molecules per volume (ρ_{Number}) was calculated for methane at the end of each simulation at $\Delta Z = 0.2$Å intervals for the continuous density profile and at every $L_Z = 3.8$Å (for discrete density profile) in the Z-direction volume segment. The number density (ρ_{Number}) was estimated for each volume segment by "summing up the number of molecules counted in each interval within this volume segment, and dividing the total by the number of intervals". The local mass density of methane was obtained by converting the density number using methane molecular weight M_{CH4} and Avogadros's number as shown in equatıon 4.2 below;

$$\rho_{CH4} = \frac{\rho Number \times MCH4}{6.02252 \times 10^{23}} \quad \textbf{(4.2)}$$

To estimate a precise density profile across the pore to indicate the presence of these interactions and obtain an average adsorbed-gas-density value as a macroscopic quantity for gas- in-place calculations using equation (4.2) above.

Figure 4.1 displays the density profile of methane. At 176^OF and a pore width of 3.92 nm, methane density is not uniform across the pore, as the values near the walls are greater indicating that adsorption has occurred. But as the distance from the pore wall increases, the oscillations were being damped. Physical adsorption of the gas was observed as the number of molecules was larger in the first layer near the pore wall. In the second layer, the molecules were under the influence of pore walls even though the methane intermolecular interactions begin to dominate, and not allowing high methane densities. The methane density in the second layer is slightly larger than the methane bulk-density (0.124 g/cc) at the pore center. The pressure in this pore was 3,043 psia which was estimated using free-gas molecules and volume at the pore center. The density profile observed indicate that, to describe the equilibrium adsorption dynamics of methane in the organic pores, the assumption made by Langmuir adsorption theory with monolayer will be reasonable. The total discrete densities associated with the adsorption are sum up to give an estimate of the adsorbed-layer density.
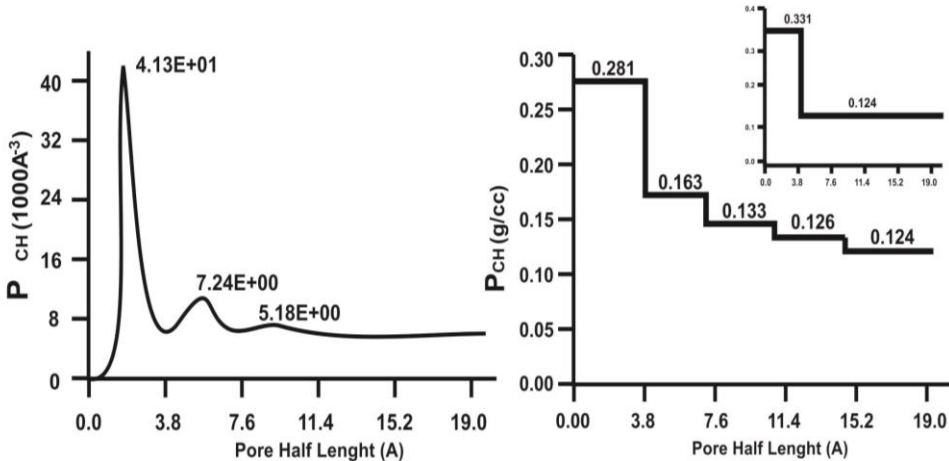
Figure 4.1: Number density (left) and discrete density (right) profile for methane at 176°F in a 3.93 nm pore [34].

4.3.1 Pore-size effects on methane adsorption

Small organic pores was constructed for supercritical methane as a result of pore-wall effects to show graded density across the layer of the pore. At the central portion of the pore where molecular influence interactions with pore wall is very small, a bulk-fluid region may exist depending on the size of the pore. A combination of molecule/molecule and molecule/wall interaction in pore size up to 50 nm, predicts thermodynamic state of the gas and its mass transport in the pore [43]. In the small pores on the other hand, molecules of methane were usually under the influence of the force field from the pore walls, therefore, pore pressure cannot be measured and bulk-fluid region cannot be observed in this pores too. Hence, rather than considering the free-gas molecules motion, the adsorbed molecules behavior should be considered. In the first layer, the adsorbed-phase density was large significantly. The larger the adsorbed-phase density, the smaller the pore. In short, physical interactions between the gas and solid is poorly described by Langmuir theory.

4.3.2 Effects of temperature on methane adsorption

In the large pore. The temperature effects on the density of methane is shown in Figure 4.2 below.
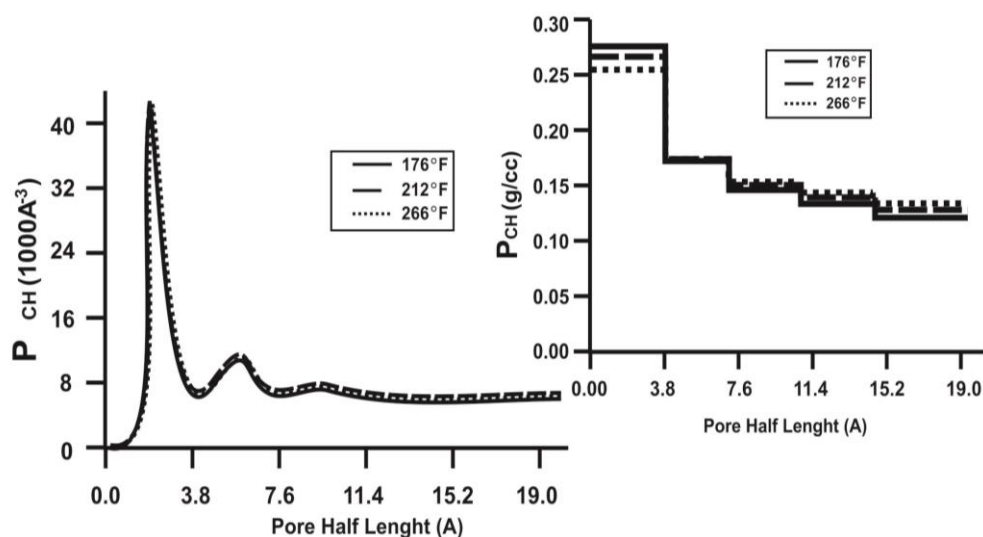
Figure 4.2: Number density (left) and discrete density (right) profile across half-length of a 3.9 nm width slit-pore as a function of temperature [34].

The predicted average density of the adsorbed-methane decreases with temperature. This indicate variations as a result of changing kinetic energy levels at the microscopic scale. The estimated values for free-gas density at the pore center corresponds to the values for bulk methane density independently estimated by using the National Institute of Standard and Technology's (NIST) thermophysical properties of hydrocarbon mixtures database, SUPERTRAPP, as shown in Table 4.3. It was clear that the numerical simulation was accurate.

Table 4.3: Effect of pressure on methane density.

Temperature (^{o}F)	Pressure (psi)	Methane bulk density (g/cm^3)	Methane bulk density* (g/cm^3)
176	2206	0.090	0.089
176	3043	0.124	0.122
176	3676	0.147	0.144
176	4141	0.160	0.159
176	4404	0.168	0.167
176	4586	0.176	0.172
176	4800	0.178	0.175
176	6272	0.214	0.211
176	7300	0.231	0.229
176	7550	0.235	0.233
176	8707	0.253	0.250

A new method presented for estimations of the total hydrocarbon volume and hydrocarbon mixtures in organic-rich shale, in the presence of capillary condensation by using theoretical results was also presented [6]. They found out that current models only considers two (2) parts of the gas (adsorbed gas on the surface of pore with density compared to liquid, and free-gas in the rock matrix) and does not regards capillary condensation part.

They suggested that, to accurately estimate shale gas reserves, a storage model incorporating the physics for fluid in nano-pores is a necessity. Such a model is also important for log data interpretation and longtime production and ultimate recovery predictions. Recent investigations indicate that, there are favorable conditions in the kerogen-rich rocks for capillary condensation to occur. The capillary condensation occurrence was verified in laboratory studies which occurs as a result of phase

equilibrium of vapor and liquid within the small pores, as there is an interaction between fluid and pore surface. Therefore capillary condensation occurrence also depends on the fluid properties just like pore size and pore surface wettability.

At reservoir conditions, pure methane will not condensate due to the high temperature condition, but will only condensate at very low temperatures. Hydrocarbon from shale reservoirs are always a mixture of multiple components. Capillary condensation in kerogen pores is facilitated by the presence of heavier components that increases the interfacial tension of hydrocarbon fluid.

4.4 Theory And Method

4.4.1 Capillary condensation of single-component fluids

When gas vapor pressure, P_V, is equal to or greater than the saturation pressure or dew point pressure, Pd, gas condensates in free space. Capillary condensation may occur and gas condenses to liquid under favorable conditions in small pores, even if the gas pressure is lower than the saturation pressure. Thompson was the first person to describe capillary condensation, and Lord Kelvin later in 1871. Kelvin Equation must satisfied in a pore with radius, r, before capillary condensation can occur. Kelvin Equation given in equation 4.3 as follows;

$$P_v \geq P_d \exp\left(-\frac{2\gamma V_L \cos\theta}{rRT}\right) \tag{4.3}$$

Where γ is the surface tension between liquid and gas phase, θ is the contact angle, V_L is the liquid molar density, R (8.31 J/mol-k) is the gas constant, T is the temperature in kelvin, P_d is the dew point pressure or saturation pressure and P_v is the vapor pressure.

The critical pore size, r_c, can be calculated by using equation (4.4) as follows;

$$r_c = -\frac{2\gamma \cos\theta}{RT \ln\left(P_V/P_d\right)} \tag{4.4}$$

The occurrence of capillary condensation in all pores with size smaller than the critical pores size (r_c) gives us two important facts; (1) when the liquid wets the pore surface the vapor pressure is smaller than the dew point pressure and, hence, capillary condensation occurs, and (2) in smaller pore, capillary condensation occurs much easier.

The pore size in kerogen ranges from few nanometers to few hundreds of nanometers, therefore, the pore in kerogen falls within the favorable conditions necessary for capillary condensation. Also, the non-polar organic matter that forms on pore surface must wet non-polar hydrocarbon strongly. A schematic storage model of hydrocarbon inside kerogen pores in an organic-rich shale is shown in Figure 4.3 below.
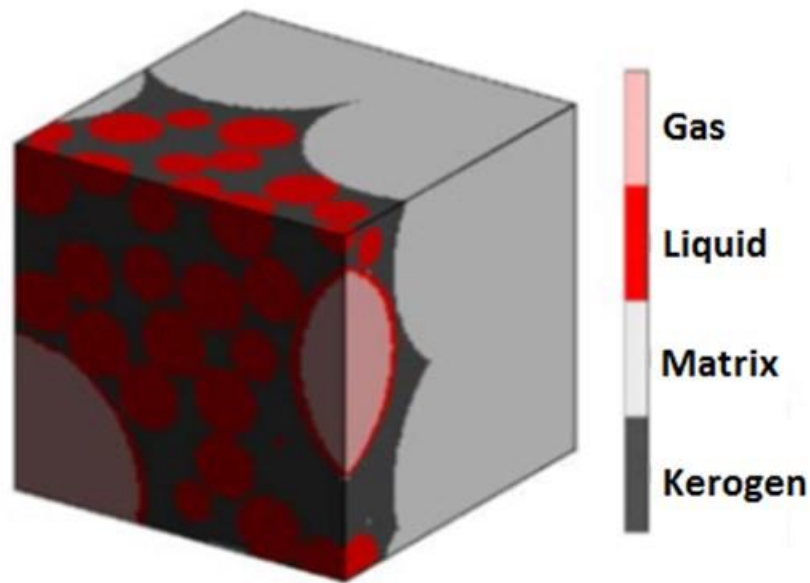
Figure 4.3: Schematic storage model for hydrocarbon in kerogen pores network in organic-rich shale in the presence of capillary condensation [6].

Inorganic matrix and embedded kerogen are represented by the grey and dark color zone respectively. The pores are divided into two (2); small pores with size equal or less than the critical size which is determined by equation (4.4), and large pores with size greater than this critical pore size. Due to the capillary condensation, the small pores are filled with liquid and the large pores are occupied by adsorbed gas on the surface of the pore walls and free gas within the pores, hence, this large pores can still be described by the traditional Langmuir model. In the Figure 4.3 above, liquid hydrocarbon inside the small pores and adsorbed hydrocarbon on the surface of the large pores with high-density are indicated by the dark red color. The hydrocarbon in the gaseous state in the large pores where capillary condensation does not occur are indicated by the light red color.

The total hydrocarbon in place according to Figure 4.3 is the summation of liquid hydrocarbon in the small pores where capillary condensation takes place, the

adsorbate found on the surface of large pore walls has its density close to liquid under reservoir conditions and free gas in the large pores.

4.4.2 Capillary condensation for hydrocarbon mixtures

The conditions under which the Kelvin Equation was obtained are not true for hydrocarbon in shale reservoir. The hydrocarbon in such reservoirs even though has methane as a major component, it contain ethane and other heavier or larger molecules. Fluid properties can be change greatly by these heavier component in a situation where capillary condensation is involved. The ideal gas approximation is not correct due to the fact that the down hole pressure is usually high. Hence, for hydrocarbon mixtures at down hole conditions with high pressure, a new model must be used to account for capillary condensation.

Hydrocarbon in the kerogen pores was considered, since inorganic pores hydrocarbon can be added to this method by the traditional Langmuir method for free-gas.

4.4.3 Critical capillary condensation pore size for hydrocarbon mixtures

It was assumed that, hydrocarbon in the vapor phase comprised of "n" components having a mole fraction for each component designated as $y = \{y_i\}$, $i = 1,2,3,\ldots n$. Conditions for capillary condensation in the free space occurs at dew point pressure, P_d. At the dew point, liquid contain all the components having mole fraction $X_{ld} = \{x^i_{ld}\}$, $i = 1,2,3,\ldots n$. At pressures lower than the dew point pressure with a different liquid composition of mole fraction, capillary condensation can occur if there is vapor in the capillary pore $X = \{x_i\}$, $i = 1,2,3,\ldots n$.

Shapiro developed a theory for multiple component mixtures which may be used to calculate the critical pore size necessary for capillary to take place at vapor pressure [44], P_v, as;

$$rc = \frac{2\gamma\cos\theta}{Pd\left[\frac{V_{vl}\left(P_{d,\ y}\right)}{V_l\left(P_{d,\ x}\right)}Z_{av}\ (y_v)\ln x - x + 1\right]} \tag{4.5}$$

where V_l is the liquid volume and it is determined as;

$$V_{l\ (P_{d.\ x})} = \sum x^i_{ld}V^i_l\left(P_d,x_i\right) \tag{4.6}$$

where V_l^i (p_d, x_i) is the liquid molar volume of component "i" at the dew point pressure; V_{vl} is the mixture volume and it is determined as;

$$\text{Vvl (Pd, x)} = \sum_{i=1}^{n} x_{ld}^i V_v^i\left(P_d, y_i\right) \qquad (4.7)$$

Where $V_v^i\left(P_d, y_i\right)$ is the vapor molar volume of component, i, at dew point pressure. X and Z (X) are defined as;

$$X = \frac{P_v}{P_d} \qquad (4.8)$$

and

$$Z(x) = \frac{Z(P_v)}{Z(P_d)} \qquad (4.9)$$

where $Z(P_v)$ and $Z(P_d)$ are gas compressibility factors at vapor pressure and dew point pressure respectively.

$$Z_{av}(X) = \frac{\int_1^X Z^{(X^1)} \big/ X^1 dx^1}{\ln X} \qquad (4.10)$$

Where $Z_{av}(X)$ is the logarithmic mean of Z(x).

The thickness "t" of the adsorbed layer is calculated using explicit methods as,

$$t = (\sigma)^{-\frac{1}{3}} \qquad (4.11)$$

and

$$\sigma = \frac{P_d \left[\frac{V_{vl}\left(P_d,\, y\right)}{V_l\left(P_d,\, x\right)}\right] \ln X - X + 1}{5RTD^3 \sum_{i=1}^{n}\left(\frac{y_i}{V_v} - \frac{x_i}{V_l}\right)} \qquad (4.12)$$

where D is the average thickness of a monolayer. A conservative value of 4Å was used in this calculation, and an experimentally determined value has to replace this value. Interfacial tension (γ), and dew point pressure (P_d) must be obtained in order to calculate for the critical pore size (r_c), and surface layer thickness (σ) in large pores.

Interfacial tension is calculated using the Katz, [45] and Weinang, [46] formulas as follows;

$$\gamma^{1/4} = \sum_{i=1}^{n} \gamma_i^{1/4} \frac{M_i}{d_i} \left(\frac{d_l}{M_l} x_i - \frac{d_v}{M_v} y_i \right) \qquad \textbf{(4.13)}$$

where γ_i, M_i, d_i, x_i, and y_i are interfacial tension, molar mass, density, liquid mole fraction and vapor mole fraction of component "i" in the mixtures, respectively. d_v and M_v are the density and molar mass of the vapor phase respectively. d_l and M_l are the density and molar mass of the liquid phase respectively.

Iterative algorithm is used for the calculation of mixtures dew point pressure.

A computer program was developed to calculate the total hydrocarbon at various temperatures and pressures considering capillary condensation based on the above model and theory, also the hydrocarbon compositions, pore- size distributions and the pore surface wettability was considered. The results obtained from this model where iterative algorithm was used to estimate dew point pressure, was consistent when compared to the results calculated by using Super Trapp (version 3.2.1, NIST) and the results from online software (Quest consultant Inc.) for ternary mixtures of 80% methane, 12% n-butane and 8% n-hexane.

Equation (4.6) which was developed for multi component mixtures of hydrocarbon was used for a single-component fluid (hexane), and the result when compared to the other results from classical Kelvin Equation, this new model theory that uses real-gas-equation of state was more accurate at high pressure.

In an isotherm curve, a jump was observed for the total hydrocarbon volume and this was attributed to the occurrence of capillary condensation. It was then proposed that, the hypothetical rock hydrocarbon volume would not be more than 100 scf/ton without the capillary condensation, hence depending on the composition and reservoir temperature, reserves can be increased three to six times in the presence of capillary condensation.

The Marcellus shale gas well composition was used to compare the hydrocarbon volume based on the traditional Langmuir model to the new capillary condensation model. The hydrocarbon mixture of the Marcellus well consist of 79.4% methane, 16.1% ethane, 4% propane, 0.1% carbon dioxide and 0.4% nitrogen. Porosity in the kerogen was only considered since capillary condensation occurs in these pores. It was observed that, the calculated volume of total hydrocarbon can be significantly higher than the predicted volume based on Langmuir traditional model, and also

observed that capillary condensation occurs when the pressure was smaller than the dew point pressure in the case of this well.

A recent studies have shown that shale gas industry is incorrectly determining gas-in-place volume in reservoirs with a large sorbed-gas by not properly accounting for the volume occupied by the sorbed and free gas phase [47]. Nanopores in the organic-rich shale has been discovered by Scanning Electron Microscopy (SEM) with pore size in a range of 3-100 nm, even though the current SEM technology cannot capture pores with size less than 3 nm. This is because, the thickness of the adsorption layer is not infinitesimally small at that scale. Hence, the finite-size adsorption layer which occupied a portion of the total pore volume may not be available for the free gas molecules quantification. The discussion on the adsorption layer effects has been extended in this study for multi-component natural gas with a sorption model known as Extended-Langmuir.

A new gas-in-place equation was formulated by combining EL adsorption with free gas volumetric and compositions, and at the same time accounting for the multi-component sorbed-phase pore space. The total gas-in-place prediction was accurate, hence, they suggested that, for shale gas with high C_2^+ composition and a high total organic content, there is the need for adjustment in volume estimation. The multi-component adsorption role in gas-in-place calculations is more important than previously thought, thus, this new method of shale gas-in-place calculation is recommended.

For reservoirs where there is a sorbed-phase component, there is an over estimation as high as 40% of the resource in place as a results of lack of material and voidage balance in calculating gas-in-place. Figure 4.4 shows a simple conceptual model that indicate the shale pore and matrix system. The effects of the sorbed-phase on porosity is represented by the dashed region in this diagram. A single-component isotherm was used for the free gas and sorbed portion of the fluid system.

It is standard to report gas-in-place in shale reservoir in terms of scf/ton (the adoption of the coal bed methane nomenclature, CBM). The shale gas-in-place volume for total gas storage are normally considered in terms of the following;

a) A volumetric component, G_f, involving hydrocarbon stored in pore space as free gas, corrected for volume occupied by the sorbed-phase. The free gas volume is quantified by modification of standard-reservoir evaluation methods.

b) Adsorbed component, G_a, with the gas physically stored on large surface area of micro and mesopores. The adsorbed gas amount has generally been quantified from the sorption isotherm measurements by establishing an equilibrium adsorption isotherm.

c) A volumetric component, G_{so}, involving gas dissolved into the liquid hydrocarbon. This volume is usually combined with adsorbed gas capacity in reservoir that contain a large fraction of liquid hydrocarbon in the pore space.

d) A volumetric component, G_{sw}, involving gas dissolved into formation water. The amount of dissolved gas is estimated from the bulk solubility calculations. Although it has traditionally not been considered important, a recent study is available discussing significant enhancement in gas solubility in formation liquids when confined to small pores
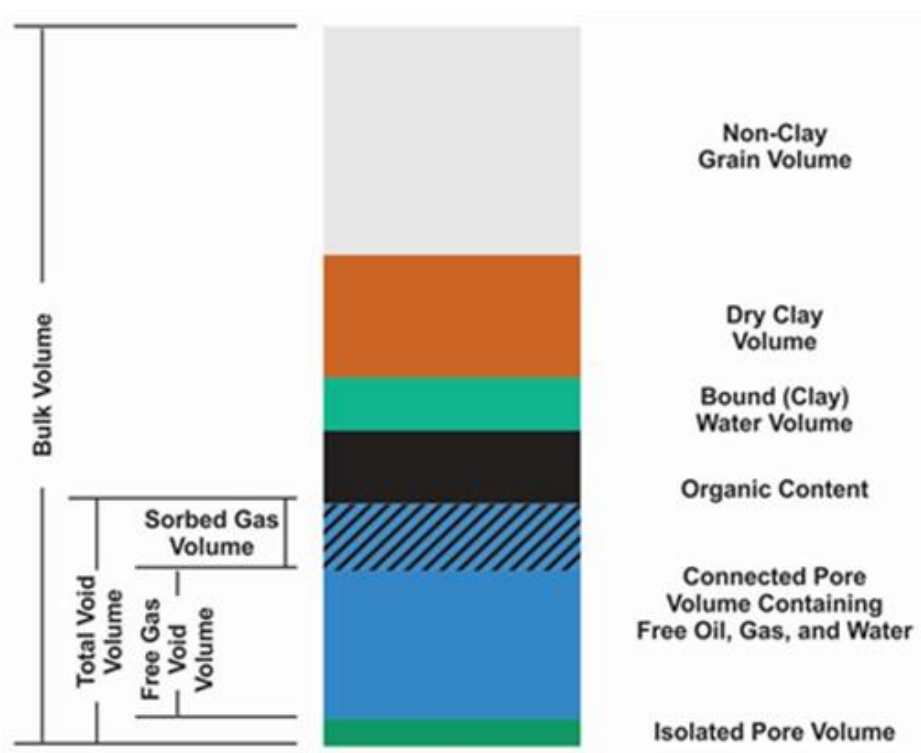
Figure 4.4: petrophysical model, showing volumetric constituents of shale-gas matrix [47].

Therefore the total gas-in-place , G_{st}, can be calculated as follows;

$$G_{st} = G_f + G_a + G_{so} + G_{sw} \qquad (4.14)$$

where;

$$G_f = 32.0368 \frac{\emptyset(1-S_W)-\emptyset_a}{\rho_b B_g} \qquad (4.15)$$

Introducing for single-component,

$$\emptyset_a = 1.318\ M\ \frac{\rho_b}{\rho_s}\left(G_{SL}\ \frac{P}{P+P_L}\right) \qquad (4.16)$$

$$Ga = GsL\frac{P}{P+P_L} \qquad (4.17)$$

$$Gso = \frac{32.0368\ \emptyset\ S_O\ R_{SO}}{5.6146\ \rho B_O} \qquad (4.18)$$

$$Gsw = \frac{32.0368\ \emptyset S_W\ R_S}{5.6146\ \rho B_W} \qquad (4.19)$$

Equations (4.18) and (4.19) are not considered in current industry standard calculation. The adsorption isotherm anlaysis include the solution gas in mobile hydrocarbons and water, and the adsorbed gas within organic matter. Hence equation (4.14) is reduced to ;

$$G_{st} = G_f + G_a \qquad (4.20)$$

For single-component reservoir system, the gas-in-place calculation equation is obtained by substituting equations (4.15) and (4.17) into equation (4.20) as follows ;

$$G_{st} = 3.0368\ \frac{\emptyset\ (1-S_W)-1.318\times10^{-6}\ M\frac{\rho_b}{\rho_s}\left(\frac{G_{SL}\ P}{P+P_L}\right)}{\rho_b B_g} + \frac{G_{SL}\ P}{P+P_L} \qquad (4.21)$$

The adsorption layer corrected for free gas volume is represented by the first term on the right hand side of equation (4.21), while the sorbed- gas volume is represented by the second term on the right hand side of the same equation. Compositon- dependent values, which mixing rules are recommended for their calculation are, the formation volume factor, B_g, molecular weight, M, the sorbed phase density, ρ_s, and the Langmuir adsorption parameters, G_{SL} and P_L.

54

4.5 Multi-component sorbed-phase correction for void volume

Within the resorvoir, organic-rich hydrocarbon, fluid composition, and phases vary. The fluid itself vary from dry gas to liquid in the reservoir. Mostly, two or three components is made up of more from 99% of the composition, and more than 40 componenents are common in reservoir where the hydrocarbon fluid is liquid. The transitions zone in uncontinental reservoir, which is sometime called the wet gas window, is large. It is therefore critical for multi-component model to be used to determine the resource in place and the phase in which it resides.

The composition and quantity of an adsorbed phase present in an organic –rich shale reservoir is determined by a multi-component adsorption model. The extended Langmuir (EL) model presented in this studies is the easiest one to used even tough there are many multi-component adsorption model in the literature, such as the Ideal Adsorbed Solution (IAS) and the 2D equation-of-state (2D EOS) model, which are consistent thermodynamically. This EL model is not thermodynamically consistent but it is widely used across the petroleum industry and can be replaced by any other adsorption model. In the multi-component adsorption model, the value taken up by sorbed phase. $\emptyset_a$, for a single- component would be replaced by any of the multi-component isotherm to give an equation for multi-component gas-in-place estimation. An EL model equation for a single component is shown to be equal to equation (4.17) as follows;

$$G_a = \sum_{i=1}^{n} G_{sLi} \frac{y_i P}{P_{Li} \left(1 + \sum_{j=1}^{n} y_j \frac{P}{P_{Lj}}\right)} \tag{4.22}$$

G_{sLi} and P_L are measured by using pure components in the laboratory. To obtain $\emptyset_{a,mix}$, we have to substitute equation (4.22) into equation (4.16) as follows ;

$$\emptyset_{a,mix} = 1.318 \times 10^{-6} \, \acute{M} \frac{\rho_b}{\rho_{s,mix}} \left[\sum_{i=1}^{n} G_{SLi} \frac{y_i P}{P_{Li} \left(1 + \sum_{j=1}^{n} y_j \frac{P}{P_{Lj}}\right)} \right] \tag{4.23}$$

Where $\emptyset_{a,mix}$ is the sorbed phase prosity of the mixture .

Mixing rules should be used to calculate the apparent molecular weight, $\acute{M}$, and the adsorbed-phase density, ρ_s, in this equation. Due to the fact that the fluids are supercritical, the adsorbed-phase density calculation is difficult. For the liquid phase

density, the use of Van der Waal co-volume constant (b) is recommended in this study. This mixing rule used here is the Kay's mixing rule.

4.5.1 Estimation of sorbed-phase gas content of gas mixture

The EL model, equations (4.22) is used to determined sorbed phase gas content of the mixture. Since there is no iteration involved in this calculations, it is very easy and yields satisfactory results even though this model is not thermodynamically consistent.

All the individual components are necessary in order to calculate the EL isotherm. Isotherm of methane and higher order carbon isotherms such as C_2 and CO_2 are available. Because of the very low dew point pressure of the fluid systems, isotherm of single- component C_3+ measurements are usually difficult. The C_3 isotherms were available but C_4 isotherms were determined based on C_1, C_2, and C_3, carbon number trend of G_L and P_L. The values in Table 4.4 below was combined with the mole fraction in Table 4.5 to estimate the EL isotherms using equation (4.21) for single component.

This single component and the EL models are shown in Figure 4.5 below. It was observed that, the EL isotherm was 37 % more than the single – component of methane isotherm. Therefore to accurately determine the amount of sorbed and nature of gas-in-place, EL or other multi component adsorption model is used in reservoir which is rich in shale gas. Also, for the calculation of average molecular weight and sorbed phase density values, the sorbed phase mole fractions can be obtain using the EL model.

Table 4.4: Gas phase mole fraction in a liquid rich gas shale.

Methane	Carbondioxide	Ethane	Propane	Butanes plus	Mixture
0.86	0.01	0.10	0.02	0.01	1.00

Table 4.5: Langmuir constants trends on a 100% carbon basis compared to carbon number.

	C_1	C_2	C_3	C_{4+}	CO_2
G_L (scf/ton)	56	91	179	232	145
P_L (psia)	1,562	811	844	355	836
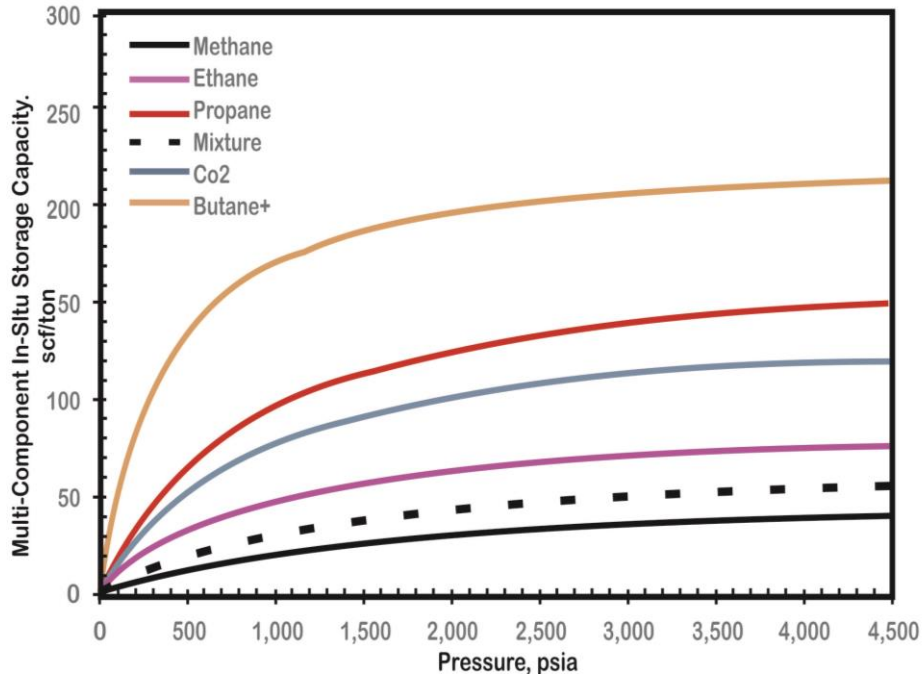
Figure 4.5: Laboratory measured single-component and extended-Langmuir
isotherms for naturally occuring gases [47].

4.5.2 Estimation of sorbed phase density of the gas mixture

For investigation of deviation from ideal gas to determine the behavior of real gas,
the earliest attempts was carried out by Van der Waals equation of state,given as;

$$\left(P + \frac{a}{V^2}\right)(V - b) = RT \tag{4.24}$$

Where V is molar volume of the real gas. To account for the finite volume of gas
moleculars ignored in the ideal gas theory, the co-volume constant (b) is deducted
from the molar volume. It was suggested that, the co-volume constant is related to
the density of the adsorbate. Experimentally, at the critical point (P_c, T_c), the
derivative of the first and second order of the gas pressure with respect to molar
volume are equal to zero. That is;

$$\left(\frac{\partial P}{\partial V}\right)_{T_c} = 0,$$

$$\tag{4.25}$$

$$\left(\frac{\partial^2 P}{\partial V^2}\right)_{T_c} = 0$$

Expression for the co-volume constant "b", and the constant "a", accounting for the intermolecular forces related to real gases can be derived using these emprical relationships for any chemical species interms of the critical temperature (T_c) and critical pressure (P_c) of that species. We have the following equations at the critical point.

$$\left(P_c + \frac{a}{V_c^2}\right)(V_c^2 - b) = RT_c$$

$$\left(\frac{\partial P}{\partial V}\right)_{T_C} = \frac{RT_C}{(V_C-b)^2} + \frac{2a}{V_C}$$

$$\left(\frac{\partial^2 P}{\partial V^2}\right)_{T_C} = \frac{2RT_C}{(V_C-b)^3} - \frac{6a}{V_C^4} = 0$$

These three equations can be solved for "a" and "b" with the following expressions.

$$a = \frac{27T_C^2 R^2}{64P_C} \quad \text{and} \quad b = \frac{RT_C}{8P_C} \tag{4.27}$$

The derived co-volume constant "b" has a unit of ft^3/lb-mole. Hence , to estimate the sorbed-phase density of that species, we take the riciprocal value multiplied with the molecular weight of that particular species as follows;

$$\rho_s = \frac{M}{b} \tag{4.28}$$

The estimated sorbed-phase density using this method and various physical properties for some naturally occuring gases are shown in Table 4.6, below.

For a mixture of gases the sorbed-phase density estimation and the pseudo-critical properties (P_{pc}, T_{pc}) must first be estimated using Kay's mixing rule, but, the gas phase mole fraction should be replaced by the sorbed- phase mole fraction. The pseudo-critical properties are estimated using the following equations and later substituted into equation (4.27).

$$T_{pc} = \sum_{i=1}^{n} x_i\, T_{ci} \quad \text{and} \quad P_{pc} = \sum_{i=1}^{n} x_i\, P_{ci} \tag{4.29}$$

If the sorbed-phase composition data is available, the mixture density can alternatively be obtained directly by the Kay's mixing rule from the pure sorbed-phase density values, as given below;

$$\rho_{s,mix} = \sum_{i=1}^{n} x_i\, \rho_s \tag{4.30}$$

Table 4.6: Various physical and adsorption properties of some pure gases and a gas mixture.

Gas	M lb$_m$/lb-mol	P$_c$ psia	T$_c$ °F	a psia·(ft^3)^2/(lb-mol)^2	b ft^3/lb-mol	ρ_s g/cc
Methane	16	666.4	-116.67	8594.8	0.6911	0.371
Ethane	30	706.5	89.92	20798.5	1.0442	0.460
Propane	44	616.0	206.08	24995.9	1.4506	0.486
n-Butane	58	550.6	306.62	51729.2	1.8654	0.498
i-Butane	58	527.9	274.46	49651.2	1.8664	0.498
Carbon dioxide	44	1071.0	87.91	13619.9	0.6863	1.027
Mixture Gas	26.96	668.4	5.9918	15786.5	0.9353	0.434* 0.462**

* from eqn. 4.28

** from eqn. 4.30

4.5.3 Estimation of gas-in-place considering multi-component adsorption layer effects

EL model is used to calculate the gas-in-place incorporating previously estimated and modeled parameters. The free gas-in-place in estimated using equaition (4.22), equation (4.23) is used to estimate the porosity of the sorbed portion and equation (4.15) is then used for the prediction of sorbed gas-in-place. Hence, the total gas-in-place is calculated using the equation below;

$$Gst =$$

$$3.0368 \frac{\emptyset (1- S_w)-1.318 \times 10^{-6} \: \acute{M} \frac{\rho_b}{\rho_{s,mix}} \left[\sum_{i=1}^{n} \frac{G_{SLi} \: y_i P}{P_{Li}\left(1+\sum_{j=1}^{n} y_j \frac{P}{P_{Lj}}\right)}\right]}{\rho_b B_g} + \sum_{i=1}^{n} \frac{G_{SLi} \: y_i P}{P_{Li}\left(1+\sum_{j=1}^{n} y_j \frac{P}{P_{Lj}}\right)}$$

$$(\textbf{4.31})$$

Also, the adsorption layer corrected for free gas volume is represented by the first term and the sorbed-gas volume is represented by the second term on the right-hand-side of equation (4.15).

Different cases was considered to determine the total gas-in-place and the result was summarized in Table 4.7. From Table 4.8, it was assumed that the total gas-in-place estimated was very close whether the single or multi-components isotherm was employed, even though the stored gas was total different. Depending on which

isotherm employed the percentage changes between sorbed and free gas is significant, hence, has a potential impact on recoverable gas-in-place, as sorbed gas requires that abondendment pressure must be lower for recovery.

Considering single component isotherm and multi-component isotherm, the difference between these two conditions is nearby 20 %, as the multi-component gives higher value. Therefore, when calculating the recoverable reserves within reservoirs containing significant amount of higher molecular weight (strong sorbing) hydrocarbons, this effect must be considered.

Table 4.7: Sorbed phase porosity values and free, adsorbed, and total gas-in-place.

parameter	value	units
ϕ_o – single component isotherm	0.0058	fraction
ϕ_o – EL isotherm ($\rho_s = 0.434$ g/cc)	0.0113	fraction
ϕ_o – EL isotherm ($\rho_s = 0.462$ g/cc)	0.0107	fraction
G_f – EL isotherm ($\rho_s = 0.434$ g/cc)	74.48	scf/ton
G_f – EL isotherm ($\rho_s = 0.462$ g/cc)	76.55	scf/ton
G_f – single component methane isotherm	91.51	scf/ton
G_f – sorbed phase density of 0.0 g/cc	109.08	scf/ton
G_a – EL isotherm	55.41	scf/ton
G_a – single component isotherm	40.41	scf/ton
G_{st} – EL isotherm ($\rho_s = 0.434$ g/cc)	129.89	scf/ton
G_{st} – EL isotherm ($\rho_s = 0.462$ g/cc)	131.96	scf/ton
G_{st} – single component methane isotherm	131.92	scf/ton
G_{st} – sorbed phase density of 0.0 g/cc	164.49	scf/ton

A report titled "XIII. Turkey" published by Advanced Resources International Inc. [23], assessed the shale gas resource in two basins in Turkey. These basins are the Thrace Basin in the Western Turkey and the Southeast Anatolia Basin along the border of Iraq and Syria.

The Thrace and Southeast Anatolia Basin was estimated using ARI estimates, to contain 64 Tcf of risked gas in place from three prospective shale formations. An estimated amount of 15 Tcf of technically recoverable shale gas resource is contained in these three formations. The reservoir properties and shale gas resource estimates are shown in Table 4.7, below.

4.6 Geological Characterization Of The Southeast Anatolia Basin

Inside the Turkish border, the Southeast Anatolia Basin emcompasses about an area of 32,450 square miles of the Arabian plate. On the North, the basin is bounded by the Zagros suture zone which marks the juncture of the Arabian and Eurasian tectonics plates.

Throughout the northern Godwana super continent (now North Africa and the Middle East), Silurian-age shale formations were deposited in the early paleozoic after major sea levels rise caused by melting Ordovician-age glaciers. Regional lows and offshore deltas with anoxic conditions received layers of organically rich sediments that present promising shale traget of late. The Southeast Anatolia Basin was part of the northern edge of the Godwana super basin but later, it was seperated to form the Arabian plate. The basin therefore shares similar geology with the Oil producing regions of Saudi Arabia and Iraq, eventhough it shows greater faulting and thrusting caused by the collision with the Eurasian plate. This region is the primary source of Turkish oil production.

Within the Southeast Anatolia Basin, the most promising source rock is the Silurian-Devonian Dadas Shale. Along the Zagros margin, the basin covers an area as the size of the Barnett shale. As the regional oil source rock, the basal member of the Dadas shale has long been recognized, though the formation was discovered recently to be the gas prone in its northern areas.

ARI mapped an area of 2,950 square miles of the Dadas shale as prospective for shale gas development using available reservoir data. The Dadas shale which is inside the gas window in most northern areas, is present over about 20% of north central Southeast Anatolia Basin. Guidance provided by TPAO (Turkish Petroleum Company, Inc.) in corporate presentations enables the establishment of the prospective area for shale gas development since detailed thermal maturity data for the formation was not available.

To the north the Dadas shale thicken deepens, and this is where it enters the gas generation window. The northern half of the shale's areal extent in Southwest Anatolia Basin within the propective area, ranges from 6,560 feet to 9,840 feet deep with an average of 8,200 feet.

Table 4.8: Turkey shale gas reservoir properties and resources [23].

Basic Data	Basin/Gross Area		SE Anatolia Basin (32,450 mi²)	Thrace Basin (8,586 mi²)	
	Shale Formation		Dadas Shale	Hamitabat	Mezardere
	Geologic Age		Devonian-Silurian	Mid-Lower Eocene	Lower Oligocene
Physical Extent	Prospective Area (mi²)		2,950	312	303
	Thickness (ft)	Interval	328 - 1,300	3,280 - 8,200	1,640 - 8,200
		Organically Rich	500	1,722	1,476
		Net	150	344	295
	Depth (ft)	Interval	6,560 - 9,840	12,136 - 16,400	8,200 - 10,168
		Average	8,200	14,268	9,184
Reservoir Properties	Reservoir Pressure		Normal	Normal	Normal
	Average TOC (wt. %)		5.5%	3.9%	2.5%
	Thermal Maturity (%Ro)		1.10%	1.75%	1.10%
	Clay Content		Medium	Medium	Medium
Resource	GIP Concentration (Bcf/mi²)		61	128	74
	Risked GIP (Tcf)		43	14	7
	Risked Recoverable (Tcf)		9	4	2

The organic rich play with a net thickness of about 150 feet [48], is primarily concentrated in the basal Dadas member (Dadas 1). Within the horizon, organic content ranges from 2% to 6% and an average of 5.5% while increasing to the north [49]. The prospective area with a thermal maturity between 1% and 1.2% Ro. is within the wet gas generation window.

ARI calculated a moderate gas in place resource concentration of 61 Bcf/square mile using the Dadas Shale reservoir characteristics discussed above. The shale formation within the 2,950 square miles prospective area was estimated to contain a risked gas in place of 43 Tcf, of which only 9 Tcf was estimated to be technically recoverable. The prospective area shows heavy faulting which could pose significant development risks. The formation nevertheless exhibits favorable properties for shale gas development. To redefine the prospective area and improve the reliability of this resource estimation, additional data on the thermal maturity and organic thickness of the Dadas Shale throughout its deposition area will help greatly.

The Southeast Anatolia Basin has been largely leased for conventional crude oil exploration with TPAO holding the majority of the lease in this area. Horizontal drilling and fracturing equipments in the country, and personnel experience limits the

ability of TPAO to exploit the unconventional potentials. Some of the international petroleum exploration companies in the area are Aladdin and Perenco.

In Turkey, the Thrace Basin covers an area of 8,600 square miles. On the north, the basin is bordered by the Istranca Massif, on the West, it is bordered by the Rhodope Massif and on the South, it is bordered by the Sakarya Massif. The Tertiary-age basin is extremely thick in the Thrace Basin. In its center, it is about 30,000 feet including a number of petroleum source rocks and reservoirs. The basin became Turkey's most important gas producing basin after the discovery of the Hamitabat gas field in 1970, accounting for about 85% of the country's total gas production. In the basin, about 350 wells have been drilled in thirteen gas field (one offshore in the Marmara Sea) and three oil fields. These wells are manily operated by TPAO.

There are two source rock formations with shale gas potential in the Thrace Basin. The Lower-Mid Eocene aged Hamitabat formation and the Lower Oligocene Mezardere formation. The Hamitabat formation is a thick sequence of sandstone, shale and marl deposited in a molasse or turbidity shollow environment. The Mezardere formation which is a deltaic environment, also contains interbedded layers of sandstone, shale and marl [50]. These shales have enough thermal maturity to be in the gas window in the deeper central-southern areas of the basin. Further data may help identify more areas with organically rich shales. The ARI identified prospective areas in the Mezardere and Hamitabat formations are primarily based on thermal maturity data. These formations only reach the gas window at great depth, usually deeper than the 5,000 meters threshold used in the analysis. This is due to the fact that the formations are relatively young. The Hamitabat shale which is 312 square miles prospective area, was constructed based on Turkey's work where the well data and laboratory analysis were used to established the area inside the gas window [51]. The Mezardere formation which is 303 square miles prospective area construction was based on Karahanoglu et al. analysis where the gas prone area of the shale was identified based on mathematical modeling of the basin's thermal history [52].

4.7 Reservoir Properties Of The Prospective Areas

The Hamitabat Shale which is the deepest and oldest shale formation in the Thrace Basin, is the most thermally matured. At the center of the basin, the shale is in the

gas window at a depth of 12,100 feet to 16,400 feet, with Ro ranging from 1% to 2.5%. Throughout the formation, organic content is highly changing ranging from fractions of percent to above 6% [53]. Total organic content (TOC) within the prospective area ranges from 1.5% to 6.4% with an average of 3.9% [54]. The Hamitabat Shale gross interval ranges from 3,280 feet to 8,200 feet thick. One third of the average shale interval (1,722 feet) is assumed to be organically rich. This was assumed due to the fact that the data on net shale thickness was not widely available. The net shale thickness is estimated to be 344 feet when a net to gross ratio of 20% was applied [55].

In Thrace Basin, Mezardere shale is also very thick and has regionally extensive interval. The prospectivity of the Mezardere shale is limited by low organic content and thermal maturity. The target shale interval within the prospective area ranges from 8,200 feet to 10,168 feet deep, even though some literature suggest that the entire Mezardere shale is outside the gas window. The total organic content with an average of 2.5%, ranges from 1% to 4% [49]. Thermal maturity ranging from 1% to 1.2% Ro, is assumed to be in the wet gas window. The Mezardere gross interval ranges from 1,640 feet to 8,200 feet thick. The same methodology, used to determine Hamitabat shale, was also used to determine the net organically rich shale of the Mezardere shale. The organically rich thickness of the shale was assumed to be 1,476 feet and the net shale thickness was 295 feet.

The ARI calculates a shale gas reource concetration of 128 Bcf/square miles for Hamitabat shale and 74 Bcf/square miles for the Mezardere shale, based on the reservoir characteristic discussed above. The Hamitabat shale and the Mezardere shale within the prospective area contain a risked gas in place of 14 Tcf and 7 Tcf respectively. Out of 14 Tcf only about 4 Tcf could be recovered technically in the Hamitabat shale. Similarly, out of 7 Tcf only about 2 Tcf could be recovered technically in the Mezardere shale, as shown in Table 4.8 above. Additional data on these formations, such as net thickness, may help provide a more accurate estimates of their potentials.

5. DRILLING AND STIMULATION OF WELLS

Horizontal wells are drilled in shale gas reservoirs for economically feasible gas production. Long horizontal wells drilling in shale creates problems relating to wellbore stability in build section due to pack-off, tight hole, and stuck pipe or lost circulation. The above problems leads to considerable amount of nonproductive time, and this in turn increase the cost of drilling. Hence, there should be measures in place to control this non-productive time to a minimum to exploit the reservoir more economically.

An integrated well construction approach was presented for exploratary shale gas horizontal wells. It is clear from their research paper that, to optimize well construction, a multi-disciplinary integrated workflow plan is necessary [56].

Shale instability and its deterioration with time makes drilling for shale gas very challenging, e.g. 90 percent of wellbore instabilities are related to shale formation. At higher inclinations, higher mud-weight (MW) is needed to stabilize the collapsing shale, but the higher mud-weight might also present the problem of formation fracturing that would lead to partial or total loss of mud. The surge during RIH (running-in-hole) with equivalent circulating density (ECD) may also have the same adverse impact. Achieving a good cement bond for casing or liner is very difficult in case of losses, which can affect fracturing operations later. The key problems at the design stage of shale-gas horizantal-well construction are,

a) severity of borehole stability that may cause stuck pipe – should be avoided;

b) difficulty in keeping the wellbore accurately within the target zone;

c) difficulty in maintaining horizontal well integrity, when encountering mud loss during either drilling or cementing.

An integrated workflow should be defined to solve the aforemention problems and/or challenges and to optimize the well design in shale gas reservoirs. Such integrated

workflow should encompass three main stages; namely the planning stage, the execution stage, and the evaluation stage.

5.1 Planning Stage

A collective system of approach was considered in the planning stage to provide a competent well construction design. The design process was started with multi-stage peer review process after organising technical experties, where all the design criteria and features were verified by all teams at every stage. The teams/technical experties involved were, well engineering team, sub-surface team, reservoir and production team. A pilot vertical hole across the formation through which curve section were to be drilled with wireline log full suites were obtained.

A complete pre-drill geomechanics study was conducted for the sidetrack horizontal section using data from the pilot hole log, to estimate safe mud-window for drilling and to determine drilling problems potential as against applying geomechanics only in the initial approach for hydraulic fracture design. Using the sonic and other petrophysical logs, the Mechanical Earth Model (MEM) was developed and calibrated with mechanical data, and micro-frac data across the target reservoir was obtained by using a wire-line based formation tester tool. The key formation below and above the reservoir that is likely to pose severe wellbore instabilities was also studied. Safe mud weight window was then estimated by using the calibrated MEM as shown in Figure 5.1.

The casing points was identified. To drill the curve section and lateral sections, mud weight of 80 pcf and 70 pcf respectively was predicted by the MEM as minimum values to avoid casing and subsequent hole collapse. For the unstable zone in the curve section, the calibrated MEM predicted a higher mud weight value but it was decided to cased-off behind a casing in this zone before entering the target zone. Hence, it was possible to use lower mud-weight to drill the target zone and potentially avoid any drilling induced fracture or loss circulation as a relatively lower fracture gradient was observed in this reservoir. As shown in Figure 5.2, the trajectory of the well is optimized to have a best-case exit from whipstock.

After evaluating the cement bond log (CBL), the whipstock was selected carefully and was set across a good CBL zone as shown in Figure 5.3 to;

(a)   avoid problematic formation zone with respect to tight hole, losses etc.

(b)   allow sufficient seperation from casing after exit.

(c)   allow planned dog-leg severity (DLS) not to exceed 4°/100 ft to avoid much directional work in problematic formations.
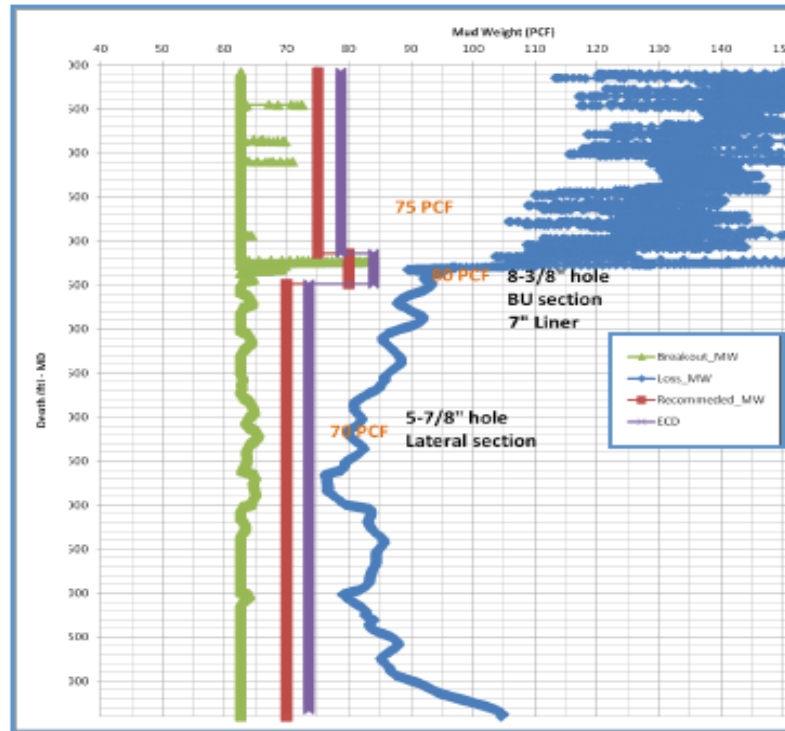
Figure 5.1: Curve and lateral section mud weight window [56].

The trajectory was set to less then 15° inclination across problematic formation to reduce directional work required, after exiting from whipstock and was not allowed to have more than 4 degree per 100 feet dogleg severity to;

(a) avoid high micro DLS and ledges in geo-mechanically unstable areas across the well profile,

(b) limit trips requirement across shale for hole conditioning, and

(c) have better hole cleaning by avoiding alanche areas from high micro DLS area.

To be able to run casing and liner smoothly, a better hole quality and optimum hole cleaning must be ensured. These sections were planned to be drilled with a rotary steerable tools. To run tripple combo and sonic measurement on logging while drilling (LWD) tools was decided in the lateral and wellbore instability intervals, since narrow mud weight windows were predicted by MEM, and to help manage the
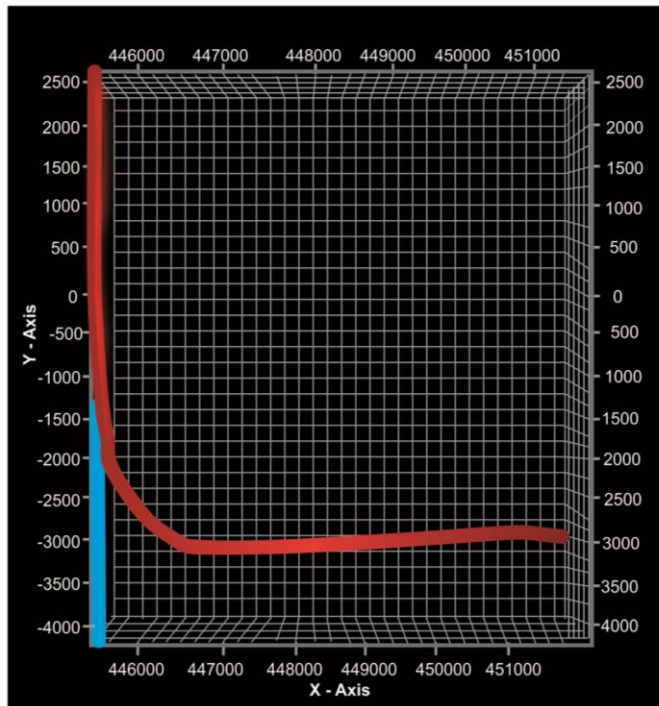
Figure 5.2: Trajectory of the well [56].
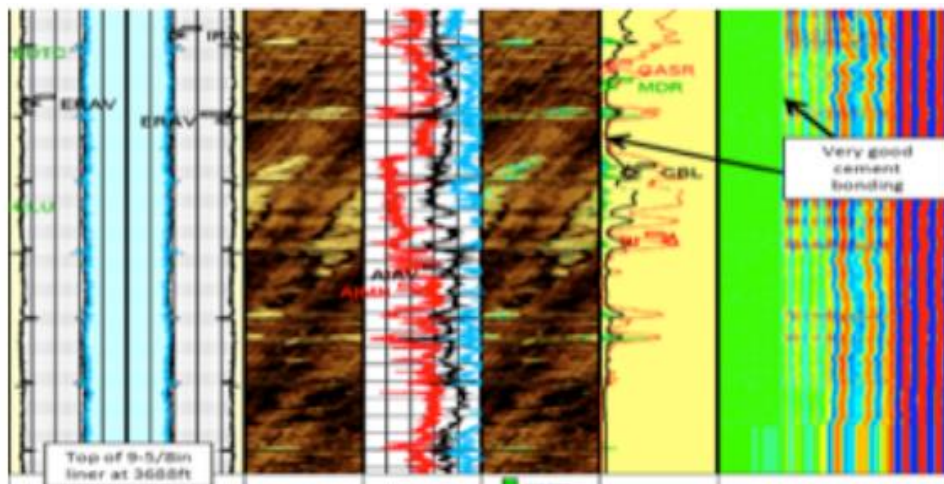
Figure 5.3: CBL for whipstock setting depth selection [56].

instabilities, a Real Time Geo-Mechanics (RTGM) monitoring tool was also run along side these tools. To calibrate the MEM in real-time and obtain optimum mud weight and drilling recommendations in case well integrity is getting jeopardize as a result of stuck pipe risk or drilling induced losses, was the main objective of RTGM. Shale stability was ensured by choosing oil based mud system as primary drilling fluid system for these wells. Breakout management was not possible to predict since there was no experience of shale gas well drilling in this field.

To track cuttings recovery at the surface and aid RTGM quantify the extend of breakout occuring in the hole, an advance mud-logging service was run. Each shale shaker was equiped with a cutting flow meter (CFM) device to evaluate the hole cleaning efficiency and increase efficiency of drilling. This device collects and quantify cutting recovery. The data obtained by this device was recorded as a standard drilling parameter. The hole cleaning efficiency was indicated by this system. The rate of ejected cutting at the shale shaker real time information was provided by the display of the cutting flow rate. A better understanding of actual cleaning is obtained by correlating this information with other data including drilling rate, mud flow rate, RPM, and torgue.

In effect, the advance mud logging tool was run to allow maximum drilling time, reducing tripping time and off bottom circulating time by indicating whether hole is breaking out or hole conditioning is needed. The following recommendations are made for planning the stages based on drilling a number of wells in shale gas reservoir successfully.

(a) Acquire a comprehensive logging suite from pilot hole.

(b) Build a pre-drilled MEM for the sidetrack and horizontals, and follow MEM mud weight recommendations.

(c) Conduct real time geomechanics monitoring, update the MEM with drilling incidents and well behavior, and adjust MW accordingly.

(d) Connection practice to be revised, at stand down CHC for 5 minutes, then wipe up and ream down.

(e) Avoid back reaming as much as possible, if need, commence after consultation with the main office in town.

(f) Monitor pick up and slack off weight closely in real time.

(g) Any increase in pickup weight, with respect to last 3 stands drilled/stripped, needs to be highlighted to company man and the main office in town.

(h) At increase in pickup weight after a stand down, just be off-bottom CHC for 10 minutes before commencing pickup.

(i) Monitor ECD and control flow according to avoid drilling induced formation fracture causing loss circulation.

(j) Closely follow up actual mud-properties against plan properties for efficient hole cleaning.

(k) Keep low end mud rheology, that is, RPM 6 and LGS content as per program to avoid high ECD and hence better hole cleaning.

(l) Keep close communication with mud loggers to keep track of excessive caving at shakers, highlight any abnormal rise in cravings return to company man and the main office in town.

(m) Avoid keeping the string stationary for prolonged period of time especially while surveying and making connections.

(n) Watch surface parameters diligently, any spike in pressure, torque, increase in drag requires drilling to stop and circulation at high RPM and maximum flow.

(o) Extreme care is required when pumping sweeps with higher density to avoid formation fracture. There should not be 2 sweeps at the same time in open hole.

(p) Add lubricants in case of high torque or stick slip is experience, OBM would help to provide lower friction factors.

(q) Utilize cuttings flow meter for hole cleaning monitoring.

(r) The liner hanger equipment was equipped such that, the liner will be run in the hole by rotation while cementing.

The expected high breakout zone was reached successfully during the execution stage. A stuck pipe situation was encountered as the pre-drill MEM predicted wellbore instability was less in severity as compared to the actual wellbore instability encountered. The drilling practice were then changed as a result of a lesson learnt from this situation. The problematic formation in nature was brittle. Hence, any mechanical action (induced by reaming, break reaming, high RPM and high tripping speed) or hydraulic impact (ECD resulting from flow rate or heavier pills, and pressure impact as a result of swab and surge load) would leads to failure in brittle, causing breakout and will finally lead to a potential hole pack-off and stuck pipe situation. Extreme precaution was then taken when entering the problematic formation to prevent possible hole collapse/pack-off by limiting any mechanical or hydraulic impact. To overcome challenges posed by the problematic formation from causing severe breakouts, the following measures were implemented;

(a) Circulate at least 5 minutes at 3-5 ft off bottom for each stand down, then wipe up and ream down. Do not back ream at any stage as it will deteriorate hole conditioning in the brittle shale section.

(b) After entering the problematic formation, the wipe up and ream down has to be attempted at a slow speed to avoid any swab or surge induced damage.

(c) While inside the problematic formation, for any trip out of the hole, that is, while stand down or POOH, reduced trip speed to 5 stands an hour to reduce swabbing effects in the hole.

(d) Close monitoring of T and D Broom stick chart is required to keep watch of hole condition in term of drag.

(e) It is not recommended to run wiper trip once entered the problematic formation as it will increase shale exposure time and at the same time would expose the hole to extra mechanical action/impact making wellbore more liable to mechanical and brittle failure (break outs). Drill down to casing point and come out of the hole as soon as possible while avoiding back reaming.

(f) If tight hole and over pull is observed, do not kick in rotary and back ream, go down BHA lenth plus one stand, start circulating and rotation along with string reciprocation to clean the hole. After at least two bottoms up, POOH on elevator to tight spot and observe. If still tight, consider increasing mud weight.

(g) After reaching casing point, and before trip out, MW should be increased at as per RTGM recommendation to prepare the hole for trip out.

(h) While drilling and reaming do not increase RPM to more than drilling RPM (± 120 RPM), this is in order to reduce mechanical disturbance of the brittle problematic formation.

These measures stated above allowed the curve section to be drilled safely and had the casing set at the desired depth. To drill the lateral section with QuanCombo LWD string, deep resistivity reading tool for bed to boundary was run in order to achieve optimum lateral well placement. Entering into any problematic formation was then avoided and for wellbore stability purposes, the MW was raised. Without any stuck pipe issues, the laterals were drilled. Drilling the laterals to planned TD was the biggest challenge as narrow mud window was creating pre-mature well TD due to encountered loss circulation. The actual ECD was closely approaching and even at a time exceeding the lost limit as indicated by MEM updates with RTGM observation and data from LWD. This is shown in Figure 5.4 below.
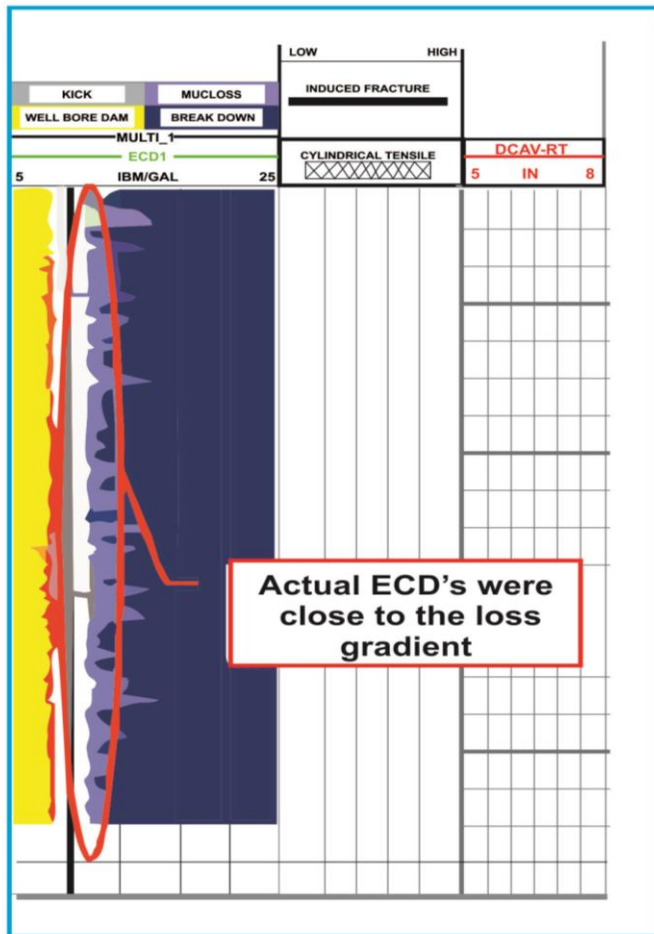
Figure 5.4: LWD and MEM updated with RTGM indicates ECD is closely following the lost limit [56].

Heavy losses and flow were reported at different intervals. As indicated clearly in Figure 5.5, cumulative plot of losses and gain shows ballooning of signatures. This pose a big problem for the well integrity and definitely will affect the productivity of the well as fracturing inefficiency will be resulted because quality of cement bond will be jeopardized.

The execution stage challenges were as follows;

(a) Wellbore assurance (stuck pipe in the curve section)

(b) Wellbore integrity (lost circulation in laterals).

In order to further optimize the performance of drilling, the challenges encountered during executing the horizontal shale-gas wells were evaluated by considering each problem at a time.
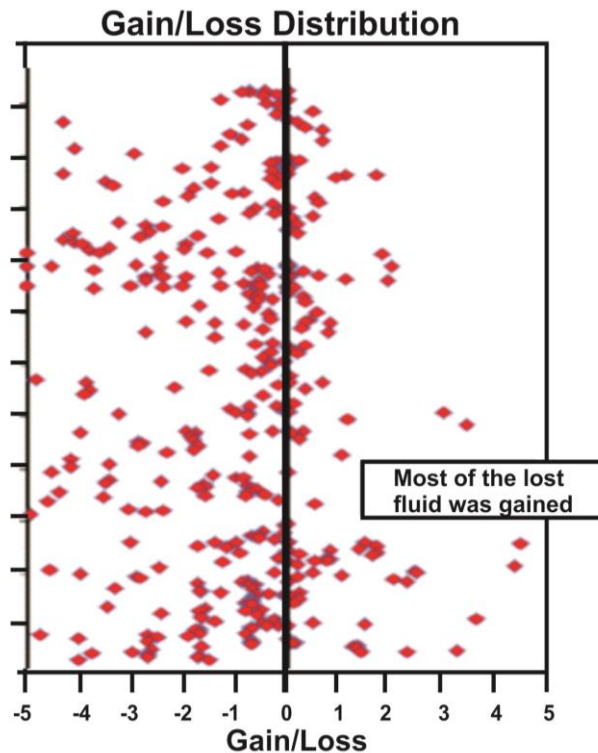
Figure 5.5: Distribution of Gain/Loss in lateral: effects of ballooning, actual ECD close to loss gradient [56].

In order to further optimize the performance of drilling, the challenges encountered during executing the horizontal shale gas wells were evaluated by considering each problem at a time as in following section.

5.2 Wellbore Assurance (Stuck Pipe In The Curve Section)

A post-drill evaluation from the MEM work indicated that, at the curve section, wellbore stability across the unstable problematic formations was directly related to an increase in inclination angle (attack angle). A sensitivity analysis was conducted on the attack angle as shown in Figure 5.6, which suggested that, at a lower inclination, the well profile cuts through the unstable formation.

It was learnt from MEM also with respect to inclination sensitivity in the curve section that, inclination should be reduced by 10 degree across the problematic formation. Hence, below the problematic formation a 10 degree per 100 feet dogleg severity can be obtained.
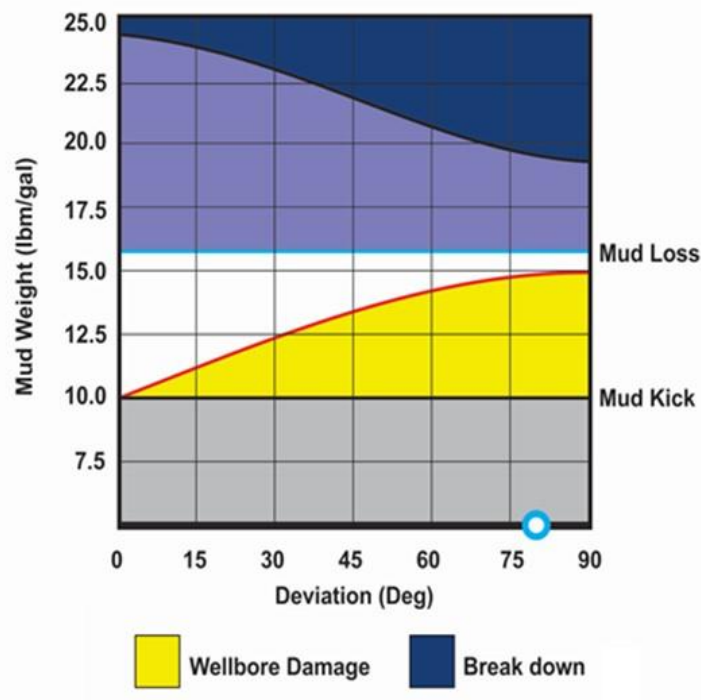
Figure 5.6: Mud weight versus deviation [56].

A new rotary steerable system (RSS) having a capacity to deliver high dogleg was used to achieved this higher dogleg severity at the curve, and is shown in Figure 5.7. High dogleg severity advantages are;

(a) reduced inclination by 10 degree across the problematic formation,

(b) improved/expand mud window by 5-8 PCF,

(c) minimized footage drilled across problematic formation by ± 100',

(d) allowed casing to be run at immediate exit of problematic formation and help secure drain hole.

Without having any stuck pipe incident in the curve section, four horizontal wells have been successfully drilled. An average of 14 days savings per curve section drilled has been achieved by using high DLS inspired well design. It was observed during evaluating the root cause for loss circulation that, drilling ECD was higher than planned ECD.
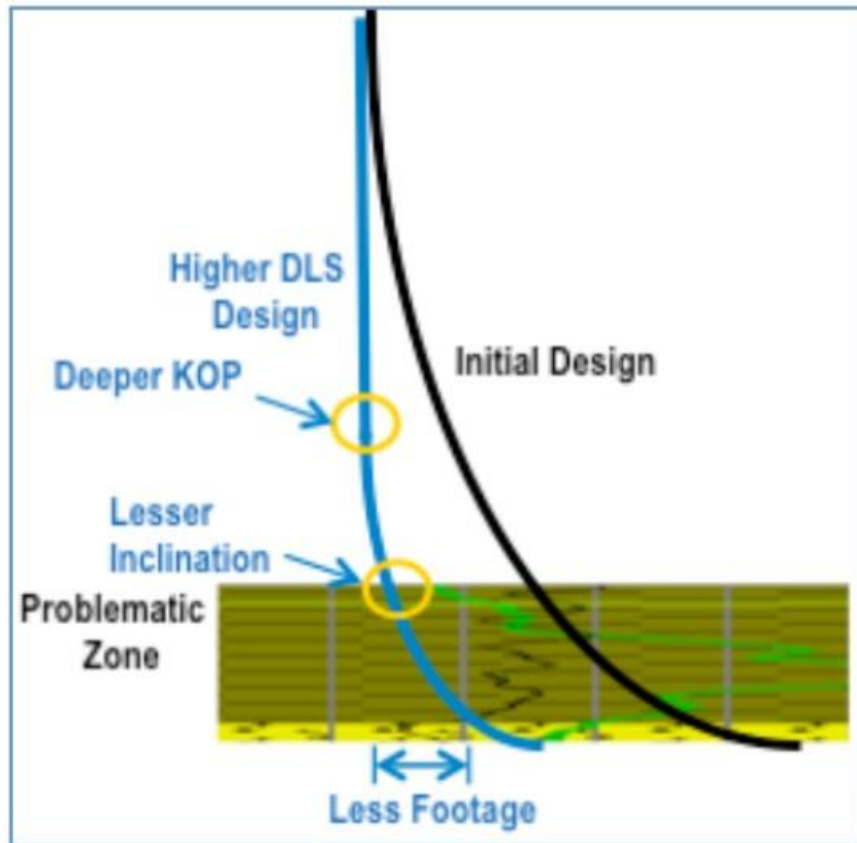
Figure 5.7: High DLS design with RSS [56].

It was also observed from mud rheology and low-end rheology evaluation that, the parameters of the mud were outside the extended range prescribed for drilling mud parameters. Increased pressure drop across the annulus and increased fluid internal friction was caused by poor hole cleaning and presence of drilled solids in the mud respectively, and this suggested to be potentially causing higher ECD than planned. It was observed that sweeps usage had an adverse effects on hole cleaning. Through cutting flow meter, the performance of sweeps was monitored and it was found out that, pumping after every alternate stand helped in increasing cuttings recovery and keep ECD in check. A positive impact on ECD reduction was obtained as a result of mud maintenance. Optimize existing mud window available at hand was observed as mud treatment to reduced drill solids resulted in immediate reduction of ECD.

It was also observed after loss circulation evaluation in the laterals that, effects of ballooning validates the lost gradient estimated by RTGM calibrated MEM. Categorically, loss circulation were caused by;

(a) ECD management, and (b) Mud maintenance, since inefficiency of mud properties maintenance resulted in higher ECD than planned, and the nature of losses were that of drilling induced losses.

During drilling the laterals, inconsistent gas percentages were recorded but well control incidents were not encountered. The weight of mud was lowered below pore pressure estimated as a test, well flow was not encountered too. This indicates that, in underbalance condition, laterals can be drilled without having any equipment at surface to manage pressure.

A 2,000 feet horizontal well was drilled in the Devonian shale using air/mist as drilling fluid, in the Wayne County, West Virginia. This well was drilled to test the concept that multiple hydraulic fractures from a horizontal wellbore can increase gas production than the vertical stimulated borehole [57].

In 1985, Morganton Energy Technology Center of the Department of Energy (DOE) awarded a contract to BDM Corporation, to investigate that in the Devonian shale multiple hydraulic fracture from a high-angle wellbore can increase gas recovery efficiency over the vertical wells. Grace, Shursen, Moore and Associates (GSM) who were the consultants on well site drilling activities, were selected by BDM because of their experience in the Grand Cangon well.

To design and execute the major field experiment, personnel from DOE, BDM and GSM constituted the project team. The main technical issues of concern based on experience from the Appalachian Basin air-drilled directional wells were listed as follows;

(a) Turning a well beyond 55° in hard rocks,

(b) Maintaining adequate directional control of well,

(c) Determining the optimum rate of angle build in hard rocks,

(d) Reducing friction and drag during drilling,

(e) Keeping the wellbore cleaned at high angles,

(f) Adopting logging tools to operate in high-angles wells,

(g) Completing the well in the horizontal section,

(h) Isolating zones for testing and for applying multiple stimulations.

One of the most important components of the program was considered to be the selection of site. Due to the availability of data and regional natural fracture network of the Wilsondale pool, Wayne County, West Virginia, was selected. The wellbore azimuth for drilling and for predicting high fracture permeability in the area was designed using these available data for the area. Inside the Wilsondale pool, the well performance and interference effects was accurately predicted by full-field simulation.

After diligently considering normalized cumulative production data, from several producing areas in the Devonian shale, also aided the selection of the Wilsondale pool area. A desk top computer program that was used to analyze the drill string for drilling rig and equipment sizing aided in planning of the well. Daily spread-sheet tracking of well trajectory and cost as well as in comparing actual drilling data with model predictions was done by an on-site portable computer.

The following well prognosis was made based on air drilling techniques and slim hole drilling used in the Grand Canyon well.

(1) Drill a 17 ½-inch (or 18-inch) hole to 630 ft.

(2) Run and set 630 feet of 16-inch conductor pipe.

(3) Cement to surface and wait on cement for 8 hours.

(4) Drill a $14^{3/4}$-inch hole to 2,000 ft using air and mist (approx. 3500 scfm).

(5) Run and set $11^{3/4}$-inch, 47#, J-55, ST&C casing.

(6) Cement back to 1,300 ft.

(7) Nipple up the wellhead and rotating head.

(8) Drill out with a $10^{5/8}$-inch bit.

(9) At 2,800 ft, run a $10^{5/8}$-inch air bit, 7¾-inch baker motor, 2.5° bent-sub, 8-inch Monel, MWD, two 8-inch DC (drill collars) and 4.5-inch DP (drill pipe.)

(10) Directionally drill at 4.25°/100 ft (if the 2.5° bent-sub does not give 4.25°/100 ft, use 3° bent-sub or a bent housing motor in combination with a bent sub).

(11) Drill to 85° to 90° at a total vertical depth of 3,423 ft (50 ft from bottom of lower Huron) which should be approximately 4,080 ft MD.

(12) Circulation rate should be 2,500 scfm with less than 10 bbl/hr mist.

(13) At times it may be necessary to make reaming runs to bring the hole into guage. If this is necessary, run a bit, 3 point, 8-inch Monel, 3 point, and two 8-inch DC. With this assembly ream through the portion of the hole causing problems.

(14) Log the well using conventional wireline tools to the free fall point.

(15) Run and set 8 ⅝-inch, 24ppf and 28ppf, J-55 ST&C casing at ± 4800 ft.

(16) Cement the bottom of casing conventionally. Place 10 ft of sand in annulus and fill annulus with class-A cement. Wait on cement for 8 hours.

(17) Nipple up wellhead, bag preventer, and rotating head.

(18) Drill out $8^{5/8}$-inch casing with a $7^{7/8}$-inch bit, 3 point, and Monel drill collar.

(19) Core 60 feet of the lower Huron at 85° to 90°.

(20) Ream out core hole with 7 ⅞-inch bit, 3 points and Monel with MWD. Drill ahead until a motor correction is required or total depth is reached.

(21) Run a $7^{7/8}$-inch air bit, $6^{3/4}$-inch motor with bent housing, $6^{1/4}$-inch Monel, and $4^{1/2}$-inch DP to make a motor correction.

(22) Drill 2,000 feet of horizontal hole in the lower Huron using air-drilling only with a minimum of 2,400 scfm.

(23) Log and test the well to the total depth.

(24) Run and set $4^{1/2}$-inch, 10.5ppf J-55, ST&C at total depth using external casing packers, completion packers and port collars.

Between October 21 and December 18, drilling operations were carried out at this site selected. The planned drilling time was 45 days but it took 58 days to complete. The vertical portion of the hole consumed most of the drilling time resulting in the wide time difference for drilling. As 3 days was estimated to drill the vertical portion, it took 15 days to drill. The horizontal portion took 43 days to drill but the

planned days were 42. Due to sidetrack, the building section of the well took longer than expected, but since no motor corrections were required in the horizontal section, it was drilled faster than expected. The rate of build was changed from 4.25° per 100 ft to 4.48° per 100 ft based upon the logs and actual kick-off point of 2,113 ft.

The total target vertical depth of the horizontal based upon the logs and actual elevation was changed from 3,420 ft to 3,390 feet ± 10 ft. From vertical, in the interval of 2,113 ft to 4,045 ft, the inclined section of the hole was built to 92°. A 10 ⅝-inch bit was used to drilled this portion, and to 3,803 ft, an 8 ⅝-inch casing was run. For directional drilling, it was started using a 7 ¾-inch low-speed motor on an air/mist system, an electromagnetic MWD system and a 2½° bent sub. Due to problems relating to motor plugging and MWD system, the progress of drilling was slow at the beginning, but as the MWD system was changed to wireline, flux gate tool, no much problem was encountered.

Initially, build rate average was 4.75° per 100 feet to a depth of 2,800 feet. A 5.25° per 100 feet was the average dogleg severity. At 3,182 feet, the build rate was decreased to 3.5° per 100 ft. In the same interval, the inclination was changed from 35° to 48°. The rate of build started to increase slightly above the 48° but after the survey at 3,246 feet, the motor failed at a depth of 3309 feet. A 3° bent-sub was run with the next motor since the inclination was beginning to lag the planned trajectory.

A portion of the hole with an average rate of build of 7.4° per 100 feet was drilled using this assembly. The assembly was pulled out of the hole after two surveys with the 3° assembly and projected inclination greater than 68° was estimated, since the building of the inclination was very fast. The depth at this point was measured to be 3, 509 ft. Reamers were used to ream the hole out because the hole was found to be tight when tripping out. Reaming was required from 2,230 ft to the total depth of the hole. The drill pipe became plugged and stuck while carrying out connections on bottom. The well had to be sidetracked since attempts to fish the BHA were unsuccessfully. The well was then plugged back to 3,175 ft and dressed to 3,239 ft with cement. To sidetrack out the right side of the hole, a 7 ¾-inch motor with 2 ½° bent sub was run.

The inclination of the well was decreased during sidetracking and the lost angle was not able to gain fast enough due to the slow building of the angle. The inclination

was decreased from 51.6° to 48° at 3,240 ft. As drilling with the down hole motor began, almost all the cutting were shale. To build the inclination faster, a 3° bent sub was run at 3,421 ft as about 7° per 100 ft inclination built was required. So the total vertical depth will be within 90° target. It was observed at 3,666 ft that the target could not be met without building over 10° per 100 ft; hence the well was plugged back and sidetracked again.

The well was plugged to 3,330 ft and dressed off to 3,362 ft with cement when the second sidetrack was initiated. A strong building assembly was run to kick off on a high side of the hole. The assembly which was made up of a 2° bent housing (6 ¾-inch OD) motor and 1.5° bent sub was used to sidetrack the hole out the top side without problem.

Borehole cleaning problems arises as directional drilling was continued to 3,827 ft, and dictated running of an 8 ⅝-inch casing. Grace et al. [57] spent many days trying to clean the 10 ⅝-inch hole with 4,000 scfm of air and 30 bbl/hr of mist. It was observed after a single shot survey was run during one of the reaming that, the inclination was 74° and not 76° the steering tool was reading. At 3,787 feet, the survey was changed to 74° from 76.3° to reflect the single shot data. At 3,803 ft (Kelly Bushing), an 8 ⅝-inch casing string, 24#/ft and 32#/ft, K-55, ST&C casing was run and cemented in place. Without problem, the casing was run to a depth of 3,543 ft and washed down several places thereafter. Tool was run through these heavy walled casing with no problems.

The next building assembly made up of 6 ¾-inch bent housing motor, had it bent set in the motor between 1 ¾o and 1⅞°, since that was the maximum bent the an 8 ⅝-inch casing can contain without pushing it with drill collars. Probably a 2° bent could have been run in this casing but that was not necessary as the smaller bend built adequately. The bent housing motor dogleg severity average was 10.1° per 100 ft. The inclination was extrapolated to be 92° at a measured depth of 4,043 ft. This was then indicated that, the angle built section was completed. At this point, the true vertical depth was 3,402.5 ft but the targeted depth was 3,400 ft for this well. Planned versus actual drilling performance for the inclination and azimuth of the borehole was compared.

A 5.6°per 100 ft built rate was obtained with the 2 ½° bent sub during drilling the 10 ⅝-inch hole. An average of 7.36° per 100 ft built was obtained with 3° bent sub. A 5.5° per 100 feet and 7°per 100 feet were the expected built rate for 2.5° and 3° bent sub respectively. A 2° bent housing motor (6 ¾-inch OD) and a 1.5° bent sub was used for the second sidetracked. Building rate angle of about 5.5° per 100 ft and 2.5° per 100 ft should be obtain from a 2° bent housing in a 10 ⅝-inch hole and 1.5° bent sub respectively, and these will sum up to 8° per 100 ft. For the first motor run, 7.72° per 100 ft was the actual built rate but during the second run, the actual built rate was 4.25° per 100 ft only. Different BHA were used for building inclination.

A 6 ¾-inch bent housing motor with a 1.8° bent of the housing was used after the 8 ⅝-inch casing was run. No expected build rate was published for the motors used in the 7 ⅞-inch hole by the manufacturer. But a 5° per 100 ft rate in the 8 ¾-inch hole should be obtained from 1.5° bent housing, hence about 7° per 100 ft in the 8 ¾-inch hole should be obtained from a 1.8° bent housing by extrapolation. At least 1°or 2° bent is expected to be added due to the reduction in hole size. A 9.8° per 100 ft was the actual build rate for the last two motor runs.

Using eleven (11) down hole motors, a total of 14 motor runs were made as shown in Table 5.1 below. Average footage drilled per motor run in 7.8 drilling hours was 176 feet and in 9.93 drilling hours, the average footage drilled per motor was 224 ft. The motors used were seven 7 ¾-inch and four 6 ¾-inch motors. The average time spent on restarting motors after it stalled or after connection was 2.71 hours per run and 3.45 hours per motor. While drilling, the motor was stalled in a few times. For restarting the motor, the procedure that works best was to pump a few barrels of water containing mist chemicals down the drill pipe prior to turning air into the drill pipe. Motor life was increased by 1.5 to 2 times by this procedure.

The air rate and mist rate were varied between 2,000 and 3,000 scfm and 5 and 35 barrels per hour respectively, to determine the causes of the poor performance of the motors. Also, apart from the soap and polymer, each chemical in the mist was dropped out one at a time from the mist as presented in Table 5.2, but the cause of poor performance of the motor was not found. No mechanical damage was observed when the motors were sent for repairs.

Table 5.1: Performance of down hole mud motor.

Motor #	Drilled Interval (ft)	Penetration Rate (ft/h)	Hours to restart	Build rate (deg/100 ft)	Bent sub, bent housing	Comments
1	102	34.0	0.00	4.42	BS 2.5	Plugged with cuttings
2	62	24.8	0.00	7.86	BS 2.5	Plugged with cuttings
2	282	25.6	0.50	4.29	BS 2.5	Motor failed
1	45	12.9	0.50	5.87	BS 2.5	Motor failed
3	381	29.9	14.0	4.27	BS 2.5	Motor failed
4	324	29.5	1.50	4.19	BS 3.0	Motor failed
5	200	28.6	0.00	7.34	BS 2.5	Pulled to change BHA
6	46	4.8	3.50	6.25	BS 2.5	Time to drill sidetrack
7	136	30.2	0.00	1.19	BS 3.0	Pulled to change BHA
7	245	24.5	0.00	5.57	BS 2.0	Pulled to plug back
8	272	18.8	5.00	6.84	BH 2.0, BS 1.5	Motor failed
9	193	21.4	10.00	3.95	BS 1.5, BH 2.0	Motor failed
10	135	15.0	3.00	10.48	BH 1.8	Motor failed
11	46	23.0	0.00	8.89	BH 1.8	Finished build
Average run	176	22.6	2.71			
Average per motor	224	22.6	3.45			

Table 5.2: Down hole motor life.

Formula	Motor runs				
	(1-4)	(5)	(6)	(7-8)	(9-14)
Foamer	X	X	X	X	X
Polymer	X	X	X	X	X
KCL	X	X	X	X	
Graphite	X	X	X		
MF-1	X	X			
Soda ash	X				
Drilling hours	5	13	11	8	8
Hours to restart	0.5	14	1.5	3.5	6

5.3 Directional Survey Implementation

An electromagnetic Measurement-While-Drilling (MWD) unit was the first system used for the steering of the down hole motors. By electromagnetic radiation, data was transmitted back to the surface. After 4 hours of drilling time, the first MWD probe at the end of the first motor run failed. The stand pressure rose up to 500 psi while restarting the motor and the seal of the O-ring in the MWD probe failed.

After 4 hours, the second electromagnetic MWD probe was quite working. Wireline flux gate system was used to replace the electromagnetic probe due to operating problems in shutting off the air-flow to transmit tool face data. This wireline flux gate steering tool was used to complete the built angle from 2,277 feet to 4,043 feet. Wireline tool was transferred through a side-door entry sub to outside the drill pipe. At air rate of 2,100 scfm, the probe operates very well but air rates above 2,100 scfm, it fails.

At the beginning of the first sidetrack, a magnetometer type probe was run and lasted for 2 hours but second probe lasted for 3 hours. And while running this probe, the rate of air was 2,100 scfm. Until 8 ⅝-inch casing point was reached, the flux gate probes were used after former probe failure. The flux gate probes for tool face were used until the final angle building (75° to 90°) was achieved, and inclinations and directions were monitored using single shots. Kinking the wireline was the biggest problem anticipated with the side entry subs.

Hole cleaning as expected was the major problem encountered in drilling the well. It was intended to start at a minimum rate of 2,000 scfm with as little mist as possible. In an hour, a little less than 10 barrels of mist was observed as the minimum pump rate. The bit plugged with cuttings though there was a float immediately above the motor at the first two motor runs. There was a problem in pulling out the drill string at the end of the run number 6 at 3,309 feet. After pulling out one stand, the hole was tight. Air was circulated to clean the hole for 1.5 hours. At 3,300 feet, the inclination was 54°. A lot of problems were encountered at 3,509 feet in getting out of the hole on the next motor run. Even though the inclination was 65° and circulation could not clean the hole, the pipe could be pull out of the hole as long as air was circulating with little or no drag. The drill string could more freely because, the air stream made a fluidized bed of agglomerate cuttings that allowed this free movement of the string.

A reaming run was made to clean the hole at 3,509 ft. During connection at the same depth, the reaming assembly became stuck. The pipe would not come out of the hole after it became plugged while making a connection. Majority of cleaning problems were encountered between an inclination of 60° and 70°, but the exact inclination was not known at this time. As reaming near the bottom, the air rate was 3,150 scfm. In order to sidetrack and fish, the hole was plugged back to 3,200 ft. A 2,100 scfm

and 20 barrels per hour mist was used to drill out the cement. The same amount of air and mist was used to sidetrack the hole. The air rate was increased to 3,150 scfm at 3,330 ft but the same amount of mist was maintained to increase hole cleaning. Due to four probes failures after 121 ft of drilling, the air rate had to be reduced. The motor was washed back in the hole at this depth, hence it shows that the well was not adequately cleaned. Inclination was 57° at this point. Drilling continued to 3,666 ft with 2,100 scfm.

On a trip, the drill pipe had to be pump out of the hole at 3,666 ft when the inclination was little above 60°. The hole was cleaned by running a ream. The drill string had to be pumped out of the hole after reaming and 1.5 hours of circulation with 3,150 scfm and 20-25 barrels of mist per hour. There was a little drag at 3,634 ft on tripping out and 60 ft of fill on the bottom of the trip. The pipe had to be pumped out at 3,700 ft. Inclination was 74° at 3,800 ft, and still the pipe had to be pump out after 2 hours of working and a circulation 4,269 scfm of air. A decision was taken to run the 8 ⅝-inch casing due to hole cleaning problems. The casing had to be circulated into the hole even though two days were spent to clean the hole.

An inclination of 92° was obtained after finishing the last motor run. The 90° inclination was reached at 4,020 ft. Using mist and 2,100 scfm of air, a 4,156 ft well was cored and drilled. The wellbore was dried and dusted after coring operations were completed with no problems related to hole cleaning. The run assembly was a bit, float sub, bottom hole three points reamer and two 6 ¼-inch Monel drill collar with a Monel crossover sub between the Monels. For drilling the horizontal section, the assembly was perfect for the hole. Inclination was reduced by an average rate of 0.25° per 100 ft and at 0.5° per 100 ft walked to the right. A depth of 3,427 ft was reached as the total final vertical depth which was 25 ft from the bottom of the lower Huron shale. The assembly did an excellent work due to the ability to control BHA. Considering the fact that motor corrections were not made, the wellbore course was on target better than expected. In an attempt to drop the assembly a little faster, the BHA weight was adjusted from 25,000 to 15,000 lbs, but bit weight had no tendency to drop the assembly.

A bit weight of 20,000 lbs was then maintained with a penetration rate of 25 ft per hour including connections. From the analysis program for the BHA, it was observed

that bit weight has no effects on the inclination tendency. A bit side force of 1,584 lbs build and 0.08° bit tilt was obtained from this program. It was clear that the assembly dropped inclination but built inclination was expected. Hence, the drop tendency of the formation was equivalent to the building tendency of the assembly plus 0.3° per 100 ft.

After completing the angle building to an inclination of 92°, a 7 ⅞-inch hole was cored. The well was core by using a standard 30-foot, 6 ¼-inch diameter core barrel modified with an inner tube stabilizer in the center. A 4-inch compact bit (RC-444) core bit which has a diameter of 7 ⅞-inch was used. Because of the center stabilizer, an aluminum inner barrel cut into 15-foot length was used. All cores were positioned in such a way that, the natural fracture directions could easily be determined.

From 4,043 ft to 4.056 ft, the first oriented core was obtained, and from 4.056 ft to 4,086 ft, the second oriented core was made with no problem. At 4,126 ft, an additional 30-foot of oriented core was taken. The core recoveries are summarized in Table 5.3 with numbers of fractures and their orientations. The planned orthogonal azimuth of the horizontal wellbore was verified from the cores.

Table 5.3: Summary of coring operations.

Interval (ft)	Core Recovery		No of fractures per core interval	Average orientation
	(ft)	(%)		
4043-4056	13 (core) 17 (cuttings)	43 (core) 57 (cuttings)	1	N37°E
4056-4086	30 (core)	100	5	N38°E ±1°
4126-4156	30 (core)	100	13	8-N39°E ±1° 5-N29°E ±7°

Hole drag is considered to be the most important problem in the horizontal section of the hole. However, hole drag was not a problem until the depth of 5,400 ft. After running the pipe string into the hole after a connection, the problem occurred. Even though all the weight could be slacked off, the pipe would not go down but can easily be rotated and pulled up. The six $6^{1/4}$-inch drill collars were used to solve this problem by placing them in the vertical hole at 1,500 ft on the next bit trip. Before the pipe start moving, it was indicated by all data that, an initial coefficient of static friction had to be overcome. Only the lower coefficient of kinetic friction was

required to be exceeded once the pipe was moving. The higher coefficient of friction can be overcome by dropping the drill string from maximum hook load that is, using the momentum of the drill pipe.

The variable for the drill string drag below 5,400 ft going down had to be changed. The coefficient of kinetic friction changed significantly during lowering the drill string but the hoisting and rotation friction coefficient had not changed much. The coefficient of friction was calculated by using a computer model. The coefficient of friction was changed until the field measured drag value equaled the drag. There was no problem running log when BHA was left out of the drill string, hence the drill pipe could move in and out freely. BHA therefore had something to do with the excessive down drag. Pipe buckling could also be the cause of this down drag.

An open hole logging suite and a down hole television camera was used after reaching total depth, to logged the 7 ⅞-inch hole. The logging system incorporated in the drill pipe was used to run the logging twice in the hole. This logging tool was attached to the bottom of the drill pipe in an encased housing.

Gamma ray, density, caliper and dual induction suite was obtained in the first logging run. The tool pad was located on the low side of the hole, hence did not position the tool to contact the hole properly and this resulted in the density and caliper tool not working properly. Temperature and gamma ray tool was run for the second logging. During tripping in the hole, the temperature was logged. The gamma ray tool which was run for correlation reasons failed. Hence for the depth temperature correlation, the 8 ⅝-inch casing seat was used. The temperature log, from examination of the logs should be a very good log for fractures detection and/or horizontal well bore production for the Devonian shale well.

The down hole television camera was proved to be helpful in fracture identification in the wellbore. Using the drill pipe to conveyed television camera logging tool was the first time this method was run. More than 250 features interpreted to be fractures were detected from the video log analysis. Most of the fractures contained stains, and this indicates gas condensate bleeding at that point into the wellbore. Within a distance of 13 ft, 14 fractures were detected (from 5,042 to 5,055 ft). A gas calculated to be produced at 2,219 mcf/d was from the same zone.

The natural fractures number was observed to varied from a low value of 5 for 200-foot interval (4,500 to 4,700 ft) to above 40 (from 4,100 to 4,300 ft). In the back portion where the borehole varied a few inches to 70 ft, the fracture occurrence frequency had increased. Over the 2,200-foot length surveyed, the mean spacing for fracture was 8.8 ft.

Casing operations were started after drilling to the total depth of 6,020 ft and finishing logging operations. There was no problem encountered during the casing operations even though the operations were slow. A total depth was cased without problem with the 4 ½-inch casing. On the 4 ½-inch casings, 14 port collars, 8 external casing packers and one cement packer were run. To avoid damage during running into the hole, immediately below and above each external casing packer (ECP), one centralizer was placed. The individual producing zones were isolated from each other by external casing packer. The cement packer which can be inflated with cement was a backup to ECP. Port collar which will be used to selectively stimulate and produced the individual producing zones were located between the packers. Test and stimulation openings available for specific isolated intervals are shown in Table 5.4.

Included in the project were horizontal logging and coring and unconventional casing installation. Research and development cost amounted to 25% of the total cost. Site management cost was 9% of the total cost. Third-party cost which was 66% of the total cost was lower when the well was drilled than they will be in future. Not included in the cost analysis was well stimulation cost. The cost analyses are presented in Table 5.5.

Commercial application for the overall cost could be lowered by extending down hole motor life, development of a more efficient and reliable MWD system for air drilling, and by reducing the turning radius.

Jason Pitcher et al. review the current common practices used in geosteering in shale for both gas and oil producing reservoirs. They presented a brief history of strategy development, with comments about its perceived effectiveness and value [58].

Table 5.4: Casing program installation for 10.5 ppf, K-55, 4 ½" from 3,736 ft to 6,011 ft [57].

Isolated intervals, feet	Number of port opennings
3736-4095	8
4095-4194	4
4194-4337	4
4337-4811	8
4811-4986	4
4986-5176	8
5176-5411	8
5411-5602	8
5602-6011	4
Special inflatable completion packer	56

Table 5.5: Horizontal well cost summary in Devonian shale [57].

	Third Party Cost (Dollars)	H & D cost (Dollars)	Project Management (Dollars)
Site selection, reclamation, well design, site acquisition and preparation		280,082	
Drilling (including directional driller)	700,572		
Coring and analysis		54,758	
Logging	41,248		
Well testing and analysis	21,950		
Contingency (plug back #1 and #2)	102,147		
Well site management (drilling, coring, logging and well testing)			116,143
Subtotals	865,917	334,840	116,143
Total well cost (excluding stimulations)	1,316,900.00		

To attempt to determine the viability of a particular strategy, examples of success and failures are examined. Alternative approaches and methodologies are finally reviewed and examined with comments about its potential application, benefits, and value.

Well placement in unconventional shale currently, ranges from simple geometric well placement to a gamut of pattern recognition systems and geosteering with geochemical and geomechanical analyses. These wide diversity of systems employed leads to uncertainty in the effectiveness of any strategy, with confusion as to the true value or merit of a particular technique. Usually, the placement of the well strategy is based on what come before with little regards as to the complexities or differences between reservoirs.

In unconventional shale, well placement is primarily associated with drilling efficiency. Regardless of the rocks encountered along the wellbore, many operators are using simple geometric well placement techniques in which a well plan is followed. The assumption here is that, the hydraulic stimulation techniques pioneered in the Barnett shale might have contacted enough rock volume to make any attempt at proactive well placement futile. Pitcher and Buller indicated that well placement may have a major effects on stimulation efficiency and associated production [59].

It is believed that well placed in a thick shale sequence can have a dramatic effect on production, and in an attempt to remove some of the geologic uncertainty, many operators are following the path of geosteering. To place the well in a predefined stratigraphy is the primary goal of geosteering. The principal methodology used is gamma ray correlation is described, along with a review of some of the concerns and issues encountered during employing this method. Some of the operators are adding resistivity measurements to improve correlation or imaging tool, such as density, to gain information about the structure, in addition to using gamma ray tools for geosteering.

Although this methods have some success, it is often difficult to quantify how successful these methods are. Alternative methods of well placement are usually discounted because tying results to the ultimate metric production is difficult. Other methods alternative to geosteering include biosteering, geochemical steering, and

steering to geomechanics. Although geochemical steering and geomechanics are rapidly gaining attention as solid proven technologies that can deliver better results biosteering has not found an application in the World of unconventional shale [158].

5.4 Geosteering With Gamma Ray

For geosteering in shale, predominate methodology is the use of basic natural gamma ray (GR) logging-while-drilling (LWD) tools. The LWD tools is thought to be one of the least understood and improperly used one. The natural occurring gamma radiations emitted by the formation is measured by the gamma ray technology. The statistical data, for interpretation, is then transmitted to the surface. The qualitative view of the rock type, such as shale or shaliness, sand or siltyness, and limestone or marl is provided by the basic gamma ray curve.

To steer a horizontal well, the effectiveness of using GR is largely depends on the quality of the data collected, transmitted, and processed. Any significant error in one of these three processes can lead to misinterpretation of the data and well placement. To correlate data from the horizontal well back to a vertical pilot hole or offset total stratigraphic depth (TSD) log, geosteering with GR uses basic pattern recognition. It is possible sometimes to see enough mineralogical variance in the GR measurements even in shale, to correlate down to the tool resolution scale (1 ft/30cm approximately).

A correlation log from a Marcellus shale well is shown in Figure 5.8 below. The gamma ray from the offset well and other curves are from real-time data, different sections of the well is represented on the total stratigraphic depth of the well in Figure 5.8. For clarity, the data has been deliberately offset on the log. The upper numbers on the depth scale are for the original well and the lower number are for the drilled well. One important aspect of geosteering with a gamma ray tool is that, the section must be constantly traversed to identify appropriate markers and correlation points. These picks which are useful in the forward planning of the well path, are used to make estimates of dip.

The real-time data of this well with high data density and low signal-to-noise ratio, is of appropriate quality. Accurate correlation and interpretation is enabled by this level of quality. In shale, a common occurrence is lateral facies changes, in which the

same stratigraphic position yields a different gamma responses. This results is demonstrated at 8,029 ft TSD in Figure 5.8, where one pass of the tool reads lower than the previous passes through this zone.

In Figure 5.9, the resulting interpretation cross section is relatively straightforward. The tool is capable, even in this area of structural complexity in the hands of skilled and proficient interpreters, of accurately identifying the structural and stratigraphic position of the well while being drilled. The gamma ray log in Figure 5.9, measured in real time along the well path is shown below the path of the well and the geological structure. To accurately determine the stratigraphic position of the well and geological structure, this display in Figure 5.9 is used in conjunction with the logs from Figure 5.8. A more detail view of the section is shown in Figure 5.10 below.

This detailed view shows how clean the gamma ray data is. With occasional instantaneous rates much faster, this well had a penetration rates of about 150 ft/hr. there is no excessive noise or gaps in the data, and it is an example of good data acquisition for gamma ray geosteering to stratigraphy. The quality of gamma ray logging unfortunately, does not always meet the standards necessary for accurate well placement. Gamma ray tools have some intrinsic limitations that are inherent in the tool design. The tool will have a higher signal-to-noise ratio if the tool in question has a small scintillation detector. Counting statistics play a very large part in how the data from downhole is acquired and processed. A sample period is set, all gamma ray counts are collected, and an average count rate determined. When the sample period is set too short, which is usually done because of high anticipated drilling rates, then the statistics will be skewed, resulting in a very noisy signal.

In shale, with ever-increasing drilling efficiency, higher drill rates mean that, detection rates of processed data through mud pulse telemetry must be very high. With a telemetry rate of one data point in every 20 seconds, for example, results in a data density of one data point per feet. Although, missing one data point results in a gap of 2 ft between data points, if not detected for a minute, the gap is 5 ft between the data points. For a 2 minutes gap in detection, results in a 10 ft gap in the log and this makes the log impossible to correlate in real time. An example of poor data

quality is shown in Figure 5.11 below, with the initial part of the well from 900 to 2,700 ft, illustrating almost the worst possible case.
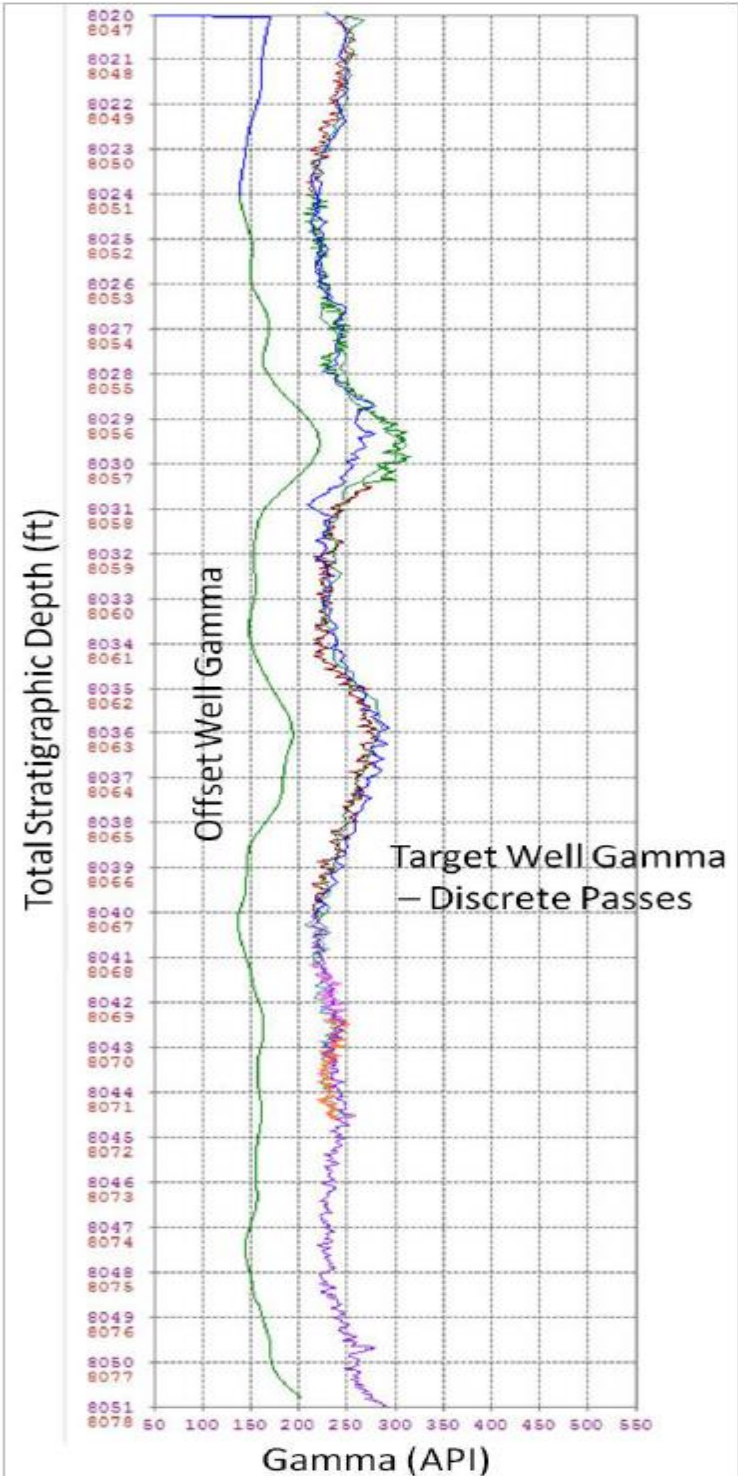
Figure 5.8: Correlation log from Marcellus well #1 [58].
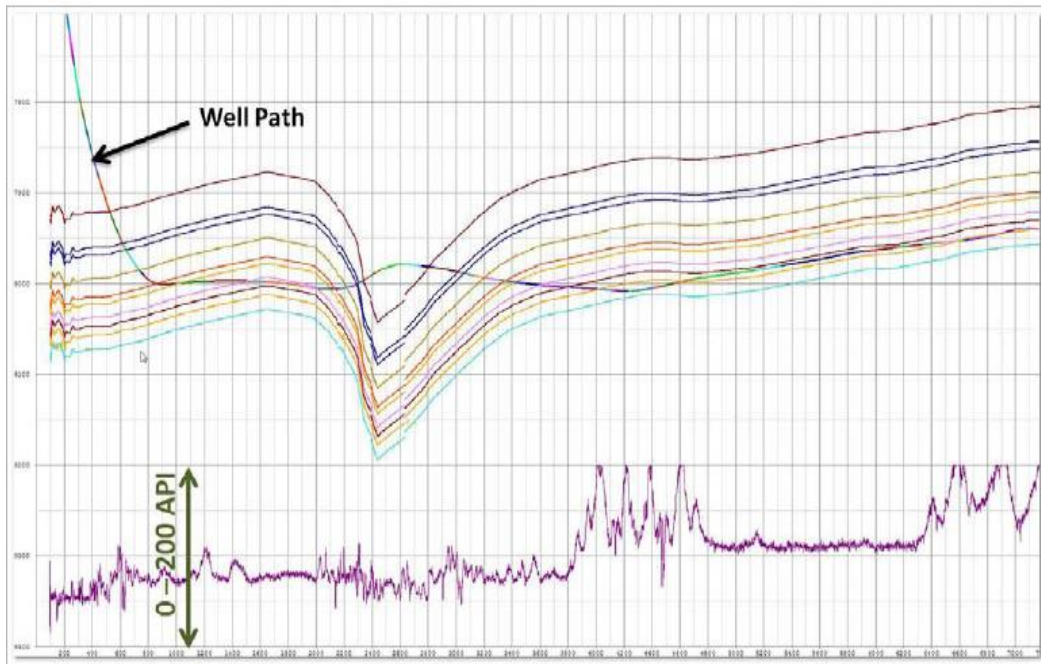
Figure 5.9: The resulting interpretation cross section of Marcellus well #1 [58].
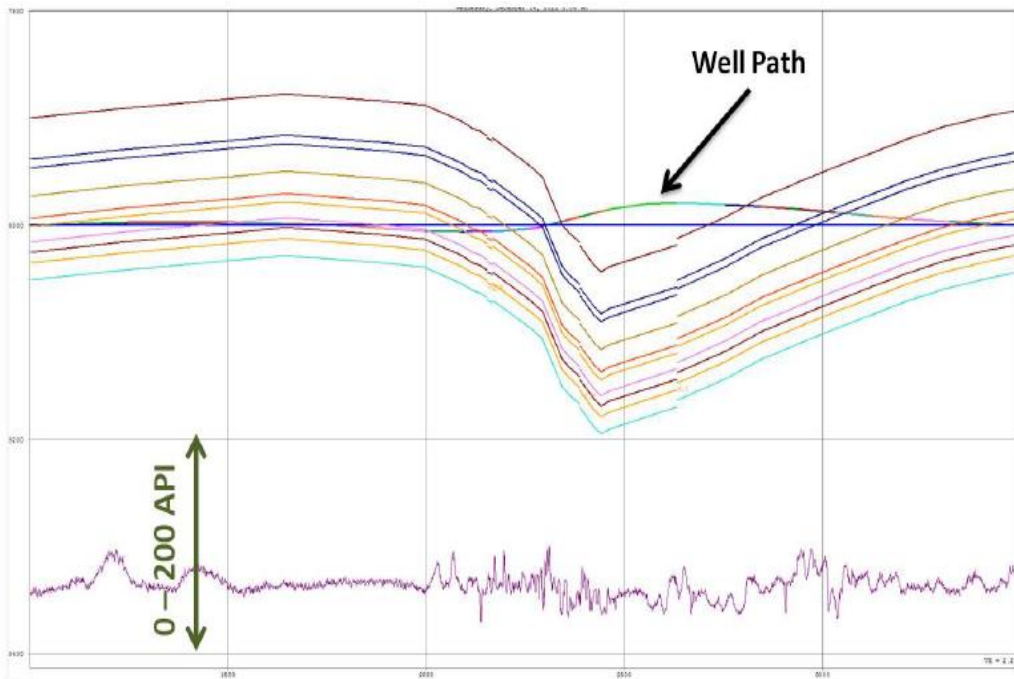
Figure 5.10: Detailed view from Marcellus well #1 [58].
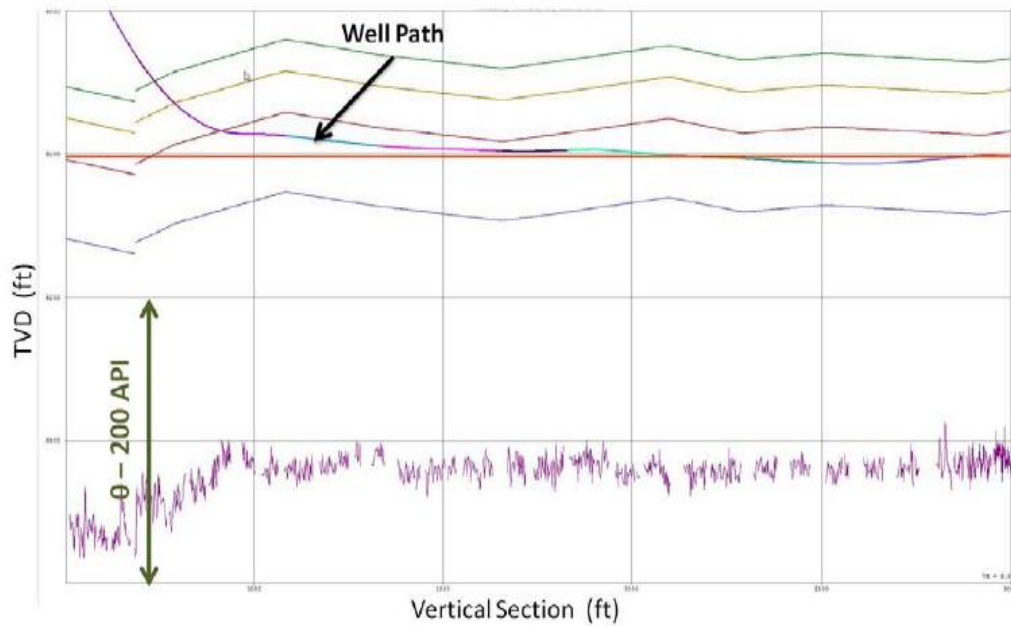
Figure 5.11: Gamma ray section of Eagle Ford well #1 [58].

The worst possible circumstances are encountered in this case. With large gaps in the log, detection rate is the first issue. A large signal-to-noise ratio is then the second issue. A very small detector in a probe based system with some tools, has a very low efficiency which results in a high signal-to-noise ratio. Poor detection, short sample frequency, a small detector, and fast drilling will result in unusable logs for correlation. This means every data point has substantial noise, with point to point swings of up to 30 API. The gaps and noise make accurate correlation almost impossible. Figure 5.12 shows a comparison against an offset correlation well. The offset well correlation log is blue in this comparison, with the composite stratigraphic passes offset to the left, and the last pass through the stratigraphic sequence is offset to the right. This indicates how difficult data of this quality is to correlate with any sense of conviction.

Data quality is one of the important considerations in geosteering in shale using LWD gamma ray. It was shown by experiences that, not all vendors adequately understand the importance of getting the best quality from their sensors. A common refrain from sales personnel is that the sensor is API calibrated, therefore is of a suitable quality. Because the API calibration does not take into account system efficiency or logging speed, this claim is misleading.
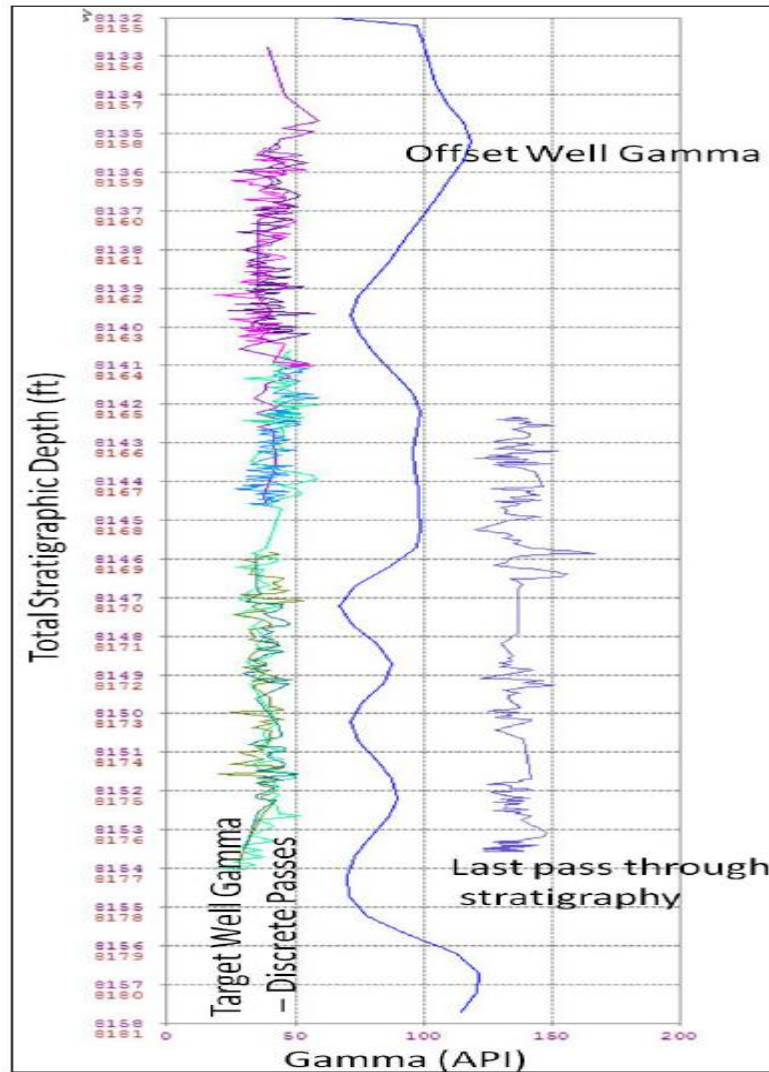
Figure 5.12: Eagle Ford well #1 logs [58].

A sensor passes the API calibration as long as it has 200 API differences between the two sections of the calibration pit. The problem of data quality disparity is usually the cause of concern between vendor's tools reading differently in the same well, or a large disparity from wireline logs in the same well.

The limitation of the various systems must be understood by the purchaser of LWD gamma services, and the effect it may have on the ability to place wells within a specific stratigraphic section. A better metric comparison could be the system sensitivity. The system will have a detection efficiency for gamma rays, for an API calibration, expressed in counts per second per API value (C/S/API). A large crystal or multi-crystal array having a detection efficiency of 0.35 C/S/API, will have more efficiency and exhibits lower signal-to-noise ratio with all other variable equal as

compared to a single small probe-based detector with a detection efficiency of 0.11 C/S/API.

Usually, with the same mud system wells are drilled with a common ROP range, therefore telemetry reliability and tool setup (sample period) become more significant variables. Well placement is affected by telemetry in that, the data for accurate correlation is just not available. New system such as EM technology, delivering data with very high reliability to the surface, are having a significant effect. When screening potential vendors for services, this aspect should not be ignored.

Azimuthal density LWD logs have a long history in Geosteering. The basic procedure is that, a source and two detectors are located on a stabilizer blade that sweeps the borehole while drilling. Density measurements are made around the borehole and transmitted to surface as the sensor package rotates. Then, the density data constructed an image of the borehole as shown in Figure 5.13, enabling features such as bedding planes and faults to be seen.

These density images generated are invaluable in providing experience geosteering geologies with an insight into the localized structure through which the well is being drilled. Corrected for borehole size and depth of investigation real time dips, enable the determination of local apparent dip and the trajectory of the well relative to that dip. Thus, this answers the question of whether the well is going down structure, up structure or parallel dip [60]. These tools are usually used in preliminary appraisal wells and step-out wells to validate structural models and confirm seismic interpretation although not in common usage for the development of shale wells.

Geochemical steering was developed for drilling thick marine shale that were very featureless on logs and in samples in the North Sea. Through the careful construction of a regional set of correlations, the value of chemo-stratigraphy in shale is maximized, using drill cuttings and densely sampled cores from existing vertical wells. A chemo-stratigraphy zonation system is developed that is largely unrelated to lithological or petro-physical characteristics, and it is on a vertical scale somewhat finer than that provided by cutting description shown in Figure 5.14 below. To provide an independent interpretation of wellbore position, samples from drilling wells are analyzed in real time and are immediately tied into this framework [61].
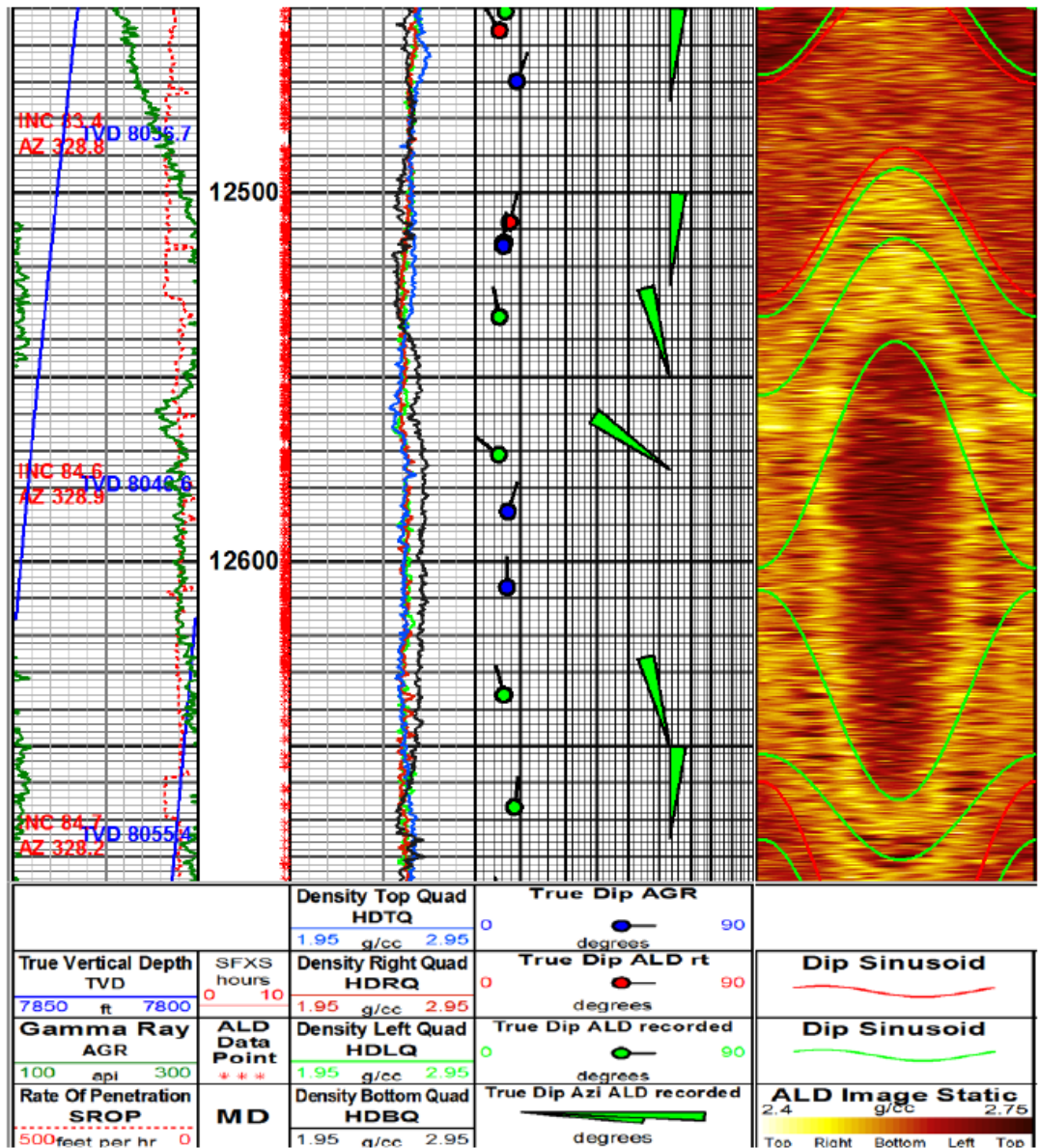
Figure 5.13: Density image used in geosteering; the sinusoids fitted to the image provide a measurement of dip [58].

This method in the shale plays is becoming increasingly common. It can provide a crude mineralogy and lithology log along the well path with samples approximately every 30 ft (10 meters) [62], as well as analogs to geochemical parameters. Although these analogs are dependent on a satisfactory calibration to core, it require a great deal of analysis. It is easy to become confused when using a simple gamma ray tool regarding the structural position, especially when sub-seismic faults are encountered. Definitive answer can be provided by chemo-stratigraphic analysis, regarding stratigraphic position very quickly after encountering a fault, usually within 100 ft

(30 meters) of a fault being crossed, and its much more rapidly than a correlation system based on LWD can manage.
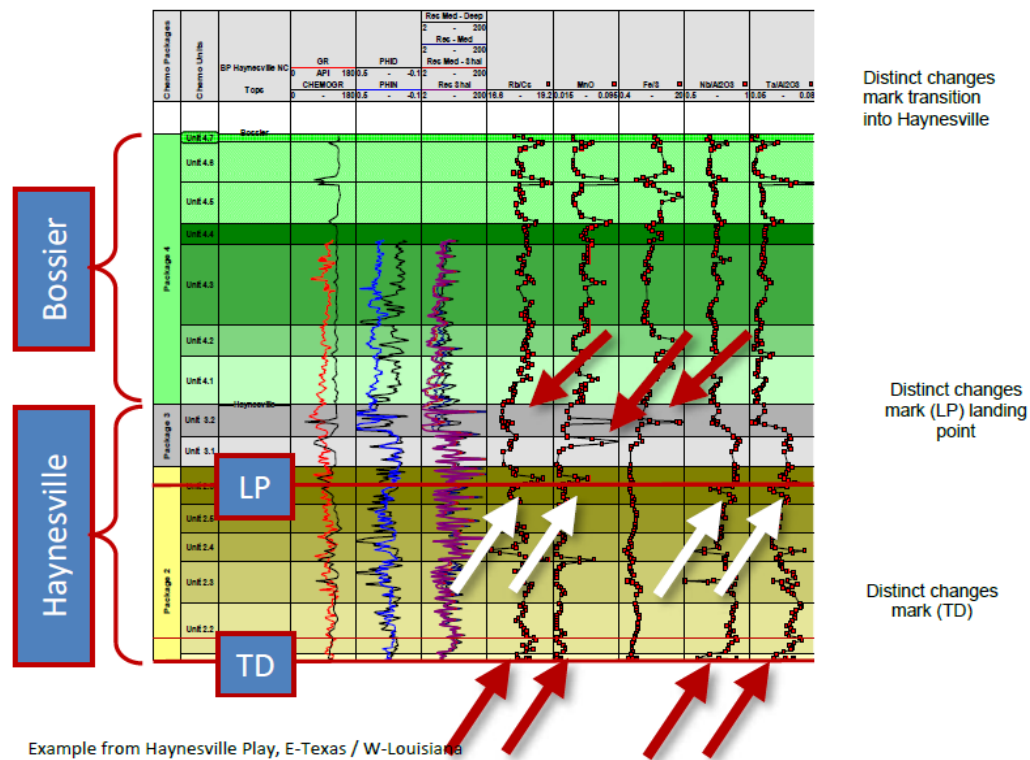
Figure 5.14: Chemostratigraphic zonation schema Haynesville shale play area [58].

In shale, the new approach to well placement is the concept of geosteering to geomechanical rock properties. This concept in shale plays is based on the fact that, the rock must be stimulated by hydraulic fracturing to enable production. Hydraulic fracturing process is governed by geomechanics. The fundamental concept of geomechanical is that, it has a controlling influence on the ability to effectively stimulate the rock in the near-wellbore environment, including the desired development of fracture complexity and the ability to maintain connectivity to an induced fracture system [59] by mitigating proppant embedment.

There is a clear link between the ability to successfully place fractures in shale and the local clay content of the rock [61]. In shale, clay content unfortunately is not directly related to natural gamma ray content because of the preferential fixing of uranium to kerogen in the marine environment [63]. It therefore means that, gamma ray measurements are not a reliable indicator of clay or kerogen in the system, as the measurement is influenced by the two variables independent of each other.

An alternative method of clay measurement is by the effect on geomechanics. In horizontal shale, sonic LWD measurements in real time can provide a viable alternative as a steering indicator. The type of sonic tool used often enable a single compressional measurement (DTC) and two shear measurements, especially the dipole. The fast shear measurement (DTS_F) is representative of the shear measurement taken parallel to layering in the rock; the slow measurement (DTS_S) is representative of the measurement taken perpendicular to the layering.

5.5 Stimulation Of Wells

Interest in horizontal wells drilling and completion has increased during the last few years to enhance productivity or ultimate recovery in shale reservoirs. The most common completion method used in shale reservoirs is fracturing, to obtain as many as possible interconnected fracture networks so that productivity will be maximized. Most wells have been completed as drain-holes and have been used as a primary production wells. Even though horizontal wells productivity could be two to five times higher than vertical wells productivity, fracturing these horizontal wells may further enhance its productivity as permeability of the shale will be improved.

Grady et al. observed that, various explosive or impact methods of dynamic fracture and fragmentation data on shale shows that, significant dynamic fracture and fragmentation rates depends on the fracture behavior [64]. Explosive breakage of rocks involves dynamic fracture since the interaction of transient wave with local free surfaces carry regions of the rock into tension, initiating fracture and fragmentation. Studies shows that, the static strength of a rock can be less than the dynamic fracture strength as much as one order of magnitude. This observation has attained fairly wide acceptance since it was substantiated by later studies.

In calculating rock blasting, a factor of seven or eight is usually added arbitrary to the known static fracture strength to account for dynamic conditions. The properties of the rock that leads to rock fracture rate-dependent are not well understood. Strain-rate region of the whole transition from "static" to "dynamic" fracture behavior is also not known, since there has not been thorough exploration of the mechanism. A nominal strain rates of 10^4/second was achieved [65] and later explosive and impact studies. In practical rock blasting operations, strain rates ranges from 10^0/s to 10^3/s but static test are in the order of 10^{-4}/s.

Wide ranges of loading rates to generate data for fracture and fragmentation have been experimentally conducted on shale oil. It was observed from the results that, both fracture stress and fragment size depends on the rate of strain exerted on the material. In this experiment, a nominal 80ml/Kg shale oil from the Anvil point mine near Riffle, Colorado was used as the material. The shale oil was considered to represent the Mahogany zone of the Green River formation. The elastic modulus of K= 18 GPa, a density of ρ_o = 2.0 Mg/m^3 and an elastic wave speed of C_l = 3.0 Km/s is represented for this material. Figure 5.15 shows the dependence of fracture stress on strain rate generated by using dynamic fracture data form gas gun. Data at the highest loading rate were obtained using gas gun impact technique by Grady and Hollenbach [66]. Strain rate of 3 x 10^3/s datum was obtained the capacity-discharge technique [67]. Lipkin with a split Hopkinson bar method were used to obtain a range of 10^2/s to 10^3/s. Felix method was used to obtain a value slightly higher than 10^1/s strain rate from a different shale oil, and strong fracture anisotropy with respect to the bedding plane was observed [68]. Little fracture anisotropy was observed in the higher strain rate obtained by using gas gun experiment [66].

In dynamic fracture studies on shale, the dependence of size of fracture on strain rate data are very scarce, since only two experimental results are available on this [69]. They used gas gun impact technique in one, and cylindrical explosive in blocks of shale oil was used in the second experiment. Figure 5.16 shows data obtained from the experiments.
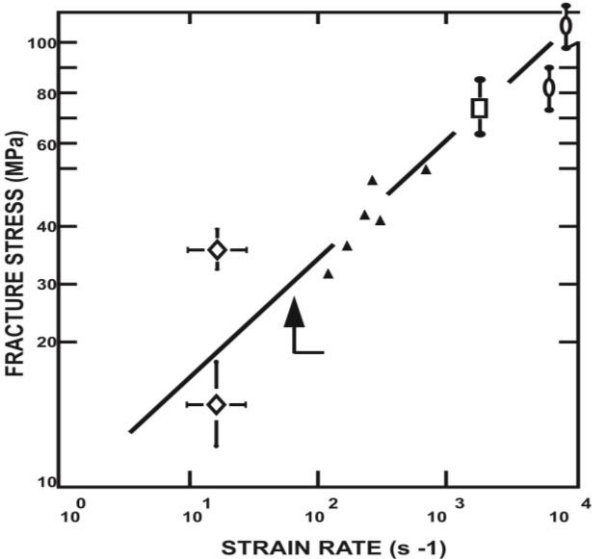
Figure 5.15: Shale oil fracture stress dependence on strain rate [64].

The data for 80 ml/kg shale oil provided by Figures 5.15 and 5.16 are still not adequate especially in a region of 10^0/s to 10^2/s strain rate in many practical blasting situations. But the magnitude and dependence of fracture and fragmentation on strain-rate data are provided clearly.
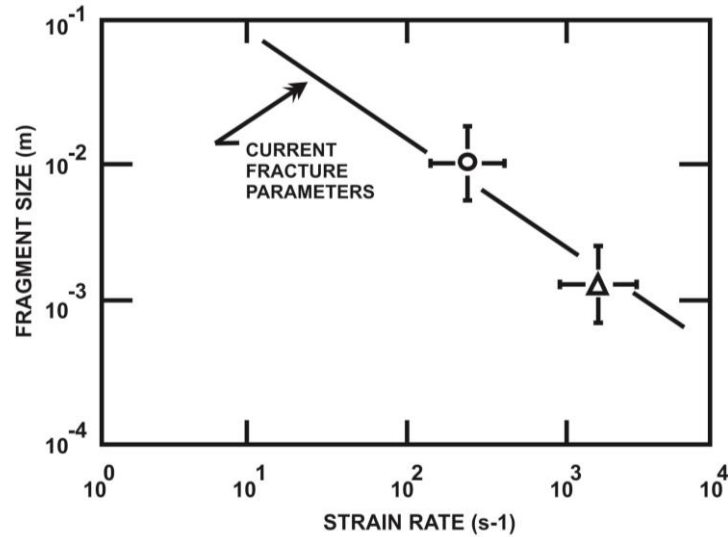
Figure 5.16: Shale oil fragment size dependence on strain rate [64].

Dynamic fracture interaction between the process of fracture and fragmentation, and the stress wave propagation of the material is very complex. Hence, to describe both phenomena, understanding the material constituents very well is required. To complete the failure process, catastrophic process is required during dynamic fracture activation and growth of many flaws and cracks, even though fracture is an intrinsically unstable. Therefore, to consider a continuum dynamic fracture description is reasonable. Based on the growth of damage, internal state variable and concomitant fracture and fragmentation process has been described mathematically. A fracture material put under stress will undergo a strain that can be estimated by a modulus, K_f, which is less than the fractured material intrinsic modulus, K.

Walsh indicated that, the fractured material modulus to a first approximation [70] can be written as;

$$K_f = k(1 - D) \qquad (5.1)$$

where,

$$D = NV \qquad (5.2)$$

N is the number of idealized penny-shaped cracks per unit volume representing fractures in the material. V is a spherical volume of the material assumed to be affected by the cracks, and it is given as; $4/3 \, r^3 \, \pi$, where r is the average radius of the penny-shaped cracks. D will be called the damage. D is a simple constant if the damage remain the same, and it is a characterizing the reduced modulus, K_f. In the material if fracture is initiated by the load applied, it characterizes the instantaneous level of fracture or damage and may be regarded as an internal state variable. A law governing the time-dependent growth of damage is needed to completely describe the material. A simple possible assumption; N cracks, under the applied load, activated growth at a constant velocity, C_g, then the damage is given as;

$$D = N \frac{4}{3} \pi \left(C_g t \right)^3 \tag{5.3}$$

Where damage growth is assumed to be initiated at $t = 0$ and ignoring any initial damage level. N (number of activated cracks) will depend on the stress applied conditions and pre-activated flaws geometry. Hence, N will not be constant. Based on Griffith criterion or under rapid loading, the idealized activation flaws could be on more recently developed dynamic fracture criteria [71]. Crack activation assumed to be governed by a two-parameter Weibull distribution is given as;

$$N = k\varepsilon^m \tag{5.4}$$

Where, N is the number of flaws which will activate at or below a tensile strain level, ε. The fracture description will be specialized to a constant tensile strain-rate loading condition, $\varepsilon = \dot{\varepsilon}_o t$, so that the above model can be compared directly with experimental results. The damage from equations (5.3) and (5.4) should be of the form;

$$D(t) \sim \alpha \dot{\varepsilon}_o^m t^{m+3} \tag{5.5}$$

A hereditary integral for the damage accumulation expression was developed by considering a careful application of the activation and growth concepts due to the finite time over which flaws activates [72]. A constant strain-rate loading specialization leads to the same strain rate and time dependence is as follows;

$$D(t) = \alpha \dot{\varepsilon}_o^m t^{m+3} \tag{5.6}$$

where

102

$$\alpha \; = \; \frac{8\pi \; C_g^3 k}{(m+1)(m+2)(m+3)} \tag{5.7}$$

From equation (5.6), the stress is related to the strain through;

$$\sigma\,(t) \; = \; K(1 - D)\varepsilon(t) \tag{5.8}$$

This with equation (5.6) yields;

$$\sigma\,(t) \; = \; K\dot{\varepsilon}_o t(1 - \alpha \dot{\varepsilon}_o^m \, t^{m+3}) \tag{5.9}$$

The damage and stress from equation (5.6) and (5.9) are shown in Figure 5.17.
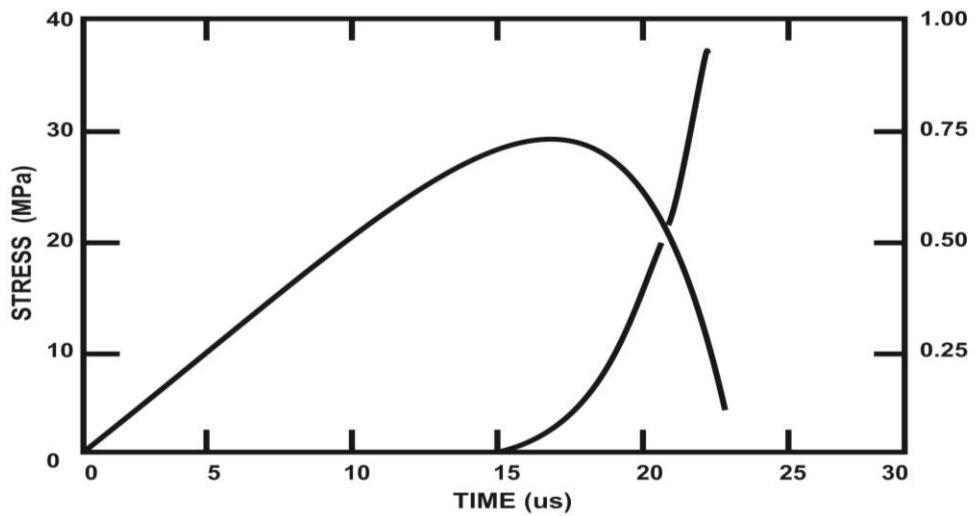
Figure 5.17: Tensile loading at a constant strain rate of both damage accumulation and stress history in Shale oil [64].

Until a particular critical time is reached, the growth of initial damage is negligible, but becomes catastrophic after this critical time. To the peak of tensile stress (fracture stress), a nearly linear-elastic loading is indicated by the stress history, and stress relaxation is catastrophic after this point. Maximizing equation (5.9) with respect to time, the fracture stress dependence on strain rate can be estimated as fallows;

$$\sigma_{M=} K(m + 3)\,(m + 4)^{-\frac{m+4}{m+3}} \; \alpha^{-\frac{3}{m+3}} \; \dot{\varepsilon}_o^{\frac{3}{m+3}} \tag{5.10}$$

At time t_f, fragmentation is defined to take place when growing cracks coalesce and material ability to support a tensile stress is loss and mathematically, can be written as;

$$D\,(tf) \equiv 1 \tag{5.11}$$

It is reasonable to expect fracture surfaces as fracture coalescence to form the sides of fragments where the mean fragment size should be of order $L_M \sim C_g t_f$, where t_f is calculated form the application of equation (5.11) to (5.6). A more detailed calculations [72] results in additional factor of $6/(m + 2)$ yielding;

$$LM = \frac{6C_g}{m+2}\alpha^{-\frac{1}{m+3}}\dot{\varepsilon}_o^{-\frac{m}{m+3}} \qquad (5.12)$$

Predicting the fracture stress and mean fragment size, results obtained from equations (5.10) and (5.12) dependence on strain rate can be compared with experimental data easily. The three parameters for fracture K, m and C_g obtained for 80ml/Kg shale oil from a best fit to the data in Figure 5.15 and Figure 5.16, yields slopes and intercepts that gives the following values; $K = 1.7 \times 10^{27}$ /m^3, m = 8 and $C_g = 1.3$ km/s.

By comparing the curves corresponding to these parameters with data in Figure 5.15 and figure 5.16, it is observed that, the fracture growth velocity, C_g, fitted value is about 0.4 times the longitudinal wave velocity in shale oil. In Figure 5.15, the fracture stress shows a $\sigma_M \propto \dot{\varepsilon}_o^{0.27}$ dependence on strain rate.

The static fracture strength of rock which depends on the specimen size is not a property of the material, and decreases as the size of the material increases. Fracture that depends on the size of the material has been demonstrated and explained by Weibull distribution of fracture producing flaws as follows;

$$N(\varepsilon) = K\varepsilon^m \qquad (5.13)$$

Statistical methods [73] indicated that, static mean fracture stress depends on the specimen value, V, through the equation below;

$$\delta_M = I_M K(kV)^{-\frac{1}{m}} \qquad (5.13a)$$

Where I_M is a constant equal to 0.942 for m = 8. Schmidt [74] carried out two tests on static tensile fracture on 80 ml/Kg shale oil parallel to the bedding planes, and the values of the fracture stress were 12 MPa and 22 MPa. With the known size of specimen from Schmidt work, the fracture parameters K and m distribution obtained from dynamic fractured data (Figures 5.15 and 5.16), can be used to estimate static fracture strength using equation (5.13) [74]. With the measured static values of δ_M = 23 MPa is in good agreement.

An explanation for strain rate dependent dynamic fracture data on shale oil has been provided by the fracture and fragmentation model described, and correlating both static and dynamic fracture strength data has been succeeded. In determining fracture and fragmentation characteristics of a rock, inherent fracture-producing flaws are paramount.

Numerous flaws activate and grow under dynamic loading resulting in failure through comminution of a finite region of the material. Rate dependence of fracture is an inertial consequence related to the finite activation and growth time of the inherent flaw structure.

Komar whose main objective was to intersect many natural fracture as possible to provide a network that will serves as channels [75] for gas flow from the reservoir to the borehole, to enhance productivity in the Devonian shale, has presented a development of a rationale for stimulation design in the Devonian shale. To initiate and propagate fractures to intersect the natural fractures that are primary source of gas containment is the objective of stimulation in the Devonian shale formation. Natural gas accumulations are governs by factors that depend on earth stresses affecting primary and secondary migration of gas and also the gas trap types in the area. Primary migration of gas is the transfer of gas from the source rock to a reservoir, and secondary migration is the rearrangement of the gas in the reservoir and accumulation into the structural traps to form producing fields. In the exploration process, primary and secondary gas migration mechanism knowledge is very important. Micro-fractures which has a high secondary or fracture porosity, can be found in most of the shale formation naturally.

Micro fractures, joints, bedding planes, faults and slickensides are made up of formation discontinuities. An excellent system has been provided by these voids for the movement of gas. Hence, the priority of fractured shale is the production of gas and oil. It has been indicated from experience of production from naturally fractured regions that, gas flow rate are been enhanced drastically by wellbore formation stimulation. It is evident in counties within eastern Kentucky and western West Virginia production histories shown in Table 5.6. Not much is known about shale fracture characteristics in non-developed areas. Nevertheless, to quantify regions of potential production, research is in progress, and to investigate techniques using advanced fracturing technology as a method of producing gas at commercial rates. In

the development of a comprehensive research program, the Department of Energy (DOE) has taken a lead role to characterize the Devonian shale as a gas resource, and to obtain stimulation methods in producing gas in commercial rates.

Table 5.6: Production History for Counties in Kentucky, West Virginia and Ohio.

		Cumulative production MMCF vs. Year							
State	County/Years	5	10	15	20	25	30	35	40
Kentucky	Floyd	142	248	328	402	480	535	596	655
	Martin	86	163	231	296	359	419	479	537
	Knott	95	168	234	297	357	415	471	526
West Virginia	Mingo	122	203	266	326	382	434	484	533
Ohio	Meiggs	44	78	112	144	176	207	238	268
	Lawrence	45	84	117	147	176	204	231	257
	Licking	26	41	52	63	72	81	90	98

Borehole explosives have been used in the historical methods for gas deliverability improvement. In geographical region of eastern Kentucky, gas deliverability was found to be improved. From different parts of the Devonian shale, mixed reactions has been obtained such that hydraulic fracturing has not been adopted universally. DOE had sponsored field test in cooperation with industries based on the potential for deliverability improvement, to acquire data on stimulation techniques in different region of shale. The test was made to improve the results obtained from hydraulic fracturing in light of production interference by retained fracturing fluids particularly with water.

Initial open flow production was used in carrying out these tests for hydraulic fracturing treatments whereas cryogenic, water and foam were used in both conventional and massive quantities, for residual fluid retained minimization in the formation. There were limited data available on field test where explosives for displaced liquids were used as well. A pilot data from wells located in selected regions at random were obtained from these observations. Hence, some locations were not all in-field wells, though were included in the development wells. Attempts were made to develop a rationale for areal site specific stimulation design. Factors

considered were discussed and compared with the results obtained from early test in the program, to indicate that a stimulation strategy is required in the Devonian shale to encourage the development of new regions for gas production.

5.6 State-Of-The-Art In Stimulation Technology

For initiating and propagating fractures, wide range of fracturing techniques are available for long distances. To select, test and evaluate fracturing methods are the objectives of the Eastern Gas shale project stimulation and R&D that will have a higher probability of connecting existing natural fractures to a single wellbore.

In a region of relatively small tectonics compressive forces where natural fracture system appear to be complex or possess multiple sets, an isotropic fracture initiation and propagation scheme might be preferred. Stimulation methods that need to be considered are;

(a) Borehole shooting with 80% gel nitroglycerine,

(b) Borehole shooting with an energy pulse tailored to the formation,

(c) Detonation of displaced liquid chemical explosives, and

(d) The dendritic fracturing process.

All the stimulation methods mentioned above may be characterized as a multi-directional fracturing process. There is data only on (a) and (b). For natural fractures suspected to have a single orthogonal set, it is more likely that the formation has been controlled by regional compressive earth stress. Stimulation methods that should be considered in this type of formation are;

(a) Conventional hydraulic fracturing, and

(b) Massive hydraulic fracturing (MHF).

There will be evaluation of the problems in all these cases to get enough energy into the borehole so that the fractures can be extended extensively to the desired length. The rationales behind these concepts are discussed in the following section.

5.6.1 Explosive fracturing

Explosive fracturing has seen little use in recent years for natural gas wells stimulation even though it is one of the oldest stimulation methods. It is mostly been

used in place of hydraulic fracturing when cost of fracturing operations need to be reduced, and when in the design of wells, conservative judgment prevail in the stimulation. A number of problems have been encountered in recent times in an attempt to improve stimulation processes by using explosive, due to poor understanding of explosive fracturing mechanisms and inadequate means of controlling and measuring underground events.

5.6.2 Conventional borehole shooting

Exclusively, borehole shooting technique is used for stimulations in the Devonian shale. Filling the entire open hole interval with 80% gel nitroglycerine, and to contain the explosive energy with sand or water to tamp (press or push down) has been the procedure. This technique goes back to the early history of the shale development with slightly change. In the borehole, the explosive energy is propagated and produced a large number of fractures approximately isotropically around the borehole, and this has been principal characteristics of high explosive placed in borehole. Hence, it is almost impossible to create induced fracture at a long distance from the borehole.

The technique has been very effective in areas where natural fracture system are emanating from low compressive earth stress in the shale. The disadvantage of this technique is that, it require extensive cleanout of the wellbore, and in regions apart from the natural fractured regions, open flow rates are less economical. Borehole explosive technique is said to achieve commercial rates of production only when the region is highly fractured. Over wide spread areas, most of the baseline production data in shale were generated by the borehole explosive stimulation process. Hence, it might be reasonable to assess the production potentials of the wells characterized on truly exploratory by borehole explosive technique. Currently, research is in progress to improve upon the borehole explosive stimulation technique.

New formulations, propellants and jet penetration technology development in the field might become new tools that are worthy of testing. Any time the state-of-the-art is considered in stimulation technology, the technique usually is the detonation of 80% gel nitroglycerine. In new areas, it should be used only for extending the baseline data set.

5.6.3 Displaced chemical explosives

The displaced liquid explosive technology was developed as results of advances in explosive technology over the past few years. To increase the probability of connecting sufficient natural fracture network to wellbore so as to achieved commercial production rates, is the basic concept in this stimulation method. In a fracture system away from the wellbore, detonation yields a low to medium order (6,000 to 10,000 ft/s) explosion that extends to the existing fractures. In the field, the actual goal is achieved and accomplished by injection of two non-detonable chemical simultaneously into a mixer located in the borehole about 200 feet below the surface where the explosive is manufacture, displaced and detonated systematically. An explosive that penetrate into the formation upon detonation through natural or induced fractures enhances the possibility of achieving orthogonal fractures. It is likely to be most effective in formations suspected to have a high density of fracture identified as a target for borehole shooting technology. An environment where displaced explosive concept will be selected over borehole explosive is yet to be seen.

5.7 Hydraulic Fracturing

5.7.1 Conventional hydraulic fracturing

Due to unknown effects of the fluid on the formation, the gelled water hydraulic fracturing application in the Devonian shale was restricted. The fear was that, the fluid-clay interaction will damage the formation during fracturing, the native small fractures could be seal off and denied the process any benefit. Kentucky-west Virginia Gas Company has experimented with 1,000 barrels hydraulic fracturing treatment since 1960 to borehole shooting as an alternative. The Big Sandy in eastern Kentucky was the area where the test was performed. In this field, natural fracture occurrence was thought to be less pronounced. Little increase in open flow rate was observed in these wells after stimulation over that observed for shot wells.

A distinct improvement in deliverability from fractured wells relative to shot wells after few years of production was observed. After the third year of production, the hydraulic fractured wells deliverability exceeded that of shot well by 75%. This was an indication that, in hydraulic fracturing, number of interconnected micro-fracture

filled with gas increases due to the longer effective radius of the wellbore. Increased in deliverability was one of the net effects. Also, a projected 350 MMcf reserves for shot wells to be produced in 32 years was forecasted to be recovered in 16 years by the hydraulic fracturing. The production rates of hydraulic fractured wells are significantly higher than that of the shot wells even though the hydraulic fractured wells cost about \$30,000 more than shot wells. Hydraulic fracturing might not be the preferred stimulation technique in a high density natural fractured region.

The use of foam as an alternative fracturing fluid over the use of water has evolved recently. Nitrogen, water, and an emulsifying agent are combined in this process in a continuous operation to produce a fracturing fluid containing 22 to 25 % of water on surface. This fluid has a high apparent viscosity and capable of carrying propellant at a density slightly more than one pound per gallon. The total inhibition of leak off due to the strength of the gas bubbles in a micro-fractured formation and its ability to redirect the hydraulic force to a single plane of least resistance by blocking off micro-fissures, are the advantages of this process. The advantages of foam fracturing are;

(1) The recovery of the fracturing fluid is more complete and more rapid than water fracturing with less time required to swab the wellbore, and

(2) That potential water-shale interfacial reactions are minimized.

The disadvantage of foam fracturing is that, foam fracturing cost higher (\$5,000) than that of water fracturing, but this cost in most cases offsets, by reduced amount of rig time service.

There have been studies to improve the process of hydraulic fracturing by testing cryogenic fracturing fluids where a mixture of liquid CO_2 and methanol or liquid CO_2 and water are used to;

(1) Reduce potential damage from formation-fluid interfacial contact, and

(2) Accelerate the cleanup process following stimulation.

The advantage of the process is that, as the pressure is released from the wellhead after the mixture is heated by the reservoir above its critical temperature, the fluid converts to a gas or gas impregnated with water and this leads to rapid cleanup from the well, and reduces the interference with the flow of gas from native fractures.

Cryogenic fracturing using liquid CO_2 and methanol provide enough data ten years ago from field test in shale formations, hence further investigation is required. Due to excessive requirement for safe handling of liquid CO_2 and methanol, this mixture is no longer used as a field service. To improve this process, the volume of liquid CO_2 has to be increased relative to water if the fracture fluid recovery improvement is required. The constraints relating to availability and supply of liquid CO2, the economics of the process and its effects on deliverability of gas must be analyzed.

Both approaches are advanced over conventional water fracturing treatment. In field test of stimulation design for formation with low pressure where reduced fluid-formation contact time and recovery of fracturing fluid are rapidly required, the use of foam and liquid CO_2 are encouraged.

5.7.2 Massive hydraulic fracturing (MHF)

To achieve fracture extension exceeding 2,000 feet, massive hydraulic fracturing which involves the treatment of large volume of water and sand is required. Equipment is required to store, mix and inject this mixture into the wellbore under pressure. A fluid volume of 2,000 to 3,000 gallon per foot of performed formation interval is required for this type of stimulation treatment. This volume of fluid is 2 to 3 times more than the volume of fluid required for conventional hydraulic fracturing for the same height. At the well site, 2 to 3 acres of land is required for this technique, and this has been a universal constraint for massive hydraulic fracturing technique.

Based on recent economics studies, if open flow potential initially exceeds 350 Mcf/d after massive hydraulic fracturing operations, $70,000 would be tolerated as the cost for MHF. The linear fracture developed is propagated into the formation further and increased the possibility of intersecting more native fracture in the shale where gas is stored. And this is the advantage of MHF technique. There is no data on production apart from initial flow rates per stimulated stage in the projects conducted by DOE/ industry, for the effectiveness of MHF to be assess.

To optimize stimulation results, it is recommended to consider several different techniques, but if there is no chance to consider many techniques, then it is very important to have a better understanding of the phenomenology of these techniques. Research programs are now putting much emphasis on determining the limitations

and capabilities of these techniques. Problems related to the various techniques must be defined and determine whether these problems are intrinsic to the method or can be solved.

An effective R & D (Research and Development) program that would maintain a proper balance between analysis, laboratory experiment and field testing must be developed to improve gas production stimulation methods by fracturing. Field testing yields limited information. Even though it is expensive, it is the final stage in the development of stimulation techniques and this makes field test very necessary. For a thorough understanding of a significant phenomenon at work, enough information is required and usually is provided by field testing. Field testing should be limited to the few most promising techniques which are well understood and already developed. For regions in which the black shale thickness and stress level are known, well established field techniques are the preferred approach for a comprehensive analysis of these factors.

Concerning the origin and nature of fracture porosity responsible for production from shale, little has been said or written and summarized about the present stage of the knowledge, though there is little doubt about the importance of fractures to production. It was suggested from cores fracture data that, from the shale, produced free gas does not come from virtually continuous zones and that, it comes from fractures with limited vertical extend found in the lower organic portion of the shale section. The fractures are found in the reservoir in which gas is entrapped in the fracture porosity, both the source and the enclosing seal is the shale. Production from the organic zone fractures generally has been correlated with increased density of fracture and mineralized fracture in those stratigraphic intervals.

Changes in mineralization, density and orientation of those fractures form the basis of the assertion that, the porous fracture facies is present in the lower organic shale and in those layers, the understanding of these fractures is important so that production from the shale formation will be very well understood. In the Devonian shale as shown in Figure 5.18, the thickness of the high organic intervals is the fundamental factor defined as the source of the hydrocarbon. It is very necessary to understand the extent of how the fracture system will affect production of hydrocarbon source after establishing sufficient availability. Within the stress field at the base of the shale, abnormal edge conditions might be created by basement

features or pre-existing structural features to cause enhanced fracture density. Micro-fractures, joints and bedding planes which is made up of the secondary porosity should be intersected by induced hydraulic fracture in order for gas migration to occur.

Commercial rates of gas flow can occur only when sufficient number of intersections

from the induced cracks occurs. Hence regions having organic rich shale deposits, the degree of fracture density must be identified as a second factor to consider. Estimated density of natural fracture system of the Devonian shale formation is shown in Figure 5.19 below. Tectonic stresses measurement can act as a regional assessment as it is directly related to fracture density formation and degree of occurrence.

For Devonian shale formation, stimulation technique desired results is to create adequate cracks extent to intersect as many native fractures bearing gas as possible in the preferred direction. Stimulation techniques choice in the various regions is the basis of the strategy. It may be logical to employ multi-directional stimulation techniques based on the geological factor of fracture density, in areas of high density of fracture, and in areas of low density of fractures, a directional stimulation technique to some extent might be logical. Different regions have been targeted for the application of explosive fracturing and hydraulic fracturing technologies as shown in Table 5.7.
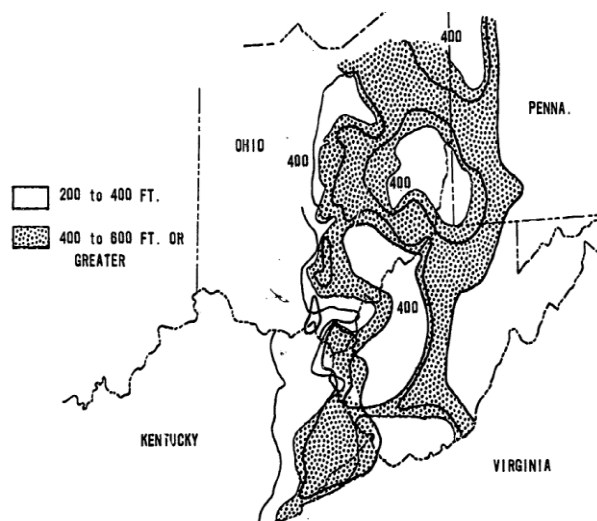
Figure 5.18: Black shale thickness extent in the Devonian shale formation [75].
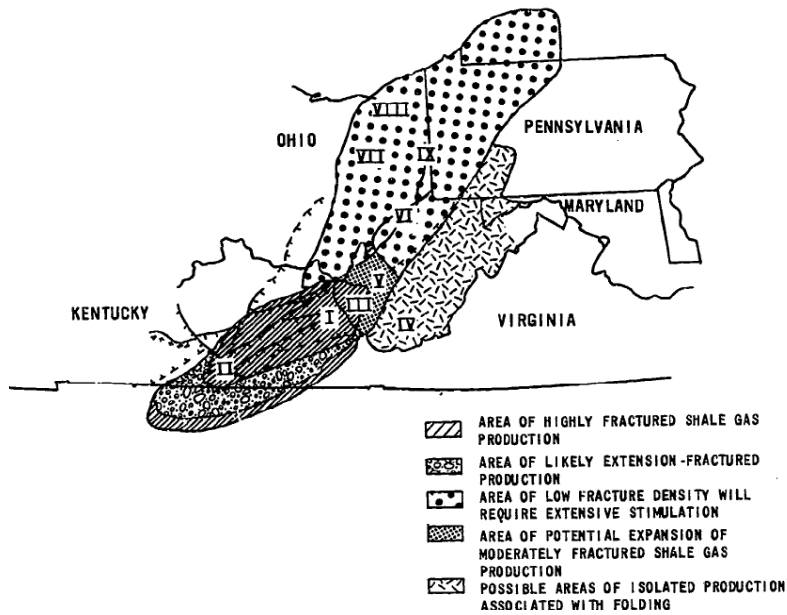
Figure 5.19: Devonian shale production character evaluation according to estimated density of natural fracture system [75]**.**

Table 5.7: Devonian Shale Formation Regional Geology Factors.

Regions	Description	Black shale thickness (ft)	Fracture density
I	Eastern KY field	500	High
III	Big sandy extension	500	High
IV	Southeast WV	400	High
V	Central WV	500	High
II	Eastern KY peripheral	350	Low
VI	Northeast WV peripheral	500	Low
VII	Central Ohio	400	Low
VIII	Lake Erie	550	Low
IX	Northeast WV. So. W. PA	600	Low

5.7.3 Rationale for statistical design

To compare experimental factors such as black shale thickness, units fracture density, and stimulation treatments, all other conditions must be kept constant or nearly as constant as possible, and this model is called the fixed effects model. As experimental errors, random variation will occur, and under similar conditions, repetition will be necessary to compare the stimulation treatments with sufficient reliability. Estimation of the experimental error is required to assess reliability by

using the results obtained from the repetitions. Variances between mean values of open flow potentials generated under different conditions are then analyzed.

Statistical design advantage is shown in the experimentation such that, the desired effects are investigated with a minimum number of observations, in accordance with the design criteria. Interactions effects that are not visible in multiple factors testing are analyzed and verified as an additional benefit of statistical design.

To determine stimulation technique type that is more effective in achieving high gas flow rates from a region of known geological factors such as black shale thickness and fracture density, remain the objective of current research investigation. A statistical designed experiment was formulated in line of this objective to determine the required test to verify the importance of the results obtained mathematically. An early interpretation of reasonable validity can be accomplished with a minimum number of repetitions in each cell of the experimental design, to analyze the effectiveness of specific stimulation technique for specific geological factor, and to find out if any factor interaction effects might be important as well. In the analysis of the results in this approach, the combination of engineering intuition and statistical inference are permitted to complement each other.

In the Devonian shale formation, borehole shot wells productions history shows that, a reliable cumulative production is predicted by an initial open flow (I0F) after stimulation. In both the low and high fracture density regions, the I0F was used as a pilot studies after borehole stimulation.

Many wells in four counties of eastern Kentucky initial open flow rates were obtained from Hunter's report for low fracture density region as a pilot data.

The mean was 118McfD and the variance was 895. For higher fracture density regions, pilot data were obtained from the report of Hunter, Bagnal and Martin as shown in the Table 5.8 below.

The calculated mean was 233 McfD and the variance was 7963. These pilot studies after obtaining the mean and the variance, and considering the criteria designed to ensure that treatments may be compared with 95% accuracy,

Table 5.8: Pilot data for higher fracture density regions.

county	State	Number of well	Average gas produced (McfD)
Putnam	West Virginia	13	124
Cabell	West Virginia	7	167
Jackson	West Virginia	19	415
Wayne	West Virginia	7	116
Lincoln	West Virginia	70	200
Kanawha	West Virginia	18	208
Martin	Kentucky	450	360
Knott	Kentucky	770	269
Floyd	Kentucky	1,000	238

the design function for characteristic curves operation was used to estimate the required number of observations in the test series as follow;

$$\Phi = \sqrt{\frac{d^2(max)}{\frac{2a}{\frac{S^2}{bn}}}} \qquad (5.14)$$

Where d = difference to detect 50% of mean. a = levels of factor A, thickness = 2 b = levels of factor B, density = 2, S^2 = variance of pilot study, and n = number of observations.

To determine the trial and error solution, a mathematical approach was generated. A statistical judgment error less than 5% was obtained and the number of observations was determined. That is, to make β and α which are errors in statistical interpretation to be an assumed value of 0.05 each, and Y_1 and Y_2 are degree of freedom in the factors. The mathematical approach (Table 5.9 and Table 5.10) was then as follows;

Low density region:

$$\Phi = \sqrt{1.94\,n} \qquad (5.15)$$

Table 5.9: The mathematical approach for low density region.

n, (a-1)	Y_1	Y_2, ab(n-1)	Φ, $\sqrt{1.94\,n}$	β
3	1	8	2.4	0.15
*4	1	12	2.8	0.05
5	1	16	3.1	0.02

Higher density region:

$$\Phi = \sqrt{0.80\,n} \tag{5.16}$$

Table 5.10: The mathematical approach for high density region.

n, (a-1)	Y_1	Y_2, ab(n-1)	Φ, $\sqrt{0.80\,n}$	β
3	1	8	1.5	0.50
4	1	12	1.8	0.30
5	1	16	2.0	0.25
6	1	20	2.2	0.15
7	1	24	2.3	0.09
8	1	28	2.55	0.06
9	1	32	2.7	0.04

It was indicated from statistical design parameters that, in the low fracture density region at least 4 repetitions are required and 8 repetitions are required in the high density region for reliable and accurate comparisons of treatments statistically.

Stimulation treatment selection strategy for the project suggest that, in relatively low fracture density regions where frequency of occurrence for the native fracture in 150 acres drainage area is small, a stimulation technique preferred to be selected is the directional extension to interconnect the increase number of native fractures filled with gas that make up the reservoir in the shale formation. Data obtained from DOE and industry activities make up the pilot studies of limited size for comparison using the hydraulic fracturing fluids in Table 5.11 below.

Table 5.11: Comparison of the performance of hydraulic fracturing fluids.

Fracturing fluid	County	Number of wells	Average gas produced (McfD)
water	Perry	8	167
	Johnson	6	87
	Letcher	11	122
Foam	Perry	2	276
Cryogenic	Wise	1	98
	Perry	1	219

The mean for water, cryogenic and foam fracturing fluids are 132 McfD, 158 McfD and 276 McfD respectively. For comparison, Perry, Letcher, Johnson and Magoffin counties have a borehole shot mean of 118 McfD. It was observed from the above data that, when a low residual fluid like foam or liquid CO_2/water mixture is used for hydraulic fracturing, the results when compared with conventional size treatment (1,000 barrels) are slightly better than borehole technology. The remaining objective to be seen is whether in achieving commercial rates of production, the risk can be reduced.

In regions of relatively high fracture density, stimulation treatments selection strategy suggests that, a multi-directional stimulation technique is a primary candidate to be chosen. For high fracture density regions, the pilot test data analyses that have been acquired include the following;

Explosive fracturing (Displaced liquids): Lincol Co., 3 wells, mean = 290 McfD

Hydraulıc fraturing:

      Water: Kanawha Co., 3 wells, mean = 176 McfD

      Cryogenic: Kanawha Co. 2 wells, mean = 450 McfD

      Martin Co. 1 well, mean = 450 (cum. 2 stages)

      Water/methanol: Kanawha Co., 2 wells, mean = 171 McfD

      MHF (Foam): Lincoln Co., 1 well (cum. 3 stages), mean = 204 McfD

      MHF (Water): Lincoln Co. 1 well, mean = 321 McfD

Borehole shot techniques: 9 counties mean = 233McfD.

The comparative analysis of the initial open flow means values after stimulation indicate that, displaced liquid explosive is an improvement over typical borehole shot type stimulation techniques in Lincoln County, West Virginia, and for increasing the possibility of achieving commercial well production rates and may be a candidate for consideration. Now, whether the cost of these processes can be made attractive enough to allow commercialization and if ratio of success to failure can be increased consistently to reduce the risk of achieving less than marginal producing gas wells is left to be seen.

The concept of hydraulic fracturing with a cryogenic design appears to be a technique that has been improve significantly. In this design, mixture of liquid CO_2/water at a ratio of 30-70 respectively was used to achieve fracture extension. A more important point is that, the fracturing fluid cleanup occur rapidly, hence any interference with the flow gas in the tiny interconnected fracture system is minimal. In light of increase production, the cost of this design is affordable even though the costs are higher than water fracturing alone. In the region of high fracture density, hydraulic fracturing design that use methanol, water or foam in large volumes are not preferred to be used. In the shale, Novel fracturing techniques like dendritic fracturing and dynamic fracturing process has not been tested under any circumstances, yet for interconnecting extensive native fracture systems, it is worthy of consideration due to the low cost of the methods. To investigate these concepts has been planned.

It is clear from data available that, low residual fracturing fluids and displaced liquid chemical explosive are chosen over borehole shot technology to achieve increased production rates. Hence, each gas producer must analyze the cost/effectiveness of these processes for shale field development in the future.

Mutalik et al. from Williams companies, Tulsa, drilled over 100 horizontal wells in the Barnett shale for unconventional gas production, where they used slick-water fracturing as a primary technique that has been used to hydraulically fracture wells, attempted fracturing two or more adjacent wells simultaneously to expose the shale to more pressure and produce from more interconnected fractures to further improve initial rates and reserves [76]. The Barnett shale which is now thought to be the largest onshore natural gas field in the USA, has a productive part estimated to cover over 500 square miles. There are 185 active operators in the Barnett shale producing

from 7700 wells and have the permit to drill additional 4500 wells according to Texas railroad commission latest figures published in June 2008.

Production currently exceeds 3.7 Bcf/d from the Barnett shale which is more than 15% of gas produced in Texas and since 2008, 3.8 Tcf of gas has been produced from the Barnett shale.

Paired offset wells simultaneous fracturing in the Barnett shale is one of the recent techniques and, it has been increasingly used by many operators. This technique is used to fracture two or more adjacent wells that are parallel to each other, simultaneously. To expose the shale to more pressure and produce from a complex (three-dimensional web) fractures by increasing the hydraulic fracture network density, and increasing the surface area created by fracturing operations, is the goal of simultaneous fracturing technique. The fracture fluid is pushed into the space between the two wells to improve the drainage area of each well that would not have been fractured if only one well had been drilled.

As a result of much more coordination and logistics, large area or location is required. Simultaneous fracturing techniques are more expensive but cost-effective because, the equipment is being used more efficiently as two wells are being completed in one week instead of two weeks. The fracturing technique when started in the Barnett shale, primarily involved dual fracturing in two horizontal wells in closed proximity to each other, operator of late are now experimenting with triple fracturing (trifectas) or even some instances quad-fracs.

5.8 Case History

The case history of three horizontal wells in eastern Parker county sequential and simultaneous fracturing is discussed. The well layout of the wells is shown in Figure 5.20 below. A 2,200 feet long lateral (well A) was drilled from a separate pad and a single pad was used to drilled well B and well C which are of lateral lengths 1,900 feet to 2,000 feet. At the heel, the space between wells A and C is 900 feet apart and about 500 feet is the minimum spacing at the toe of the wells. Well D, a fourth stand-alone well, having an effective lateral length of 2,400 feet was drilled less than half a mile to the north. Only one well could be drilled due to lease constraints on the well D pad.

Wells A, B and C was hydraulically fractured by using both sequential and simultaneous fracturing techniques. The first, well A was completely fractured hydraulically over five stages, and followed by simultaneous fracturing of wells B and C in the following week. The four wells production performance over the first six months of their production life, the initial potentials (IPs) for the three wells simultaneous/sequentially fractured is 3.3 MMscfd to 3.5 MMscfd and the average range for the first month is from 2.1 MMscfd to 2.9 MMscfd. Well D, the stand alone well has a significant lower IP of 2.3 MMscfd with a lower average production of 1.2 MMscfd in the first month. The simultaneous/sequentially fractured wells initial results are very encouraging and this indicate that, in the vicinity of the simultaneous fractured wells, more complex fracture network had been created and is contributing to enhanced well performance significantly.

The average five months production graph of the three simultaneous/sequentially fractured wells indicated that, production from the three wells was almost doubled the stand alone well D, which was completed and had about a month first sales later than the sequentially/simultaneous fractured three wells. Well B which has a possible draining area larger to the east has the best production among the three wells.

Well A which had enhanced production, fracture network was possibly enhanced as a result of the subsequent simultaneous fracturing of wells B and C, and this may be due to interference effects from the two offset wells.

Mostly, a significant interference of the prior stage including potential charging of the reservoir is observed in successive stimulation of multi-stage treatment. The fluid from the prior stage is pushing the subsequent stages fluids away at a certain elevated pressure due to the generated increased stress by the volume of pressurized fluid. Reactivation of existing fracture network in general, is thought to be less important than creating new fracture network.
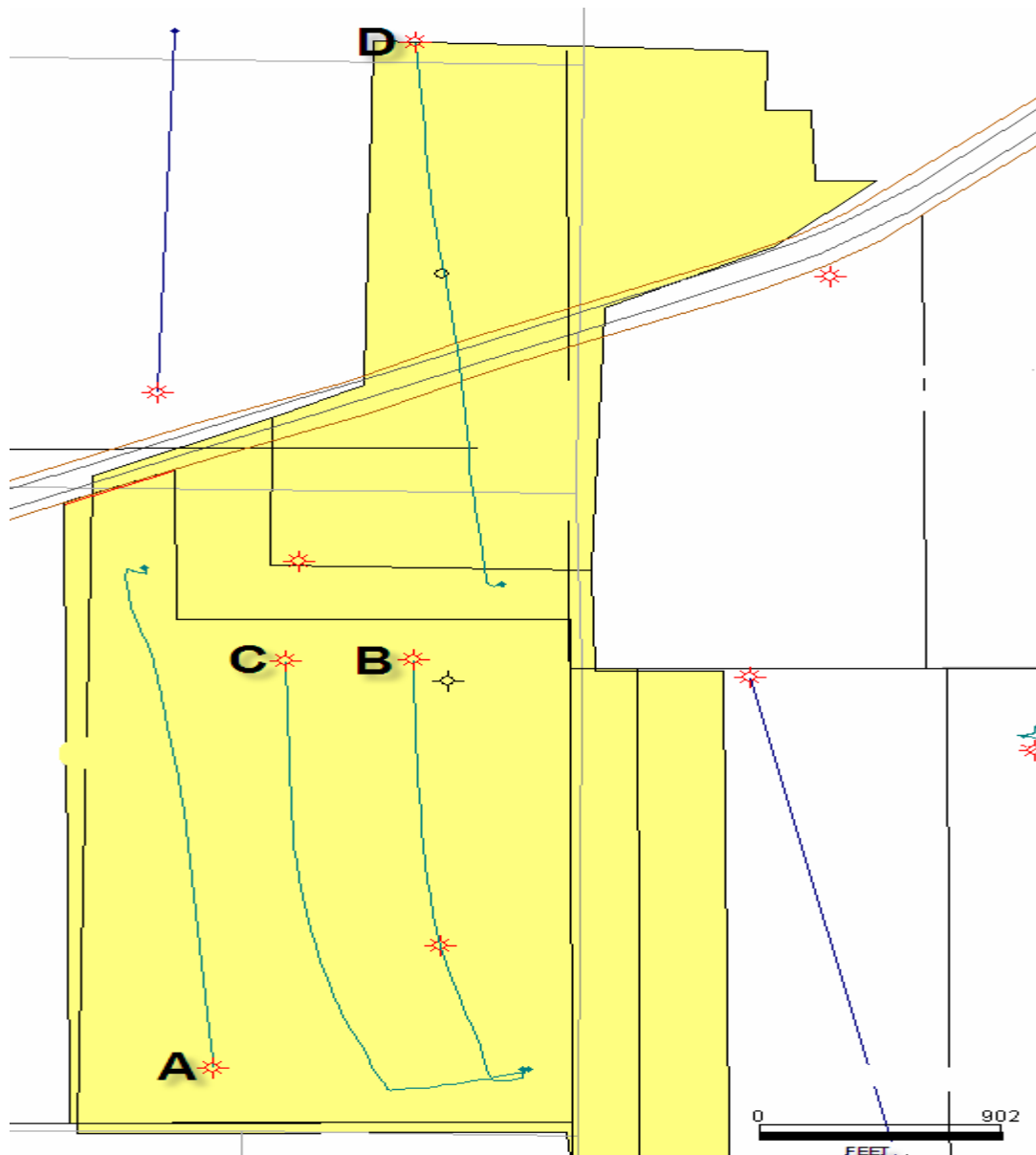
Figure 5.20: Map Showing the Location of the Wells [76].

The three wells production data appears to show that, the results from simultaneous-fracturing technique is more enhanced fracture network and gains in production compared to the sequentially fracturing technique. More data is required to assess this inference as this aspect needs to be understood further.

The IPs comparison of the simultaneous/sequentially fractured wells versus the stand-alone well D is shown in Table 5.12 below. Average IP comparison based on the first 30-days of production for the three wells, indicate improvement in a fourfold due to sequential and simultaneous fracturing. The simultaneous fractured wells based on IP/linear feet of lateral drilled, indicated enhancement in five fold. The

Estimated Ultimate Recovery (EUR) factor calculations summary is shown in Table 5.13. The decline curve analysis was used to estimate the EUR and an assumed drainage radius of 500 feet from the horizontal wells and from the horizontal wells heel and toe was used to estimate gas-in-place (GIP). A combined drainage area of 130 acres was calculated for the three wells (A, B and C) and 85 acres drainage area was calculated for well D. calculated corresponding gas-in-place based on reservoir gross thickness of 335 feet and a reservoir porosity of 3%, was 21.1 Bcf for wells A, B and C, and 13.8 Bcf for well

D. the adsorbed GIP was based on a gas content of 96 scf/ton.

Table 5.12: IP Comparison Summary [76].

Well	Actual lateral, ft	30-day average actual, Mcfd	IP/Lateral length, Mcfd/ft	Current rate, Mcfd
Well A (sequential fracturing)	2,195	2.576	1.17	885
Well B (simultaneous fracturing)	1,955	2,864	1.46	890
Well C (simultaneous fracturing-infill well)	1,889	2,097	1.11	655
Average	2,013	2,512	1.25	810
Well D (stand-alone well)	2,413	615	0.25	467

A four-fold increase in recovery factor 6.4% for well D to a recovery factor of about 26% for the simultaneous fractured wells was indicated in this analysis. A 2.5 fold benefit was shown by the average EUR per lateral length and for simultaneous fractured wells, 0.9 MMcf per feet of lateral versus 0.37 MMcf for stand-alone well D per feet of lateral was shown. The discussed case history indicated that, as a result of simultaneous fracturing the three wells, a significant improvement in IPs, EURs and recovery factor was observed compared to the stand-alone well D.

Table 5.13: Calculations summary for EUR and Recovery Factor [76]

Well	Actual lateral, ft	EUR, Bcf	EUR/Lateral length, MMcf/ft	Recovery factor
Well A (sequential fracturing)	2,195	2.06	0.94	
Well B (simultaneous fracturing)	1,955	2.22	1.14	
Well C (simultaneous fracturing-infill well)	1,889	1.18	0.62	
Average	2,013	5.46	0.90	25.9%
Well D (stand-alone well)	2,413	0.89	0.37	6.4%

5.8.1 Production data analysis

In hydraulically fractured wells, conventional graphical interpretation techniques are based on flow regimes analysis such as linear, bi-linear or pseudo-radial flow. The Barnett shale formation wells have low permeability, hence time to radial flow can be impractically long and most production wells data can be characterized as either bi-linear or linear flow. The flow in bi-linear occurs inside both the fracture and outside the fracture perpendicular to the fracture as shown in Figure 5.22. Bi-linear flow will occur in fractures having a low permeability over a long period of time. Linear flow on the other hand, occur only perpendicular to the fracture.

Bi-linear flow in fractures having sufficient permeability will last for a short period of time before starting to flow linearly.
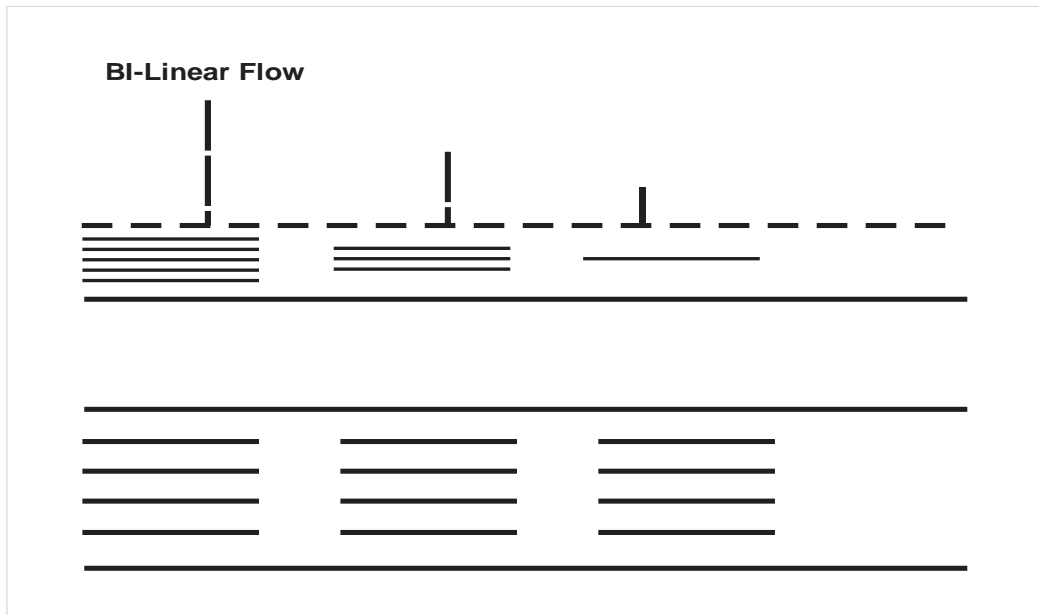
Figure 5.21: Flow Regimes for Bi-linear Flow [76].

Well D production data in a plot shows that, the production data is much closer to bi-linear flow (1/4 slope) compared to the other three wells, which can be represented by linear flow (1/2 slope). This means that fracture quality in well D is not as good compared to the three other wells, and may be attributed to the fracture type created. It is possible that better fractures were created for the three Southern simultaneous fractured wells compared to well D.

5.8.2 Fracture data analysis

A possible reason behind the benefits of simultaneous/sequential fracturing technique was evaluated by reviewing the fracture data obtained from the fracturing operations. The interaction of fluid from different fractures was suggested to provide additional energy to enhance the fracturing intensity through either higher net pressure or forced diversion of the fluid as they contact other fluid-filled fractures.

The four wells fracture fluid recoveries and net pressures are summarized in Table 5.14 below. Better production results are showed in well A and B, which are having higher net pressure ranging from 1,000 psi to 1,600 psi compared to the other two wells. Well production performance also appears to correlates with the percentage fluid recovery. Rapid fracturing fluid cleanup with a higher percentage of load recovery (greater than 50%) has been suggested to actually be an indication that fracture network was not generated significantly and that only a simple " balloon"

like fracture was generated, which can quickly be deflates back into the wellbore. Further analysis required in this regards since the data in Table 5.14 is not consistent with the above observation. Wells A and B had higher fluid recoveries in the first 100 hours of flow back ranging from 20.8% to 10.5% respectively, and fluid recovery for the other two wells ranges from 3% to 4%. Despite well C being a better well compare to well D, had a relatively poorer fluid recovery. Due to the simultaneous fracturing and high network of fracture generated in the vicinity of the wellbore. It is possible that part of the flow back fluid was recovered in the offset wells A and B, both of which yield higher recoveries.

Table 5.14: Net Pressure and Fracturing Operations Fluid Recoveries Summary [76].

Well	Lateral length, ft	Net pressure, psi	Fluid Recovery			
			100 hours		300 hours	
			Barrels	Percentage	Barrels	percentage
Well A (sequential fracturing)	2,195	1,000 to 1,400	10,738	20.8	22,292	43.3
Well B (simultaneous fracturing)	1,955	1,500 to 1,600	4,749	10.5	11,197	24.7
Well C (simultaneous fracturing- infill well)	1,889	400 to 900	1,421	3.0	1,457	Maximum barrels
Well D (stand-alone well)	2,413	200 t0 300	3,073	4.0	6,359	Maximum barrels

5.8.3 Parker county simultaneous fracturing study

A comprehensive study was undertaken based on public information to evaluate the data of simultaneous fractured wells in Parker County to further quantify the benefits from simultaneous fracturing. Based on first date of production, 29 groups of simultaneous fractured wells in the Parker County was identified being in the same

month or within one month of each other. The performance of production of these wells was compared with that of the stand-alone wells drilled from the simultaneous fractured well a distance of about 1 to 1.5 miles. A total of 3 wells constituted a group, a stand-alone well and two simultaneous fractured wells. The simultaneous fractured and stand-alone wells were drilled by the same operator, almost about 75% of the cases.

The analysis was based on production performance alone and general guidelines were provided. The influence of other parameters such as local geology, fracture design, fracture injection rates, number of completion stages etc, was not considered though all these factors can affect the performance of production. The distribution of the simultaneous fracture wells by well spacing and quadrant are shown in Figure 5.22 below. About 55% (16 groups) of the 29 groups had wells spacing of more than 1,000 feet and the rest were about 500 feet of spacing. The eastern half of the Parker County where the thickness of the reservoir is relatively high was the location that most of the drilling activities were conducted. Almost 72% (21 groups) of the well groups were in the southeast quadrant and 90% (26 groups) were in the eastern half of the Parker County.

Production data analysis for simultaneous fractured wells in the Parker County time-lag between first sales of simultaneous fractured and stand-alone wells was evaluated as a possible factor in the success of the simultaneous fracturing over the stand-alone wells. Distribution of simultaneous fractured well groups between first sales of simultaneous fractured with less than 3 months' time-lag and stand-alone wells in the Parker County sorted by well spacing and quadrant are shown in Figure 5.23. About 50% of well groups fell in this category with most of the wells drilled on 1,000 feet spacing.

Summary of the production improvement seen in each of the Parker County quadrants are shown in Figure 5.24. The comparison of monthly peak production is done in the first or second month of the well life in most cases. Well analysis in the southeast quadrant that accounted for more than 70% of the wells group suggested that, wells that had time-lag less than 3 months between the simultaneous fractured wells and the stand-alone wells had the best rate of success due to simultaneous fracturing, to see incremental production and reserves.
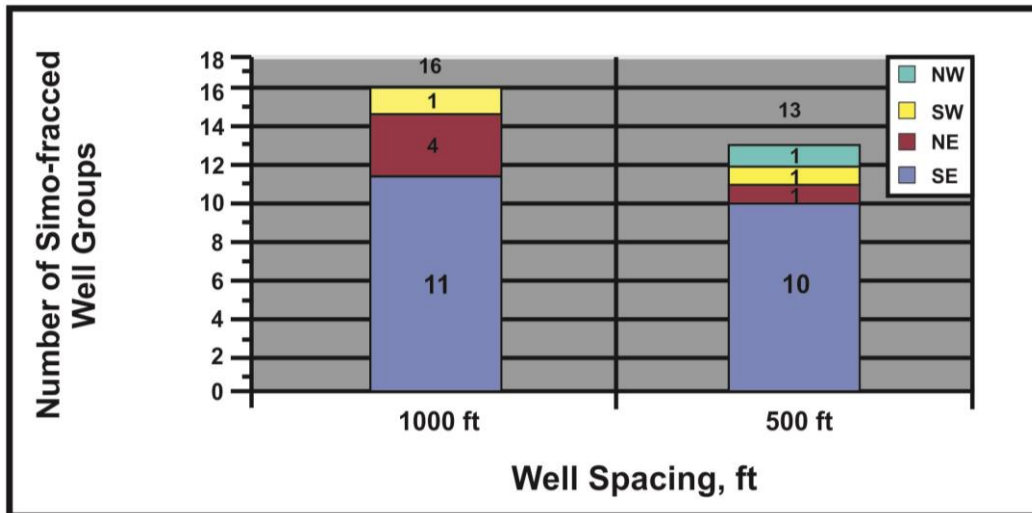
Figure 5.22: Distribution of Parker County Simultaneous Fractured Well Groups by Well Spacing and Quadrant [76].
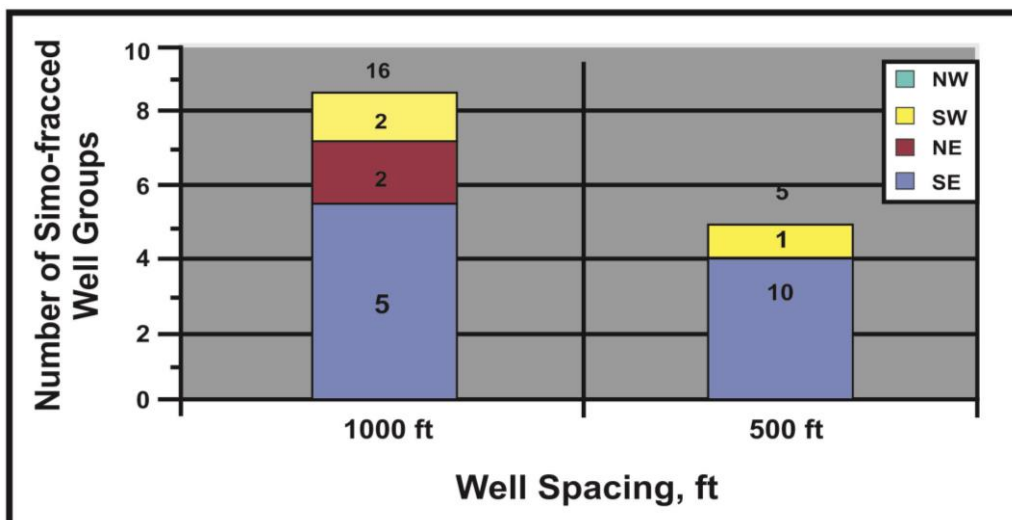
Figure 5.23: Parker County of Simultaneous Fractured Well Groups Distribution with Time-lag less than 3 Months between First Sales of Simultaneous Fractured and Stand-alone Wells Sorted by Well Spacing and Quadrant [76].

Irrespective of when the wells, in the northeast quadrant, were completed the simultaneous fractured wells performed significantly more than the stand-alone wells. This may again be attributed to factors that include variation in fracture design, injection rates and regional geology.

128
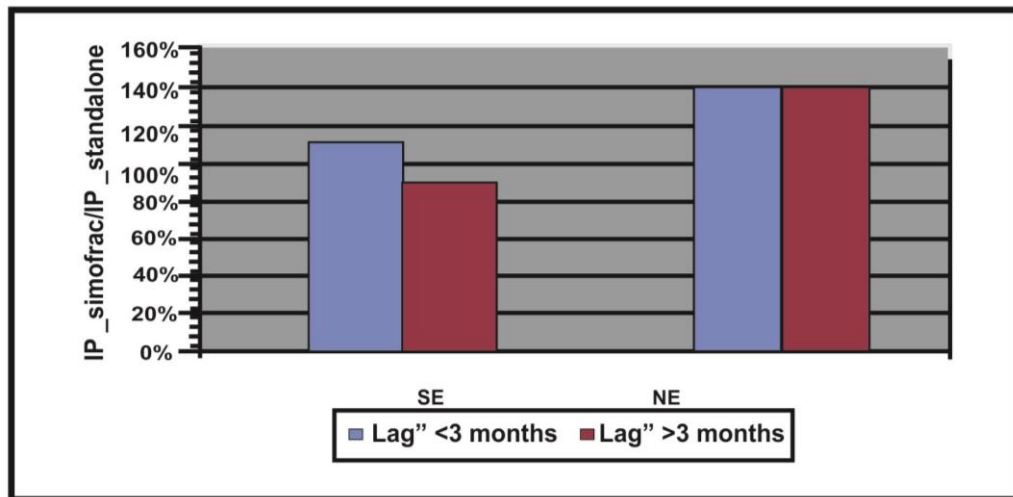
Figure 5.24: IP Average enhancement of simultaneous fractured wells over stand-alone wells in Parker County sorted by well quadrant [76].

5.8.4 Johnson county simultaneous fracturing study

Johnson County has seen significant increase in drilling activities in recent years and in the Barnett shale formation, some of the best producing wells have been drilled in this County. To date, the number of simultaneous fractured wells is significantly higher in Johnson County compared to Parker County. Based on first date of production, a total of 104 groups of wells simultaneously fractured in Johnson County were identified to be in the same month or within one month of each other.

The simultaneous fractured wells distribution by well spacing and quadrant is shown in Figure 5.25, of which about 33% (34 groups) had wells drilled on 500 feet spacing. Some of the operators due to thick shale resource and the presence of Voila in the eastern part of Johnson County, have begun experimenting with 250 feet of spacing and again 33% (34 groups) of wells drilled had the 250 feet of spacing. About 40% (40 groups) of the well groups in terms of location by quadrant were in the northeast quadrant of the Johnson County while another 33% (34 groups) were in the northwest quadrant.

The Johnson County production data analysis for simultaneous fractured wells showed time-lag between first sales of simultaneous fractured and stand-alone wells, in the success of simultaneous fracturing over the stand-alone wells, was a key factor.

129
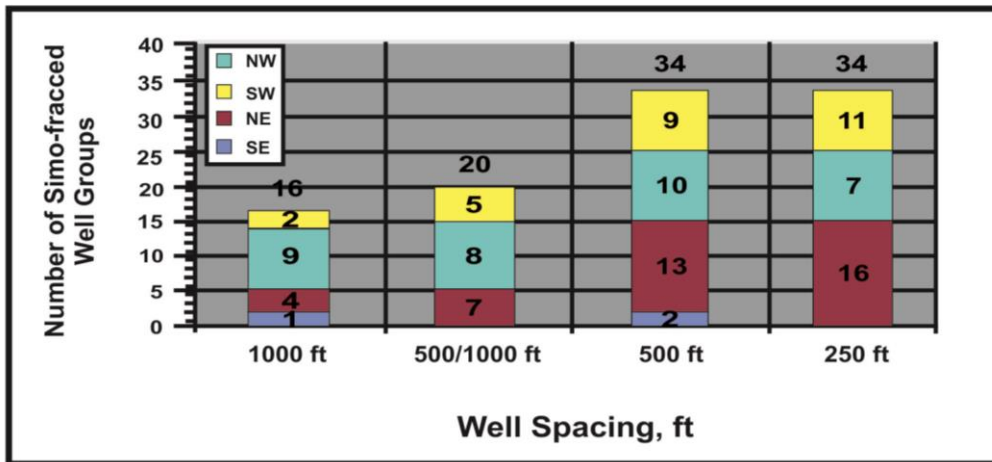
Figure 5.25: Johnson County Simultaneous Fractured Wells Groups Distribution by Well Spacing and Quadrant [76].

Wells with less than 3 months' time-lag between the simultaneous fractured wells and the stand-alone wells data analyzed was suggested to have the best success rate due to simultaneous fracturing, to see incremental production and reserves.

The distribution of simultaneous fractured wells with time-lag less than 3 months between first production from simultaneous fractured wells and stand-alone well shown in Figure 5.26 was sorted well spacing and quadrant. It was shown by comparing Figure 5.25 and Figure 5.26 that, only 20% to 30% of the well groups fell in this category, and majority of the simultaneous fractured wells (70% to 80%) were drilled four months to more than three years anywhere after the stand-alone well was drilled.

A few cases were identified where the stand-alone wells were drilled by different operators later after the simultaneous fractured wells on an offset lease. The simultaneous fractured wells in such cases did better than the stand-alone wells. A summary of production improvement of simultaneous fracture wells over the stand-alone well shown in Figure 5.27 was also sorted by well spacing. These comparisons in Figure 5.27 were based on comparing monthly peak production in the first or second month of the life of the well in most cases.

An average improvement of 56% in simultaneous fractured wells production wasshown in the results over offset non-simultaneous fractured wells. The greater the well spacing as expected, the lower the interference and depletion effects.
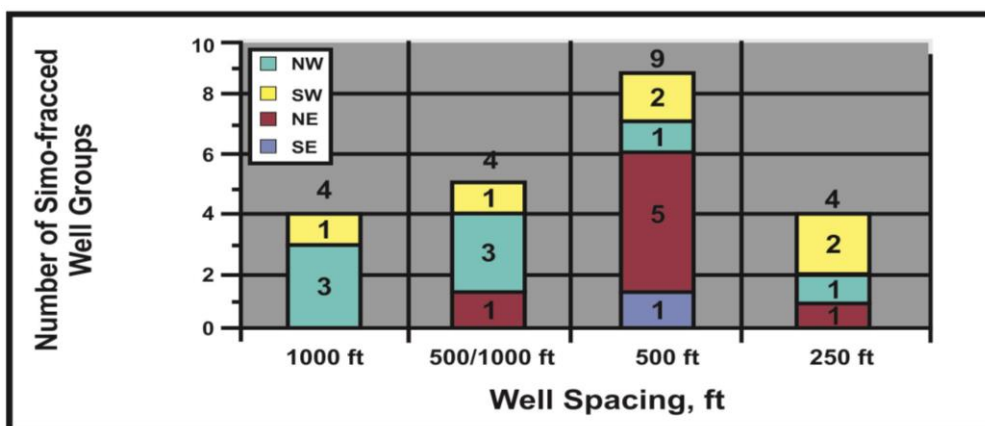
Figure 5.26: Johnson County of Simultaneous Fractured Well Groups Distribution with Time-lag less than 3 Months between First Sales of Simultaneous Fractured and Stand-alone Wells Sorted by Well Spacing and Quadrant [76].
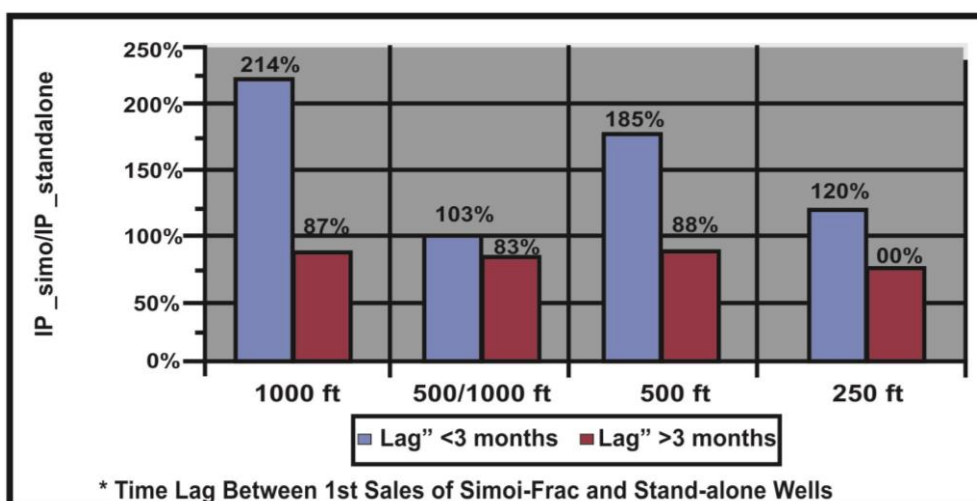
Figure 5.27: IP Average enhancement of simultaneous fractured wells over stand-alone wells in Johnson County sorted by well Spacing [76].

Hence, there is a greater incremental gain from wells with spacing of 1,000 feet compared to well with spacing of 500 feet and it goes in that order.

Production performance fell significantly if the simultaneous fractured wells were drilled beyond 3 months and the simultaneous fractured well average IP less than the stand-alone well (85% of the stand-alone well). This may be due to possible interference and depletion effects that might cause changes in the stress profile in the wellbore vicinity. The 250 feet spacing wells had the lowest IPs compared to the

stand-alone well at 80% due to the fact that it was most affected by interference and depletion effects.

Figure 5.28 shows a summary of production improvement sorted by quadrant for Johnson County. An average of 33% in production from simultaneous fractured wells shown by the results over offset non-simultaneous fractured wells. The simultaneous fractured well average IP was 87% of the stand-alone well due to the fact that simultaneous fractured wells were drilled beyond 3 months. The lowest initial potentials of simultaneous fractured wells compared to the stand-alone wells (70% factor) were in the northeast quadrant of Johnson County which has generally seen prolific producing wells were surprising.

This can be attributed to the fact that Voila barrier was present in most of the northeast quadrant, which has resulted in operators fracturing and high injection rate in the area and there have been excellent stand-alone wells though without simultaneous fracturing. The stand-alone wells and simultaneous fractured wells (identified from maps) in some cases might not have been completed by the same operator. In the results, the contrast may be due to differences in fracture design, injection rates, completion design, etc.
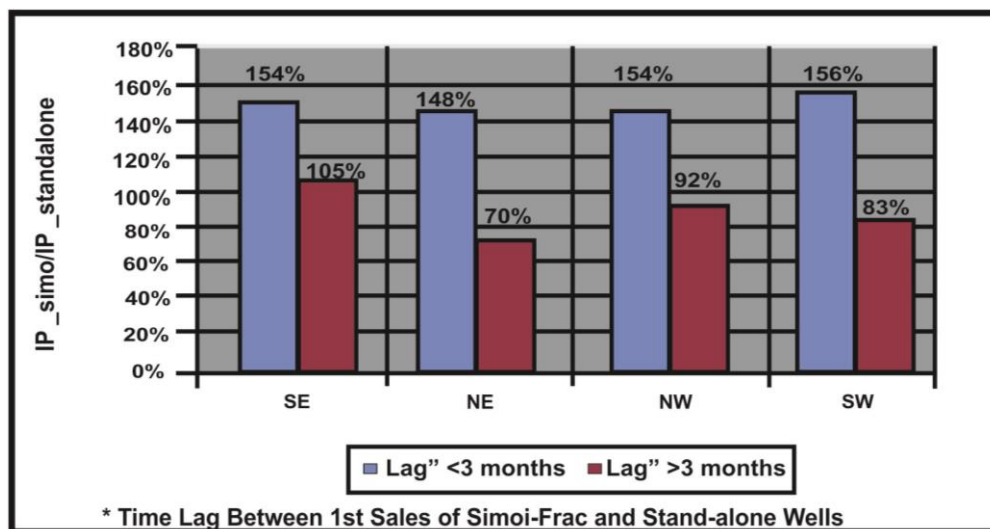
Figure 5.28: IP Average enhancement of simultaneous fractured wells over stand-alone wells in Johnson County sorted by well Quadrant [76].

Leonard et al. described an integrated completion diagnostic methodology assessing potentially optimizing completion strategies in the Barnett shale formation. The purpose of their work was to determine the most cost-effective and completion

strategy that will create more fracture network to improve productivity in the Barnett shale formation [77].

5.9 Early Barnett Shale Completion Procedures

In the1980 through to late 1990's when water fracturing begun to be used, early hydraulic fracturing treatments incorporated 30 to 50 lb/gal gels first crosslink with Titanium and Zirconium and later crosslink with borate compounds. Due to the improvement in cleanup and low cost in large volume high rate slick water fracturing treatment, it has grown in popularity. This technique inability to transport into the complex hydraulic fracture network, a very large volume of proppant was its main disadvantage. Horizontal wells in early 2000 was used to increase the wellbore's exposure to the reservoir and to reduce the number of surface locations in populated areas of Ft. worth basin where horizontal lengths ranges from 1,500 to 5,000 feet laterally. At the beginning, horizontal wells completions were put into cemented and un-cemented laterals. To contact as much reservoir area as possible with a conductive flow path to the wellbore and at the same time containing the fracture treatment within the shale interval was the goal in both cases. Barnett shale expands outside the "core area" of Wise, Tarrant and Denton counties into area like Bosque, Erath, Jack, Hood, Parker, Somervell and Palo Pinto counties made it possible for areas in which Barnett shale has no Viola zone to act as a barrier between the underlying water-bearing Ellenberger zone and Barnett. And this has led to all the most significant fracture height growth containment.

5.9.1 Current Barnett shale completion procedures

In both "core" and expanded areas, the industry trended gradually towards cemented laterals. It is common to complete the well using 5-7 slick-water fracturing stages pumped at 50-80 barrels per minute while avoiding excessive fracture height growth, to maximize fracture network area created. Slick-water fracturing fluid volume in the expanded areas is in the range of 500,000 to 1,000,000 gal and the volumes of proppants ranging from 250,000 to 700,000 pounds per stage are common. Proppants can be chosen from a range of 100 mesh to 20/40 white sand but larger volume of the smaller proppant are usually used in the early part of the fracturing because of its ability to be transported by the low viscosity water further, and then followed by

smaller volume of the larger mesh proppants to build conductivity near the wellbore. Some of the keys to the successful completion of the Barnett shale was identified and described. These are;

(a)   Large fractured network length and area,

(b)   Large proppant volumes,

(c)   Large fracturing fluid volumes,

(d)   Contained fracture height growth,

(e)   Faults/karst avoidance,

(f)   Effective cement zonal isolation (cemented laterals), and

(g)   Fracturing load recovery.

 Also factors contributing to less than optimum Barnett shale completion was
 identified and described and includes;

(a) Gaps in the fracture network area,

(b) Inefficient fracture initiation,

(c) High horizontal stress anisotropy,

(d) Inefficient per placement, and

(e) Improper centralization and cement slurry design (cemented laterals).

Variables that could possible influence the success of Barnett shale completion additionally, but which were less clearly define were;

(a) Horizontal zonal isolation (cemented laterals),

(b) Volumetric load recovery, and

(c) Nature and extent of inter-well communication.

Using the completion diagnostic technologies of radioactive tracing and spectral gamma ray, logging as well as chemical tracing and flow back samples analyses; it was intend to focus especially on the effects of these variables on Barnett shale well performance.

Areas in which the study were conducted including three counties in the west/southwest region of the Fort Worth basin is shown in Figure 5.29. One of the areas was in the traditional "core" area and the other two areas were in the expanded area. In the northeast part of the Hood County, is where the Mitchell Ranch wells are

located. The thickness of Barnett shale in this location is 280 feet, which interpretation is base on the dip-corrected thickness observed in the Range Mitchell Ranch 1H pilot hole, and supported by regional mapping. Approximately, the Maddox area to the northeast of Mitchell Ranch well is 12 miles in the southeastern of Parker County. These wells lie a few miles closer to the Paleo-Fort Worth basin center and the thickness of Barnett shale over there is about 310 feet. The Stevenson wells which are about 25 miles east/northeast of the Mitchell Ranch area and 14 miles to the east of Maddox area, are located in the south central Tarrant County. Thickness of the Barnett shale in these well is 375 feet. The hydraulic fracturing results for four set of simultaneously fractured wells assessed were chosen from these area. Well performance of these wells (Mitchell Ranch 1H/5H, Mitchell Ranch 2H/6H, Maddox 1H/2H and Stevenson 1H/2H) after simultaneously fracturing completion, was compared with well performance for other wells fractured individually in adjacent areas of Parker, Tarrant and Hood Counties.
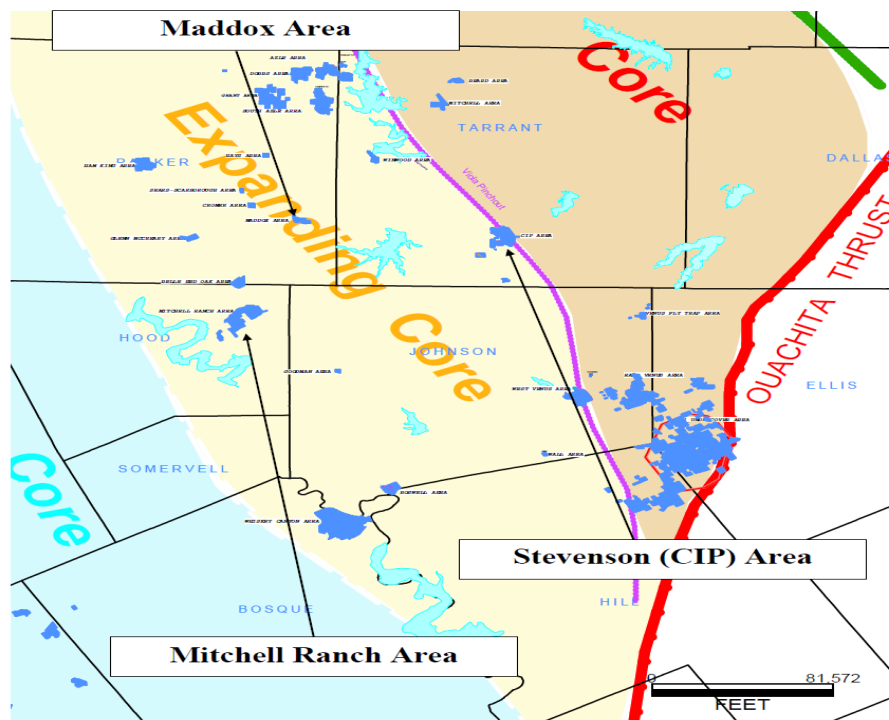
Figure 5.29: Map of Fort Worth basin with the three study areas highlighted [77].

5.9.2 Well configuration and completion procedures

Maddox area: Two horizontal wells were drilled in the Maddox study area from a common are perpendicular to the perceive fracture orientation as shown in Figure

135

5.30. The wells were drill in the northwesterly direction (~N 50 degrees W) as parallel laterals. The lateral length of the 1H (gross perforated interval) of 3223 feet and the 2H lateral length was 2863 feet. The two lateral wells were approximately 830 feet in the target Barnett shale formation. With seven stages per each well. These wells were fractured by stimulating using the same fluid and sand volume at all stages were pumped at 60 barrels per minute. The fluids were pumped by two completely separates full crews in these simultaneous stimulation treatments. These same treatments were designed to start at the same time, and each subsequent fracturing stages timing was set up to mirror the offset parallel lateral.
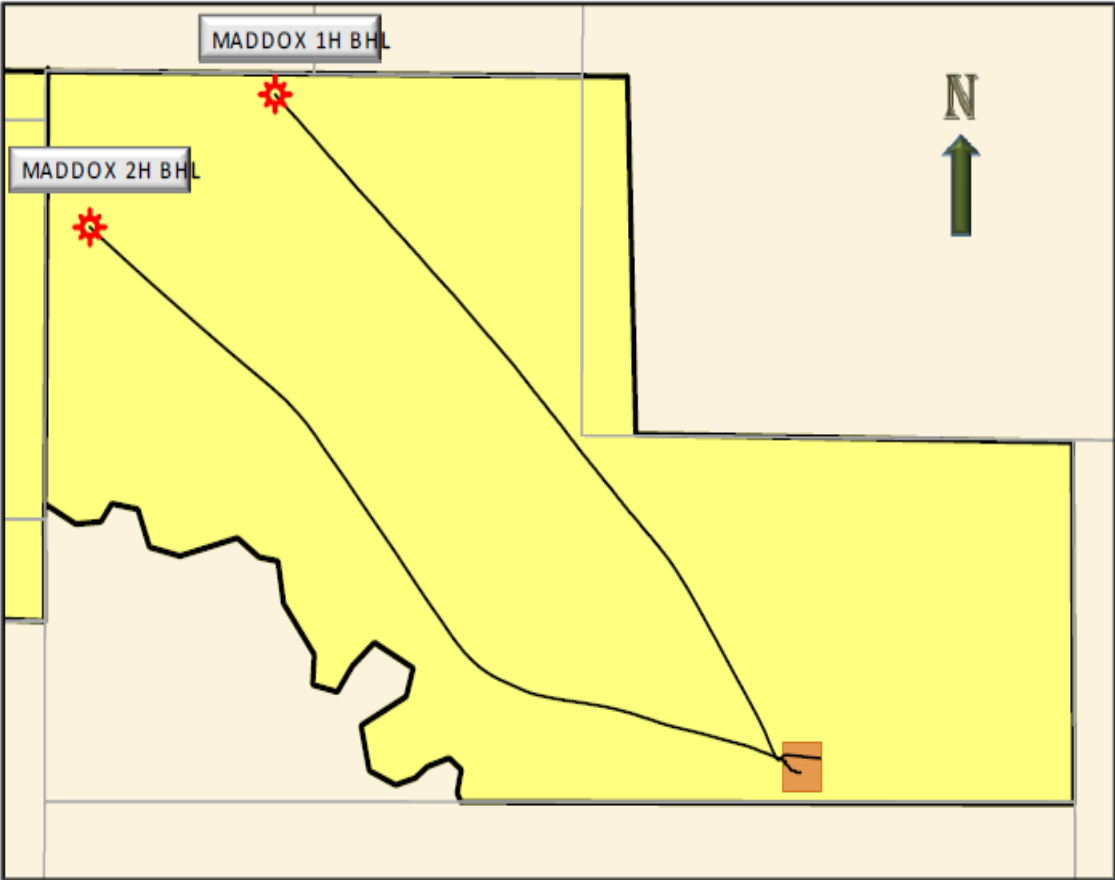
Figure 5.30: Maddox Wells plan View [77].

With two perforated intervals stage, both wells were completed with the first stage being shot tubing-conveyed while the subsequent stage were all perforated with pump down guns (6 spf, 25 gram, 0.42 inch diameter, 60 degree phasing). The fracture stages were all broken down with acid after perforating and were isolated with composite fracturing plugs. The 1H that has 247 feet between clusters and 247

feet between stages has 36 holes per stage. The 2H also having 36 total holes per stage had 217 feet between clusters and 217 feet between stages.

Mitchell ranch area: Four horizontal wells were drilled in the Mitchell Ranch study area, perpendicular to the suspected fracture orientation from two surface locations about 700 feet from each other as shown in Figure 5.31. In the southeasterly direction (S 45 degrees W), two of the wells (#1H and #5H) were drilled with lateral lengths (gross perforated intervals) of about 2,500 feet. In the
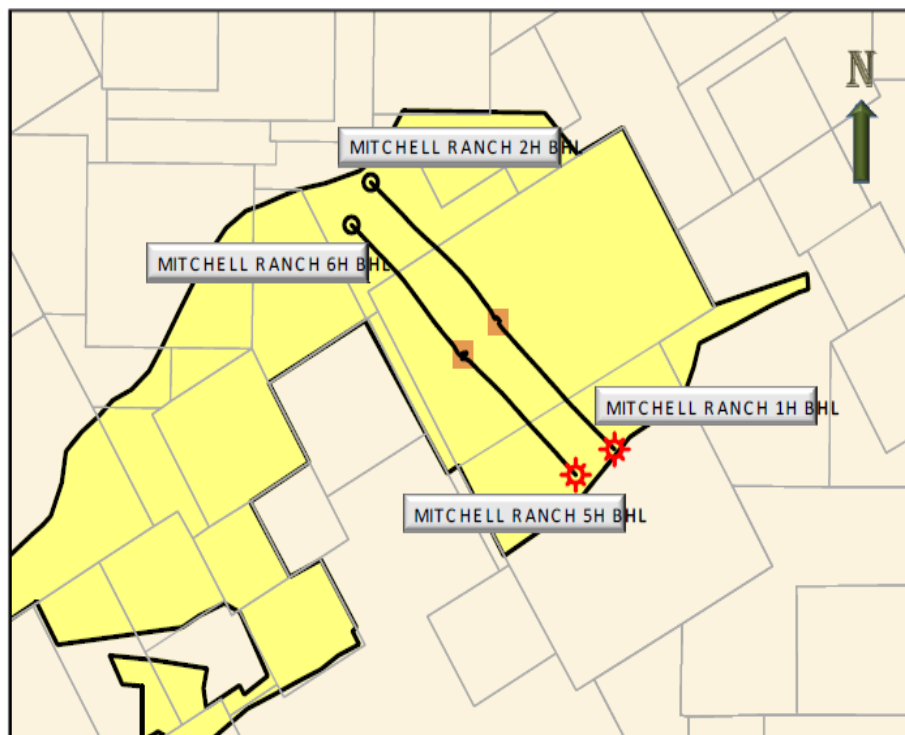
Figure 5.31: Mitchell Ranch wells plan View [77].

Northwesterly direction (N 45 degrees W) the other two wells (#2H and #6H) were drilled with lateral lengths between 2,800 feet and 3,200 feet. Both pair of parallel laterals in the Barnett shale formation was about 1,000 feet from each other. With the same fluid and sand volume pumped at 60 barrels per minute, each pair of parallel lateral was fractured stimulated with multiple stages using the simultaneous stimulation technique. The third stage of the #1H had no simultaneous stimulation due to the presence of faults/karst in the interval in the parallel offset 5H well, and this the only exception.

All the four wells were completed in the Maddox area with two perforated intervals per well. The first stage was perforated with short tubing-conveyed, and all the subsequent stages were perforated with pump down guns. The intervals were all shot

6 spf with 25 gram charges, 0.42 inch diameter hole and 60 degrees phasing. There was two 5 feet perforation cluster (30 holes/cluster) and about ~180 feet from each other in the 1H and 5H stages. There was a space of 180 feet apart for the individual stages. The 2H and 6H which were spaced 210 feet apart had two 4 feet perforation clusters (24 holes/interval), and the individual stages were spaced 210 feet apart. For all the four wells, all the fracture stages were broken down with acid after perforating and before starting the fracturing operations, and composite fracturing plugs used to isolate the stages were run with pump-down perforating guns.

Stevenson area: Two horizontal wells drilled in the Stevenson study area from a common location perpendicular to the perceived fracture orientation are shown in Figure 5.32. In the southeasterly direction (~ S 70 degrees E), the wells were drilled as parallel laterals. The lateral lengths (gross perforated interval) were 3125 feet for the 1H and 2605 feet for the 2H. The two laterals in the Barnett shale were approximately 450 feet apart in the target formation. Using simultaneous stimulation technique, these wells were stimulated with seven stages (1H) and six stages (2H). The same fluid and sand volumes were use to stimulate each stage by pumping at 73 barrels per minute.

Both wells in the Maddox and Mitchell Ranch areas were completed with two perforated intervals per stage where the first stage shot tubing conveyed and the subsequent stages were all perforated with pump-down guns (6 spf with 25 gram charges, 0.42 inch diameter hole and 60 degrees phasing). Fracture stages were all broken down with acid after perforating and composite fracturing plugs were use to isolate the stages. The 1H that has 255 feet between cluster and 255 feet between stages had sixty holes per stage. The 2H that has 265 feet between cluster and 265 feet between stages also has sixty holes per stage.

Discussion: A substantial data review of other individually fractured Barnett wells in adjacent Counties, were under taken as a prelude to the analysis of the simultaneously fractured wells studied. The dataset was put into four groups and listed as follows,

(a) Completion/stimulation data,

(b) Fracture geometry diagnostics,

(c) Flow-back and inter-well communication diagnostics, and

(d) Well performance.
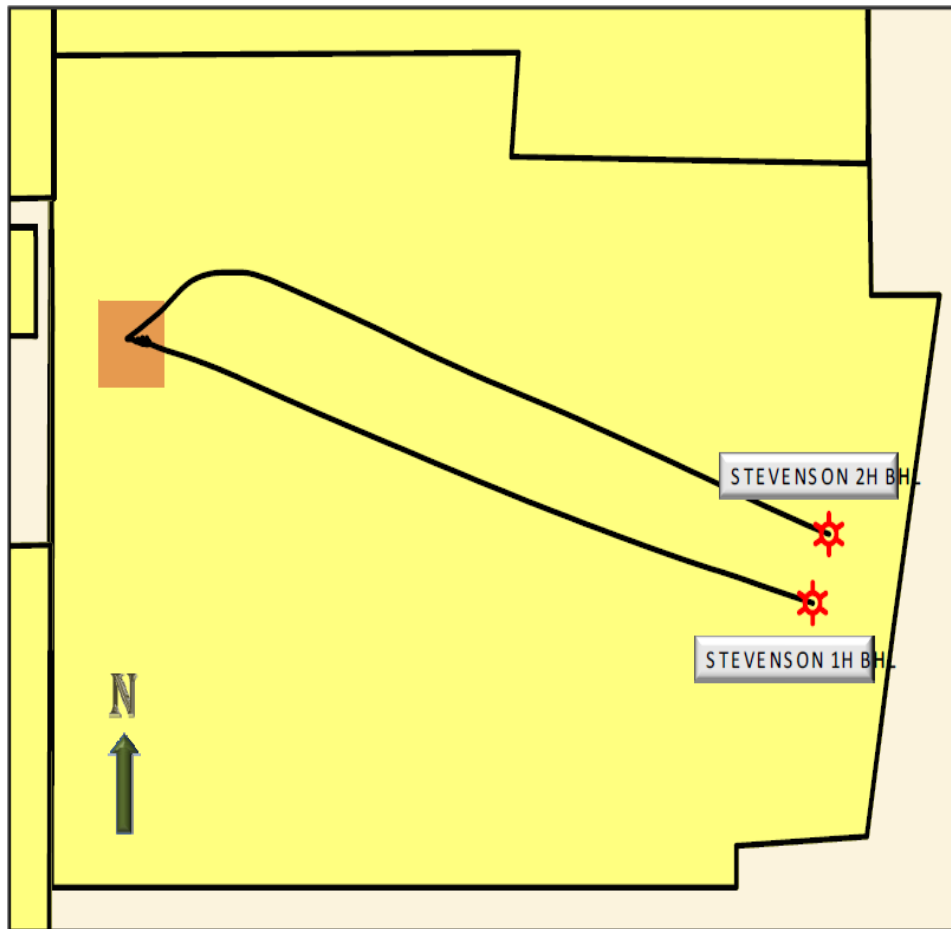
Figure 5.32: Stevenson wells plan view [77].

To assess the keys mentioned above to a successful completion in individually fractured Barnett wells, as a baseline for comparison with the same data for simultaneously fractured study wells was the intention of the analysis.

The objective of this work was to evaluate the use of employing radioactive tracing and spectral gamma ray logging to assess the near-wellbore fracture geometries and to assess the flow-back/cleanup of fractured wells using non-radioactive chemical tracing along the with the nature and extent of inter-well communication. These processes were carried out using radioactive isotopes Sc-46 (Scandium), Sb-124 (Antimony) and Ir-192 (Iridium) and the spectral gamma ray logging measurement was done using a spectral gamma ray logging tool deployed on coiled tubing. The fracturing fluid was chemically traced using fluorinated organic compound.

For both radioactive tracing, the simultaneous fracturing and the individual fracturing was performed typically with alternating isotopes from stage to stage in a given well. The Stevenson 1H and 2H, which were trace with the alternating isotopes (Sb-124

and Sc-46) in individual 1H stage and a single isotope (Ir-192) throughout all the stages in 2H, was the only exception. The goal for the later was to determine whether one or more of the three isotopes were communicated physically across, to the parallel offset well which was 450 feet away. There was evidence of the Ir-192 isotope in the spectral gamma ray log of the 1H and evidence of the Sc-46 isotope in the log of the 2H as seen in Figures 5.33 and 5.34.The radioactive-traced proppant was therefore communicated across to both of the simultaneously-fractured wells. In these two wells, chemical tracers were not run. Hence the magnitude of inter-well communication could not be quantified. This means sufficient fracture width was generated between the two wells to allow the 40/70 mesh tracer beads and possible proppant as well to travel the distance of 450 feet between the wells.

Within 1-3 day of fracturing the last stage, spectral gamma ray logging tool deployed on coiled tubing were normally run. The log data resulting images after processing were carefully analyzed to determine perforation cluster coverage, lateral fracture growth between clusters, lateral fracture growth between stages intervals, gross lateral fracture growth, and evidence of questionable cement isolation. Throughout all fluid segments of each individual fracturing stage, a unique chemical tracer was added at 1 ppm with the exception of flushers and pre-pads. Individual flow-back samples upon commencing were collected from the treated well according to a sampling schedule pre-established. A gas chromatograph/mass spectrometer analysis procedure were used to analyze the flow-back samples. The concentration of each chemical tracer pumped into the treatment wells as well as any offset simultaneous fractured or individual wells, were identified and quantified automatically by this analysis procedure. These recovered chemical tracers concentrations, were converted to the corresponding fracturing fluid volumes recovered using mass balance, for both treatments well and interfering offset wells. The fracturing fluid volume pumped to arrive at the flow-back efficiencies then divided the recovered fracturing fluid volumes computed. The resulting volumes were also reported in terms of total load recovery percent, total fracturing fluid recovery percent and inter-well fracturing fluid recovery percent. These recovery percentage, were all based on the actual amount of each chemical tracer recovered during the sampling period.

Based upon the number of measured and computed well production values, the well post-completion performance was assessed for each well. There is a good reasonable

correlation between the ultimate production performance and second month of production.
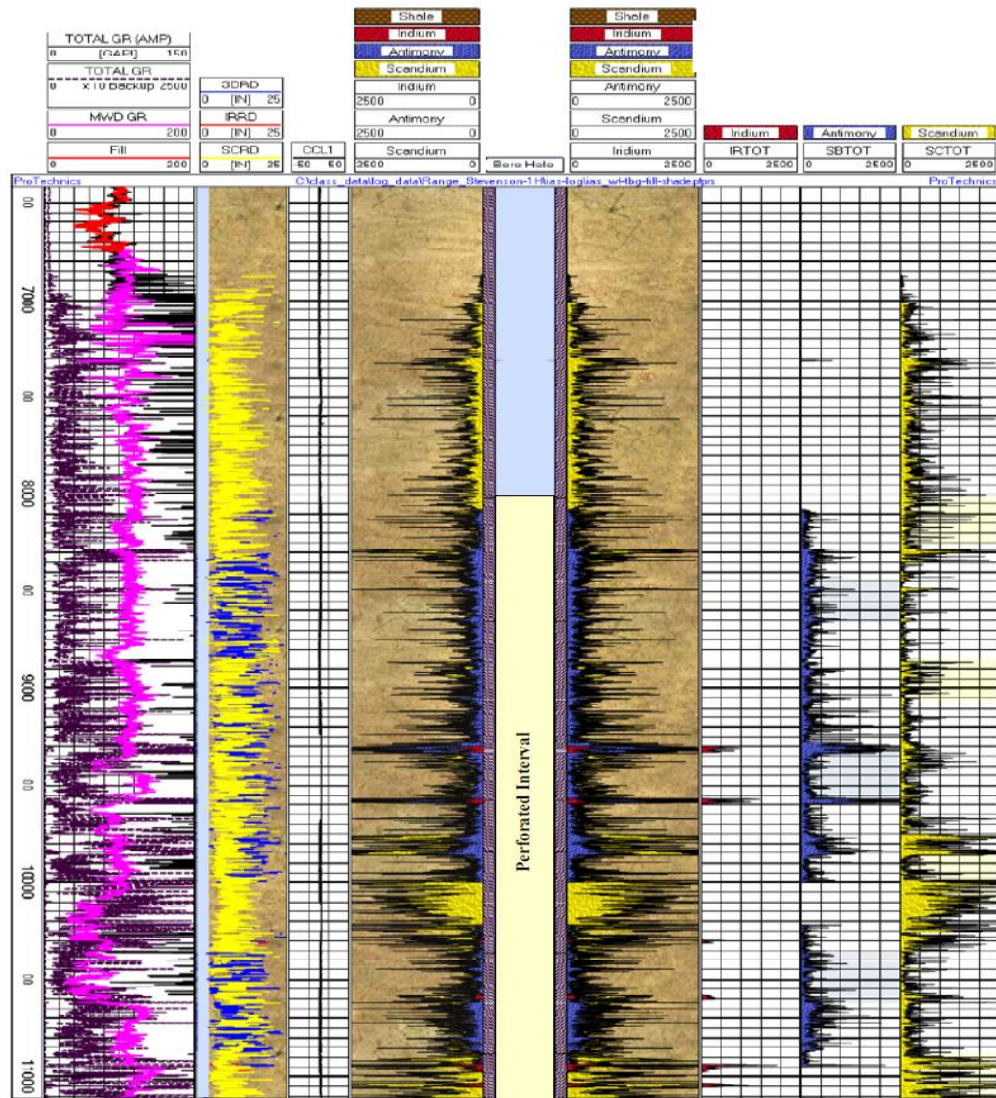
Figure 5.33: Stevenson 1H post-fracturing spectral gamma ray image [77].

Each well's average gas rate for the second month of production for this reason was used as the primary sorting criteria for assessing the well post-completion performance. The total fluid recovery and the percentage of load recovered additionally were calculated for each well. From well to well, there were significant variation in fluid recoveries and this were believed to be the reflection of variation in the complexity of fracture networks.

A number of observations and comparisons were made, in the radioactive tracing and spectral gamma ray logging to assess near-wellbore fracture geometries and chemical tracing to assess fracturing fluid flow-back/cleanup and inter-well fracturing fluid

communication for the four sets of simultaneously fractured wells. Data for the results that follow were taken from tables and from the figures.
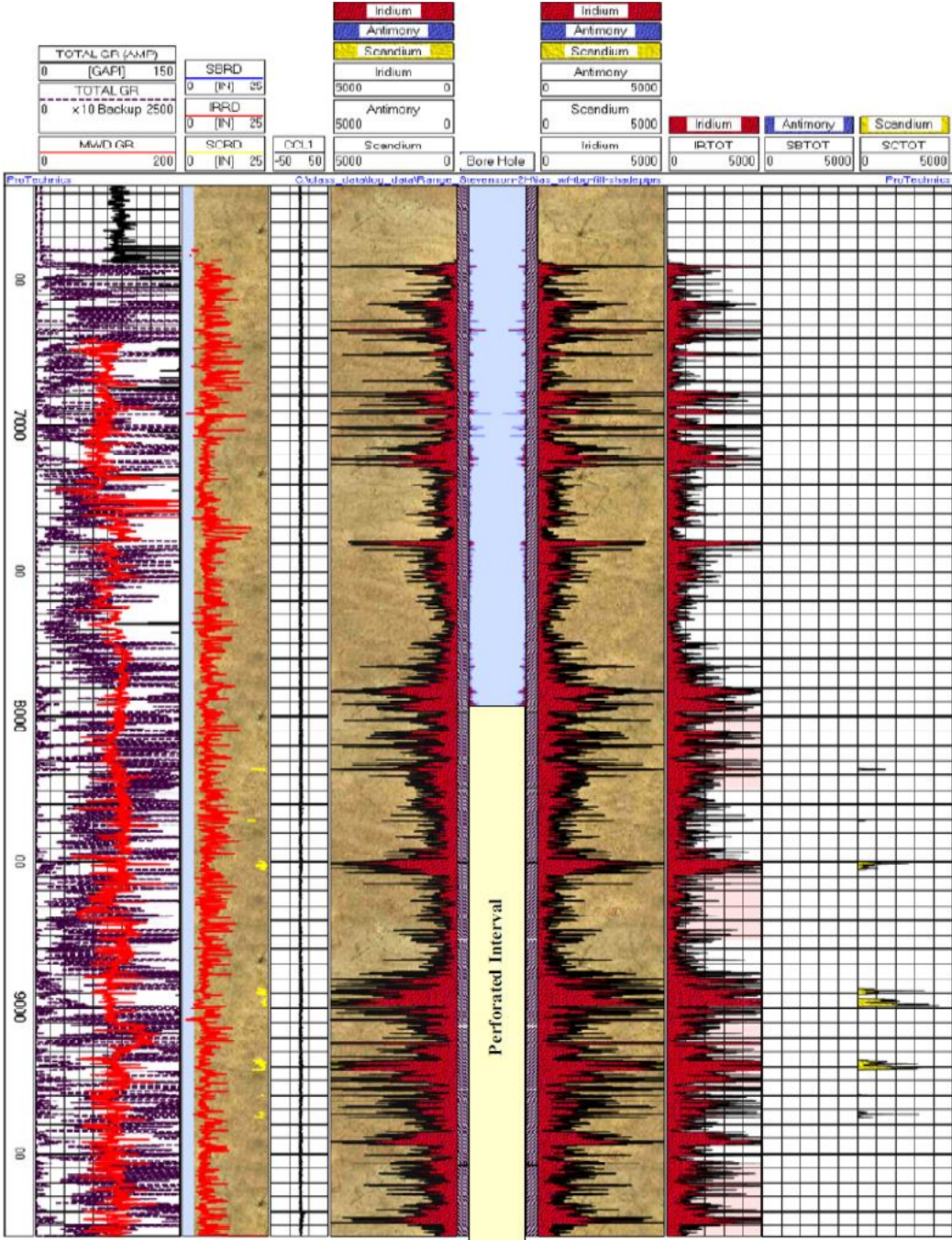
Figure 5.34: Stevenson 2H post-fracturing spectral gamma ray image [77].

Starting with the 1H and 2H simultaneously fractured wells (830 feet apart) in the Maddox County, fractured with the same fluid volumes and proppant volumes as a function of laterally treated gross interval, a number of comparisons can be made considering the data from the two-targeted diagnostic technologies. Lateral fracture growth by both fracturing treatments was reveal by spectral gamma ray images

(Figures 5.35 and 5.36), remained laterally constrained with modest lateral fracture growth beyond the innermost perforation cluster. In both wells, the same figures provide an evidence of substantial transverse near-wellbore fracture initiation.

The fracturing fluid flow-back/cleanup measured by the flow-back efficiencies calculated from chemical tracer measurements reveals that, significantly more fracturing fluid recovery from the Maddox 2H (about 11% in 300 hours of flow-back) compared with the Maddox 1H (about 4% in slightly over 300 hours of flow-back). The inter-well communication was too extensive from Maddox 2H to Maddox 1H (about 4% from 2H to 1H, compared with about 1% from 1H to 2H). The well prime post-completion performance indicator of the second month average gas rate production was higher for the Maddox 1H (2196 MCFD) compared with the Maddox 2H (1993 MCFD). This difference at least, may be attributed to the larger gross perforated interval in the Maddox 1H (3223 versus 2863 feet). From this dataset, it appears the previously held to be advantageous factor of greater fracturing fluid recovery and minimal inter-well fracturing fluid communication are not positive trends in term of ultimate well performance.

There are differences observed in the Mitchell Ranch 1H and 5H simultaneously fractured wells fluid volumes and proppant volumes pumped. Because the Mitchell Ranch 5H was fractured in 6 stages and the Mitchell Ranch 1H was completed in 7 stages (one 5H stage was skipped due to the presence of fault), the Mitchell 1H employed about 17% larger fluid and proppant volumes. The larger volume placed as a function of laterally treated gross interval was more significant than the larger volume pumped. From the spectral gamma ray images (figures 5.37 and 5.38), it was observed that a substantial lateral fracture growth beyond the innermost perforation cluster in the direction of the heel was experienced in the Mitchell Ranch 5H. However, the Mitchell Ranch 1H showed more laterally-constrained fracture growth with anecdotal evidence of substantial transverse near-wellbore fracture initiation compared with the Mitchell Ranch 5H's more longitudinal near-wellbore fracture initiation. The net results is apparently far more fluid and proppant placement across the Mitchell Ranch 1H per gross feet fractured than across the Mitchell Ranch 5H. A part of the extended fluid and proppant at least moving outside the perforated interval might be related to poor cement isolation, hence the importance of this metric has been high-lighten by this observation.

Fluid recoveries is higher in Mitchell Ranch 5H (about 18% in slightly over 1,200 hours of flow-back) than in the Mitchell Ranch 1H (about 14% in slightly over 1,200 hours of flow-back). These fluids recoveries were measured by the calculated flow-back efficiencies, shown in Figures 5.39-5.40 and Figures 5.41-5.42. In addition, there was twice as much inter-well communication from Mitchell Ranch 5H to Mitchell Ranch 1H (about 4% from 5H to 1H, compared with about 2% from 1H to 5H).
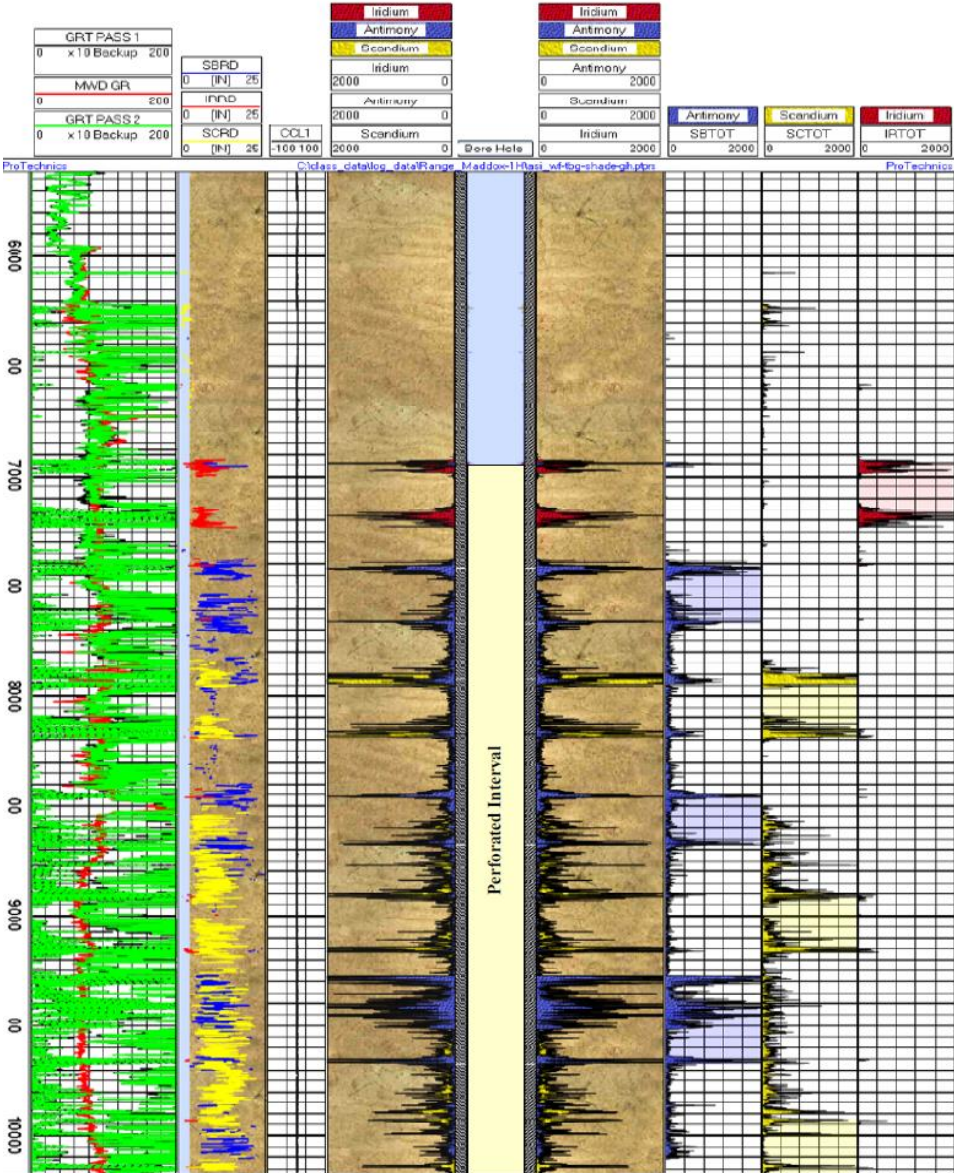
Figure 5.35: Maddox 1H post-fracturing spectral gamma ray image [77].
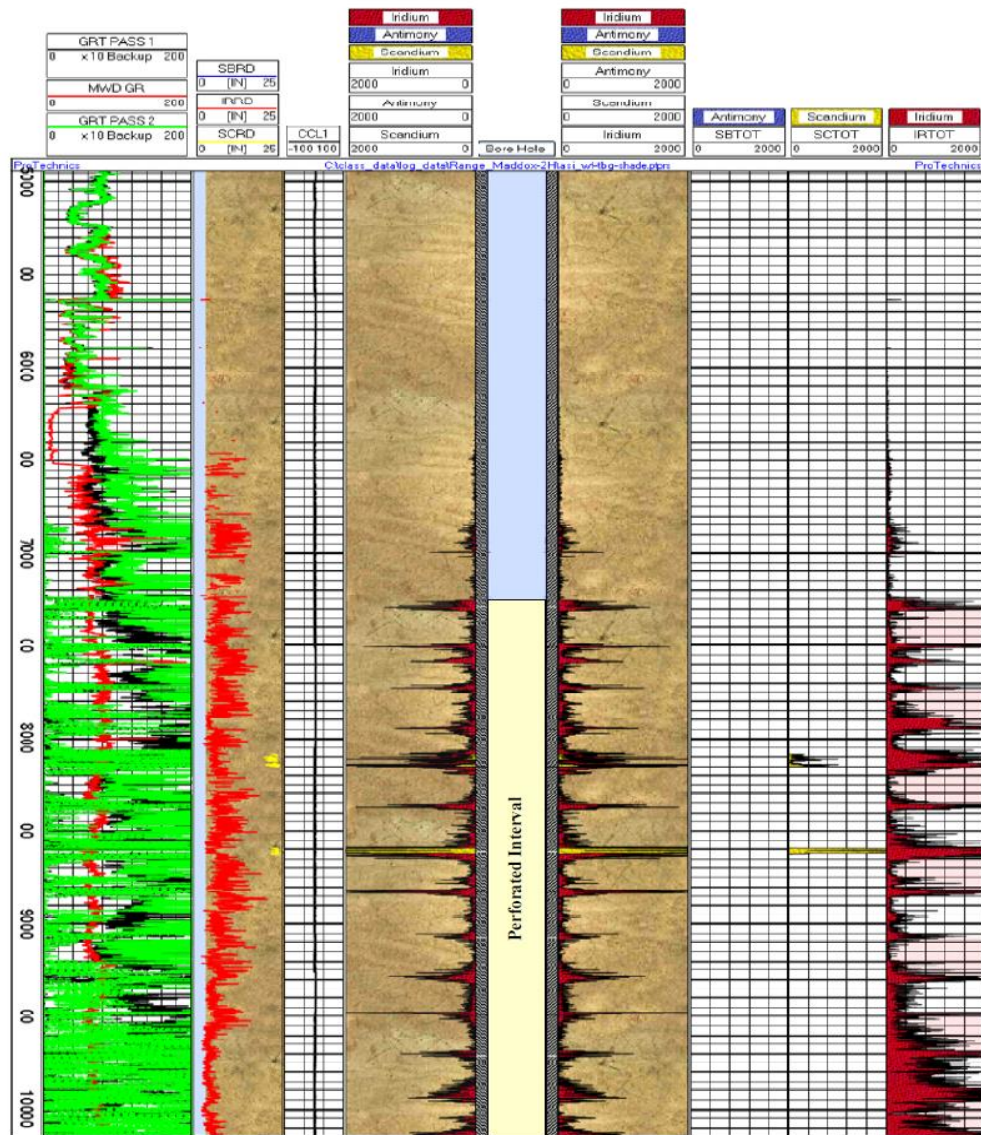
Figure 5.36: Maddox 2H post-fracturing spectral gamma ray image [77].

Second month of production comparison shows a higher gas rate for the Mitchell 1H (1517 MCFD) compared with Mitchell Ranch 5H (1097 MCFD). Greater fracturing fluid communications are not necessarily positive indicators of well post-completion performance in the well dataset from Maddox. To take advantage of the extraneous proppant placement in the lesser performing Mitchell 5H well where the lateral fracture grows into adjacent shale interval, reentering the well to add some appropriate phase perforation across the adjacent shale interval may be considered.

The Mitchel Ranch 2H and 6H (1,000 feet apart) which were completed with comparable fluid volume and proppant volumes spectral gamma ray (Figures 5.43 and 5.44) shows that, the Mitchell Ranch 2H had substantial lateral fracture growth

beyond the innermost perforation cluster. However, the Mitchell Ranch 6H showed more laterally constrained growth with unreliable evidence of substantial transverse near-wellbore fracture initiation compared with the Mitchell 2H's longitudinal near-wellbore fracture initiation.
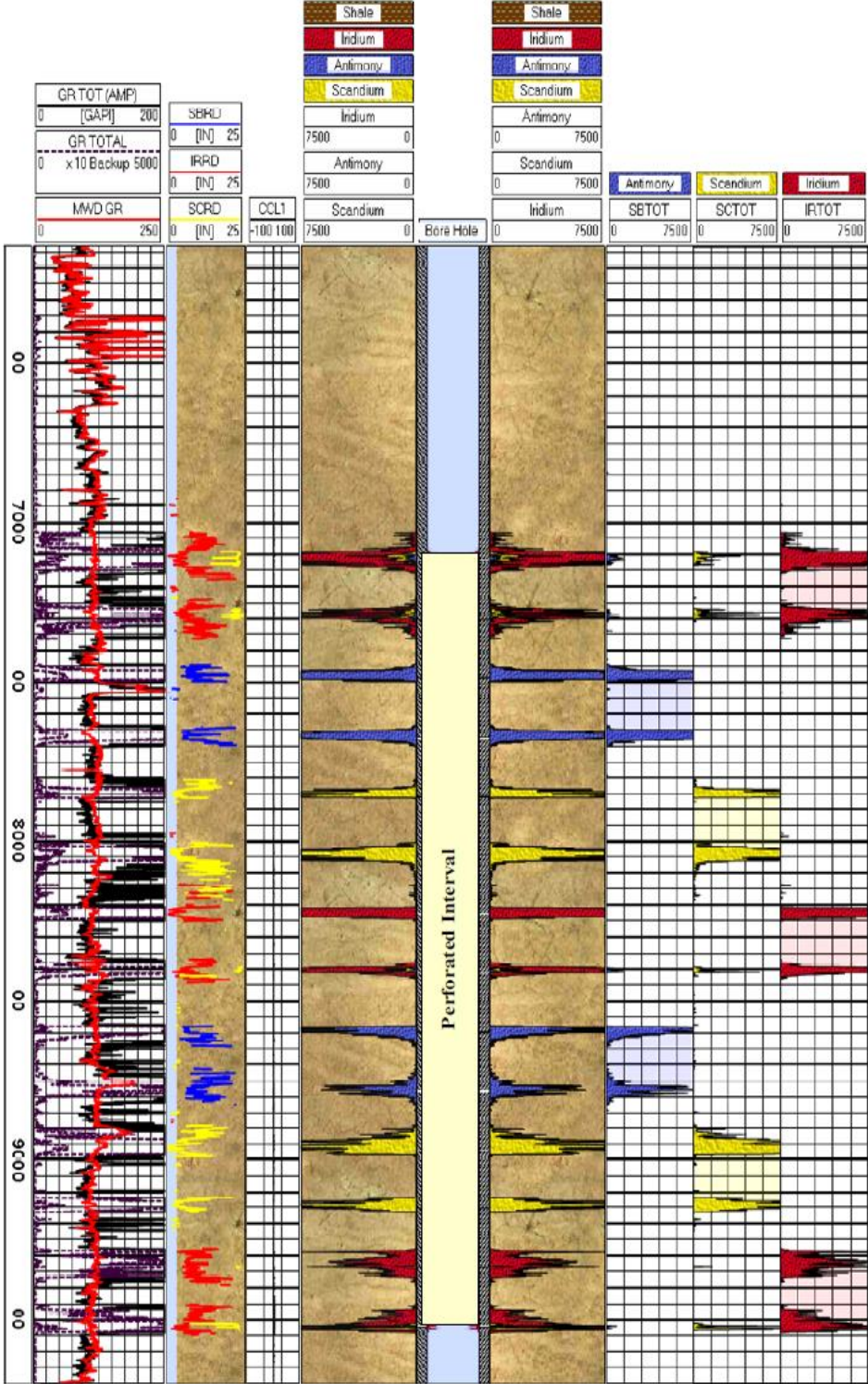
Figure 5.37: Mitchell Ranch 1H post-fracturing spectral gamma ray image [77].
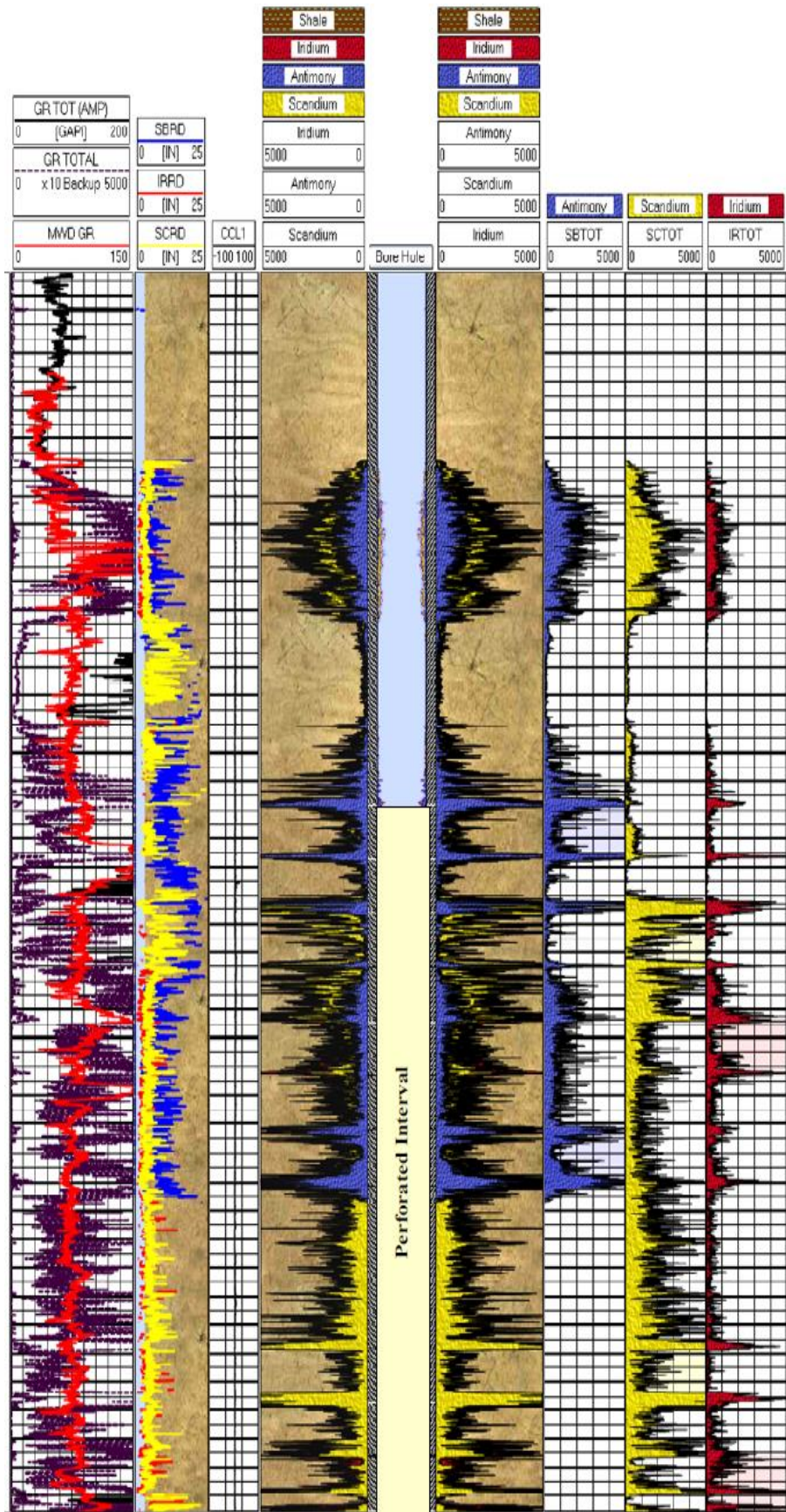
Figure 5.38: Mitchell Ranch 5H post-fracturing spectral gamma ray image [77].
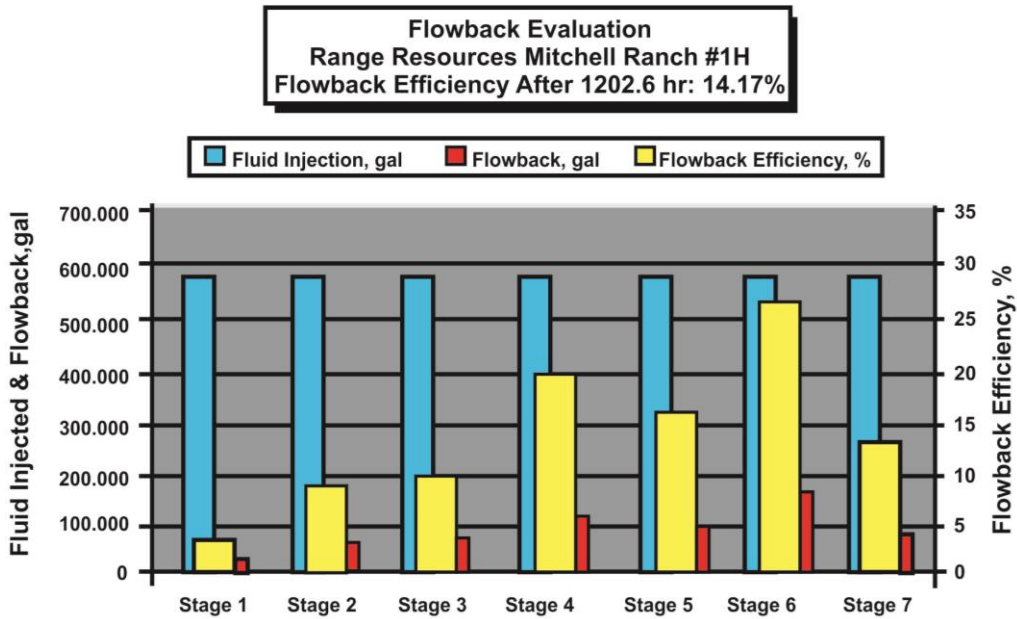
Figure 5.39: Mitchell Ranch 1H flow-back efficiencies [77].
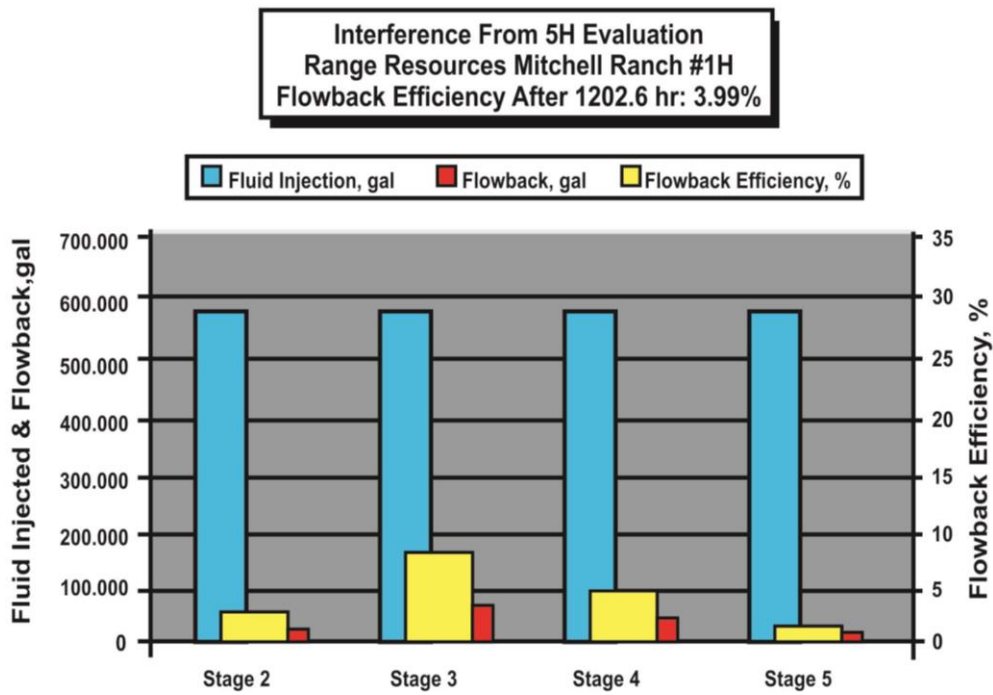
Figure 5.40: Mitchell Ranch 1H inter-well communication from Mitchell 5H [77].
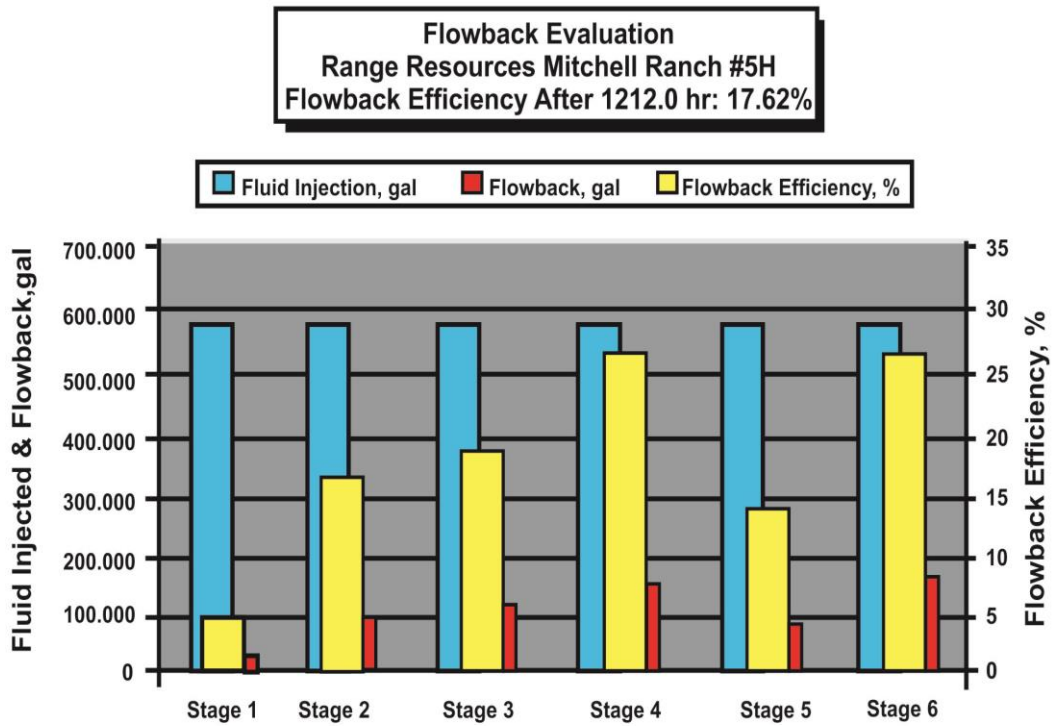
Figure 5.41: Mitchell Ranch 5H flow-back efficiencies [77].
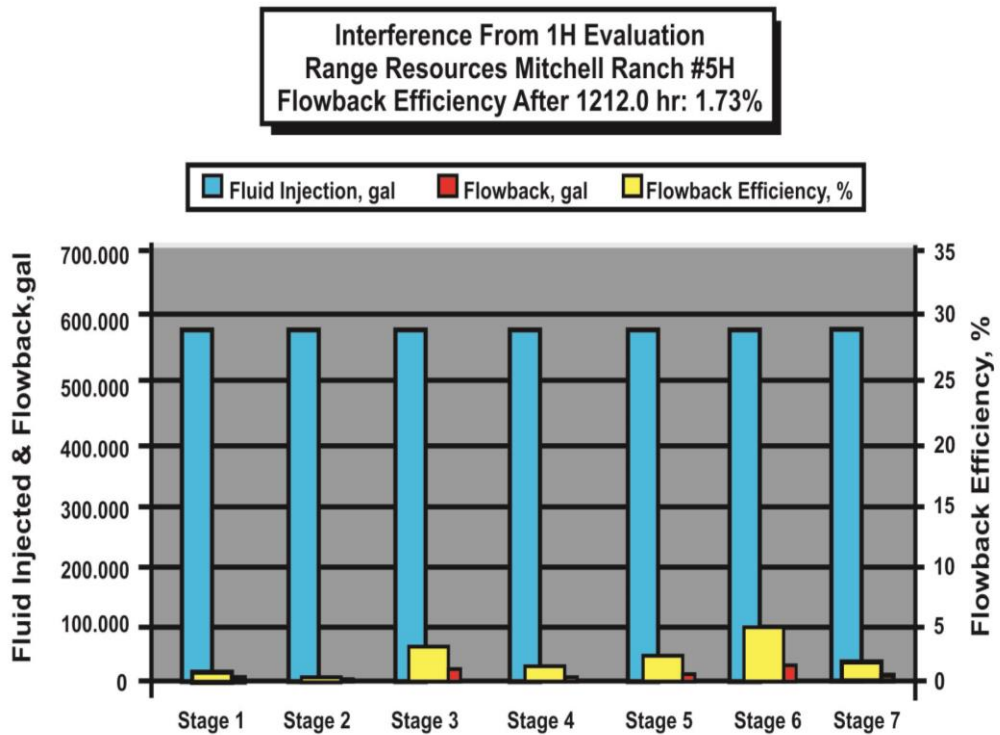
Figure 5.42: Mitchell Ranch 5H inter-well communication from Mitchell Ranch 1H
[77].
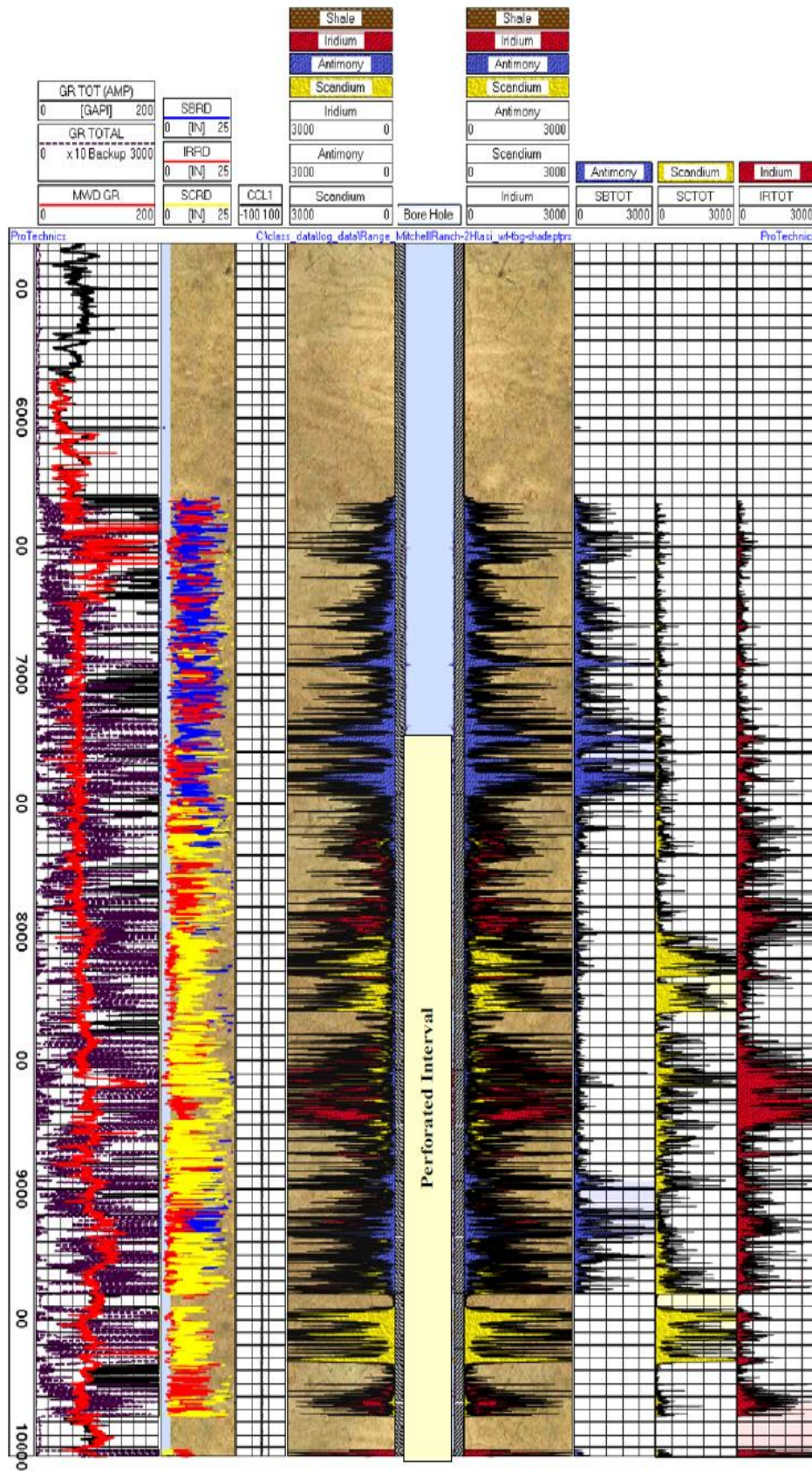
Figure 5.43: Mitchell Ranch 2H post-fracturing spectral gamma ray image [77].
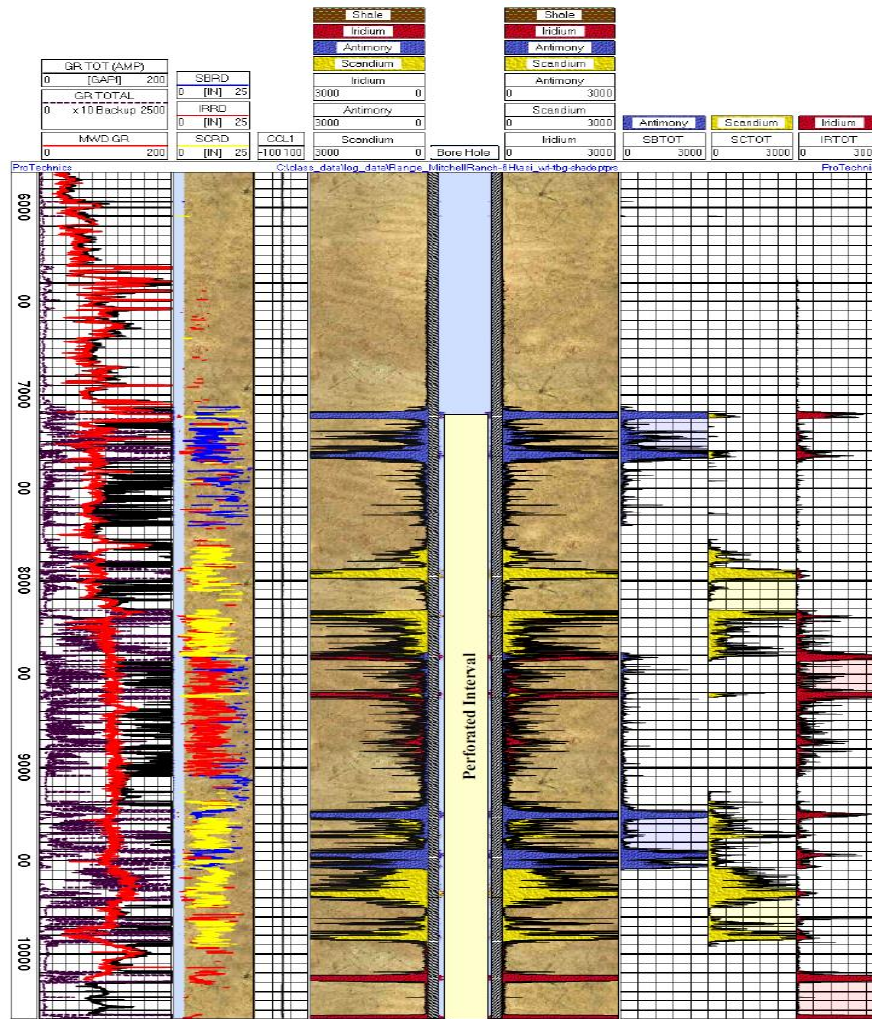
Figure 5.44: Mitchell 6H post-fracturing spectral gamma ray image [77].

Across the Mitchell Ranch 6H per gross feet fractured, the net results is apparently far more fluid and proppant placement than across the Mitchell Ranch 2H. Again, extended portion of the fluid and proppant vectoring outside of the perforated interval may be related to poor cement isolation.

Observations from fracturing fluid flow-back/clean computed from flow-back efficiencies (Figures 5.45-5.46 and Figures 5.47-5.48) indicate that, there is much higher fracturing fluid recoveries from the Mitchell Ranch 2H (about 20% in 820 hours of flow-back) compared with the Mitchell Ranch 6H (about 11% in 760 hours of flow-back). For these two well the sampling time did not match as closely as with other pairs but the substantial difference in fluid recoveries cannot be explained fully based on the sampling time increments of about 8%. From the Mitchell Ranch 2H to the Mitchell Ranch 6H, there is significantly more inter-well communications (about 6% from 2H to 6H compared with less than 0.5% from 6H to 2H). The well with the

poorest flow-back/cleanup for the third pair of wells is the one with the highest inter-well communication. The stage that shows most effective cleanup/flow-back interestingly is also the ones that show extensive inter-well communication.
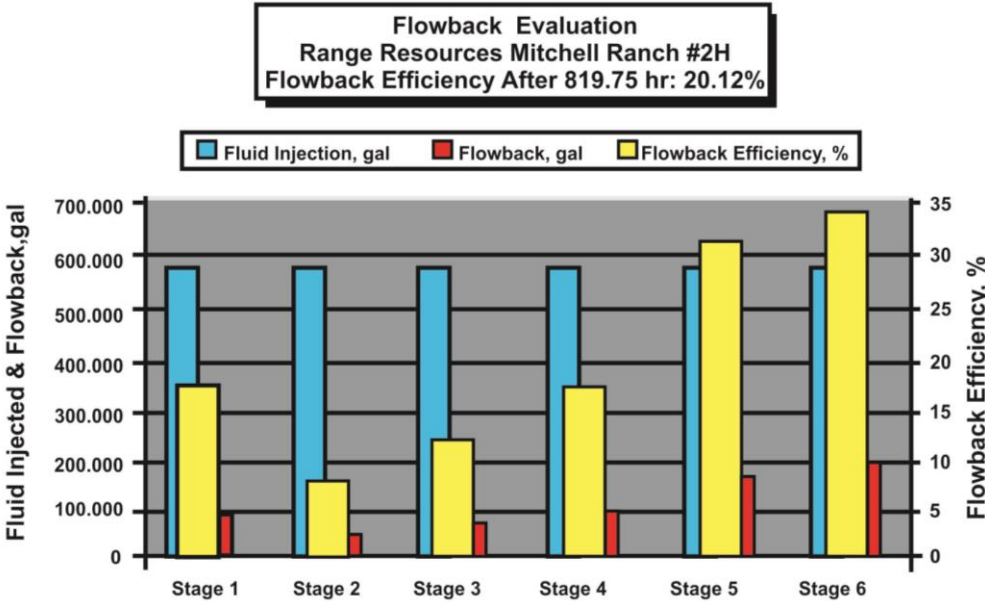
Figure 5.45: Mitchell Ranch 2H flow-back efficiencies [77].
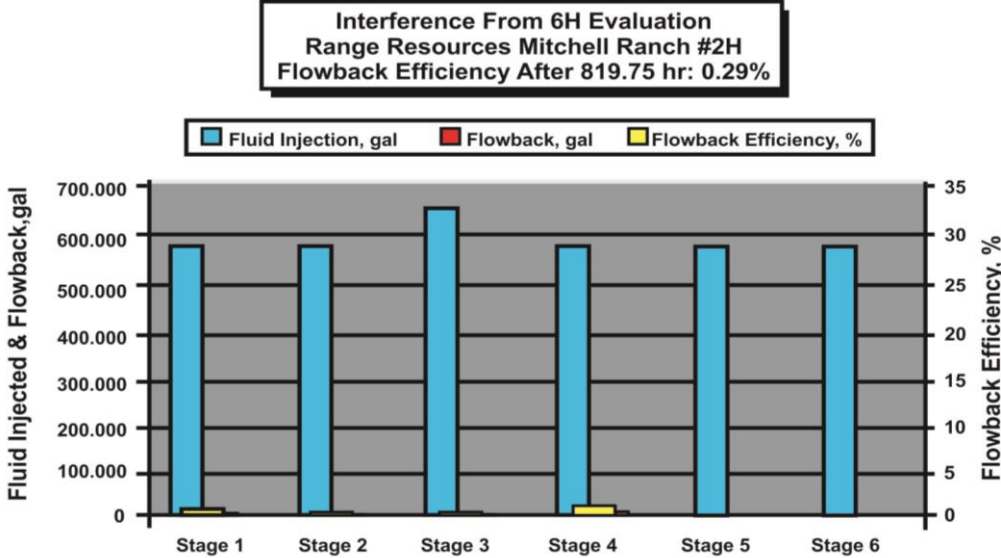
Figure 5.46: Mitchell Ranch 2H inter-well communication from Mitchell Ranch 6H [77].

A second month production performance comparison reveals a substantial higher gas rate for Mitchell Ranch 6H (1408 MCFD) compared with Mitchell Ranch 2H (812 MCFD). Greater fracturing fluid recovery and minimal inter-well fracturing fluid

communication as in the previous other well, are not necessarily positive indicators of well post-completion performance.
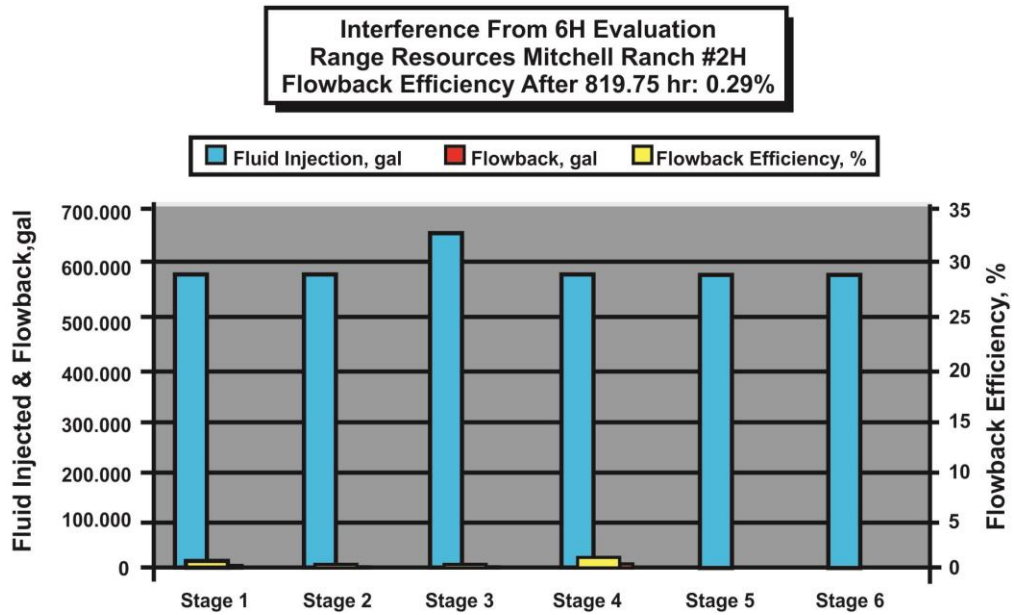
Figure 5.47: Mitchell Ranch 6H flow-back efficiencies [77].
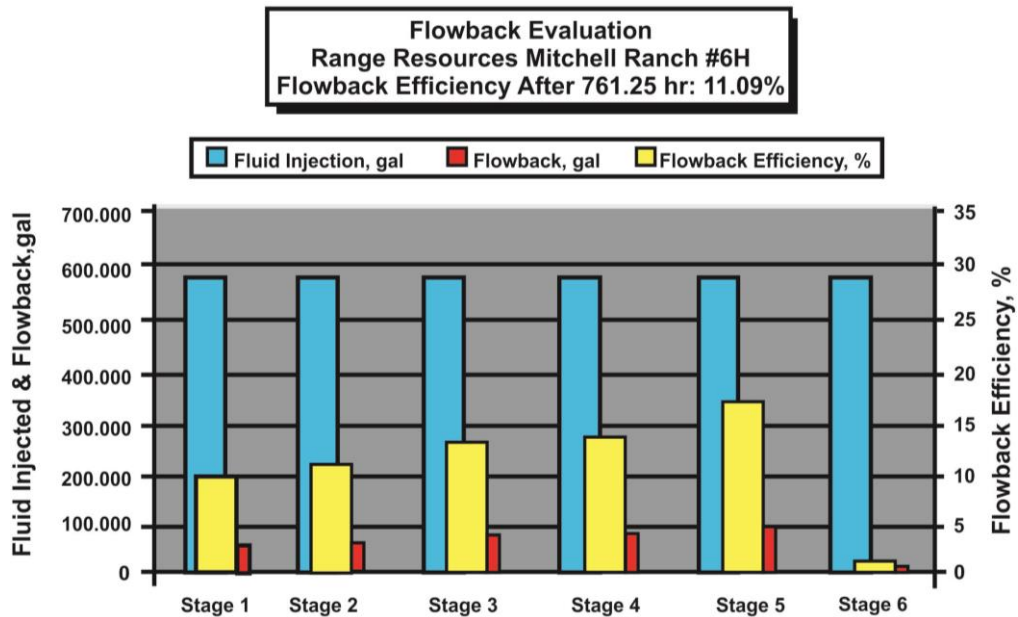
Figure 5.48: Mitchell Ranch 6H inter-well communication from Mitchell Ranch 2H [77].

The last simultaneously fractured pair of well which is 450 feet apart is the Stevenson 1H and 2H. The Stevenson 1H that has a lateral length of 500 feet longer employed about 7% lager fluid volumes and about 17% larger proppant volumes in the form of additional fracturing stage. The images of the spectral gamma ray reveal

that lateral fracture growth was poorly constrained by both fracturing treatments with sufficient lateral fracture growth beyond the innermost perforation cluster. Different from the previous three pairs, both of the Stevenson 1H and 2H wells provides anecdotal evidence of substantial longitudinal near-wellbore fracture initiation. The fluid and proppant placement per gross feet fracture are not particularly high and this can be attributed the substantial lateral fracture growth. At least the extended fluid and proppant vectoring outside of the perforated interval is partly attributed to poor isolation of cement. For these two wells, it should be pointed out that the pair is in the "core area" where cement isolation may be less critical unlike the previous three pairs. Simultaneous fracturing of un-cemented parallel lateral in the "core area" may be choice of the strategy due to the reduced possibility of fracturing into water in that area.

There is no fracturing fluid flow-back/cleanup or fracturing fluid inter-well communication computation performed because these two wells were not chemically traced. Second month production average rate of gas comparison, reveals substantial higher rates both wells (8166 MCFD for Stevenson 1H and 6212 MCFD for Stevenson 2H). Throughout the study throughout the study, the highest second month average gas rate of production observed either by simultaneous fractured or individually fractured wells was exhibited by these wells. This observation was attributed to be partly as results of their larger than normal proppant volumes and partly reservoir quality ("core area" location).

In the assessing of the keys to a successful completion within the entire dataset of individually fractured and simultaneously fractured wells in the Barnett shale formation, many observations in general was made as follow,

(a) Larger proppant volume per gross fractured feet of lateral appear to be advantageous

(b) Effective horizontal zonal isolation appears to be advantageous in some areas

(c) The nature and degree of fracturing fluid communication with $500 - 1,000$ feet offset wells may be a more positive barometer for well's post-completion performance than is the well's own fracturing fluid flow-back/cleanup

(d) Longer perforated lateral lengths is no guarantee of superior post completion well performance

(e) Transverse near-wellbore fracture initiation is not necessarily critical to post-completion well performance in the "Core Area"; however, in the expansion areas it appears to be a more significant factor.

Babatunde et al. presented a new hydraulic fracturing technique called Channel hydraulic fracturing which was used in the Marcellus shale [78]. The Marcellus shale that is part of the Devonian black shale group extending from New York through Pennsylvania into sections of West Virginia and Ohio is located in Northeastern section of the United States. Conservatively in the Marcellus, shale the gas-in-place is estimated to be 168 trillion cubic feet. The Marcellus shale where hydraulic fracture treatments are required for effective and economic production of natural gas has its permeability values expressed in nanodarcies.

Hydraulic fracture treatment to create a conductive proppant pack for enhanced reservoir fluid flow into the wellbore, consist of pumping large quantities of high viscosity gelled fluids or low viscosity slick-water fluids along with proppants in large quantities. The deliverability of the hydraulic fracture to the wellbore describes the fracture conductivity. The deliverability of the reservoir to the well dominates productivity in ultra-low permeability reservoirs and not necessarily on the conductivity of the fracture. However, to minimize residual damage to the formation and proppant pack, fracture conductivity plays an important role to ensure adequate flow-back of the reservoir fluids.

Channel fracturing is a novel hydraulic fracturing technique in which geomechanical modeling, fiber-laden fluid technology pumped in a unique manner and perforation strategy are integrated for the creation of high conductive channels in the proppant pack to increase several fracture conductivity. Stable channels are being created by the channel fracturing techniques for hydrocarbons to flow through rather than depending on the permeability of the proppant pack. Conductivity is shown to be increased greatly by these open-flow channels. Some of the benefits of these open-flow channels also include the reducing of the pressure drop across the fracture, help improve fluid cleanup and polymer recovery, and increase the effective fracture half-length and stimulated reservoir volume, thus leading to improved production. Channel fracturing which is applied in other low permeability unconventional reservoirs in the United State had shown significant increase in production over the conventional fracturing techniques. In the Eagle Ford shale in Texas, over 1,400 total of successful channel fracturing stage treatment have been pumped in the Bakken

Shale in North Dakota and Montana, the Lance formation in Wyoming and Almond formation in Wyoming.

Two main issues in this study have been investigated,

(1) To determine whether the Marcellus shale gas play properties are geomechanical good enough for the application of the channel fracturing technique.

(2) The possible increase in production in the Marcellus shale well that may be obtained if the benefit of increasing fracture conductivity and effective fracture half-length using channel fracturing technique is considered.

5.10 Description of the Channel Fracturing Technique

Channel fracturing involves the generation of pillars of proppant that allow for high conductivity channels within the proppant pack. As shown is Figure 5.49, the left section of the image represents a proppant pack in a conventional fracture and the right section of the same image represents a proppant pack in a channel fracture.
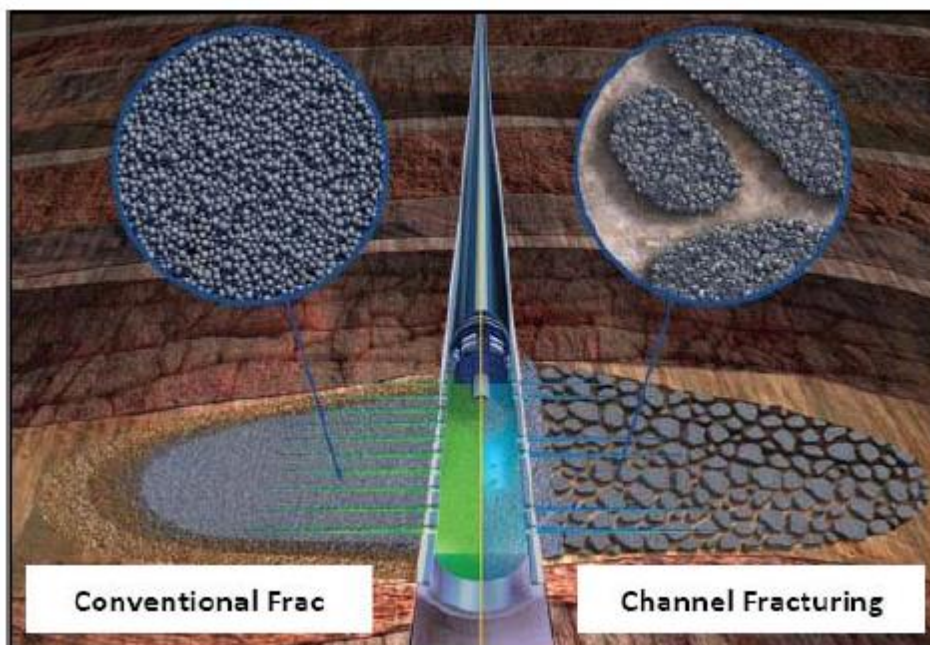
Figure 5.49: Channel fracturing representation [78].

The conventional proppant-filled fracture permeability may be derived from the Darcy's equation while the open fracture channel permeability may be derived from

the Navies-Stroke equation. Comparison of these equations theoretically indicates that, the permeability value of a relatively thin channel may be in the orders of magnitude higher than the permeability in a proppant pack.

5.10.1 Applicability in the Marcellus shale

A unique design and pump schedule involved in the channel fracturing technique along with fiber-laden technology and geomechanical modeling. Below is a review of each applicability criteria with respect to the Marcellus shale.

Well orientation: In the Marcellus shale majority of the producing wells are horizontal wells. Increased in reservoir contact and general delivery of productivity in horizontal wells are better than vertical wells in the same field. In both horizontal and vertical wells, channel fracturing technology is applicable and been proven successful. Most of the stage treatments in channel fracturing executed to date were performed in horizontal wells.

Channel fracturing technique pumping schedule is based on a conventional hydraulic fracture schedule. The ultimate different is that, during treatment the proppant is delivered in short pulses, and separated by pulses of clean fluid. Less proppant is used to generate effective fracture geometry similar to or greater than a conventional fracture, and this is one of the advantages of the technique. In the Marcellus, an already established hydraulic fracture design for a well can be converted to channel fracturing design. Gelled fluid or slick-water can be pumped at the pad stage of the treatment. A fiber-laden is used to pumped proppant laden stage to cross-linked, fluid to ensure the generation of stable proppant pillars. During the proppant pulse, the polymer loading is not likely to affect final fracture performance due to the reservoir fluid flow through the channel created and the channel also allow for improved fracture cleanup. As in conventional fracture, the pumped cross-linked fluid should contain breakers and other additives in addition. The amount of proppant required for the treatment will be reduced substantially in converting slick-water treatment to a channel fracturing treatment.

At the end of the treatment, the tail-in stage, which is a short stage requires continuous addition of proppant to ensure a stable and uniform connection between the wellbore and the channeled fracture. When less proppant is used to convert a conventional fracture schedule to a channel fracture schedule, production is expected to be similar or higher. In the Marcellus shale this advantage is a monumental since

the environmental impacts of transporting materials will be reduced. The logistics involved with well stimulation, will also be reduced as well as the overall footprint of a well completion on a local community.

Perforation scheme: The proppant pulses needs to be separated to enhance the generation of channels and usually it is achieved by the fluid design. If further separation of proppant pulses is required, it can be achieve by a special heterogeneous perforation scheme, which consist of cluster of perforations separated by non-perforated intervals. The current perforation strategy used in horizontal wells in Marcellus is similar the channel fracturing perforation scheme. As compared to the conventional perforation strategy, the channel fracturing perforation strategy is design with more clusters of perforations. The perforation phasing and density as in the conventional design are typically the same and number of perforated holes may be preserved.

5.10.2 Geomechanical property modeling

For the applicability of the channel fracturing technique, the Young's modulus to the closure stress ratio is an important consideration, since pinch points that may affect the fracture conductivity negatively will be caused by a low Young's modulus formation in a high closure stress environment. In a formation where the Young's modulus to closure stress ratio is maintained above 350, the channel fracture is also expected to be maintained. A ratio as low as 200, channel fracturing has been known to be maintained, but this analysis was done using a conservative value of 500.

To determine the applicability of the channel fracturing technique in the Marcellus shale formation, 160 well logs across the Marcellus shale formation was considered. For each well a property model was created with an arithmetic averaging of attributes across zones, as shown in Figure 5.50 is a property modeling for a single attribute.

The Young's modulus, Poisson's ratio and stress, which are geomechanical properties were distributed into 3-dimensional grid. The Young's modulus to the stress ratio was calculated for the lower Marcellus, Cherry Valley, upper Marcellus and the gas bearing formation immediately above the upper Marcellus. From a 3D model, grid maps of the applicability ratio are generated for the different zones under consideration. These maps are shown in Figure 5.51 and Figure 5.52 below.
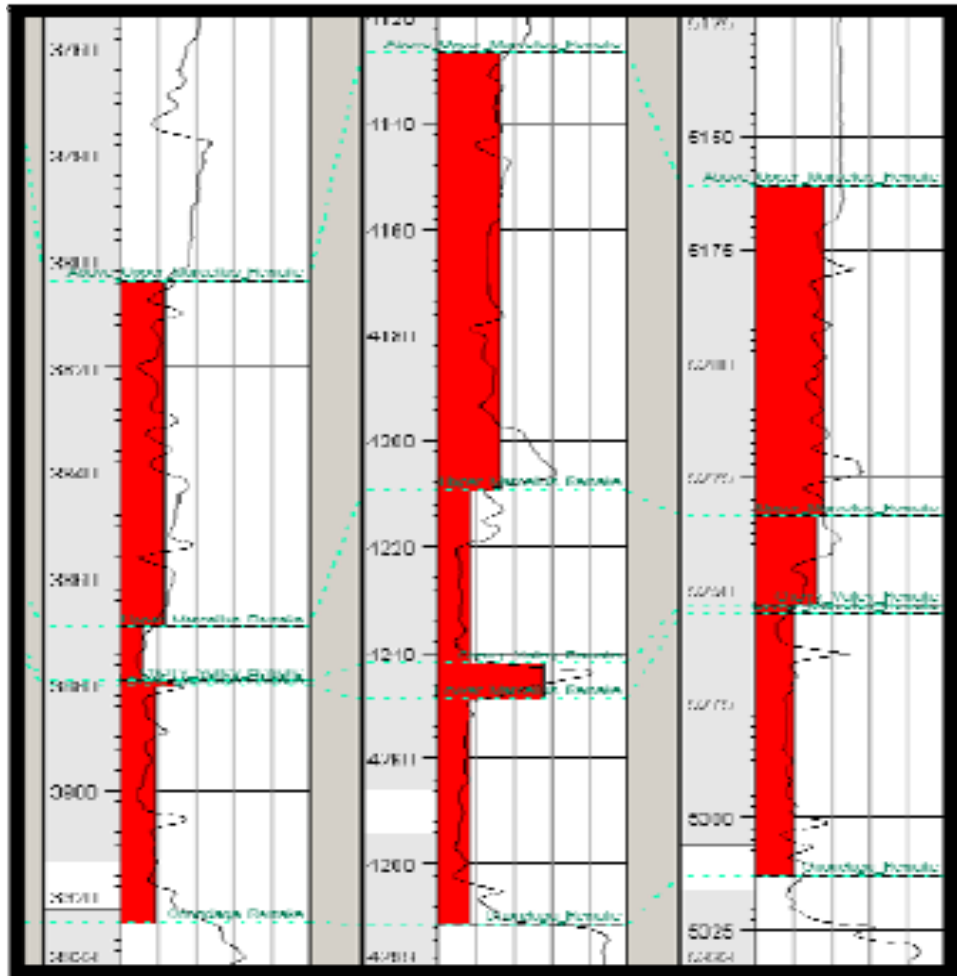
Figure 5.50: An Example of Geomechanical Property Model [78].

On the map the section with the ratio of applicability greater than 500 is rated as good and present are geomechanical properties required for channel fracturing. Regions which are rated nominal has its ratio ranging from 350 to 500 and these regions are expected to support channel fracturing, meanwhile further study on a well to well basis is recommended. Regions where channel fracturing are rated poorly (a ratio of less than 350 regions), channel fracturing should be considered in these areas after careful study and design.

After the analysis of the results, it was observed that the geomechanical properties of Marcellus shale support channel-fracturing technology and the technology is applicable in almost all the Marcellus shale.
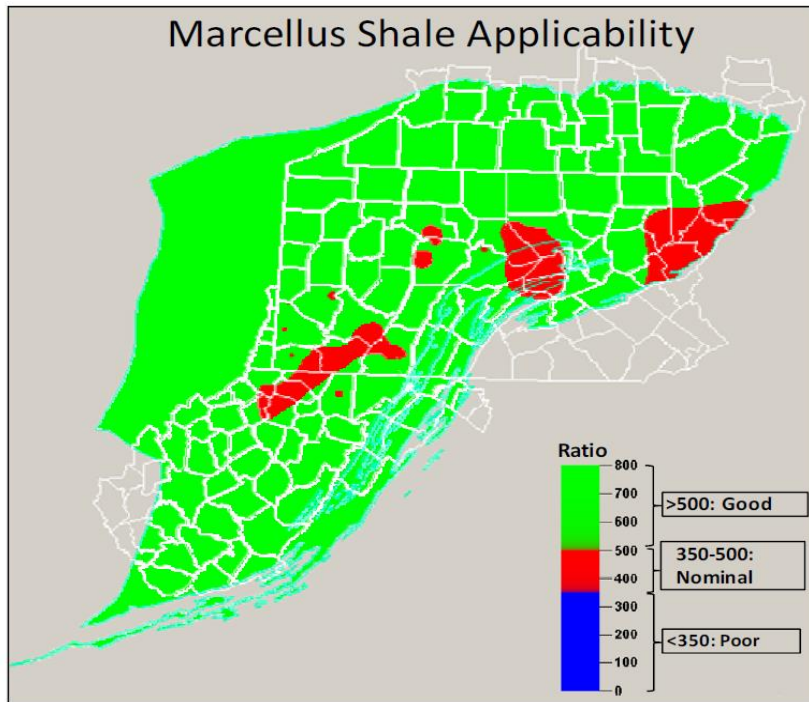
Figure 5.51: Composite Map of Geomechanical Applicability of Channel Fracturing in Marcellus shale [78].
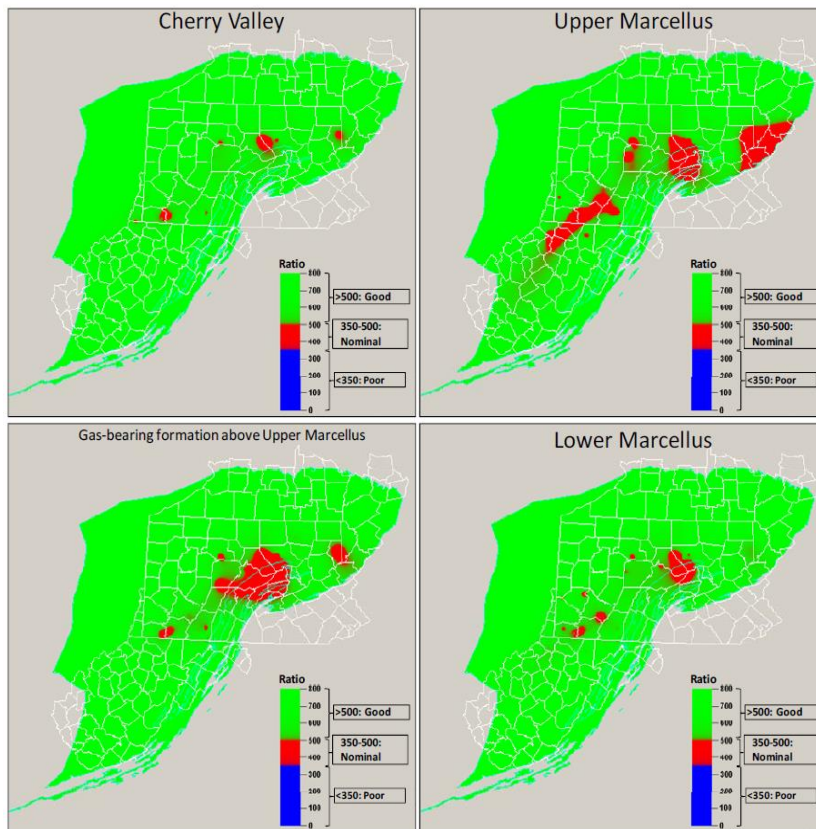
Figure 5.52: Map of Applicability of Channel Fracturing in the Marcellus Formation [78].

5.10.3 Comparative analysis of conventional hydraulic fracturing and channel fracturing

Well A whose horizontal section was placed in the lower Marcellus shale was drilled in the northeastern Pennsylvania, was completed with 14 stimulation stages separated by an isolation plug. About 500,000 pounds of proppant was used in each hydraulic fracture treatment stage. To determine the azimuth and geometry of the fracture and effectiveness of the stimulation, micro-seismic monitoring of the hydraulic fracture was ran. The well was flown back and has been produced for 8 months.

5.10.4 Production history match and analysis

Using a non-linear regression production evaluation and, reservoir simulation software packages production history match was performed on well A. the reservoir and fracture properties of well A is shown in Table 5.15 below. The flow behavior of multiple transverse fractures orthogonal to the wellbore, were predicted by the model matches. The fracture half-length initial estimates were obtained from the micro-seismic data evaluation and a reservoir schematic model shown in Figure 5.53.

Table 5.15: Well A reservoir and fracture properties.

Wellbore Radius (ft)	0.325
Number of Fracturing Stages	14
Shale Thickness (ft)	165
Reservoir Pressure (psi)	4,156
Drainage Area (acres)	200
Porosity (%)	3.3
Temperature (^{o}F)	160

From the tubing pressure, gas and water production rates, the bottom-hole pressure was calculated using Hagedorn and Brown flow correlation in nodal analysis software [79].

The Rate Normalized Index (RNI) plot, also known as the log-log or normalized pressure integral (NPI) plot, was used for the transient rate analysis on the low frequency production history [78]. Also, Poe's method of analysis, which converts the production data into a constant pressure solution using the superposition time for fracture flow regimes, was used for the transient rate analysis on the low frequency production history [80]. Note that the fracture properties can be inferred from the

fracture flow regimes. The fracture properties were calibrated using both of the aforementioned techniques and the micro-seismic interpretation. The resultant match for both the gas rate and the cumulative gas production history for well A are shown in Figure 5.54.
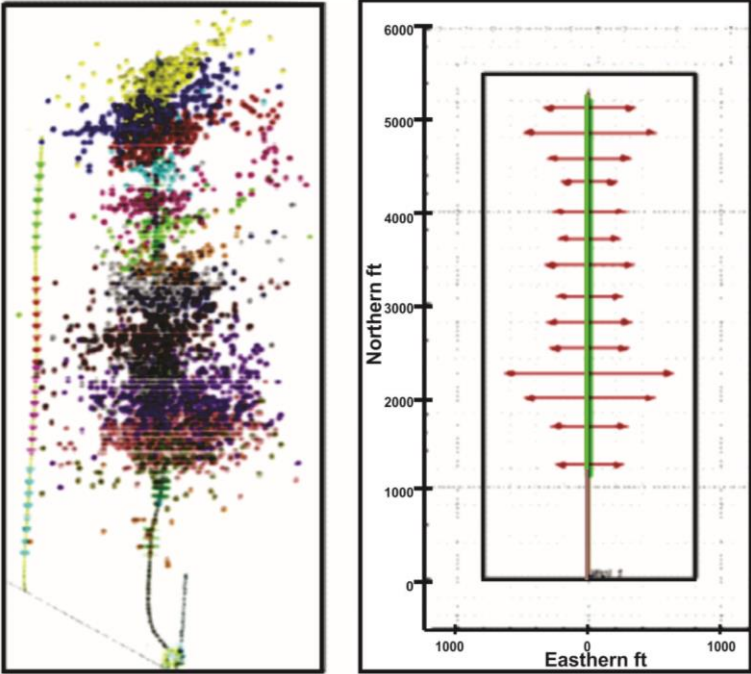
Figure 5.53: Creation of Initial Model from Micro-Seismic Fracture Geometry [78].
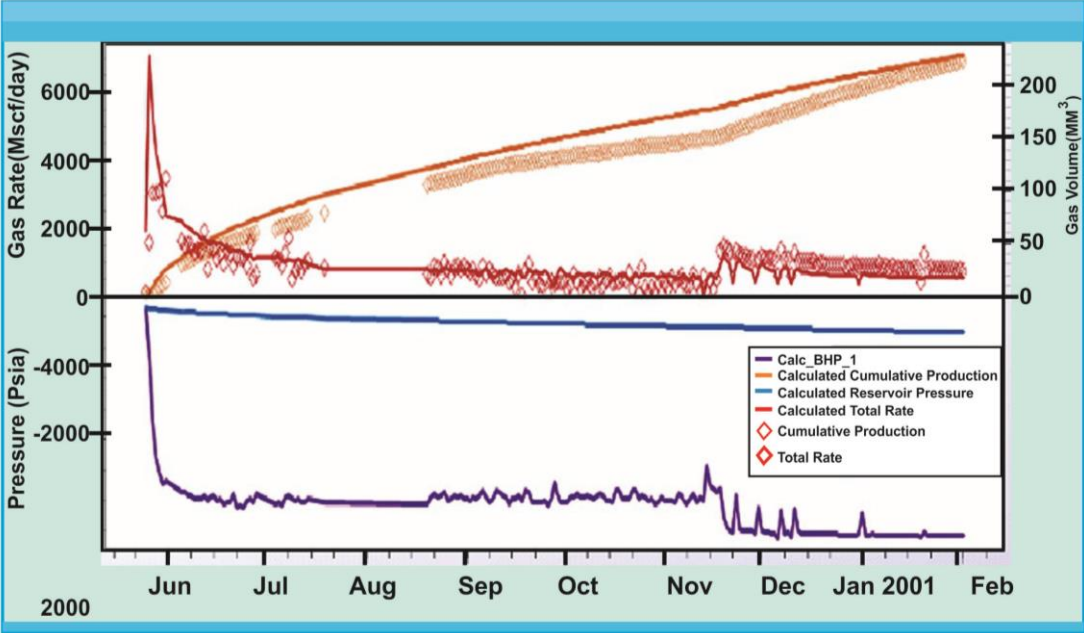
Figure 5.54: Well A Production History Match [78].

5.10.5 Production simulations

The numerous benefits of channel fracturing include enhanced productivity in the wells, creation of longer effective fracture half-length, increased effective stimulated reservoir volume, allow for better fluid cleanup and produces fracture conductivity orders of magnitude higher than conventional fracture conductivity. Well A history match model was used as the base case and the only varied parameters for the sensitivity analysis are fracture conductivity (F_c) and effective fracture half-length (X_f). The channel fracturing conductivity values used as an input in the model were obtained from accounts of channel fracture conductivity in literature. The sensitivity study on well A is summarized in Table 5.16 below.

Table 5.16: Sensitivity study summary on well A [78].

Sensitivity case	First 8-month Cumulative Production (MM scf)	Increase in Cumulative Production (%)
Base case: conventional fracturing, F_c = 1.3 md-ft	229	---
F_c = 20 md-ft	239	4
F_c = 50 md-ft	250	9
F_c = 75 md-ft	251	10
F_c = 1,800 md-ft	251	10
F_c > 75 md-ft, + 15% X_f	287	25
F_c > 75md-ft, + 30% X_f	317	39

Well A fracture conductivity and half-length sensitivity study results are shown in Figure 5.55. It was observed from the results that a 10 percent increase in production over 8-month period was obtained due to the improvement in fracture conductivity in well A. When the transmissibility was beyond 75 md-ft, the cumulative production became insensitive to fracture conductivity. For very low reservoir permeability, the effect of improvement in fracture conductivity on improving the productivity in shale may be the least. Yet, in this simulation model, the improvement in conductivity offers a benefit of 10 percent increase in the initial gas production. If the fracture half-length is improved 30 percent, then, an additional 39 percent increase in productivity could be obtained.
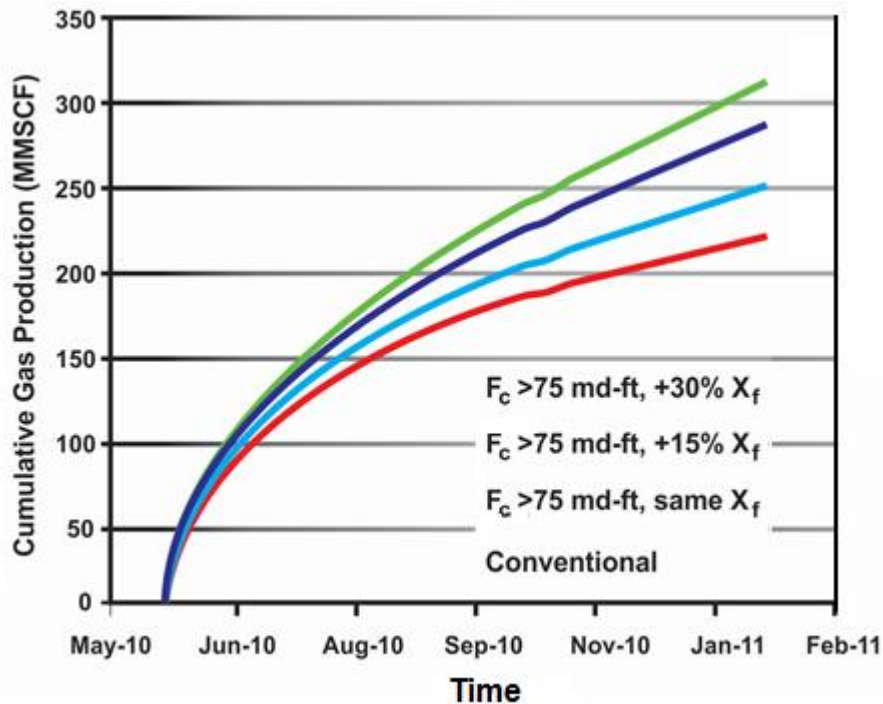
Figure 5.55: Conventional Fracture and Channel Fracture Potential Cumulative Gas Production [reconstructed after 78].

In the Eagle Ford shale gas field, the results from channel fractured wells showed 51% normalized increase over the conventional slick-water treatment results, and concluded that the dominant contribution to performance of channel fracturing in shale is because of an increased effective stimulated volume of the reservoir.

The 10% increase in gas production obtained from conductivity improvement because of channel fracturing treatment in well "A" in comparison can be considered as a lower boundary of productivity improvement. Depending on potential increase in effective half-length, additional increase may be achieved from channel fracturing technique. The relative impact of channel fracturing technique on the characteristics properties of the fracture such as half-length and conductivity can be assess using the simulation results generated by the methodology.

Donald L. Turcotte et al. indicated that natural gas production in the United States of America, reached its peak in production at 22.7 trillion cubic feet (Tcf) in 1973 [81]. Production then declined as gas reservoirs are depleted, for a decade thereafter. In 2005, production of natural gas took off again and risen to 25.3 Tcf in 2012. Gas pricing strongly influenced the rapid increased in the availability of natural gas. The wellhead price was $2.6 per thousand cubic feet on January 1ˢᵗ 2000 and increased to

$8.00 in January 1st 2006. It was down again to $2.89 by January 1st 2012. The impressive increases in gas production and decrease in the price of natural gas over a decade or so are due to a variety of hydraulic fracturing, or fracking, in which low viscosity of water are pumped in large volumes into low permeability shale formations. This type of hydraulic fracturing is call 'Super fracking'. The difference between the super fracking and the established hydraulic fracturing is that, the traditional hydraulic fracturing involve low volume of high viscosity water and the super fracking involves high volume of high viscosity water.

The reduction in the price of natural gas over the past years was due to the replacing natural gas in place of coal in electric generation plants. The emission of carbondioxide was reduced by a factor of two from the power plants.

Some of the environmental concerns associated with high volume fracking are as follows,

1. Super fracking reduces the water volume significantly in some areas for other purposes where large volume of water is needed.

2. As the injected water returned to the wellhead, and it is adulterated by additives and natural contaminations from the rocks, such as radiogenic isotopes. The disposal of such wastewater creates a number of environmental concerns such as leakage and induced seismicity.

3. Leakage of methane gas into the atmosphere as wells in the Dakota's Bakken shale produces gas in addition to oil. In addition, flaring which is practice in this site is undesirable in terms of air pollution.

4. Leakage of methane gas or other fluids into shallow aquifers appears to be associated with the well casing itself or with cementing of well casing to the rock. Due the fact that the high volume fracking injections occurs generally at depths of few kilometers below underground water aquifers which are not deeper than 300 meters, leaks of fracking fluid from shale into ground water are unlikely. Fracking fluids flow backwaters and drilling mud however, spilled on the ground occasionally.

5. High volume fracking trigger earthquakes. As numerous small earthquakes are generated by high volume fracking, the possibility of large earthquakes cannot be ruled out. The largest earthquake attributed to high volume

fracking however had a magnitude of 3.6, which is too small to do surface damage.

Some larger earthquake including a magnitude of 5.7 quake that struck Oklahoma in 2011, have been attributed to waste water injection.

The super fracking used for gas is as well used for oil productionand is relatively a newcomer. The super fracking arrived on the scene about 30 years ago and became economically viable around 1997, with profound consequences as shown in the natural gas number cited above. We will have some few words to say about the traditional fracturing although our focus will be on high volume variant. But we will first examine the shale that house oil and gas.

5.11 Fossil Fuels' Underground Home

Shales are a rock equivalent of mud, as sandstone are rock equivalent of sand. Shale can extend horizontally for more than a thousand kilometers and have porosity of 2 to 20%. Black shales are known to be the main source of hydrocarbon because of their color and organic content. The pores of black shales are filled with 2 to 18% by weight of carbon in organic compounds. In shales, the representative grain is less than 4μm wide and as a result, surface tension forces due to those fine grains strongly restrict fluid flow. Large volumes of organic matter deposited in muds beneath the sea form the black shale. The deposition and and subsequent burial must occur under anoxic conditions if the organic carbon is to be preserve, and this is the reason why 90% of World's oil originated in well-defined periods encompassing 200 million years out of the past 545 million years. The black is the currently is the largest known region forming organic rich clays as future black shales.

The thermal gradient of the environments in which sediments are deposited is about 30^oC/Km. Time and heat produce oil from the organic material at sufficient depth. The oil produced is located in a window 2 to 4 Km below the surface where temperatures ranges from 60^oC to about 120^oC. The oil breaks down, at depths of about 3 to 6 Km and associated higher temperatures of about 90 to 180^oC to produce gas. The deposition and burial of the organics must occur in an environment with restricted water circulation (anoxic conditions), otherwise the carbon in the sediment will be oxidize by water. The fine grain that form shale enforce that restriction via surface tension.

In the black shales, oil and gas formation increases fluid pressure; the resulting hydraulic forces yield a network of fractures. The pore pressure must be about 85% of the pressure generated by the weight of overlying rock for that natural fracking to comeabout. Tectonic activity and the structure and mineralogy of shale are the factors responsible for natural fractures and their orientations.

The granular permeability is surficient to permit oil and gas to flow to the closely space fracture that provide pathways for vertical migration although the the granular permeability of shales is low. One consequence of natural fracking is a pervasive set of fracture. Fluid pressure is reduce by the upward movement and takes the fossil fuel from their source in the black shale to reservoirs that can be exploited for production or to the surface as gas seeps.

The results of natural fracking can be seen in the Monterey shale in California, the source rock for major oil field in Los Angeles, Ventura, Santa Maria, and San Joaquin sedimentary basin [82]. One of the largest hydrocarbon seepage areas in the World is the Northern Santa BarbaraChannel, separating the Santa BarbaraCoast from California's Channel Island [83]. In the Monterey shale, oil and gas leak upward through natural fractures and tectonic faults. About 15 Km west of Santa Barbara at the Coal Oil Point seep field is the most intense area of natural seepage, where the resulting oil slicks can be as much as 10 Km long, in the region existence of beach tars was recorded by the earliest Spanish settlers and English explorers centuries ago. Natural fracturing in some cases has enable the extraction of fossil fuels from tight shale reservoirs. Natural fracture and faults more often allow the migration of oil and gas to high porosity reservoirs. The oil and gas once trap there can be extracted with traditional production wells. The oil and gas fraction that is recovered from the production reservoir however is low, typically 20 to 30 %. Several methods had been employed by energy producers to enhance recovery. Flooding the production reservoir is one of the process: Water or another fluid injected in the injection well, drives the oil and gas into the production wells. The second process is then hydraulic fracturing. Hydraulic fracturing technique involves the high pressure injection of water so as to create fractures in the production reservoir to enhance migration to the production well. The traditional low volume fracking enhances production from high permeability reservoirs. But for tght shales

reservoirs, high volume super fracking is the method of choice for extracting oil and gas.

About 75 – 1000 m^3 of water whose viscosity has been increased by the addition of guar gum or hydroxyethyl cellulose is required for traditional fracking. To create a single large fracture or a few fractures through which oil or gas can flow to the production well. The fractures are keep open with help of a large volume of sand or "proppant". Traditional fracking is now applied routinely by energy producers to granular reservoirs such as sandstone that have permeabilities of 0.001 – 0.1 Darcy. (Darcy is a measure of fluid flux corrected for the viscosity of the fluid and the pressure gradient driving the flow). Carl Montgometry and Michael Smith estimated that, some 80% of the producing wells in the USA have been treated with traditional fracking [84].

The rock natural permeability allows oil and gas to migrate to the single open frature and then make their way to the production well. Traditional fracking however, does not successfully increase oil and gas production from tight shales reservoirs in which few fractures exist or in which the natural fractures had over time been sealed by deposition of silica or carbonates.

The granular permeability in tight shale formations is between 10^{-9} Darcy and 10^{-7} Darcy, a good six orders of magnitude or so lower than usual for sandstone reservoir. Super fracking was developed with its large volume of water and high flow rates to extract oil and gas from them. The viscosity of the water is decrease by additives usually polyacrylamides; the treated fluid is generally called slick water. The volume of water used in sper fracking is 100 times more than the volume of water used in traditional fracking. To create many fractures relatively close together (so called distributed damage) is the objective of high volume fracking [85]. Those fractures allow oil and gas to flow out of the rock and to the production well. Most of those fractures are reactivated natural fractures that had been sealed previously.

High volume fracking involves drilling the production well vertically until it reaches the target depth which includes the production reservoir. Then directional drilling extends the well horizontally into the target stratum, typically for a distance of 1-2 Km. A section of the well is block off using packers and well explosives used perforate the well casing. Reservoirs that are 3 – 5 Km deep is a desirable target to

ensure that the overlying material can generate enough pressure to drive out the oil and gas.

The injected slick water at high pressure through the blocked off, perforated well, creates distributed hydrofractures. The fluid pressure drops at the end of the fracking injection and fraction of the injected fluid flows back out of the well. Productions then begins.

High volume fracking in our view is only successful in the absence of significant preexisting fractures permeability. This is because, significant fracture permeability would provide pathways along which the injected fluid can flow. The pressure therefore will be too low creates distributed new fractures.

Small earthquakes: A distribution of microseismic event that documents the complex fracture network generated by the fracking is created by high volume fracking. About 10% of production wells nowadays are accompanied by one or more vertical monitoring wells that have seismometersdistributed along their lenths. Microseismic events can be located by seismometers in real time and the data they provide can help minimize injection rates.

From the Barnett shale in Texas as shown in Figure 5.56 [86], relatively narrow cluster of seismicity is produced by the first two of the four injections, whereas the third and fourth injection produced much more broader cluster that indicate a less localized fracture network. A possible explanation for the differences focuses on the role of preexisting natural fractures: injections into the closely spaced natural fractures may lead to the narrow cluster of the fractures, whereas the broad cluster may reflect an extensive new fracturing network needed to access natural fractures.

The microearthquakes accompanying super fracking would register in the -3 to -2 range on the Gutenberg-Richter scale, too small to be felt at the surface. However the magnitude of distribution of the microearthquakes satisfies the same scaling at tectonic earthquakes.

The Barnett shale was formed during the Lower Carboniferous period about 323 million to 340 million years ago. The shale is located in the Fort Worth basin of Texas. The concentration of the organic carbon in the productive Barnett shale ranges from less than 0.5% by weight to more than 6% with an average of 4.5%. The depth of production ranges from 1.5 Km to 2.5 Km. The maximum thickness of the

gas production stratum is about 300 m, relatively flat and has only slight tectonic deformation.
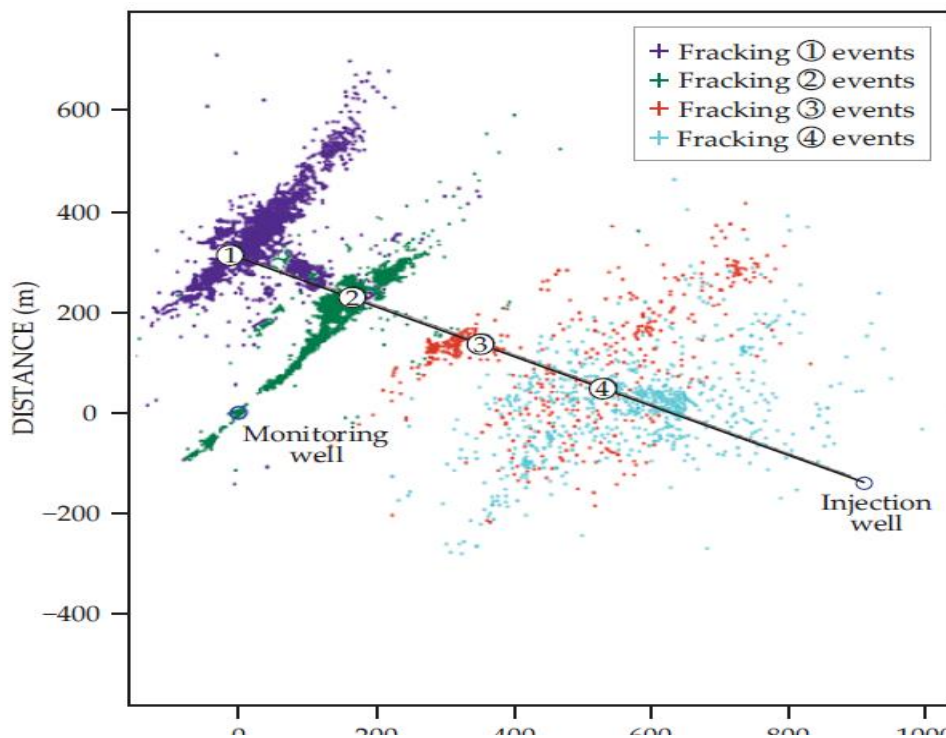
Figure 5.56: Small earthquakes related to four high volume fracking of the Barnett shales in Texas [86].

In the barnett shale, most natural hydraulic fractures have been completely sealed by carbonate depostion [87]. Between the carbonate and shale, the bonding is weak, hence a high volume fracking injection can open the sealed fratures with relatively ease [88]. The injected slick water leaks through natural fracture without producing further damage but Donald L. Turcotte et al. Suggest that once the frature is opened, the natural fractures prevent subsequent high volume fracking injections from creating distributed fractures.

The Barnett shale was the largest producer of tight shale gas in the US until being overtaken by the Marcellus shale in the Appalachian basin. The Barnett shale annual production of 0.5 Tcf of gas is an appreciable fraction of the total national annual production of about 25 Tcf. The US Department of Energy in 2011 estimated the accessible gas reserves in the Barnett shale to be 43 Tcf [89].

The Bakken shale which is located in the Williston (also called the Western Canada) basin is black shale. It was formed during the Late Devonian Lower Mississippian

period about 340 million years to 385 million years ago. The Bakken shale unlike the Barneet shale, has yielded large amount of oil. Most of the oil comes from North Dakota, which apart from Texas, produce more oil than any State.

The Bakken has little tectonic deformation and mostly horizontal. It consist of two black shale layers seperated by a layer of dolomite (calcium magnesium carbornate) and is the first formation in which high volume fracking is demonstrated successfully at effectively extracting oil from the a tight shale. It is clear that high volume fracking is essential for significant oil production at Bakken but the relative contribution of the black shale layer and the dolomite layer to production are not clear. Typically, the shale has 5% porosity but the bulk permeability is very low, typically 4×10^{-9} Darcy. Most of the natural fractures are tightly sealed and this allow super fracking to create distributed frctures through which oil can flow to production wells. In the Bakken shale formation, the producing formation is 1.5 Km to 2.5 Km deep and a thickness of 40 m.

In the Bakken shale formation, about 6,000 producing wells were operated in July 2013 and were primarily horizontal. These wells contributed to an annual oil production rate of 300 million barrels (Mbbl), or 4.8×10^7 m^3. From Department of Energy, the oil reserves estimates in the Bakken shale are 3.6 billion barrels (Bbbl) [89], again half as much the total US production of 2.37 Bbbl for the year 2012.

The long time viability of high volume fracking is affected by several technical concerns in addition to the environmental issues spelled out above. These technical concerns are; the efficiency of recovery, the high volume fracking of tight shale reestablsihes the natural fracture permeability and also produces new fractures, can super fracking be modified so that it become effective in extracting oil and gas from black shale reservoirs such as the Monterey shale, that have open natural fractures. The type of analysis employed in this studies is called invasion percolation from a point source [90] wich is a graph-theory type analysis.

Since shale plays are similar to other coal bed methane or tight sand play; each reservoir [91] Presents the practical use of shale petro-physics for simulation design optimization and the objective of the paper is to investigate uniqueness of each shale play, explained that the journey of selecting completion type should begin in the

laboratory for an emerging is unique and the completion and stimulation method should be determined based on its individual petro-physical properties.

To understand how the shale reservoir should be completed, understanding of the mechanical rock properties and mineralogy will help significantly. Some critical information needed to find productive shale reservoirs are actual measurement of absorption-desorption isotherm, kerogen type and volume. Significant correlation with the availability of this type of data, can be drawn by integrating the wire-line log data as a tool to the geochemical analysis. Hence, once the wire-line log analysis is calibrated with core data, it becomes a very useful tool in extending the reservoir understanding and stimulation design as one moves from the wellbore where actual lab data was measured.

Some statistical significant correlations between the wire-line log analysis and measured mineralogy, acid solubility and capillary suction time results for shale reservoirs, were revealed in a recent study conducted to review a laboratory database representing principal shale mineralogy and wireline log data from many of the major shale plays. From mineralogy, a method was derived to calculate the mechanical properties of the rock from mineralogy. For shale reservoirs, understanding of the mineralogy and fluid sensitivity is important in optimizing the completion and stimulation treatment for the unique properties of each shale play.

Petro-physical models driven by wireline log that are common in the industry to classify the shale by lithofacies, brittleness and emulate the laboratory measurement of acid solubility and capillary suction time test are the results of this study.

5.12 Information Necessary for Successful Hydraulic Fracturing of Shale Formation

Before a stimulation treatment is designed for a shale reservoir, the list of items that need to be known are presented in Table 5.17 below. These list are common for conventional as well as for shale reservoirs.

Through a calibrated petro-physical analysis, majority of geomechanical consideration can be answered [92]. Using a series of laboratory measurements, most of the geochemical considerations can be addressed. The possibilities of success in placing the treatment and identifying the issues that arise along the way, can be

increase greatly by addressing these considerations. Neglecting these issues is referred to relying strictly on "tribal" knowledge, or trial and error. Combining the two can help obtain the best of both worlds.

The basic assumption for this study is that, the shale in question meets some basic screening criteria as a potential target. For a potential organic and silica-rich shale, the target would be have a cumulative total organic content (TOC-FT) > 30, gas content of 40scf/ton and a thickness greater than 30 feet [93]. But this criteria is not the primary objective of this work.

Using some common laboratory measurements, the geochemical considerations can be determined. In Table 5.17, the test mentioned for geochemical considerations are acid solubility test (AST), capillary suction time test (CST), X-Ray diffraction (XRD), or chemo stratigraphy, a laser induced breakdown spectral (LIBS), and hardness number (BHN). To determine the optimal amount of salt need to minimize the effects of the frac fluid on the clay mineral, more specialized test such as the clay glycolation test, methylene blue test, specific surface area, and ensiling test which can accurately predict shale swelling and dispersion so that the fracturing fluid will be optimal for that specific formation, can be run. The subject of this paper is the practical use of these test results and not the specific details of each test.

A universal petro-physical model that does not need any external calibration would be ideal. To help ensure accuracy in the estimation of mechanical rock properties, Young's Modulus and Poisson's Ratio, mineralogy and TOC, any petro-physical model will need laboratory measurement. Only the relationship used to derive brittleness, acid solubility and closure stress will be discussed because the petro-physical model is not the main topic of this study.

The concept of the brittleness of the rock combines both Poisson's Ratio and Young's Modulus. The ability of the rock to fail under stress (Poisson's Ratio) and maintain the fracture (Young's Modulus) once the rock fractures are determined by the combination of these two components. Ductile shale makes a good seal, trapping the hydrocarbons from migrating out of the more brittle shale below. Ductile shale however is not a good reservoir because the formation will want to heal any natural or hydraulic fractures. Brittle shale is likely to be naturally fractured and also will be more likely to respond well to hydraulic fracturing treatment.

Table 5.17: Information necessary for stimulation treatment design [81].

Geomechanical Considerations	Important For	Determined By
How brittle is the shale?	Fluid type selection	Petro-physical model
What is the closure pressure?	Proppant type selection	Petro-physical model
What proppant size and volume?	Avoid screen outs	Petro-physical model/tribal knowledge
Where the fracture should be initiated?	Avoid screen outs	Petro-physical model/tribal knowledge
Geochemical Considerations	Important For	Determined By
What is the mineralogy?	Fluid selection	XRD/LIBS/ petro-physical model
Fluid water sensitivity?	Base fluid salinity	CST/BHN/Immersion test
Can acid be used if necessary?	Initial issues--- etching	AST
Does proppant or shale flow back?	Production issues	Tribal knowledge
Are surfactant beneficial?	Conductivity endurance	Flow test/tribal knowledge

There is the need to quantify the brittleness factor in a way that will combines both rock mechanical properties in shale. Unlike this method, other mineralogy based methods of determining brittleness are mainly based on core measurements [94]. The advantage of using the petro-physical interpretation is that, it is much more common to have a log across the zones of interest that covers the shale as well as the bounding rock layer, than it is to have core data covering the entire interval that will be hydraulically fractured when the core method is used. The graphical representation of this concept is shown in Figure 5.57. For Poisson's Ratio, the lower the value, the more brittle the rock and for the Young's Modulus, as the Young's Modulus increase, the more brittle the rock will be. The brittleness caused by each component is utilized and then averaged to give the brittleness coefficient as a percentage. This is because, the units of Poisson's Ratio and Young's Modulus are very different.

Form Figure 5.57, the ductile shale points will fall to the northeast quadrant, and the more brittle shale to the southwest quadrant. A good fracture barrier as well as a

good seal for the reservoir is provided by the ductile shale. The brittleness from Poisson's Ratio and Young's Modulus can be calculated using the following equations,

$$YM\_BRITT = ((YMS\_C - 1)/ (8 - 1))* 100 \qquad (5.17)$$

$$PR\_BRITT = ((PR\_C - 0.4)/ (0.15 - 0.4))* 100 \qquad (5.18)$$

$$BRITT = (YM\_BRITT + PR\_BRITT)/ 2 \qquad (5.19)$$

In this model, the static Young's Modulus and Poisson's Ratio used are derived using the process described in Mullen et al. (2007) [92].
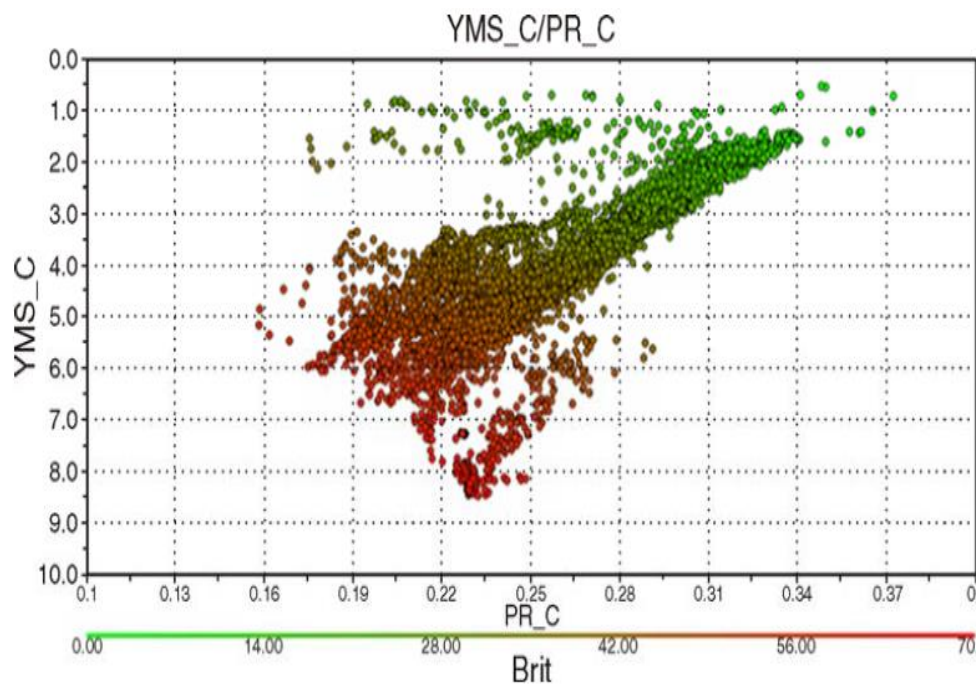
Figure 5.57: A cross plot of Young's Modulus and Poisson's Ratio [92].

The brittleness of the curve can be interpreted in two ways. The first is to distinguish between the ductile and the brittle shale. It is usually done as color shading on the petro-physical analysis (Figure 5.58). The second is to overlay the closure stress gradient to look for hydraulic fracture barriers. The ductile shale can be distinguish from the brittle shale by selecting a brittleness cutoff value as the brittleness value in clay-rich shale. The higher the brittleness value above the cutoff value, the more likely the shale will be brittle. This means natural fractures may be present and the shale should respond well to hydraulic stimulation.
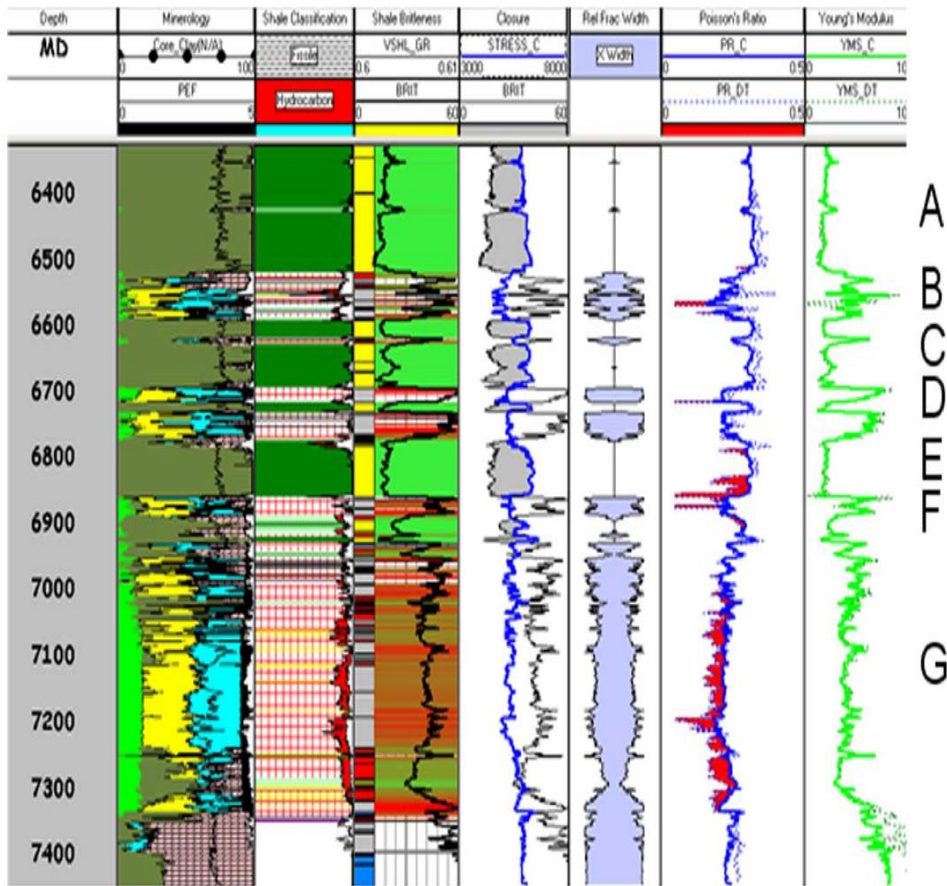
Figure 5.58: The geomechanical portion of the petro-physical analysis [92].

In this model, the "closure stress determination" used is modeled after Barree [95]. The simplified form of this model is shown below.

$$\sigma_{cls} = \frac{v_c}{(1-v_c)\left(p_{ob}-C_B\,p_p\right)} + p_p + \varepsilon\,E_c \qquad (5.20)$$

where,

σ_{cls} : closure stress, psi

v : composite determination of Poisson's Ratio

p_{ob} : overburden pressure, psi

C_B : vertical Biotas coefficient

P_p : pore pressure, psi

ε : strain coefficient

E_c : composite determination of Young's Modulus

176

5.12.1 Fracture width determination

The hydraulic fracture width can be calculated with a reasonable estimation of the mechanical rock properties. In determining the proppant sieve-size, this calculation is very important. The fracture width calculation as described in the equation below, is a function of the fluid pump rate, fluid viscosity, fracture half length and shear modulus of the formation.

$$G = \frac{E_c}{3 \, (1 - 2 \, \nu_c) \, 10^6} \tag{5.21}$$

$$X_w = 3 \left[\frac{q \, \mu \, (1 - \nu_c) \, X_f}{G} \right]^{0.25} \left(\frac{3.414}{4} \, B \right) \tag{5.22}$$

where,

G : shear modulus, psi

ν : composite determination of Poisson's Ratio

E_c : composite determination of Young's Modulus

X_w : fracture width, ft

X_f : designed fracture half length, ft

q : anticipated stimulation treatment pump rate, bbls/min

μ : fracturing fluid viscosity, cp

B : the degree of brittleness

5.12.2 The practical use of petro-physical analysis

Considering the brittleness, closure stress and fracture width calculated from the petro-physical model in Figure 5.58 and Table 5.18, the practical considerations will help determine the frac fluid type, the fracture height for volume considerations and proppant size and type that should be used.

The proppant to be used is considered first. The recommended proppant type as a function of closure stress is represented in Figure 5.59 below. The permeability of pack is reduced because of proppant crushing as the stress is applied to the proppant. Generally, the proppant size is selected by the minimum fracture width generated by the frac-fluid viscosity and pump rate (see Figure 5.60). In Table 5.19, using the

brittleness computation as a general guideline to fluid type selection is demonstrated. The fracture geometry becomes more complex as the brittleness increases. The proppant may act more as a wedge in high brittleness shale, providing a high conductivity flow path for hydrocarbons to migrate to the wellbore. The fracture becomes more like conventional bi-wing fracture geometry as the shale becomes more ductile (lower values of brittleness).

The difference between the composite determined and calculated Poisson's Ratios is the gas effect that is observed only from the dipole sonic measurements.

Table 5.18: Analysis and recommendations for stimulation design based on data shown in Figure 5.58 [81].

Zone	Brittleness (%)	Thickness (ft)	Closure Stress, (psi)	Frac. Barrier, (Y/N)	Frac. width @ 100 bbl/min	Recommendations			
						Fluid type	Proppant size	Proppant type	Frac?
A	15.3	400	6,134	Y	0	-	-	-	N
B	56	82	4,650	N	0.038	Slick water	30/50	Sand	Y
C	18	103	6,261	Y	0	-	-	-	N
D	59	91	5,150	N	0.038	Slick water	30/50	Sand	Y
E	18	85	6,350	Y	0	-	-	-	N
F	22	40	6,040	Y	0	-	-	-	N
G	45	350	5,600	N	0.038	Slick water	30/50	Sand	Y

Figure 5.59 illustrates the recommendations of proppant type based on closure stress the proppant will be subjected to during the life of the well. In stimulation design, the next step is looking at the laboratory measurements on core samples. Here, the objective is to provide a mineral composition of the shale, acid solubility and an idea of the fluid sensitivity of the shale. If the shale shows a high degree of fluid sensitivity, more advance testing is recommended to help find the optimal base fluid salinity to minimize any damage that might occur due to incompatible fluid system. To calibrate the mineral composition in the petro-physical model, the mineral composition determined by XRD is used. Incorporating this data into the petro-physical model is a way of extending the core data to the entire formation since it is not practical to measure a sample every half-foot of shale.
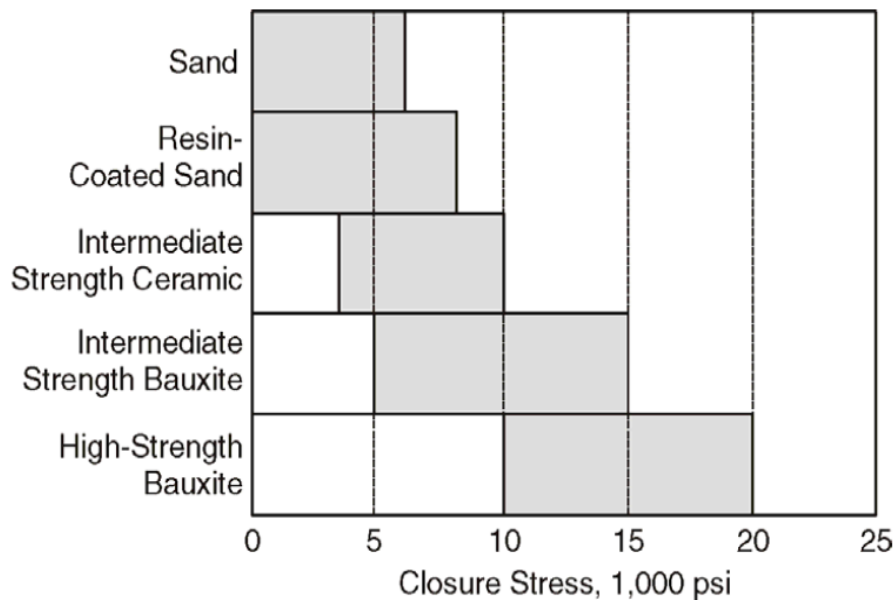
Figure 5.59: Recommendations of proppant type based on closure stress [81].
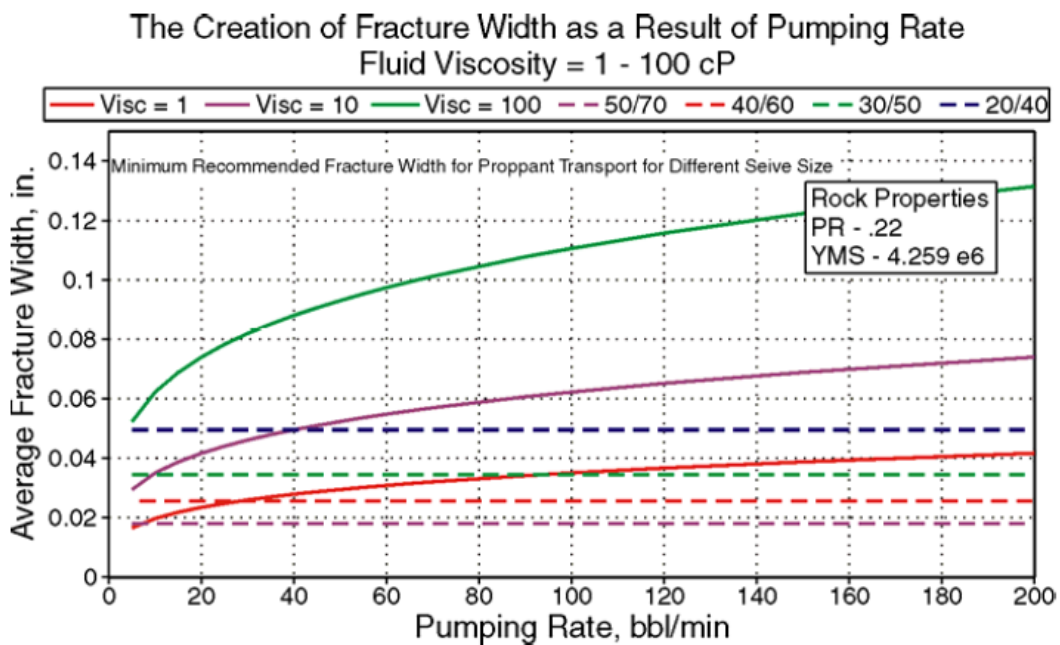
Figure 5.60: Proppant size selection based upon the minimum recommended

fracture width for common proppant sizes [81].

Table 5.19: Fluid system recommendations based on the brittleness calculation [81].

Brittleness	Fluid System	Fracture Geometry	Fracture Width Closure Profile	Proppant Concentration	Fluid Volume	Proppant Volume
70%	Slick Water			Low	High	Low
60%	Slick Water					
50%	Hybrid					
40%	Linear					
30%	Foam					
20%	X-Linked					
10%	X-Linked			High	Low	High

5.12.3 X-Ray diffraction/chemostratigraphy- a laser –induced breakdown spectral

Mineral components must be known in order to adequately characterize the shale. The XRD/LIBS (X-Ray diffraction/chemostratigraphy- a laser –induced breakdown spectral) analysis was grouped into three categories for this study: quartz, carbonates and clay. The quartz group included quartz, feldspars and pyrites. The carbonate group included calcite, dolomite and siderite. The clay group included the total clay.

In the database, the volume of mixed layer clay was also recorded, and was used for comparing with CST data and the total non soluble minerals like pyrite, siderite, kaolinite and chlorite. For the possibility of creating movable fines, this summation was used in conjunction with the AST as a test, should acid be used in the stimulation treatment. In this study, a ternary diagram was used to display the mineral makeup of each shale investigated.

The objective of this study was to be more of a practical guide in comparing shale reservoirs but this was rather simplistic view of the full power for XRD or LIBS analysis. Using the XRD mineralogy, the determination of brittleness is based on a modified technique developed [95]. Based on the mineral percentages of quartz, carbonate and clay, Young's Modulus and Poisson's Ratio are measured using this technique. The results are then used as inputs to equations 5.17-5.21

Acid solubility testing (AST) measures the volume of a rock sample dissolved when immersed in acid. Since there is the likelihood of significant generation of fine grains that will lead to plugging of the proppant pack and damage around the perforations, low to moderate acid solubility can be used as flag.

Acid is frequently used as a breakdown fluid or used to reduce near-wellbore friction in most shales during fracturing operations. It is recommended to use a blend of

weak acid and surfactants if acid is needed, to etch low AST shale. Without releasing non soluble mineral in the shale, a blend of weak acids and surfactants gives a benefits of roughing the surface of the fracture plane contacting more surface area. To reduce high treating pressure at low pumping rates, the reactive fluids are usually used in shale to help the fluid find its way into the fracture network in the formation.

In petroleum industry, shale and clay stability has been an ongoing problem for both the service sector and operating companies. The method of capillary suction time test (CST) is simple and easy to use and is applied as a reliable but rapid method for screening large numbers of formation samples including cuttings, pieces of full core, ends of core plug and rotary sidewall coring tools (RSCT) samples.

Operators use the CST method on the drilling site to conduct the test at rig-site while drilling. Because of sample preparation variation however, the test should only be used as qualitatively as "yes" or "no" indicator of clay swelling and dispersion related cat ion exchange. Samples are normally sent to a laboratory in fracturing applications rather than evaluated at rig-site, though it is common for confirmation testing to be needed quickly. In this case CST can be used to its greatest benefit. Comparison is made typically with a given by comparing CST time of deionized (DI) water and a fixed concentration of KCl (that is 3%).

It can be quickly concluded if the difference is significant, that minimum swelling and dispersion potential exist, and if needed at all, the KCl required is minimum. Conversely, when running XRD, the presence absent of swelling potential is quickly confirm by running CST when mixed layer, illite/smectite clays are identified. Before fracturing operations, a composite sample can often be used in the CST test as low-cost rapid-turnaround indication or confirmation test.

Sufficient sample distribution and density is required when translating to a fluid recommendation, to represent the rock package contacted by the fracturing fluid. In the gas shale and tight gas formations, less KCl is usually the rule. Indications of the effects of fluid on the softening of the fracture face is provided by Brinell hardness number (BHN) test. The fracture face softening effect can be reduce by optimizing salinity.

The fingerprint of the barnett shale: Four Barnett shale wells were considered in the study. In its mineral composition, the Barnett shale itself is not consistent. Four distinct lithotypes are suggested by this data:

Lithotye 1: Quartz-clay and no carbonate, Well 2.

Lithotype 2: Carbonate dominate with smaller portions of quartz and clay, Well 3.

Lithotype 3: Quartz dominate with smaller portions of carbonate and clay, Well 4.

Lithotype 4: Quartz-clay dominate with varying amount of carbonate, Well 5.

Dan Buller et al. presented a comprehensive approach to the evaluation of an unconventional resource play drilled in the Haynesville shale in east Texas, conducted a research on factors that could possibly enhance hydraulic stimulation in horizontal shale gas well, with much emphasis on petrophysical evaluation [96]. They proposed that, for shale reservoirs, economic recovery in horizontal wells requires optimum multistage hydraulic stimulation. In shale gas evaluations, important parameters to consider include gas-filled porosity and total organic content (TOC). Also, some of the mechanical rock properties required to target and design individual horizontal fracture stages in the best zones are brittleness index along with mineralogy. Careful correlation and calibration to petrophysical measurements obtained in either vertical pilot holes or direct offset well, is required in this type of formation evaluation.

Conventional core analysis and a chemostratigraphy analysis of drill cutting, free gas, effective porosity, a shale analysis linking mineralogy, a shale brittleness index, and a clay linked transverse anisotropy using open hole and logging while drilling (LWD) logs, is verified on separate vertical and horizontal control wells. Pulsed neutron spectroscopy logs were also run to develop a cased-hole evaluation solution from neutral network (N-N) modeling that could replicate open-hole wire-line or LWD logs and chemostratigraphy mineralogy results.

In north Louisiana, the Haynesville shale is black, organic rich shale that covers Caddo, De Sato, Red River, and Bienville parishes. In east of Texas, it covers primarily Harrison, Panola, Shelby, and San Augustine counties. In the northeast part of the play, the depth ranges from approximately 10,300 ft and in the southeast, the depth ranges approximately 14,000 ft. The Haynesville shale lies below the Bossier shale; the Haynesville lime or Smackover lime lie below the Haynesville shale

throughout the area. Both of these formations can a targeted for drilling but the Haynesville shale is of special interest because of thicker net pay and a higher reservoir pressure with a gradient between 0.85 and 0.90 psi/ft. Due to varying depositional environment, the shale thickness varies between 80 and 350 ft, and the facies also varies between calcite-rich shale with little clay to calcite-rich shale with large amount of bedded clay and lesser amount of calcite [97].

Abundance of reservoir information can be provided by advanced evaluation suites. Resource identification and a calculation of original gas in place is the primary purpose. New formation analysis and presentation techniques however, are required for a comprehensive mechanical description of this shale to select an optimum horizontal target [91], [98]. The same type of formation subsequently can be used to select and design optimum fractures stages along the horizontal well. Few operators are currently beginning to log their horizontal wells, but to strategically plan or locate the horizontal fractures, they are not using any log data.

The completion practice used currently is still evolutionary as more fracture stages per lateral have yield better results as more surface area is contacted. Depending on the location or on the operator, perforation clusters and spacing per fracture stage have been increased or decreased. Depending on the job design, the fracture treatment pressure and rates which also indicate serious stratigraphic formation differences must be accounted for. There are significant geologic differences to be recognized along the horizontal wells and this assertion is supported by the post-fracture production data. If we better understand the rock that is actually being stimulated per individual fracture stage, a step change in horizontal estimated ultimate recovery (EUR) can be made.

In east Texas, vertical representative of the Haynesville shale wells were cored and logged in Rusk, Harrison, and Panola counties by BP America in 2009 as part of an exploration program determine best practice and opportunities for their initial horizontal program within the resource play. These wells were known to be within the boundaries of a more clay-rich but thicker Haynesville shale package that is much less homogeneous than its north Louisiana counterpart [97]. In the east Texas, there are challenges in optimizing and understanding the mechanisms for increasing gas production in a more problematic facies that leaves little margin for errors.

Using full core analysis (including X-ray diffraction (XRD), inductively coupled plasma (ICP), and stress testing), laser induced breakdown spectrometry (LIBS) chemostratigraphy elemental analysis of cutting calibrated to core mineralogy, geochemical log analysis calibrated to core mineralogy, three dimensional mechanical elastic properties analysis, and a PNS log for through casing neutral net evaluation calibration, a complete reservoir characterization was attempted. To obtain brittleness index [91] was one of the objectives; to determine if a function of Poisson's ratio and Young Modulus (Figure 5.61), could help quantify areas within which fracture conductivity is easier to achieved.
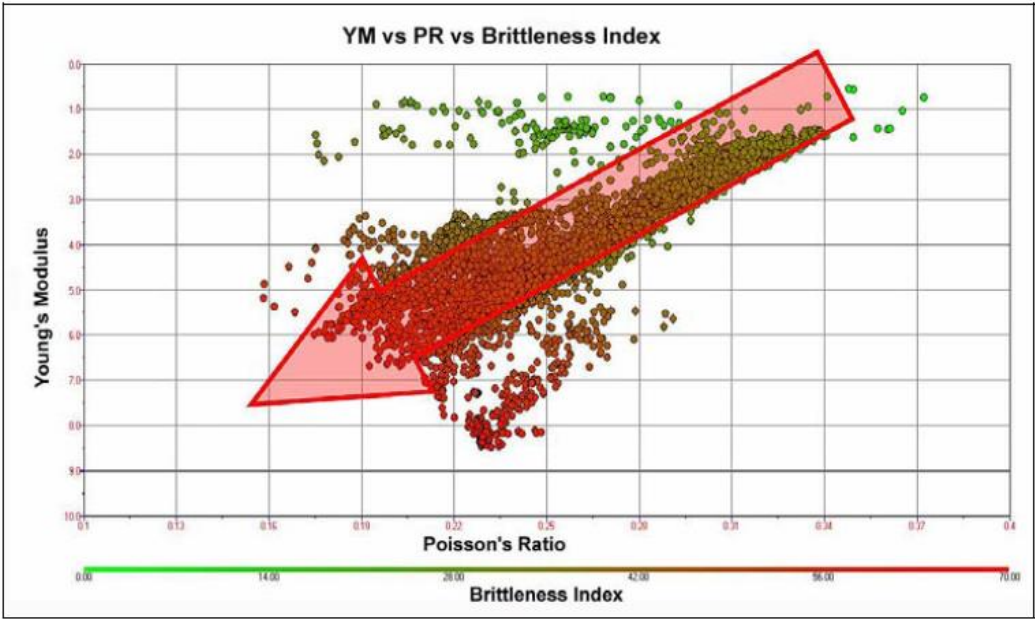
Figure 5.61: Young modulus and Poisson's ratio showing brittleness index [81].

Two horizontal wells were subsequently drilled using the calibrations and learnings from the vertical wells. The evaluation of the horizontals consist of LWD triple combo and dipole sonic, LIBS chemo stratigraphy cuttings samples analysis, and PNS after the pipe was set. Using a conventional spacing of 110 ft between 2 ft perforations cluster, ten fracture stages were pumped. With 12 shots per cluster, each stage had four perforation clusters. A fairly generic water fracture design was used to attempt to place 80,000 lbs. of 100 mesh sand and 220,000 lbs. of 40/80 hydro-proppant per fracture stage, though Whether or not the fracture is optimized for this shale can be debated. Within 45 days of cleanout, post-fracture production logs were run after a stable gas and water rate had been established. The results were evaluated, conclusions were reached, and recommendations were proposed.

184

Many vertical wells including old and new were exploited for various levels of formation evaluation, ranging from standard triple combo data to the full blown analysis as described previously. In Panola County, the BP Glaspie #10 is provided as the most complete petrophysical data set for analyses. For chemo stratigraphy calibration, the well was fully cored and sample cuttings were employed. The open-hole was log with both vertical triple combo and dipole sonic, wire-line conveyed triple combo, geochemical, and cross dipole sonic logging. Cased-hole logging on the other hand consisted of PNS (pulse neutron spectroscopy) with subsequent neutral net calibration to open-hole data.

A full core was retrieved and an XRD lithology analysis was performed. The matrix was dominated by quartz, chlorite, calcite illite and a mixed layer of illite and smectite clay. For the whole core, the volume of clay mineral as a percentage of the total matrix averages more than 30%. The effective gas filled porosity of the shale will be limited by this amount of clay would make the shale softer and more ductile with a higher Poisson's ratio.

5.13 Chemical Analysis – Sample Cuttings

On drilling rigs, LIBS is a versatile analytical technique used for the real time acquisition of elemental data [99]. For the analysis of drilled cuttings, the LIBS instrument is compact, portable, and well suited, enabling results to be immediately applied to decision-making for drilling operations. The data can be generated within 30 minutes as the sample preparation is relatively simple and rapid. For more than 40 elements, robust data can be acquired for most shale and lithofacies (including rare earth elements and other low-abundance trace elements).

To establish a chemo-stratigraphic zones for the interval of interest, a pre-horizontal-drill study of the core and cuttings from The Glaspie #10 was conducted on ICP-optical emission spectroscopy/mass spectrometry (ICP-OES/MS) instruments. For future horizontal real-time cuttings analysis, the resulting data was used to calibrate the LIBS instrument for well site application. The chemo-stratigraphy helps to unravel the interplay of detrital, carbonate, and organic minerals with the paleo redox environmental proxy elements (nickel, vanadium, cobalt, molybdenum, and uranium) in shale and in particular shale gas plays, providing clues as to the highest total organic content (TOC) values and potential sweet spots to target. LIBS data obtained

from the cuttings while drilling enables immediate correlation to the chemo-stratigraphic zonations, improves the knowledge of the stratigraphic location of the wellbore, and enables the adjustment of wellbore (geosteering or chemosteering) as desired. The same elemental data can be used to predict mineralogy accurately through robust empirical modeling, which initially is ideally verified against mineralogy derived from XRD analysis.

Fourteen separate elements were measured using the state of the art neutron activation spectroscopy tool [100], which is run in combination with a standard spectral gamma ray, measuring elements potassium, uranium, and thorium. The same XRD and ICP data from the full core that was used to calibrate the LIBS chemostratigraphic analysis, oxides closure models were verified and calibrated for neutron activation spectroscopy tool to convert the elemental data into actual dry weight minerals as in Figure 5.62 below.

Using the geochemical processed mineralogy, a multi mineral analysis was subsequently performed. The wet volume fractions of calcite, dolomite, quartz, chlorite, illite and sodium feldspar were solved for. Using m = 1.6 and n = 1.9 in the saturation equation for a bulk fluid analysis, it best match the core derived gas volume (Figure 5.63).

Core stress analysis and integration: Single-stage tri-axial compression test were conducted on multiple as received shale samples on deviated, horizontal and vertical samples at in-situ stress conditions. With the pore pressure drained to atmospheric pressure, these tri-axial compression test were conducted at room temperature. Dynamic mechanical properties were also obtained simultaneously using the ultrasonic wave transmission tests. Dynamic and static moduli as seen in Figure 5.64, comparisons were possible as a result of these tests.

Laboratory testing indicate that the Young's modulus value is greater when measured horizontally than vertically. Poisson's ration value averages slightly less when measured horizontally than vertically [81]. Transverse anisotropy which is significantly observed in Young's modulus can be classified as shown in equation 5.23.
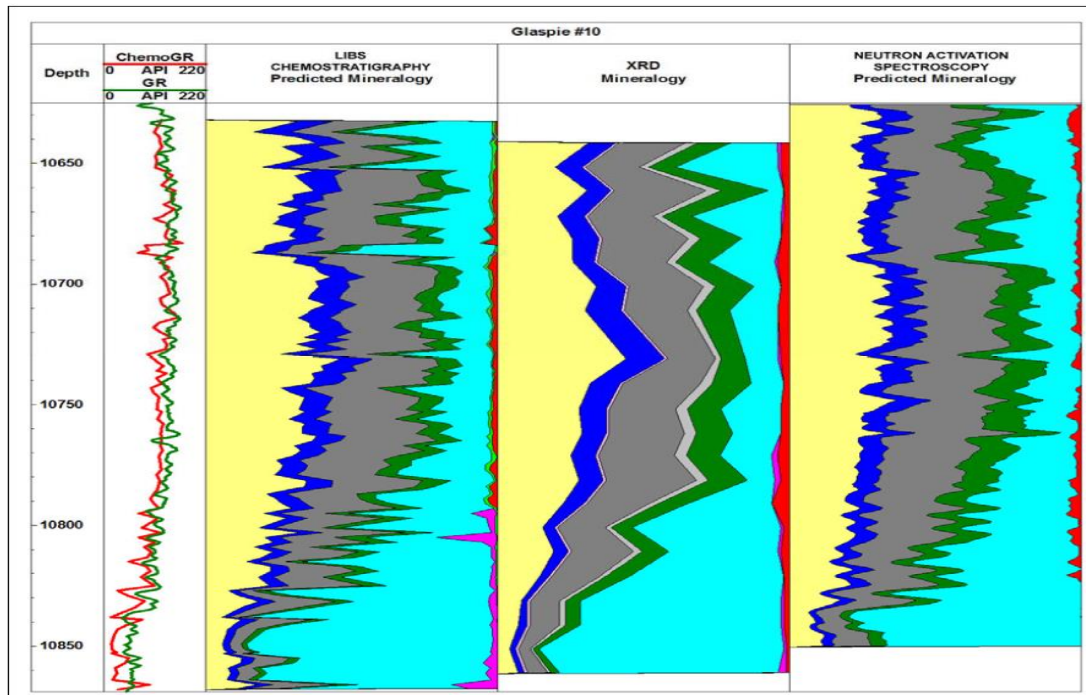
Figure 5.62: Comparison of LIBS chemo stratigraphy and neutron activation spectroscopy mineralogy results compared to XRD mineralogy [81].
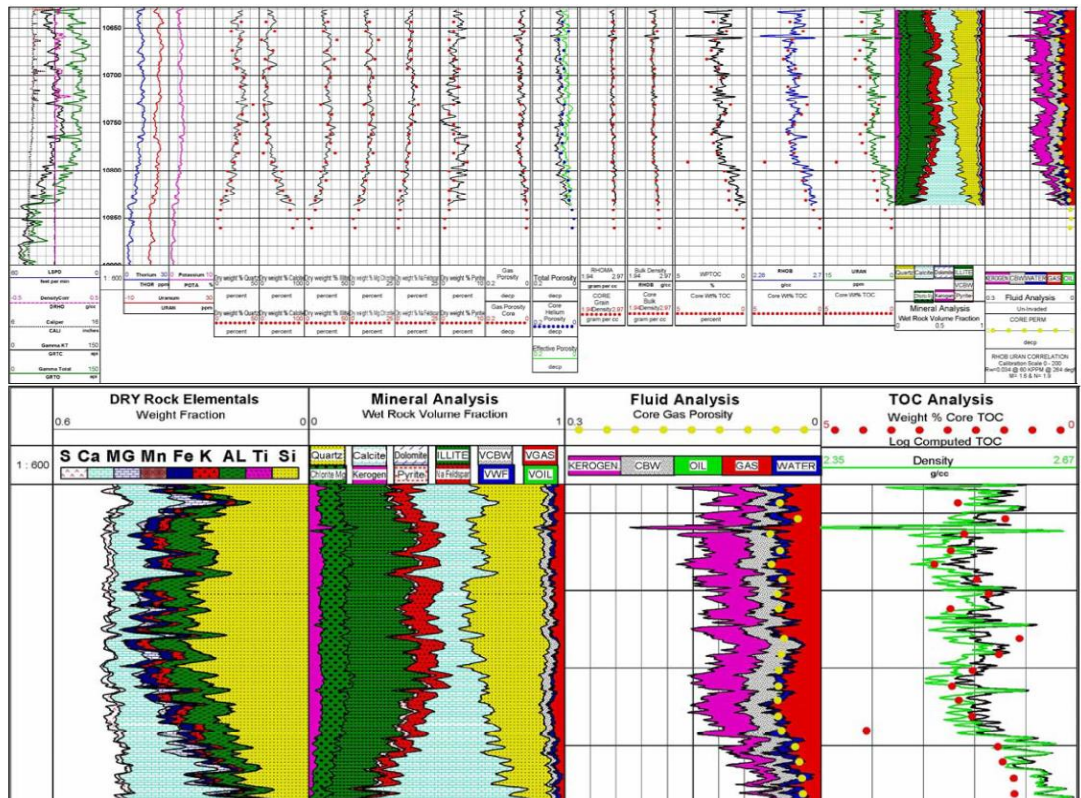
Figure 5.63: BP Glaspie #10 geochemical neutron activation spectroscopy data calibrated to core minerals and core gas porosity [81].

$$\Delta YME\_TIV = \frac{YME\_HORIZ - YME\_VERT}{YME\_VERT} \times 100 \qquad \textbf{(5.23)}$$

This ΔYME_TIV term quantifies the percentage increase in the horizontal Young's modulus over the vertical. A cross plot of the anisotropy term with differing minerals reveals that, this anisotropy can be modeled as a linear function of clay volume as shown in Figure 5.65 below.
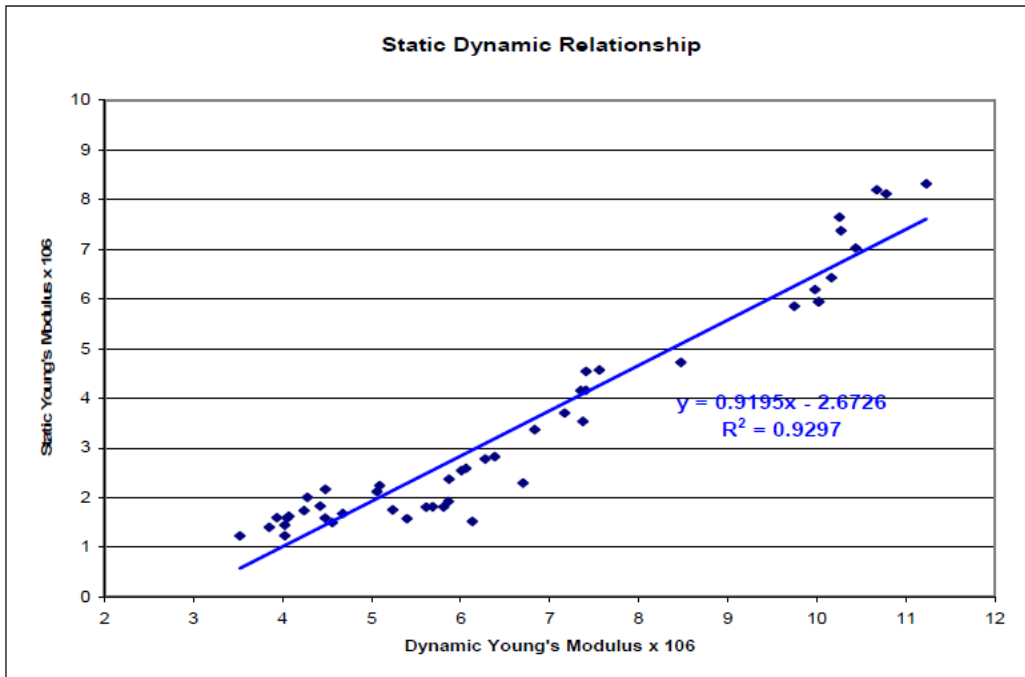
Figure 5.64: Static Young's modulus versus dynamic Young's modulus for Haynesville shale core in BP Glaspie #10 [81].

This clay effects serves to increase the minimum horizontal stress required for hydraulic fracture initiation and for subsequent treating pressures by increasing E_h / E_v term in the stress equation (equation 5.24).

$$\sigma_x \propto \frac{E_h}{E_v} \left(\frac{V_v}{1 - V_h} \right) \sigma_v' \qquad \textbf{(5.24)}$$

Pulsed neutron spectroscopy calibration of triple combo neutral net model and subsequent shale analysis: This technique which is used to convert primary pulsed neutron data to open-hole triple combo data through the application of neutral net processing, is well understood [101]. In varied lithologies and mechanical configurations around the world, this technique has been applied successfully since 2005. A series of more than 300 vertical Moncos shale wells logged in the Rocky Mountains between 2006 and 2007 were of particular interest, in which the cased-

188

hole pulsed neutron N-N modeling process completely replaced conventional open-hole logging.
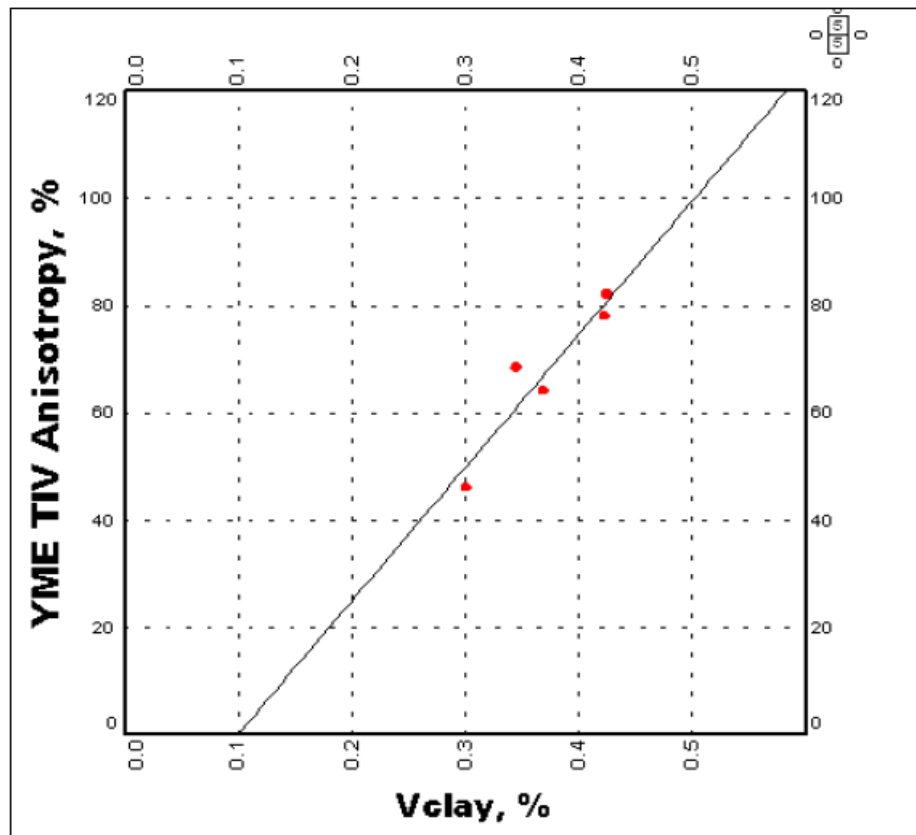
Figure 5.65: Young's modulus TIV anisotropy versus clay volume [81].

In the Haynesville and Eagle Ford shale, it became apparent that operators in more recent geo-pressured shale plays were reluctant to obtain horizontal logs as a result of perceived high risk and expense, an open-hole alternative which was reliable and proven was available for application.

The tools are then calibrated to an already acquired open-hole data set. A minimum data set is defined such as deep resistivity, neutron porosity and bulk density, but it can also include photoelectric absorption and compressional sonic. The capture elemental spectrum lithology obtained after calibration recently become the logging standard because of its enhanced logging speed. A basic mineralogy interpretation consisting of total clay, silica, and calcite is readily achieved [102]. A potassium yield spectrum is also available in addition to the calcite and silica, but its resolution in the pulsed gamma spectrum is better suited for use as a quality check of areas showing higher total clay.

A great deal of analysis is focused on examining the differences in vertical versus horizontal shear anisotropy as described in the discussion of the Glaspie #10 core, when predicting accurate stress model for fracture stimulation. Those studies surprisingly demonstrate that, the total clay volume makes a large contribution to variations observed between vertical and horizontal shear measurement. An accurate total clay estimate consequently is indeed important to any evaluation though we need to be careful since there may be other bedding in lower clay intervals that could also influence horizontal anisotropy.

To target those intervals containing the best free gas that have the opportunity for complex fracture generation for surface area drainage, a method of quantifying shale ductility is required. A discrete function of Young's modulus and Poisson's ratio; a brittleness index, was developed and implemented [91]. To calculate the brittleness index, the use of a best source dipole shear and gas corrected compressional velocity is required.

When sufficiently large database of vertical dipole information is acquired in an area such as the BP east Texas acreage, neutral net modeling of synthetic DTC, DTS, Poisson's ratio and Young's modulus can proceed from a standard triple combo data and at least a three component lithology model consisting of clay, calcite and silica [104]. Synthetic correlations of Young's modulus are usually very robust and Poisson's ratio is acceptable if the calculation is constrained by the analyst, to maintain the synthetic Poisson's ratio within an accepted envelope for a particular shale type using standard deviation analysis.

LIBS chemostratigraphy prediction of relative brittleness: To a larger degree, the hardness or brittleness of a rock is controlled by its mineralogy, it is therefore possible to model a relative brittleness index (RBI) which can be use in assessing the ability of the rock to fracture. The brittleness of the rock is controlled by a combination of relative abundance of carbonate and quartz compared to the clay content. The BP Glaspie #10 shows fairly equal volume of clay, silica and calcite as shown in Figure 5.66, but the Haynesville shale is typically more dominated by carbonate than silica (quartz).

As calculated from the LIBS chemostratigraphy data, the RBI has been modified to take into account the relative effect of carbonate on brittleness in the Haynesville

shale. Every proxy element is multiplied by a brittleness coefficient as shown in equation 5.25 and equation 5.26, which accounts for the mineral mechanical properties, mineral grain to grain relationship (texture), and overall distribution of minerals in the rock.

$$RBI = (Brittle\ Mineral\ Proxies) / (Brittle + Ductile\ Mineral\ Proxies) \qquad (\textbf{5.25})$$

$$RBI = (abM1 + abM2\ ....) / (abM1 + abM2 + abM3) \qquad (\textbf{5.26})$$

Where: Mn = Mineral (n = 1, 2, 3 …), a = mineral specific brittleness factor and b = mineral distribution factor.

Even when a perfect analog is used to actually measure the mechanical properties, the RBI calculation is a very useful proxy for geosteering while drilling a horizontal well or for analyzing cuttings after the well has a set of pipes to delineate more optimum fracture targets.

For this paper, two horizontal wells were drilled and evaluated. These wells are BP T. W George A9H located in the Blocker field, Harrison County, Texas and the BP CGU 13-17 located in Carthage field, Panola County, Texas. Both wells had vertical pilot wells immediately adjacent as shown in Figure 5.67. The initial lateral control consequently was perceived to be good. George A8H which is vertical pilot to horizontal George A9H, is deemed to be more homogeneous with regard to a fairly constant 30% clay volume. A wide varying amount of clay throughout the vertical section was clearly indicated in the case of the CGU 13-17H.

CGU 13-17H Panola county horizontal placement: Figure 5.68 shows the vertical control well, identified as a target in the lower Haynesville A interval that had the chance with fracture growth upward, to contact slightly better rock by brittleness index analysis. On this well, a LWD quad-combo (with dipole sonic) and horizontal PNS log were run for fracture planning and diagnostic purposes. The well evaluation was more of a correlation tool in the end, which highlighted the difficulty of effectively fracturing a well that is drilled too near a clay stone.
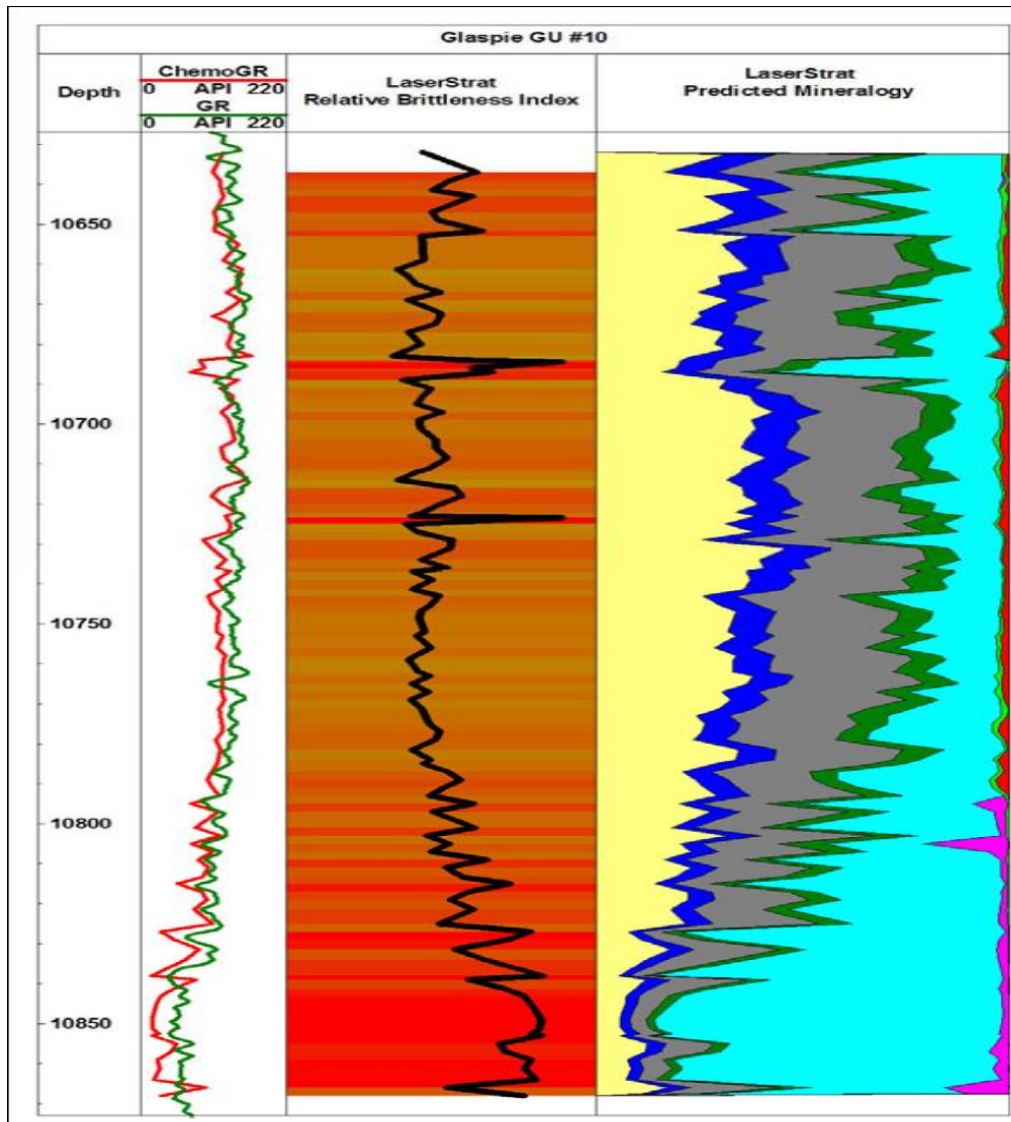
Figure 5.66: LIBS chemostratigraphy relative brittleness index calculation, BP Glaspie #10 [81].

It became apparent, after LIBS, LWD suite, and PNS were logged, evaluated and correlated to the steering data, that the well path has become stuck in the base or below the intended target window as shown in Figure 5.69 below. There is a ductile clay below the window and more ductile layer above the window at ± 10,630 ft. At the depth of ± 10,630 ft, the vertical drill rate change and temporary mud log gas suppression suggest a zone of radical different mechanical properties. It is this difference that may steered the horizontal well low and kept it there, more than the directional drillers.
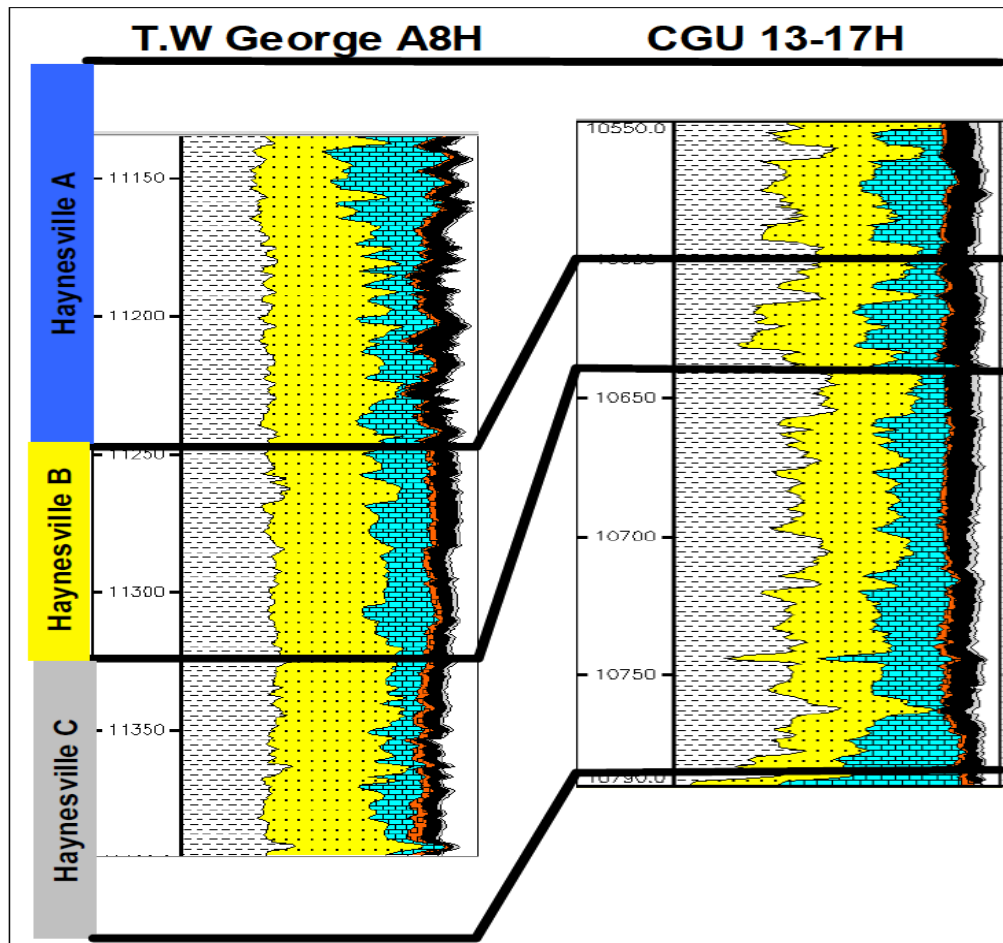
Figure 5.67: Vertical pilot wells and BP volumetric interpretations for BP George A9H and BP CGU 13-17H [81].

A target window at ± 10,590 ft would have been a better option for this well base on what we know now. The exploration team working with open-hole logs affected by significant tool pushing was part of the problem in the upper part of the shale on the vertical pilot hole.

The green numbered fracture stages in Figure 5.69 were considered successfully with > 70% of proppant placed. The red numbered stages place less than 30% of designed proppant. Yellow stages placed between 30% and 70% of the proppant.

CGU 13-17H LIBS Chemostratigraphy relative brittleness: From the LIBS data, this well indicates a wider range of relative brittleness than the log shale analysis. The RBI may be over sensitive to small changes in calcite, when there are fairly equal amounts of mineralogy, demonstrating the difficult nature of interpreting a general clay stone.
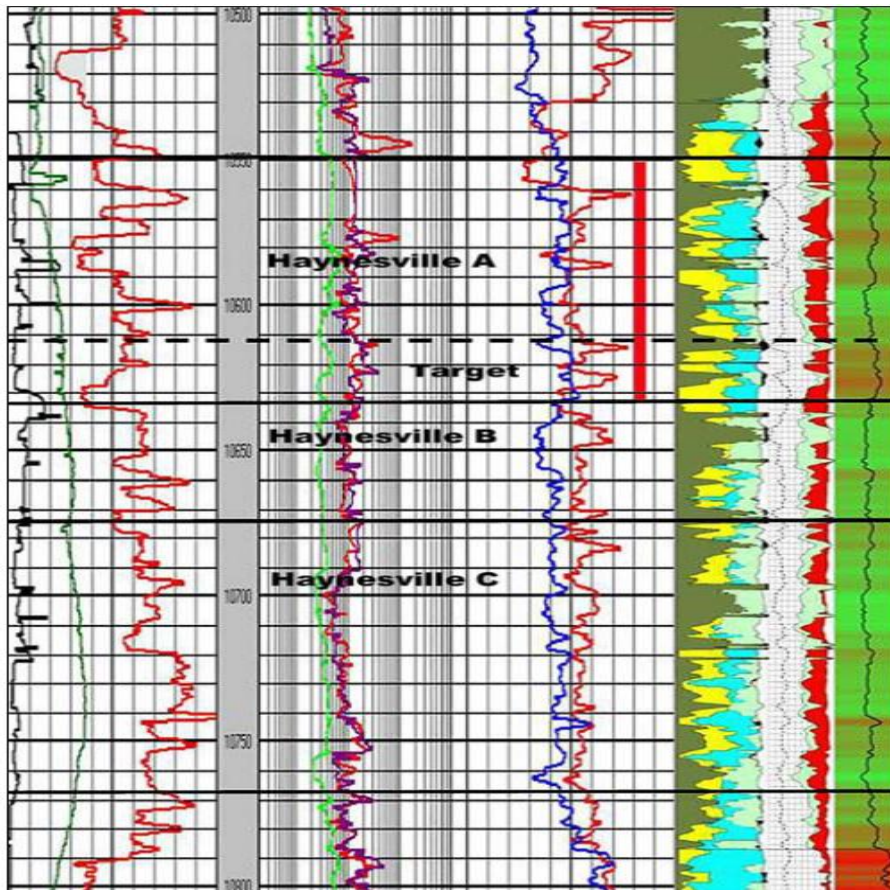
Figure 5.68: BP CGU 13-17H vertical pilot shale analysis showing an area of that has the optimum ability to fracture (in red) [81].
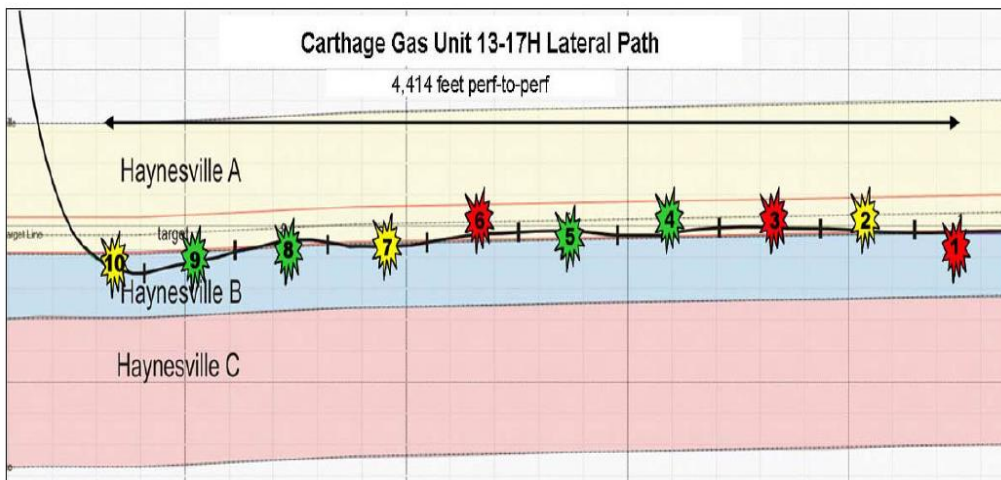
Figure 5.69: CGU 13-17H correlated 4,400 ft lateral path within the Haynesville shale [81].

CGU 13-17H Horizontal shale evaluation: The shale evaluation and transverse isotropic vertical axis symmetry (TIV) ratio analysis were conducted the same

manner as in the T. W. George A9H. The total clay increased to 60% or greater and hence, became trapped below the primary target. Because of the large clay volume, a very large TIV anisotropy would be expected across large sections of this well.

Due to the high clay, the well shows a wide variations in the brittleness index and TIV ratio. It was also shown in the calculated fracture index that stimulation can be accomplished, but would need entry point at optimum spots and an entirely different type of fracture design. In this environment, high rate water fractures are probably less effective. The more ductile clay stone will absorb the proppant and limit the height growth unless a hybrid crosslink gel is used to place larger proppant across the more vertical section. Also, this strategy would help maintain near-wellbore conductivity over time.in this type of well, the best option is to select target intervals with the most net feet of rock with similar mechanical properties. The rock with the least amount of clay, lowest TIV ratio, and highest brittleness index should be targeted. Clearly distinct lithology changes along the horizontal well that should be used to cluster similar types of rock into separate fracture stages were shown by the shale analysis.

The same fracture design and treatment employed in George A9H was used on the CGU 13-17H. No attempt was made to use the horizontal data to plan the fracture stages. As a result very poor proppant placement was achieved. The placed conductivity in this well was poor due to the high volume of clay, insufficient conductivity in the proppant pack itself, poor initiation site selection, and fracture stages that straddled lithological boundaries. The actual normalized treating pressure of the CGU 13-17H were lower during the pad placement except for stage 3, than those of the George A9H, but this differences were not related to place conductivity. In ductile shale, the proppant just cannot be effectively placed by a low viscosity fluid [91].

Even when a majority of the proppant was placed in a particular stage, production logs results indicate relatively poor performance. More perforation cluster in addition indicated little or no gas entry post-fracture stimulation than the George A9H. The most important issue with the underperformance of the CGU 13-17H is that, this horizontal well was seen traversing into a zone of varying amount of clay immediately below the primary zone of interest. The logs were designed to be used as a post-fracture production evaluation tool only, and no attempt was made to

actually use the well evaluation tool that were run to plan or design the fracture stimulation stages.

A review of more recent shale stimulation methodologies are necessary based on the result of the two horizontal wells completions examined in this paper. A high pressure, ductile shale and clay-rich shale such as the Haynesville in east Texas, is now recognized as the toughest stimulation completion challenge in the industry.

During core experiments, it was observed that complex, narrow width fracture are initiated when there is high TIV anisotropy, whereas planar wider fractures are initiated where the rock is more homogeneous [104]. These results can be correlated to near-well fracture behavior, and are critical to proppant placement and gas production [105].

Higher clay system are the most subjected to high pressure drawdown effects that cause proppant embedment by fines intrusion that seals off production because of the less effective fracture conductivity. Even if these clay rich zones are not vertically persistent, still act as a near-well chokes and must have higher proppant conductivity through which gas is delivered. These clay-rich zones are the most susceptible to pressure cycling effects that can cause more embedment over time. Smaller effective fracture widths in higher clay intervals in addition, are also more prone to post-fracture digenesis cementing of the proppant pack because, there is much less surface area to actually fill [106]. This aluminum-silicate cementing occur under higher temperature and pressure conditions when high strength proppant are not chemically neutralized by surface coating or manufacturing design.

In the statistical analysis of the impacts of completion methodology on production, the Haynesville shale play was considered [107]. The goal of every operator is always to optimize the methodology for stimulating a shale play in the early development. Since the Haynesville shale play is now under development with several wells having produced for 12 months or more, wide trend in production can help determine which completion methodology create the best producing wells.

The uniqueness in temperature, pressure, and lithology that characterizes the Haynesville shale creates the expectation that proven techniques of other unconventional shale reservoirs may not necessarily produce the same results in the Haynesville shale. Taking into account trends developed from cross-referencing

completion strategies in laterals with public production, Haynesville shale wells production appear to be heavily dependent on geographic location and total number of hydraulic fracturing treatments performed.

Determining the optimum methodology of stimulating the reservoir is often done by operators by predicting the best case completion strategy and executing that stimulation in the field to obtain baseline cases against which to initially qualify the success of the subsequent changes to completion strategy; with each new well stimulation, an operator may change variables such as number of stages, amount of proppant, and proppant type, with the anticipation of increasing production success with each change.

Due to the fact that each operator is quantifying their own decision matrix in regards to effect on production, the early well sample size is generally small and geographically focused, and any instance of adversity in completion of the reservoir could drastically and inaccurately affect this learning curves. Database of completion variables from 286 wells completed after January 1, 2009 with public production data was combined, a multi-operator and multi-regional sample was obtained for determining variations in completion strategy and subsequent effects on production.

Wells that were completed through October 1, 2010 were only investigated in this study, and this sample size was about 24% of the entire population of the Haynesville shale horizontal wells completed over this time interval. The database for trends and correlations provides a wider range of completion variables than single-operator studies. This because, it is not uncommon for operators to make relatively minor deviations from the original designs to reduce uncertainty in the results.

Statement of assumptions and definitions: Several assumptions are being made that will not always hold true when associating only completion techniques to the actual production. All the wells in the analysis though are held equally just because they are Haynesville shale producing laterally, underlying inequalities are introduced by several differentiators. Lateral lengths, wellbore placement and overall well construction differs from well to well; however, the targeted portion of the Haynesville shale along with the general lateral length over time, did experience more unified consistency.

Flow back methodology [108], [109] remains a potential factor on overall production that has not remain constant across the Haynesville shale reservoir. Several operators of the play in fact have suggested that flowing back the wells less aggressively ha led to an increase in their estimated ultimate recoveries (EURs). Certain apparent trends could be prone to some masking for this reason, when variations in well construction and flow back parameters for this analysis are disregard.

Various trends and charts displays portrayed through this dataset may be prone to data segregation or production normalization to compare the wells from a more normalized viewpoint. For instance, it is shown that the well's production is highly dependent on geographic location. Hence, only certain wells that are geographically similar may be pulled into an analysis to determine trends for wells with similar expected results. Production normalization likewise, will be required in some instances to account for other variations such as number of stages, to adequately single out a certain completion variation as a variable of focus.

Any graphic presented also that displays a trend line are not intended to imply a linear relationship with the presented variables, but rather clearly communicate whether a suspected trend follows upward or downward ; all trend lines are created through computer-generated software providing best fit and are not manually positioned by the authors.

On the Haynesville shale, the most widely accepted factor holding influence today, is likely well location. Many operators and analysts therefore have already developed and presented maps detailing which areas are the sweet spots of the Haynesville shale. Twelve month cumulative production in the map shown in Figure 5.70, not only reiterate this perception but also is used to guide appropriate well segregation to improve fairness in these analysis.

Only certain wells of geographic similarity will be pulled into each analysis to remove any bias in production based location vicinity to the play's sweet spots in many of the following graphics. Which wells are being represented in each analysis will be specified, and the depiction below serves as validation for using a well-segregation approach.
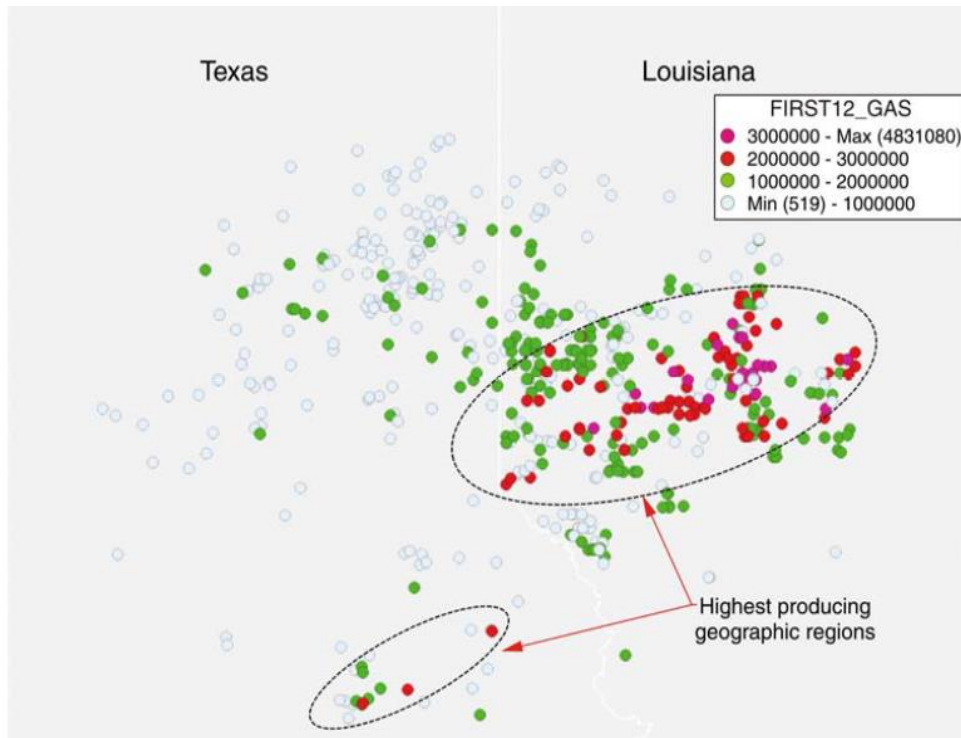
Figure 5.70: Geographic well locations of Haynesville shale laterals with their corresponding 12-month cumulative gas production [107].

When stimulating a low permeability, unconventional reservoir, another completion variable that would logically be expected to influence production is the number of hydraulic fracturing stages performed during the wellbore completion. The targeted goal as with many shale plays currently, is increasing the amount of stimulated volume of the reservoir achieved with each lateral.

The Haynesville shale is a softer rock than most North America shale plays, hence the fracturing profile is not prone to shattering complexity like that of Barnett shale. It would then be expected that, the best way to increase the stimulated volume of the reservoir in a Haynesville shale lateral would be to increase the number of stimulated entry points along the wellbore (increase the number of stages).

The review of the data reinforces this theory by depicting an increase in production with an increasing number of stages per well. This trend, not only witnessed on a play-wide basis but also when analyzing specific geographical regions. In many of the fields, in fact the trend strengthen in its correlation as the viewing window shrinks. The importance of the number of stages along the lateral seemed to become readily recognized by the operators in the play through the early development of the Haynesville shale.

Most of the completed Haynesville shale horizontals and all of the wells included in this study, are completed with pump down plug and perforation methodology. There is usually more than one perforation cluster shot with predetermined spacing between them when completing a lateral with plug and perforation methodology. The intension is that, more of the laterals can be stimulated simultaneously during the hydraulic fracturing treatment.

An operator must make their decision balancing time effectiveness with fracture certainty when relying on limited-entry technique to stimulate each cluster. The more clusters are perforated in a specific treatment stage, the uncertainty exists as to where the proppant and fluid will ultimately end up. By running fewer perforation clusters over the same lateral length however, the operator would have to perform more treatment stages over the entire wellbore, and this increases the completion time or sacrifice stimulating certain areas of the wellbore by increasing the spacing length between the clusters.

The most commonly seen quantities of cluster shot per stage for Haynesville shale are four and six, making up to 46% and 36% of the wells in this dataset respectively. To analyze the effectiveness of the multiple cluster, data points from the core Haynesville shale region were divided up to six regions that were highly concentrated with wells in fairly close vicinity. These six groups are shown in Figure 5.71 below.

It will be expected theoretically that, if the limited-entry technique with the multiple cluster is performing as desired [108], the trend will therefore show an increase in production as the total number of cluster along the lateral increased. This expected trend as shown in Figure 5.72 is prevalent only in some of the well grouping; primarily group 1 and 2, which fall more to the center of the Haynesville shale core region.

When reducing the data set to include only the well that were fractured with only four cluster per treatment intervals however, the trend of the data set groups 4 and 5 becomes more convincing as shown in Figure 5.73 below (groups 3 and 6 lack sufficient number of data points).
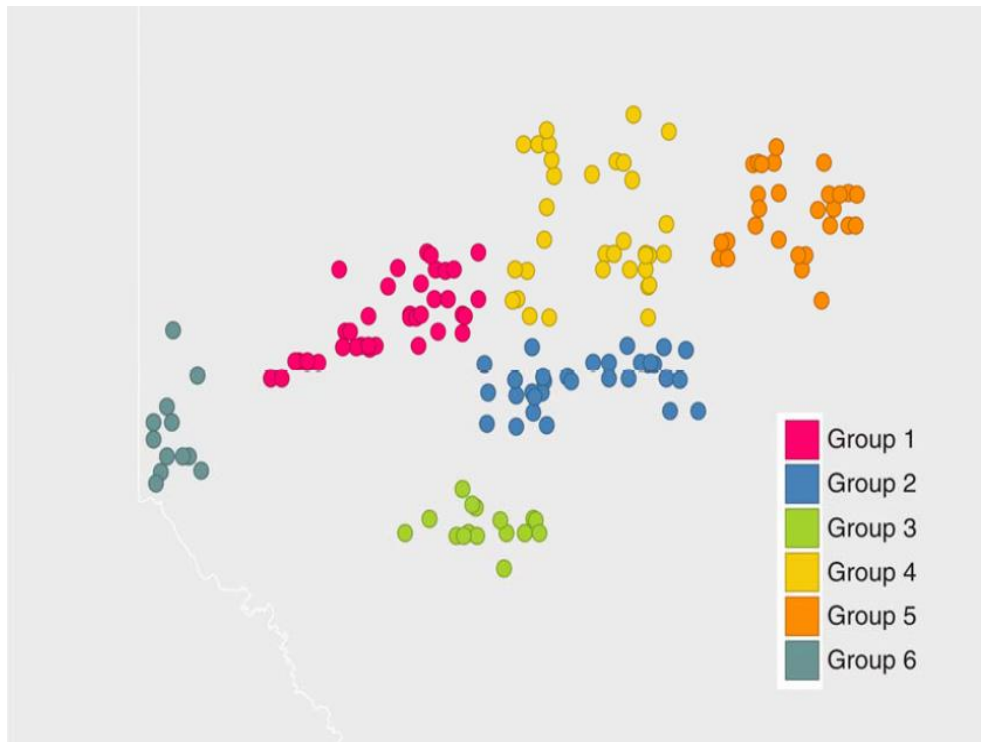
Figure 5.71: Map demonstrating the geographical segregation of various wells in close vicinity used in the analysis [107].

This may show that, because the outliers from the expected trend of these two groups occurred when more than four clusters were performed per treatment interval. The rock quality is less prone to successful limited-entry fracturing of the more than four clusters further away from the center of the core region where the treatment is performed.

It may likely be occurring in some of the outliers that, though six clusters are being shot for each fracture stage, only four transverse fractures are actually being initiated and properly stimulated; or all the six fractures are open, but not all have been adequately stimulated as a result of attempting to evenly direct flow of fluid and proppant to too many entry points.

The ability for a fracture treatment to successfully stimulated more than fracture clusters, appears to diminish as the rock properties transition from the more consistently brittle core region to the more ductile streaked rock of the outer areas. In the center of the core (data set groups 1 and 2) however, up to six fracture clusters can be stimulated in one treatment stage with apparent impact on the overall production.

201
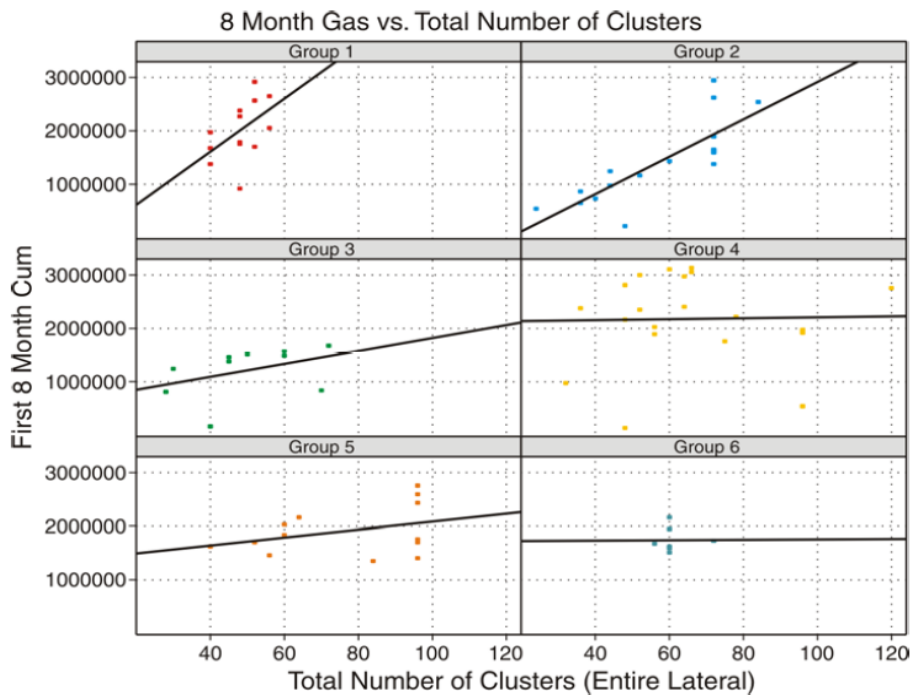
Figure 5.72: Scatter plots of the six grouped set depicting whether the increase is perforation cluster over the entire lateral leads to an increase in production [107].

It is strongly suggested by regional geologic studies that, the core area is relatively free of clay (less than 20% by volume) and dominated primarily by calcite matrix that actually enhances gas storage capacity. The calcite does not necessarily make the shale more brittle. It is only more brittle than the laminated clay found in the north and west of the play.

In the upper half of the shale is where the calcite shale is marginally more brittle than the lower half of the shale, and this is where core area is actually targeted. This area is also where the best chance for fracture height growth exists because of marginally less vertical heterogeneity than the lower half of the shale.

It is shown in Figure 5.74 that, the volume of clay also has been shown to influence a vertical versus horizontal Young's modulus anisotropy that has been confirmed with multiple tri-axial stress test on full core. In the horizontal, the more horizontal clay layers encountered per unit volume can contribute to a near doubling of measured Young's modulus when compared to that in the vertical. Experiments performed on these cores shows that, complex narrow width fractures are initiated when there is

high Young's modulus anisotropy, and planner wider fractures are initiated at area where the rock is more homogeneous [104].
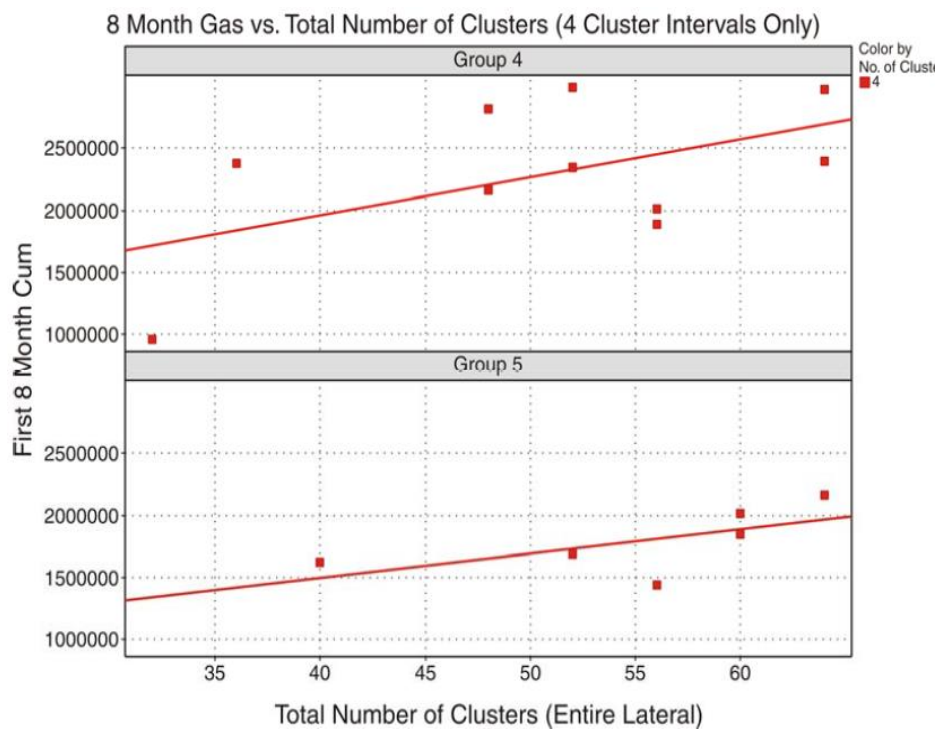
Figure 5.73: Scatter plot depicting strengthening of trend for data set groups 4 and 5 [107].
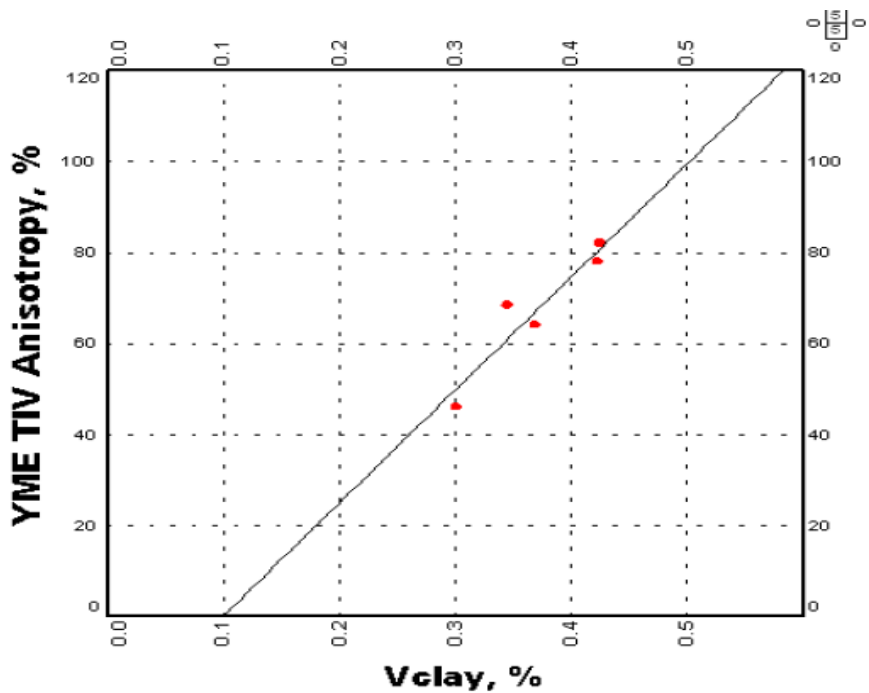
Figure 5.74: Young's modulus anisotropy versus clay volume from tri-axial stress measurements [107].

These results can be correlated to the near-wellbore fracture behavior, and also these results are critical to proppant placement and gas production [105]. For each stage in the Haynesville shale, treatment of the current data set ranges in treatment injection rates from as low as 30 bbl/min to as high as 100 bbl/min. in stimulation in several ways, adjusting the pumping rate higher or lower can effectively be used. The injection rate is usually used to provide turbulence required to carry proppant in the absence of sufficient viscosity, generate additional fracture height by initiating fracture growth through the laminated formation barriers, and provide sufficient limited entry points at the perforations, which can allow for simultaneous stimulation of multiple perforation clusters.

These three considerations are applicable to a Haynesville shale horizontal treatment and could also provide positive impact to the overall production of the well. For effectively stimulating with a multi-cluster plug and perforations technique, the need for limited entry is apparent. The transport of proppant using turbulence is important for moving the proppant across the Haynesville shale horizontals that may commonly exceed one mile in the lateral length, and is further emphasized in the job where the viscosity of the fluid remains low.

Since the Haynesville shale and the Lower Bossier shale (as the Haynesville shale wellbores sometimes cross faults or miss-steer into the Lower Bossier) being highly laminated in their formation structure, a certain treatment rate may be needed to effectively achieve the desire fracture height. The effects of average injection rate on production in the core region by combining the previously identified data set groups 1, 2, and 3 are details in Figure 5.75. These data set groups were chosen because, they are adjacent in the geographic location, and also provide a good variance of average injection rates used for the treatment of the fracture.

The softer the shale, the more crucial the conductivity of the fracture becomes [105], [109], [110]. In the case of the Haynesville shale it will be expected that, the factor impacting conductivity such as proppant amount, mesh size, proppant type, and proppant concentration would show an impact on providing longevity to the production by reducing the initial decline.
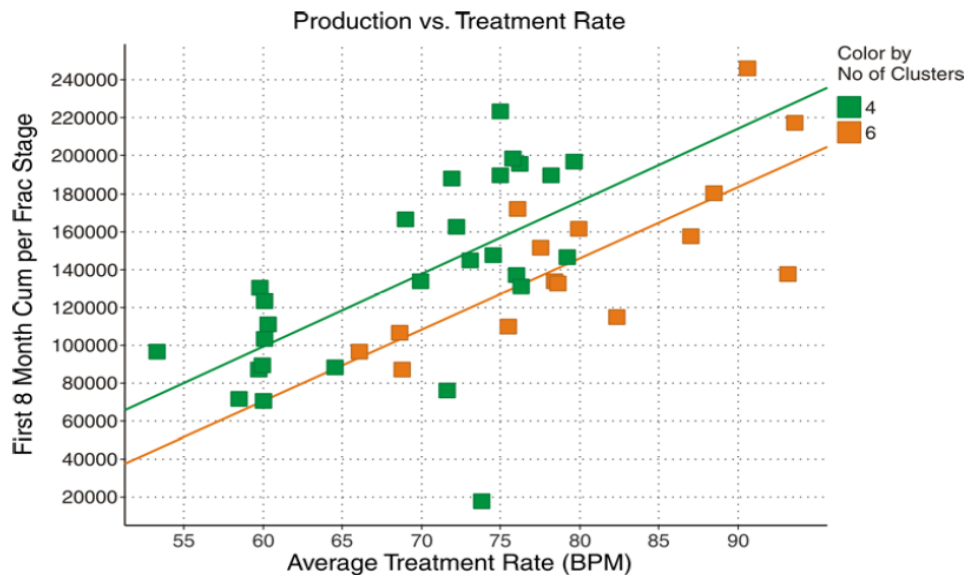
Figure 5.75: Scatter plot depicting the first 8-months cumulative production versus the average treatment rate [107].

It is very difficult to find a regional selection to demonstrate any clear trends and provide enough variance to relate production to proppant and conductivity variables, with the current data set; any of the concentrated regions of the data set lack adequate variance between the variables after reducing out the well that have not produced long enough to consider decline. The entire data set was filtered to include only the wells that had produced longer than 12-months and had experienced a peak month of 420 MMcf or higher to provide an appropriate conductivity analysis in the early development of this play.

At the time of study, only twenty wells of the data set were fitted into this category. Conclusions made from this data samples may not be indicative of this play, yet the analysis can still be used to generalize what factors seem to provide production sustainability for the wells that appeared to be highly successful in their early days of production. The 12-month production from these twenty wells of data set is plotted against conductivity variables to determine whether enhancing the conductivity has had an influence on sustaining production.

As seen in Figures 5.76 and 5.77, a trend is produced depicting that more proppant placement leads to a higher monthly production after 12-months. This trend when comparing to an entire lateral basis and when normalizing the production and proppant to a per stage basis, hold true for both. Also in Figures 5.77 and 5.78, proppant concentration seemingly shows influence. The proppant concentration is

demonstrated as a function of the entire completion proppant amount divided by the entire completion fluid volume on an entire lateral comparison. The actual maximum proppant seen during the treatment is used on a stage-normalized comparison.

In the Haynesville shale, the type of proppant placed in the wellbore should greatly affect the overall conductivity of the fracture since this play is such an over pressured reservoir with closure stresses exceeding 10,000 psi. With the current data set however, the various types of proppant such as resin-coated sands, synthetic ceramics, and high-strength bauxites could not be adequately tracked to tie both type and amount to each individual well. The obstacles to tracking this were presented by many wells running up to four different types of proppant in the same treatment stage and/or changing proppant type in the middle of completing the lateral because of proppant shortages. It is however worthy to mention that 100-mesh white sand which is ran on to majority of the Haynesville shale fracture stages, is included in the proppant amounts.
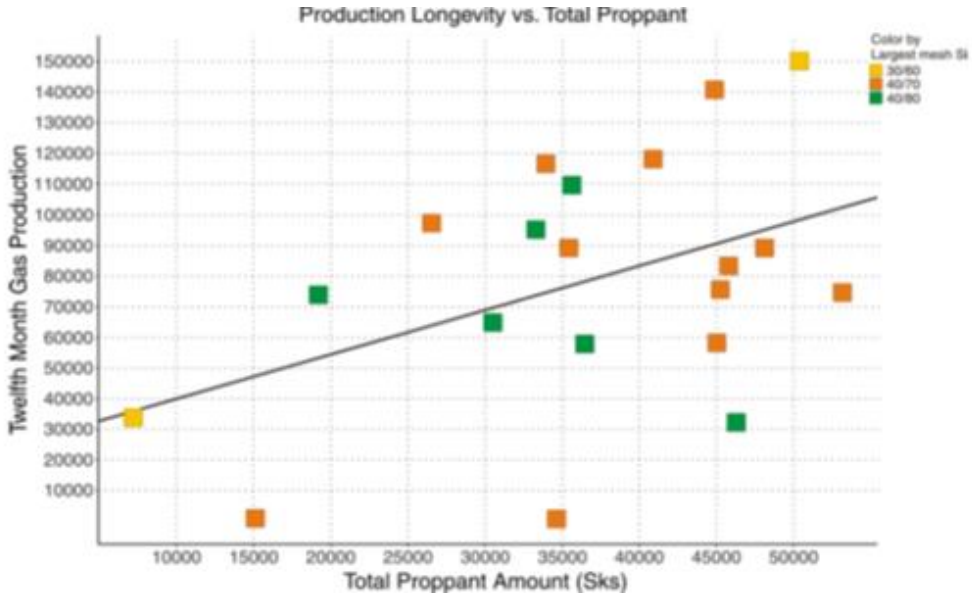
Figure 5.76: Scatter plot demonstrating each well's 12th month of production compared to the entire amount of proppant placed in the well's completion [107].

The data set does not show even distribution of cross linked-gel jobs and low viscosity job using only linear gel or friction reducer, yet the fluid type has been included in this analysis because the decision of which fluid type to use in shale is often a highly debated topic among industry experts. The sample subset is reduced to

the wells located in the core regions of the Haynesville that have produced for 12 months or more.
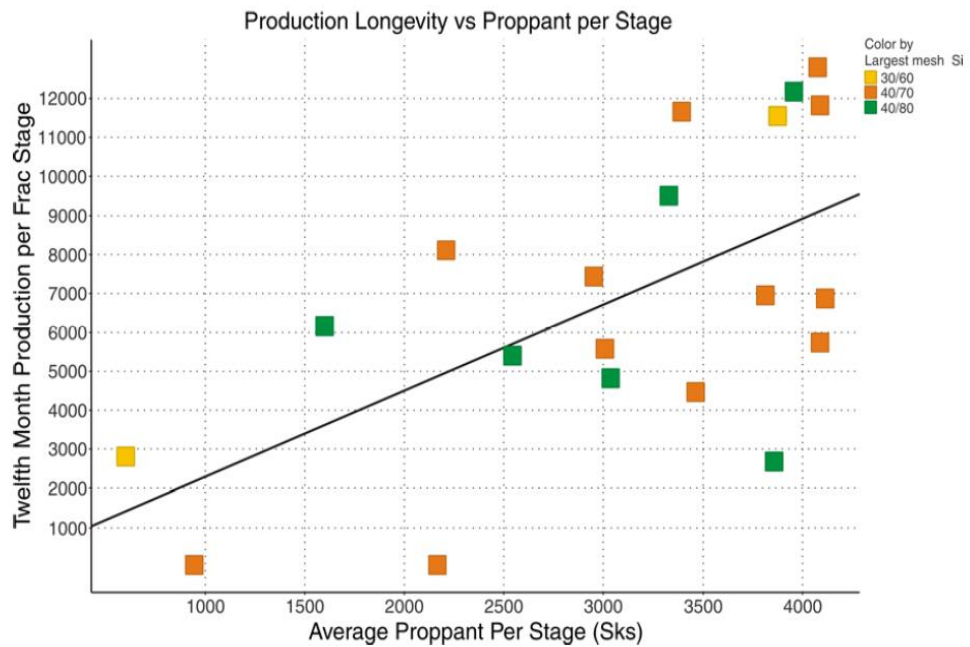
Figure 5.77: Scatter plot demonstrating each well's pre-stage normalized 12th month of production compared to the average amount of proppant placed in each treatment stage the well's completion [107].
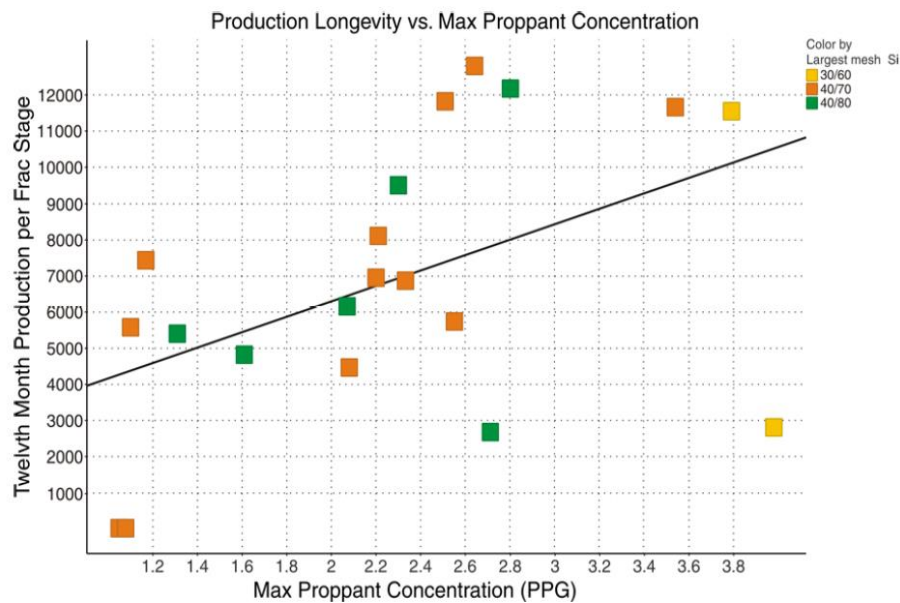
Figure 5.78: Scatter plot demonstrating each well's pre-stage normalized 12th month of production compared to the maximum proppant concentration placed on average fore ach treatment stage [107]**.**

Much caution should be observed when drawing any conclusion statement from the data because only eight wells featured using cross linked gel systems (either in hybrid format or for the entire treatment) compared to 45 wells using only linear gel and/or friction reducer (polyacrylamides). Continuing to keep and analyze the database will prove or disprove any observation as more and more wells are added to the sample and production time lengthened.

6. PRODUCTION TECHNIQUES

In the shale gas and shale oil industry, there is a huge demand to accurately forecast production from the reservoirs. There are several methods used to predict production from reservoir, some of these methods are analytical simulation, several different decline curve analysis (DCA), and numerical simulation. These methods have their own advantages and disadvantages, but to forecast rapidly and to some extent of accuracy, the DCA techniques can readily be used with available production data. The Arp's decline model which is a traditional DCA methods in use in the industry were developed originally for wells in Boundary Dominated Flow (BDF) but the dominant flow regime in shale reservoir is a long-duration transient flow. Hence newer models are needed in the industry to match transient flow regimes and for production forecast using these transient flow models. To match and forecast wells with transient flow followed by BDF, the Arp's model and Duong model have all the ability with a minimum terminal decline rate.

A revision to Duong model was proposed in order to provide a better fits to data in BDF regimes after analyzing actual well production and analytical simulation results of selected shale gas wells, to compare the various DCA models to ascertain with the lowest discrepancy in estimating the remaining reserves [111].

Horizontal wells completed with multi-stage hydraulic fractures encounter various flow regimes in the life of the well. Most of the flow in the life of the wells may be dominated by specific flow regimes like formation linear flow, but apparent BDF caused by fracture interference in higher permeability reservoirs with increasingly close fracture spacing may appear after production initiation within a few months or years. In the Marcellus shale with multiple-stage fracture, the different flow regimes in a horizontal well are shown in Figure 6.1.

The traditional Arp's decline model is based on empirical observation which states that, a well's loss ratio (rate of change of the reciprocal of instantaneous decline rate)

is usually constant with time. Arps assumed a constant loss ratio, b, to derive the hyperbolic decline model in equation 6.1

$$q = q_i \left(1 + D_i t\right)^{-1/b} \tag{6.1}$$

Where; q_i is the initial rate, volume/time, b is the constant loss ratio, also known as the hyperbolic decline exponential, dimensionless, D_i is the initial decline rate, 1/time.
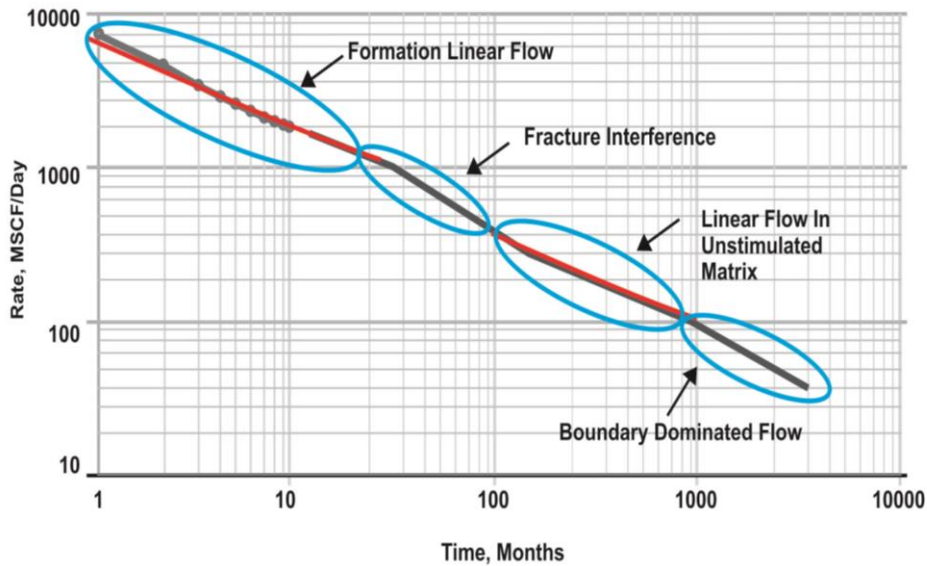
Figure 6.1: Typical horizontal well with multi-stage fractures flow regimes [111].

It has been demonstrated by many authors that the transient bi-linear and linear flow regimes in reservoirs has a corresponding b values of 4 and 2 respectively, and also, showed that, for the BDF regimes the values of b lies between 1 and 0 depending on the reservoir characteristic, reservoir fluid and operating conditions.

The minimum terminal decline model where data is modeled and forecast using the hyperbolic Arps equation (6.1) up to a certain pre-selected minimum decline rate after which the decline shifts to an Arps exponential decline model (b = 0), is a modification of the Arps decline model. The minimum decline model presents forecasts that appear to be reasonable but with no physical basis.

Valko proposed the stretched exponential decline model (SEDM) [157] which is given in equation 6.2 below.

$$q = q_o \, exp\left(-\frac{t}{\tau}\right)^n \tag{6.2}$$

where τ is the characteristic time constant, time, n is the exponent, dimensionless and q_o is the initial production rate, volume/time.

While q_o determines the start of production profile, the n and τ parameters can be considered as shape and scale factor respectively. The advantages of the SEDM over the Arps model are, (a) estimated ultimate recovery (EUR) is bounded, and (b) unlike the Arps model which is design for BDF, the SEDM is designed to model transient flow. The SEDM model has been tested on grouped data set in previous studies and for historical production period exceeding 36 months, it has proved to work well.

The Duong model which as a practical matter assumes long-duration linear flow is a new forecasting technique [112]. In this Duong method, two equations are required to calculate model parameters a, m and q_1. Using linear regression analysis equation 6.3 is used to calculate the parameters m and a.

$$\frac{q}{G_p} = at^{-m} \qquad (6.3)$$

a and *m* can be calculated using graphical technique as shown in a log-log plot in Figure 6.2. The vertical-axis intercept and the slope corresponds to a and m respectively. After determining *a* and *m*, q_1 is obtained by plotting flow rate versus time t (*a,m*) using equations 6.4 and 6.5. A straight line passing through the data using linear regression analysis provide the slope q_1, and the intercept q_∞. Figure 6.3 shows the graphical interpretation of the calculation of q_1 and q_∞. A semi log plot of production decline forecast for the Barnett shale well 42-121-32269 in Denton County, Texas using *a*, *m* and q_1 is shown in Figure 6.4.

$$q = q_1\, t(a,m) + q_\infty \qquad (6.4)$$

$$t(a,m) = t^{-m} e^{\frac{a}{1-m}\left(t^{1-m}-1\right)} \qquad (6.5)$$

A brief discussion of how Duong suggested calculating the parameters *a*, *m*, q_1 and q_∞ are presented in the previous section. It was observed that unrealistic result for both field and simulated cases if a non-zero q_∞ is used especially when only 6-12 months of historical production data are available.
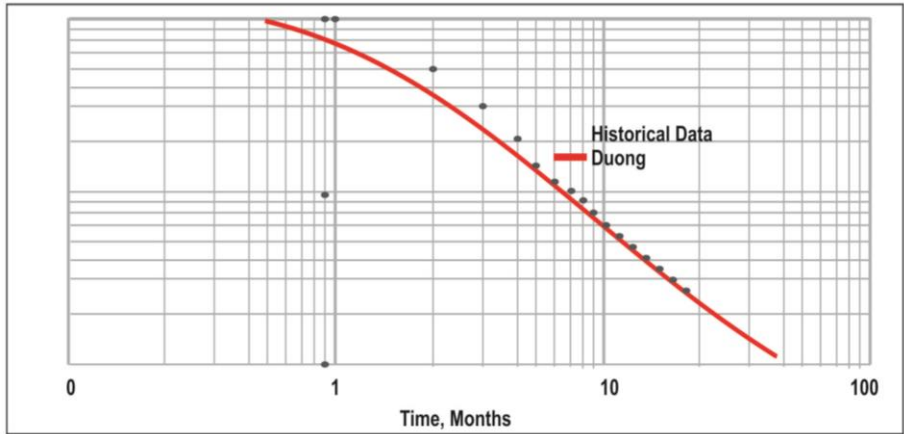
Figure 6.2: Determination of *a* =0.731 and *m* = 1.067 as for a well in Barnett shale, Denton County, Texas [111].
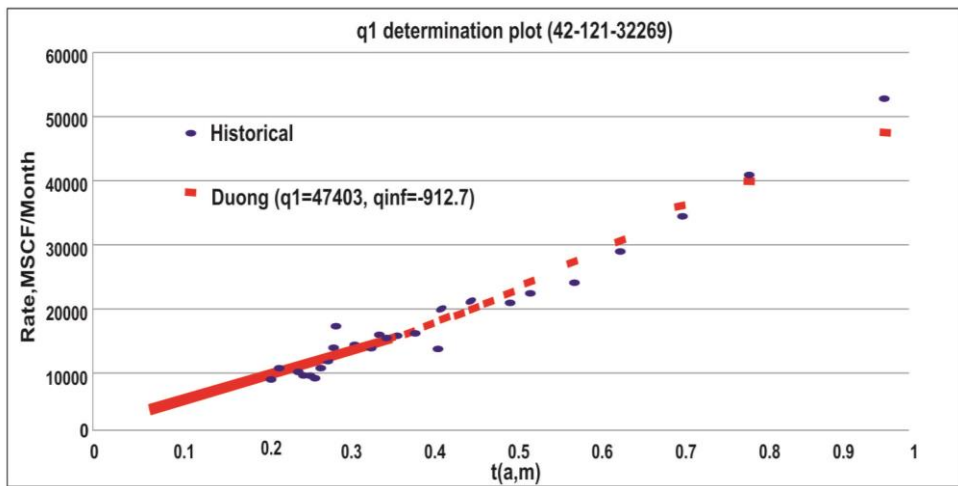
Figure 6.3: Determination of q_1 for a well in Barnett shale, Denton County, Texas [111].

Duong suggested that a plot of *q* versus *t* (*a,m*) should provide a regressed straight line through the origin, but, it was not proved to be the case because of the conditions of current operations [112]. It was also observed that for a well with less than 18 months of production history, a minimum error in estimating the remaining production will occur if the regressed line is forced to pass through the origin, i.e., $q_\infty = q$. The unrealistic effects of using q_∞, with a match of production history for a well in Barnett shale, is shown in Figure 6.5. In contrast to Figure 6.5, Figure 6.6 shows reasonable production forecast when q_∞ is set to zero.

212
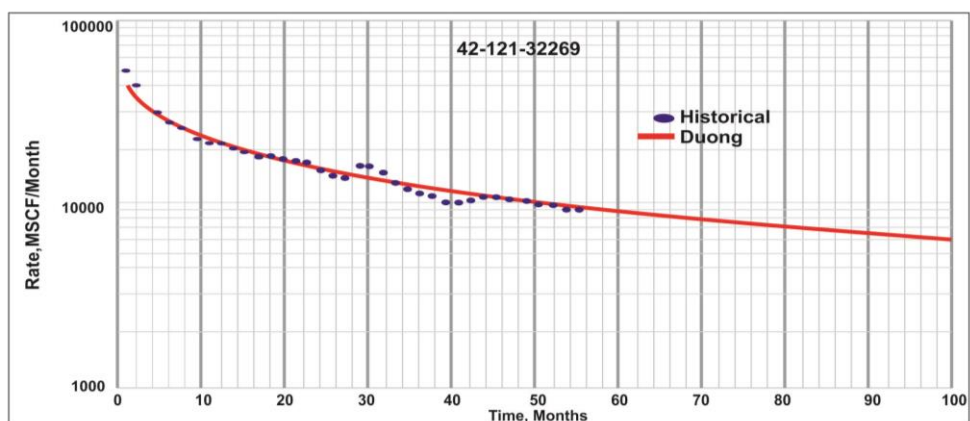
Figure 6.4: Duong production forecast for Denton County shale well [111].

Another modification made to Duong model was to switch to Arps BDF after a certain rate or time to account for later BDF. The Duong model which is a one-flow-regime model was designed essentially to model only transient flow. Hence to account for later BDF, which is evidence in some Barnett well and some of the newer shale wells with increased in permeability and with closer fracture spacing in simulated reservoir volume, is highly required. Imposing a minimum terminal decline rate model on Arps hyperbolic decline model at later time in a production history is similar to this approach. A b-value of 0.4 was used for the Arps model after switch.

A b-value of 0.5 should be used for gas wells with flowing bottom-hole pressure of zero and b-value of 0.4 should be appropriate to be used if the bottom-hole pressure is about 10% of the reservoir pressure. The decline rate at the time of switch is the contentious issue for the modified Duong with the switch to Arps. Further investigations are needed to determine the decline rate at which to switch to minimize forecasting errors for a given well or reservoir. It was switched at a decline rate of D_{switch} of 5% in this study since D_{min} of 5% is used by many as a minimum terminal decline rate in shale. A comparison between the modified Duong (forcing $q_\infty 0$), Duong with of D_{switch} of 5%, and the original Duong ($q_\infty \neq 0$) for a 30-years simulated Barnett well life is shown in Figure 6.7 below, where the D_{switch} produces a better forecast.

213
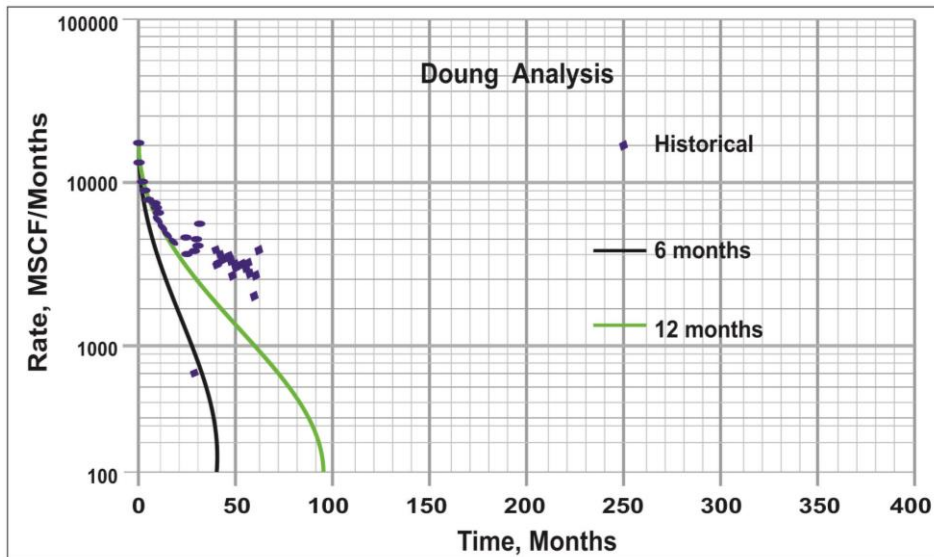
Figure 6.5: Duong forecast having a large negative q_∞ [111].
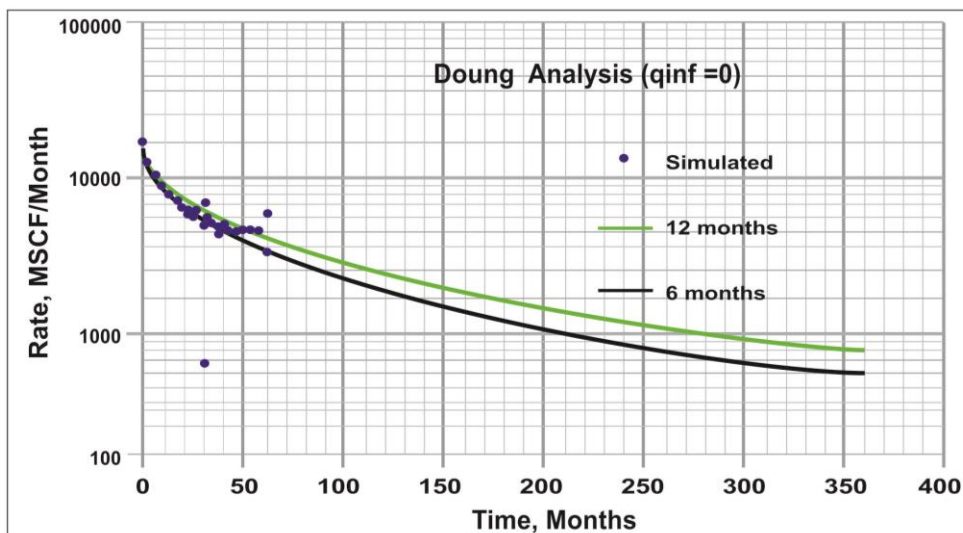
Figure 6.6: Duong forecasts, forcing $q\_\infty = 0$ [111].

Comparing deterministic models using field data: From over 1,500 wells 250 wells were randomly selected and analyzed as field data in this study, and these wells were from Denton, Wise, Tarrant and Johnson Counties in the Barnett shale and Van Buren County, AR in the Fayetteville shale. The three deterministic methods were compared using a statistical method. Hind-casts were performed by using matching a portion of the historical production data after which the remaining known production was compared to the forecasts
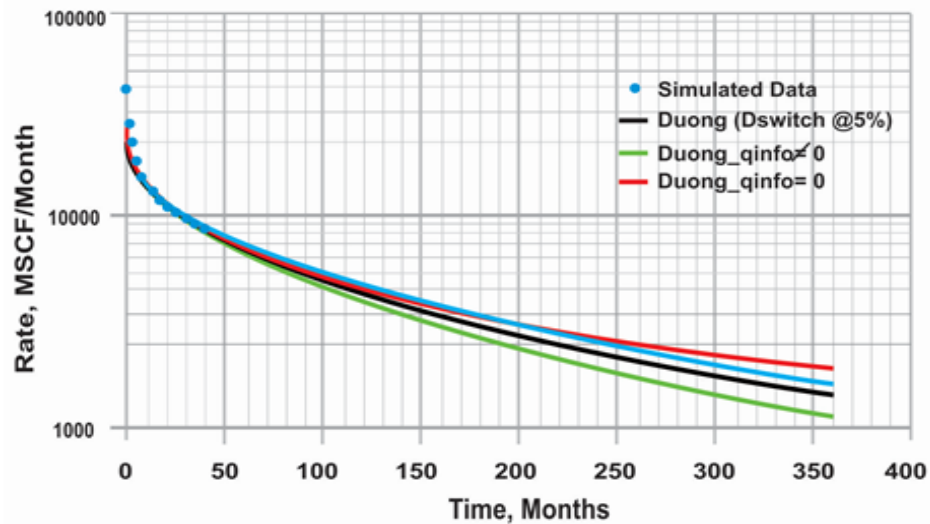
Figure 6.7: Comparison of the original Duong, Modified Duong and the Modified Duong (Dswitch @ 5%) for Barnett shale simulation. (48 months history matched) [111].

A model had an associated discrepancy for every individual well in the remaining production, hence the models results that do not match the wells' observed data set precisely had a large standard deviation of discrepancy in reserves, and those model results that do match the observed results precisely but not accurately had a low standard deviation and high mean error. The mean and standard deviation of the error/discrepancy should be small in the remaining production before a model can be accepted. The mean and standard deviation of the discrepancies in the remaining production for each well is tabulated in Table 6.1 for a 250 well data set. A pictorial example of accuracy and precision in the context of percentage discrepancy in reserves for a data set is given in Figures 6.8 to 6.11. Figure 6.8 is a good forecasting model since it has a low mean and standard deviation. Figure 6.11 is highly unreliable model because it is neither accurate nor precise. Hence it was observed that the model that offers the best statistics is shaded yellow in the tables.

It is evident in Table 6.1 that the modified Duong (D_{switch} at 5%) method with respect to the discrepancy in the remaining production reserves has a blend of small mean error and small standard deviation. This means that in forecasting production for the selected data set, Duong method (D_{switch} = 5%) is both accurate and more precise than other models. Though, in some cases, the modified Duong method has a higher mean discrepancy in the remaining reserves than other models, the viability of the

215

error describe by standard deviation is much less than for other models, hence considered the best model in this comparison. Considering the 24 months of matched data for instance, similar mean discrepancies in remaining production were provided by both the Arps (D_{min} 5%) and Modified Duong (D_{switch} at 5%) methods, meanwhile the standard deviation of the discrepancy in remaining production of Modified Duong is lower than the Arps method, which means that the Duong method in this case is more precise than the Arps method, even though both have the same accuracy.

Table 6.1: Comparison of Modified Duong, SEDM and Arps (Dmin=5%) for field data set [111].

History Matched (months)		Duong_Dswitch@5%	SEDM	App (Dmin 5%)
6	Mean	-15.98	40.91	10.97
	Std.Dev	29.24	39.06	33.16
	% Wells < 15% error	45.60	20.00	43.20
12	Mean	-7.77	6.44	5.04
	Std.Dev	17.48	27.75	22.57
	% Wells < 15% error	66.80	48.40	63.20
18	Mean	-6.90	5.06	3.03
	Std.Dev	14.41	21.90	19.01
	% Wells < 15% error	71.60	59.20	69.20
24	Mean	-2.49	4.49	2.21
	Std.Dev	16.13	20.51	18.92
	% Wells < 15% error	72.80	64.40	71.60
36	Mean	-5.04	4.41	2.77
	Std.Dev	17.88	21.93	22.54
	% Wells < 15% error	71.63	64.91	68.86
48	Mean	-5.45	1.63	0.05
	Std.Dev	18.08	27.12	26.99
	% Wells < 15% error	77.16	69.04	77.66

It was assumed in this study that a model that leads to an absolute error less than 15% in remaining production was an acceptable match. The modified Duong method in Table 6.1 has the highest percentage of wells with absolute error/discrepancy less than 15% in remaining production for any amount of history match. This fact together with the small mean error and small standard deviation of error in remaining

production made it possible to conclude that the Modified Duong (D_{switch} at 5%) model is the best among the rest of the methods, and therefore has the potential to offer more accurate and more consistent forecasts than the other methods though discrepancy and error still remains. For a given reservoir and operation conditions, the Modified Duong method can be made more accurate if the optimal D_{switch} value is determined.
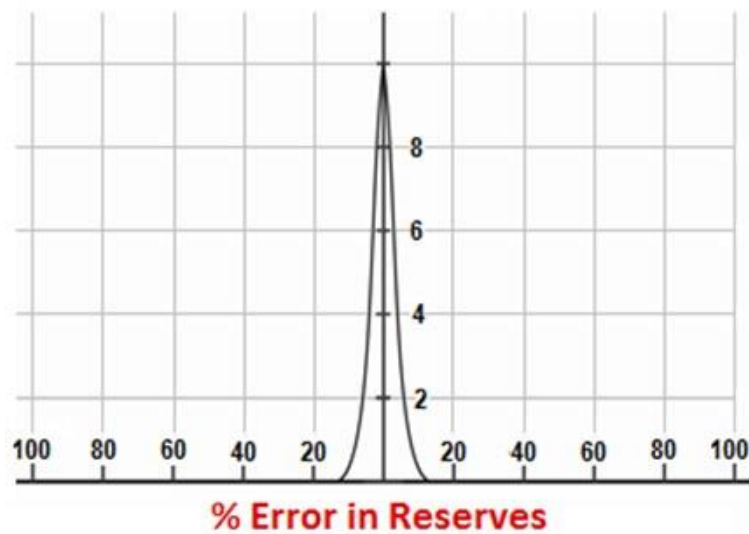
Figure 6.8: High accuracy and high precision [111].
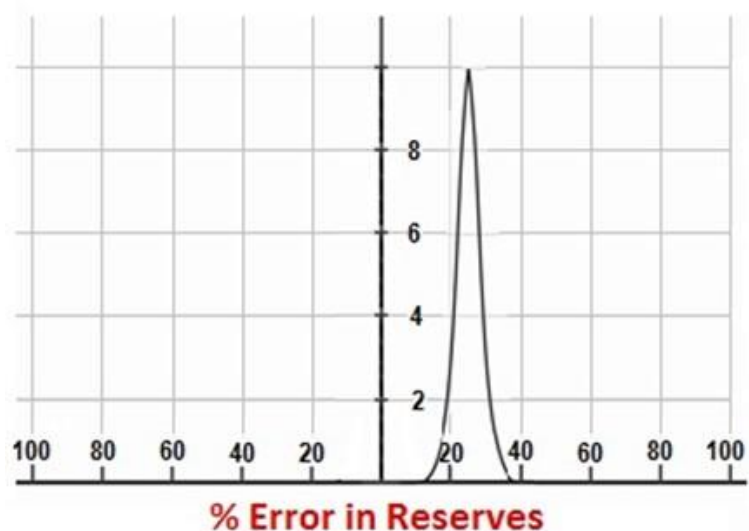
Figure 6.9: High precision but low accuracy [111].
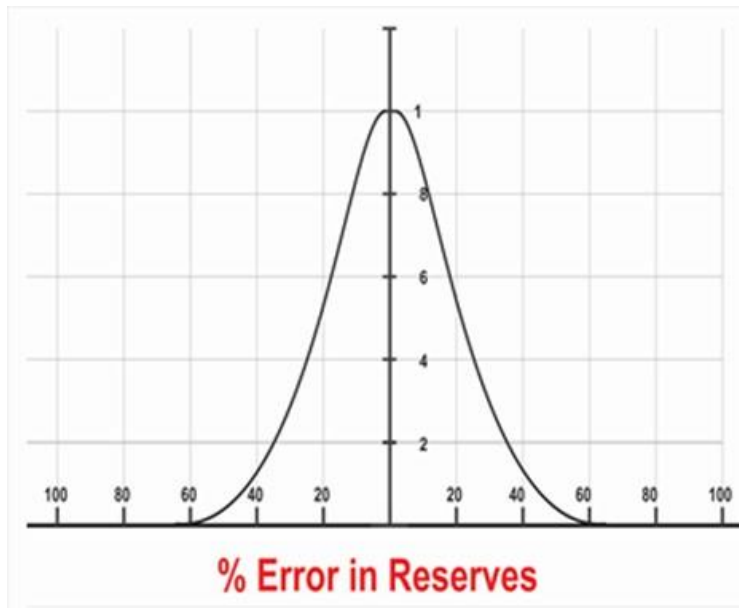
Figure 6.10: High accuracy and low precision [111].
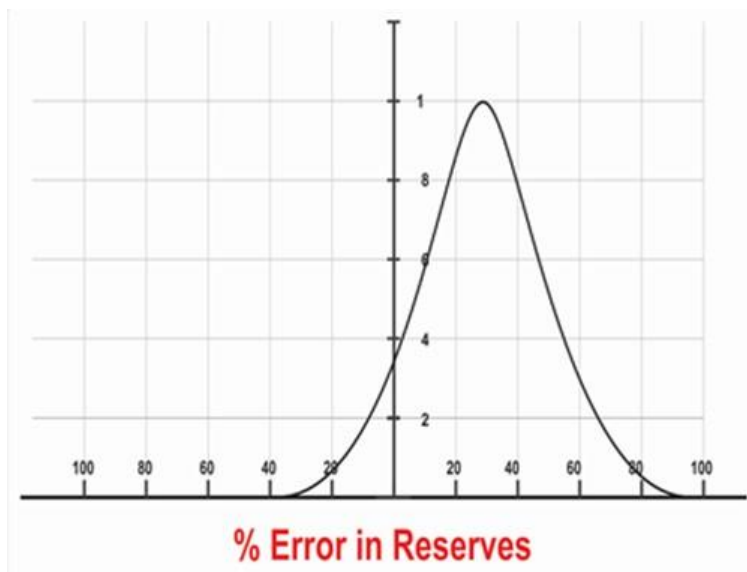
Figure 6.11: Low precision and low accuracy [111].

In this study, the inability of the SEDM to accurately forecast with 6-24 months of historical production data was also observed. It was shown and indicated in Figure 6.12 and Table 6.1 respectively that SEDM does not forecast production accurately when limited historical production data only is available. The SEDM forecast within given 6-18 months of data are consistently declines exponentially, but the SEDM forecasts for match data greater than 24 months are comparable to the Modified Duong ($D_{switch} = 5\%$) and Arps ($D_{min} = 5\%$) forecasts as shown in Figure 6.13.
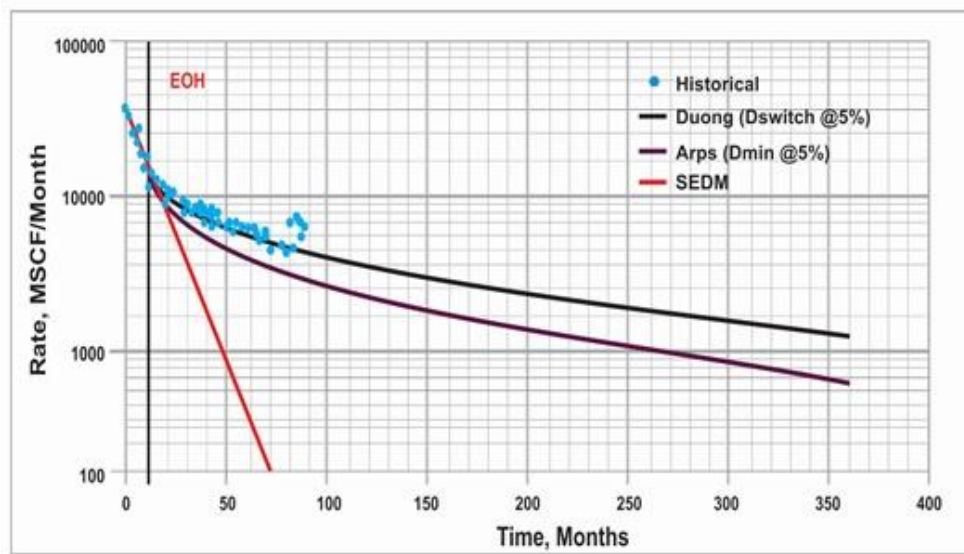
Figure 6.12: Comparison of various empirical models for matching 12 months of historical data [111].
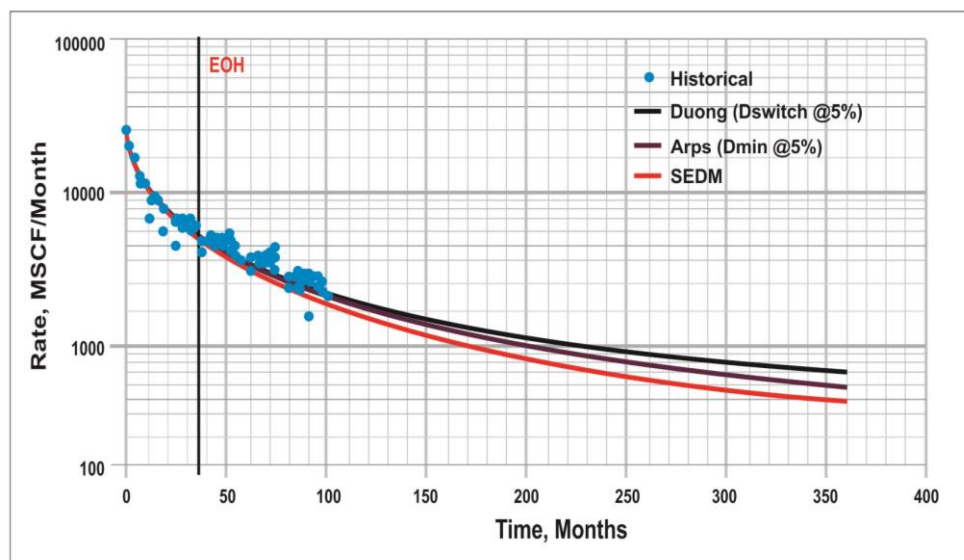
Figure 6.13: Comparison of various empirical models for matching 36 months of historical data [111].

6.1 Comparing Various Deterministic Models Using Simulated Data

There is lack of long term field data on production among the recent developed resources including shale reservoir, to match and forecast production on a long term basis accurately, hence multiple simulations are performed to compensate for lack of long term field data to forecast production in shale wells. Analytical simulation

software was used in Fetekete's Well Test to simulate production data up to 30 years of the well's life. The Barnett shale and the Marcellus shale were simulated in this study. For the software inputs, reservoir and completion properties were used and were consistent with the properties presented in SPE papers such as SPE 133874 (Chong et al., 2010), SPE 146876 (Cipolla et al., 2011), SPE 144357 (Strickland et al., 2011), SPE 96917 (Frantz et al., 2005), SPE 125530 (Cipolla et al., 2010) and SPE 147603 (Ehlig-Economides, 2011) for the Barnett shale, and SPE 133874 (Chong et al., 2010),), SPE 125530 (Cipolla et al., 2010), SPE 144436 (Thompson et al., 2011), SPE 151413 (Lee et al., 2012), SPE 163376 (Shadravan & Amani, 2012) and SPE 147603 (Ehlig-Economides, 2011) for Marcellus shale.

A composite model with horizontal well and multiple fracture stages to simulate a hydraulically fractured horizontal shale gas well was used to simulate the alteration of the effective permeability in the Simulated Reservoir Volume (SRV). For the 50 simulations, the discrepancy/error in the remaining production is shown in Table 6.2. At early time (6 month) it is evidence that the Modified Arps (D_{min} 5%) works best. The simulated data results in comparison to the results of the field data are closely parallel to the trend of the field data. None of the model forecast accurately for short match histories (6 months) compared to the field data even though Arps ($D_{min}=5\%$) method perform best with lowest standard deviation and mean in the error/discrepancy of remaining reserves. The Modified Duong model for the rest of the match histories (12-48 months), turn out to be the best method except in the 36th month case where the SEDM and Duong model have similar statistics. It was concluded for the field data that Modified Duong model for match histories between 12 and 24 months works well. As more history is match, the SEDM and the Modified Arps ($D_{min}=5\%$) forecasts become more accurate. The models that are better statistically are shaded yellow in the tables similar to the field data modeled. The data from Table 6.2 is graphically displayed in Figures 6.14 and 6.15. For the field data, the SEDM underestimates the future production for shorter periods as shown in Figure 6.14. All models forecasts are similar after 36 months but the more accurate representation of the true EUR forecast was provided by Duong model.

Table 6.2: Comparison of discrepancy (% error) in remaining production for Modified Duong, SEDM and Arps (Dmin=5%) for a simulated data set [111].

History Matched (months)		Duong_Dswitch@5%	App (Dmin 5%)	SEPD
6	Mean	22.23	-12.38	38.62
	Std.Dev	19.56	19.80	14.39
12	Mean	5.55	-15.17	22.37
	Std.Dev	17.43	20.98	17.96
18	Mean	-4.33	-18.27	21.40
	Std.Dev	16.09	21.16	19.36
24	Mean	1.00	-18.64	14.96
	Std.Dev	13.10	18.47	18.31
36	Mean	-5.04	-16.79	10.32
	Std.Dev	17.88	13.31	16.24
48	Mean	-5.45	-13.75	10.41
	Std.Dev	18.08	10.81	18.72
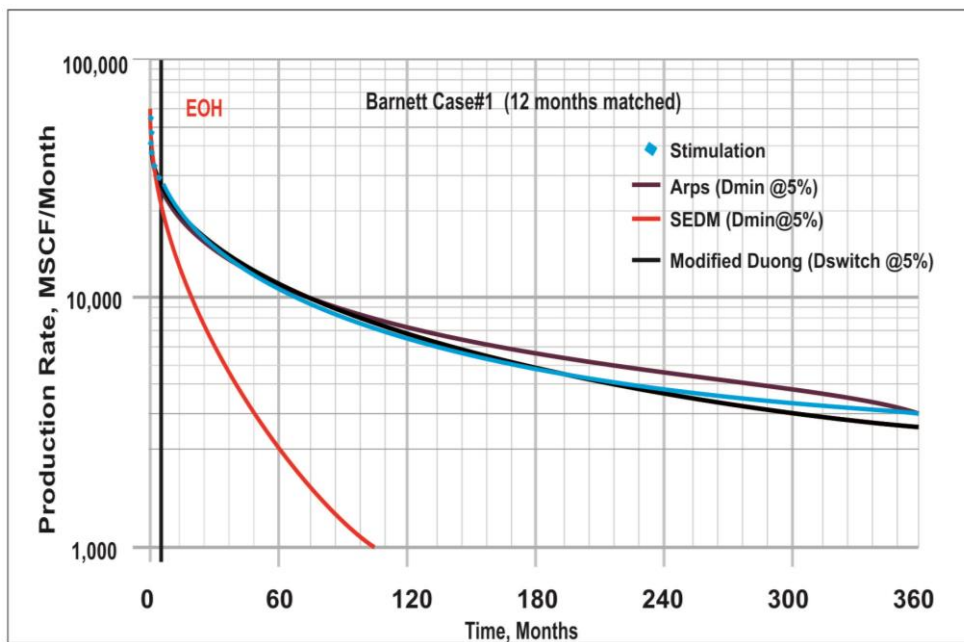
Figure 6.14: Comparing various empirical models for a Barnett simulation matching 12 moths of historical data [111].
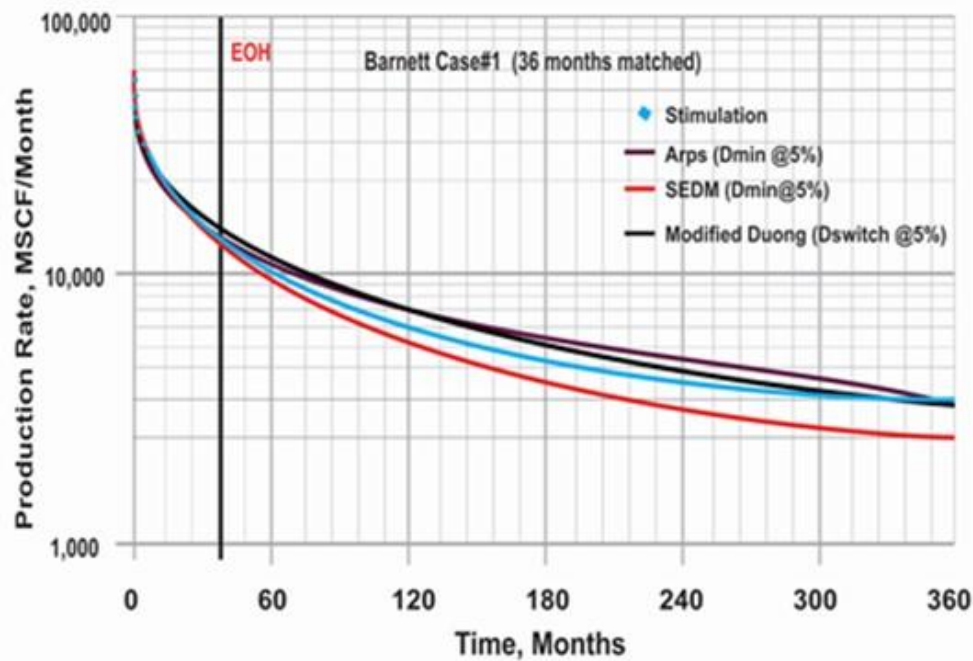
Figure 6.15: Comparing various empirical models for a Barnett simulation matching 36 months of historical data [111].

6.1.1 Comparing various deterministic models for grouped datasets

All the analysis performed up to now was on individual wells. Using grouped dataset in shale gas reservoirs can reduce processing time substantially. The behavior of different decline models when applied to grouped data sets are shown in Figures 6.16, 6.17 and 6.18. The forecasting model with the least discrepancy in remaining production such as in the case of the individual data sets is shaded yellow in the tables. Decline model comparisons for 130- wells in the Johnson County, Texas (Barnett shale) are shown in Figure 6.16 and the results of various models for 18 months of matched history are displayed in Table 6.3. It can be seen that apart from the Arps (D_{min}=5%) model which overestimates the true production, the SEDM and Duong models gives reasonable forecasts.

The model comparison of a group of 81 wells from the Barnett shale is shown in Figure 6.17. For the same wells, various models forecast results after 36 months of production history are given in Table 6.4. Similar to the case for Johnson County, Arps (D_{min}=5%) model over estimates the true production and the Duong and SEDM methods give reasonable forecasts. It is observed in Figure 6.17 that Duong method the yields the lowest discrepancy in remaining reserves for the well set.

In the Wise County the Arps (D_{min}=5%) model overestimated the production as compared to the true (observed value for field data) historical data similar to the previous two Barnett Counties, and the SEDM and Modified Duong (D_{switch}=5%) provides acceptable results but in the case the smallest discrepancy was provided by SEDM as can be seen in Table 6.5.

In the Van Buren County, AR (Fayetteville shale), 107 grouped wells with model comparisons are shown in Figure 6.19 and Table 6.6 shows 18 months matched history of various models results. For this group, the Arps (D_{min}=5%) model underestimate the true production and a reasonable forecast again was produced by both SEDM and Duong model with SEDM providing the lowest discrepancy in remaining reserves.
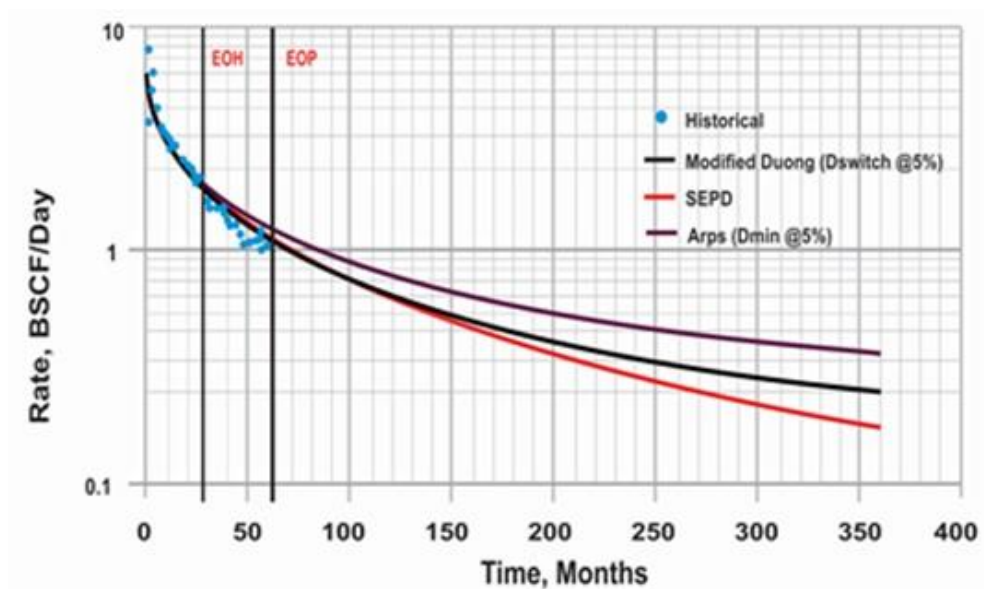
Figure 6.16: Comparison of 3 empirical models for a 130-well Johnson County group using 18 months of matched data [111].

Table 6.3: Discrepancy (% error) in remaining reserves for 130-well Johnson County group [111].

Method	Reserves (after EOP) (B scf)	Average Reserves (after EOP) (B scf / well)	% Discrepancy
Arps (D_{min} @ 5%)	197.168	1.517	-17.7
Modified Duong (D_{min} @ 5%)	132.856	1.022	-4.8
SEPD	116.648	0.897	-7.2
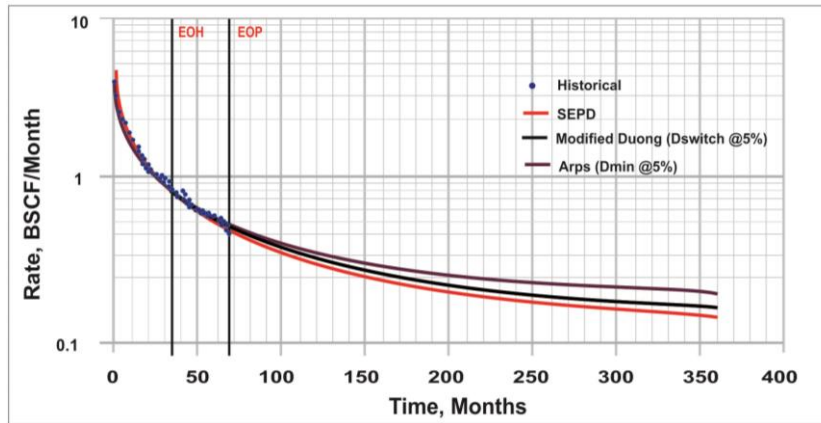
Figure 6.17: Comparison of 3 empirical models for 81-well Denton County group using 36 months of matched data [111].
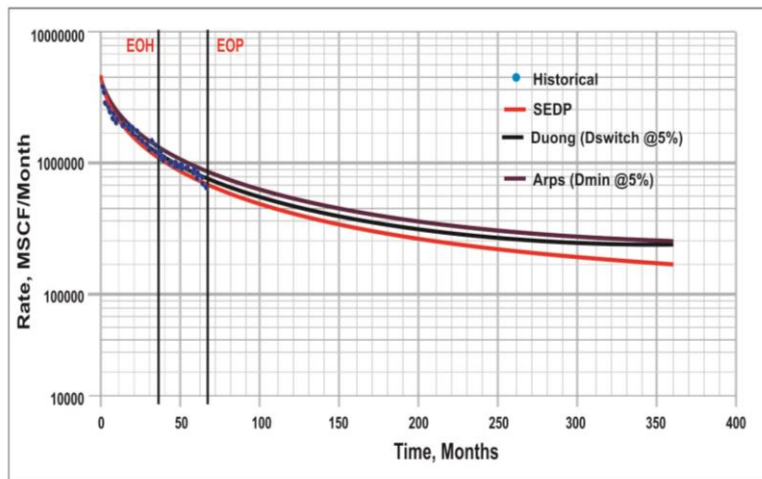
Figure 6.18: Comparison of 3 deterministic models for 127-well Wise County group using 36 months matched data [111].

Table 6.4: Discrepancy (% error) in remaining production for 81-well Denton County group [111].

Method	Reserves (after EOP) (B scf)	Average Reserves (after EOP) (B scf / well)	% Discrepancy
Arps (D_{min} @ 5%)	90.007	1.111	-2.0
Modified Duong (D_{min} @ 5%)	75.244	0.929	1.5
SEPD	71.074	0.877	2.2

Table 6.5: Discrepancy (% error) in remaining production for 127-well Wise County group [111].

Method	Reserves (after EOP) (B scf)	Average Reserves (after EOP) (B scf / well)	% Discrepancy
Arps (D_{min} @ 5%)	153.346	1.207	-9.0
Modified Duong (D_{min} @ 5%)	135.140	1.064	-7.0
SEPD	118.967	0.937	-4.3
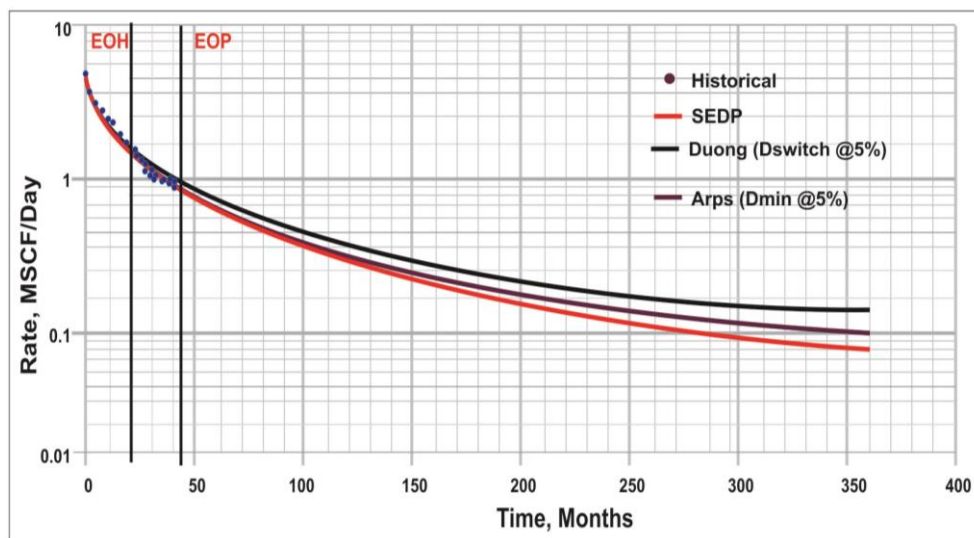
Figure 6.19: Comparison of 3 empirical models for 107-well Van Buren County group using 18 months of matched data [111].

Table 6.6: Discrepancy (% error) in remaining production for a 107-well Van Buren County group [111].

Method	Reserves (after EOP) (B scf)	Average Reserves (after EOP) (B scf / well)	% Discrepancy
Arps (D_{min} @ 5%)	83.092	0.777	7.3
Modified Duong (D_{min} @ 5%)	106.799	0.998	-5.7
SEPD	77.114	0.721	4.4

A proposed model called the Shale Gas Predictive Model (SGPM) which was developed to mitigate challenges associated with the production of shale gas was

presented [113]. This model is simple and easy to use and focuses much on the flow around individual wells while overall mass is conserved. The primary production mechanism from shale is attributed to the fracture network in the reservoir. The reside gas in the shale matrix system is forced to flow through chemical desorption and then through diffusion into the fracture network to travel to the matrix-fracture interface. Gas that exists in the free-state in the fracture apart from the adsorbed gas can also flow to the wellbore. Within trends shale vary both vertically and aerially and these alterations demand stimulation changes within a single to obtain best recovery and also for shale wells there is no one-size-fits for all completion designs. For shale gas deposits, key reservoir parameters include reservoir thickness, total organic content, thermal maturity, free gas saturation, adsorbed gas fraction and permeability. The initial gas production rate of which may persist for more than 20 years decline rapidly to a fairly low rate.

The nature of the isotherm curves and the depth of the reservoir (reservoir pressure) determine the dominant mechanism. Fractures which can be present either naturally or hydraulically fractured or both are critical for the reservoir shale gas production. To assume a dual porosity/permeability system and additional near wellbore grid resolutions to mimic the hydraulic fractures is the common way by which shale gas production is modeled. To model gas production from shale, the primary components are;

(a) Gas flow from tight matrix into fractures, (b) Characterizing the matrix blocks, that is well spacing, (c) Conductivity of fracture network, (d) Gas desorption and diffusion process, and (e) Stress sensitivity of the flow properties of the fracture network.

To build a proper shale gas simulator, the necessary design parameters and sufficient conditions that should be considered must be presented [114]. Much was emphasized on two defining features (non-instantaneous dynamic distribution of fluid and transport of fluids in interconnected nano-pores) that make modeling of these reservoirs different from the conventional systems. To account for a fairly complicated reservoir pore structure, the advocates for a quad-porosity that includes pores in the organic matter, inorganic matter, natural and hydraulic fractures with heterogeneous wettability, and different relative permeability and capillary pressure functions. Further, to avoid overestimation of gas-in-place, proper formulation

accounting for the effects of adsorbed gas, pore-size and compressibility effects. In tight porous media, the intrinsic permeability should be corrected for fluid behavior and pore-size distribution. Fluid properties to wall proximity and non-instantaneous capillary equilibrium effect and rate-dependency of relative permeability correction should be incorporated to account for the gradual re-distribution of fluids, was stated as a recommendation.

To capture gas flow behavior from shale gas, different methods are cited in literature. Detailed physical processes describing models can be built in a numerical setting where fractures can be discretely modeled matrix blocks are assigned to transfer gas into fracture blocks through desorption and diffusion (e.g. Cipolla et al., 2009; Rubin, 2010; Lewis, 2004; Wang, 2011; Mangalvy, 2011). To accommodate acceptable accuracy without consuming prohibitive CPU time, different techniques are prescribed in achieving this goal. It is suggested for instance that the Stimulated Rock Volume (SRV) can be modeled as a Local Grid Refinement (LGR) with different properties of the fracture in an otherwise Dual-Permeability based grid with larger fracture spacing [115]. The conceptual argument was that the highly non-linear and complex SRV fracture network which effectively connects the exposed reservoir surface area to the wellbore is the major source for production, hence should be emphasized in the modeling environment. It was also maintained that both the pressure dependent fracture and desorption properties can influence production towards only the latter part of the production history. And as such it is difficult to forecast productivity based on the early life of the well. In literature there are other attempts to modeled fractures directly using Discrete Fracture Network. Another important aspect of fracture conductivity determination (which results in the gas production in shale gas well ultimately) is to model the behavior pf proppant in both propped and un-propped fractures. Proppant transport is commonly accounted for through correlations established in experiments since it is not very well understood. But it is very important to note that, in all these detailed approaches there are several shortcomings. For instance, the grid-based numerical techniques such as highly conductivity elements to represent fractures usually are resource intensive and time consuming. An optimal collection of algorithms available can be the best-of-art-practice for conventional reservoirs very well. Generally, selection of this collection requires expertise and experience. For small to medium size company eager to go

into shale gas production, this may be a bottleneck and discouraging. A quick and intuitive technique that can provide go-no-go business decision making capability is usually required. Reservoir engineers additionally need to frequently prepare reserves estimates where a methodology that can focus on well-by-well basis is needed. In this situation of shale gas production to be specific can be cumbersome and usually over-ambitious especially where numerous wells are drilled in smaller spacing to set up, execute and maintain a grid-based simulation model. Hence the desired model is the one that concentrates on individual wells and runs relatively quickly to enable repeatability and faster turnaround.

There are other techniques published in literature that modify existing material balance techniques for conventional reservoirs to address this issue specifically. Specific to unconventional reservoirs, attempts were made to preserve the equations similar to conventional reservoirs using modified variables, for instance p/z* instead of P/Z. however, these analytic techniques have the usual drawbacks of over-simplified geometry and underlying physics assumptions.

Specifically, models equipped to shale reservoir declines are developed and published. Probabilistic forecast models that account for inherent uncertainties in model parameters was developed using Stretched-Exponential Decline Model [116].

The conceptual framework of King et al. has been enhanced by SGPM by adding horizontal wells deliverability with multiple intersecting fully penetrating vertical fractures for multi-phase flow [117]. The following points are possible as a result of SGPM;

(a) Addition of concepts of productivity in horizontal wells with multi-stage fractures has enhanced capability of the existing modeling techniques.

(b) The developed models have been agued and tested against production data from different unconventional gas plays.

(c) Visualization mechanism is integrated to examine predictive results, diagnose production results and other intermediate/final computational outputs.

(d) Assimilation of a Windows^{TM} Graphics User Interface (GUI) for the productive tool to upload input data into the software seamlessly and execute the numerical model systematically.

This offers the operator an alternative way to match history, assess and predict reserves in shale gas and other unconventional resources. The turnaround time in the algorithm on one hand is much faster as compared to grid-based simulation techniques, and by incorporating, more physics makes it yield better accuracy compared to simpler analytic techniques on the other hand. The user interface again with the help of data input and the plotting routines makes it possible to analyze the results. Multi scenarios can be compared and contrast using the integrated framework without difficulty.

SGPM model formulation involves solving material balance and deliverability equations simultaneously with inherit conceptual framework [117] and multi-stage fractured horizontal wells deliverability [118]. The feasibility of coupling these two separate concepts whose originality of the algorithm stem from its extension to capture multi-phase flow (gas and condensate), was tested first for both vertical and horizontal wells (Figure 6.20).
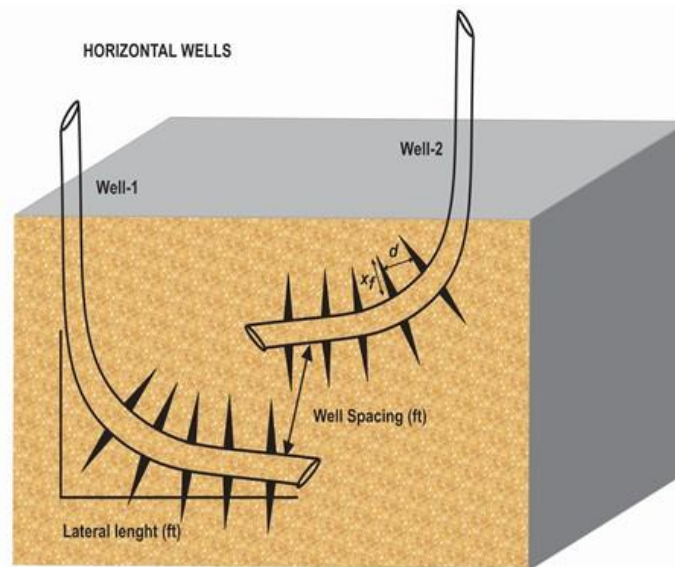
Figure 6. 20: Schematic diagram showing multiple horizontal wells modeled in SGPM [113].

How much a well can produce from a given volume of simulated rock can be computed using the deliverability equations; however, the availability of gas restricts the actual production when the coupled mass balance equation is used. The overall methodology is summarized as follows,

(a) Gas material balance has options for different isotherms and diffusion coefficients

(b) Water material balance equation is coupled in the model to match history production from unconventional gas reservoirs.

(c) Gas, condensate and water inflow equation are modified to reflect multi-stage fracture flow.

(d) Newton method is applied to solve the system of non-linear equations, which improves the convergence properties of the technique.

(e) Finally, advanced graphics are added both to plot simulation results and/or to diagnose existing production behavior. This can reveal possible spatial relationship among flow attributes and expose possible 'sweet' spot in the reservoir.

Equation 6.6 is an example of gas material balance equation presented [117]. When gas condensates are present, appropriate equations are used. It can be notice that the material balance equation is augmented for adsorption, and is active only when the pressure is below desorption pressure. Adsorption for any generic (table look up) or closed form analytic like Langmuir isotherm used in this study can be used.

$$G_P = C(V_b, T)\left\{\frac{(1-S_{wi})p_i}{z_i} - \frac{[1-C_\emptyset\,(p_i-p)](1-S_w)p}{z}\right\} + G_d \qquad (6.6)$$

where, G_p is the cumulative gas production in Bscf, G_d is the cumulative gas adsorption in Bscf, p is the current reservoir pressure in psi, p_i is initial pressure in psi, c_w is the water compressibility in 1/psi, c_ϕ is the rock compressibility in 1/psi, S_w is the current water saturation, S_{wi} is the initial water saturation, z_i is the initial z-factor, z is the z-factor at current reservoir pressure, and $c\,(V_b,T)$ is a function of bulk volume and temperature. Similarly, as shown in equation (6.7), water material balance equation is expressed with

$$S_w = \frac{S_{wi}\,[1-C_w\,(p_i-p)]+\frac{W_e-B_wW_p}{PV}}{[1-C_\emptyset\,(p_i-p)]} \qquad (6.7)$$

where, p is the current reservoir pressure in psi, p_i is initial pressure in psi, c_w is the water compressibility in 1/psi, c_ϕ is the rock compressibility in 1/psi, S_w is the current water saturation, S_{wi} is the initial water saturation, z_i is the initial z-factor, z is the z-factor at current reservoir pressure, W_e is the cumulative water influx and W_p is the cumulative water production in MMstb.

From a horizontal well with multiple fractures, total deliverability can be computed using equation 6.8. A case where 5 equidistance fractures constitute the geometry of the horizontal well is considered as a special case. The derivation of equation 6.8 was based on superposition of the fracture stages. Equation 6.8 in SGPM is generalized to any number of fracture stages. The fractures are however equidistance but can have their half-lengths vary.

$$q_t = \frac{C\Delta m(p)}{\left[\ln\frac{r_e}{(4dr_{we1})^{qr1}(3d^2)^{qr2}(2d)^{qr3}}\right]} \tag{6.8}$$

Where; d is the spacing between hydraulic fractures (ft), $m(p)$ is the gas pseudo pressure (psi^2/cp), q_r is the ratio of rate of a particular hydraulic fracture to total rate, r_e is the drainage radius (ft), r_{we} is the equivalent radius (ft).

The assumptions made are as follows,

(a) The fractures are vertical, transverse, and fully penetrating, and have finite conductivity.

(b) Formation fluid can only enter the wellbore through the fractures at the perforated intervals.

(c) The fractures are placed equidistant from each other along the horizontal lateral.

(d) There is no pressure loss in the lateral length of the horizontal well.

(e) The model accounts for desorption and changing fracture permeability as a result of time dependent reservoir pressure.

Using Newton's method, the non-linear set of equations are linearized and solved for variables of interest (pressure/rates and saturations). This model has never loses its purpose since it was developed exclusively for unconventional reservoirs unlike other models which forces models developed for conventional reservoirs to work for unconventional reservoirs. Addition of asset-specific physics is allowed due to its framework is easily controlled. Alternatively, other dependents models (fracture mechanics, basin analysis model etc.) can be integrated easily to expand its applicability. During history matching the bulk volume (simulated volume) of the reservoir that the well is exposed to, can pose a problem. Providing post-job look-back of the efficacy of the fracture job, this can be argued to be the SRV.

The Marcellus shale, which extends to west central New York to the northeast and extends to Pennsylvania, Ohio and West Virginia to the southeast, has its minor portions in Virginia and Maryland. The total organic content of the black shale that is deposited at a depth of 4,000 -8,500 feet is 3-12%. This shale was formed because of the deposition of organic material when shallow continental seaway existed in the area, followed by rapid burial of these deposits because of plate tectonics in the area believed to be the source material for the natural gas present. The horizontal well of the Marcellus shale was modeled, the inputs properties in Table 6.7 and the gas rate match, and the associated cumulative production in one year approximately is shown in Figure 6.21 below.
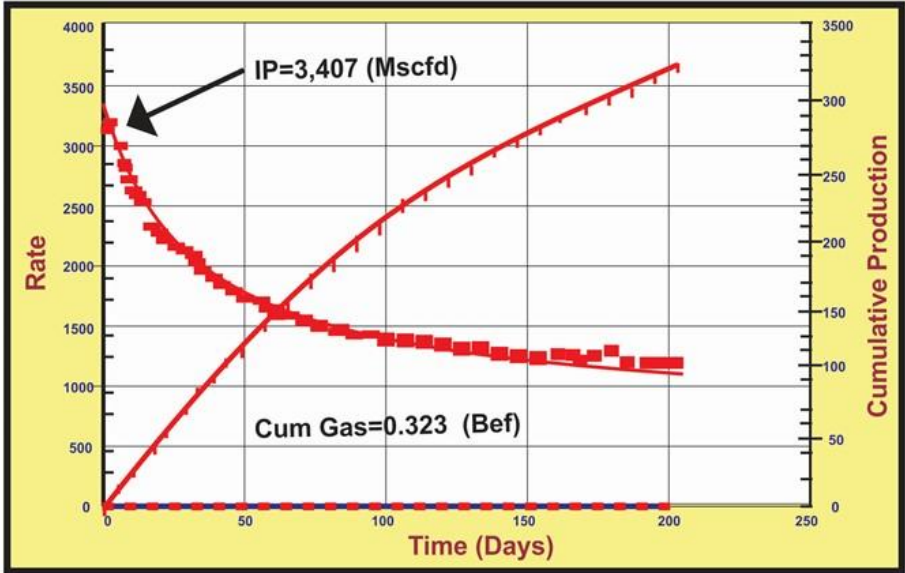
Figure 6.21: The match to gas production rate and cumulative production in Marcellus shale play [113].

This rapid burial of the sediments resulted in the generation of high pressure and temperature required for the formation of oil and gas in large quantities entrained in the shale matrix porosity. The uplift and erosion of the Marcellus formation subsequently has resulted in the natural formation of vertically oriented fractures [119].

In the lower Antrim shale, productions come from two black-shale intervals (the Lachine which is 80-120 feet thick and the Norwood which 20-50 feet thick). Gas in the Antrim shale is primarily sorbed gas with a concentration ranging from 50-100 scf/ton, is biogenic of origin. Productivity is largely depends on the development of natural fractures that are well connected and are initially water saturated.

In the lower Antrim shale, productions come from two black-shale intervals (the Lachine which is 80-120 feet thick and the Norwood which 20-50 feet thick). Gas in the Antrim shale is primarily sorbed gas with a concentration ranging from 50-100 scf/ton, is biogenic of origin. Productivity is largely depends on the development of natural fractures that are well connected and are initially water saturated.

Table 6.7: Input data used for Marcellus shale play simulation.

Depth (ft)	7,876
Thickness (ft)	162
Reservoir pressure (psi)	1,250
Desorption pressure (psi)	1,225
Diffusion coefficient (ft^2/day)	0.005
Lateral length (ft)	2,100
Fracture half-length (ft)	125
Number of stages	7
Simulated volume (Bcf)	4.02

An average of 50Mscf/d of gas and 25bbl/d of water from 8,300 wells was produced in 2005, and with high concentration of CO_2 the gas rate very from well to well. Out of 10Tcf of gas potential, cumulative production of 2Tcf has been produced. The wells depths in the Antrim shale ranges from 400 to 2,000 feet deep and after 6 to 12 months of dewatering, gas production is 125 to 200 Mscf/d with decline of 8% per year after two years. At a spacing of 30 to more than 160 acres per well, typical well produces, a cumulative of 400 to 800 MMscf with initial gas in place of 5 to more than 35 Bcf/square mile. Most wells hydraulically fractured in two stages with nitrogen-foam, were vertically drilled.

Table 6.8 values were used as input properties to model the vertical wells in the Antrim shale. The gas rate match and cumulative production associated for about 20 years of production are shown in Figure 6.22 below.
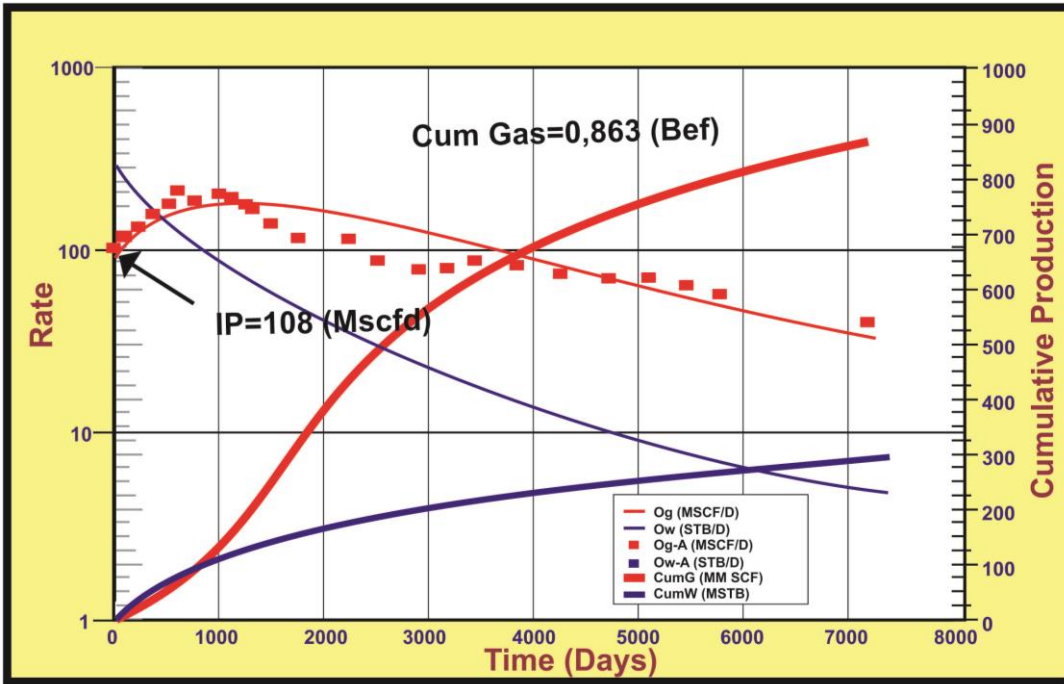
Figure 6.22: Production match showing gas rate and cumulative production in Antrim shale play [113].

Table 6. 8: Input data used for Antrim shale play simulation.

Depth (ft)	1,000
Thickness (ft)	100
Reservoir pressure (psi)	400
Desorption pressure (psi)	380
Diffusion coefficient (ft^2/day)	0.30
Simulated volume (Bcf)	4.14

6.1.2 Multiphase flow-eagle ford production

The Eagle Ford formation that is known for its hydrocarbon rock potential (sourcing overlaying Austin Chalk) has been considered as recently as a potential target for exploration. The Eagle Ford formation is between 5,000 feet and 13,000 feet below the surface in South Texas where it has hydrocarbon potential and its thickness ranges from 50 feet to 300 feet. This formation is composed of organic-rich calcareous mudstones and chalks that were deposited during the transgressed sequences. The deeper deposit (10,000-13,000 feet) which is oxygen deficient tend to be organic rich and have resulted in the productions of large quantities of dry gas from the wells. The shallower Eagle Ford (5,000-8.500) on the other hand, is much

more condensate rich gas and potential volatile oil in the shallowest areas since it has not attained the hydrocarbon maturity level.

With the input properties in Table 6.9, and gas condensate input properties in Table 6.10, the Eagle Ford shale horizontal well producing dry gas was modeled and the gas production rate and cumulative production associated with about first 250 days of production are shown in Figure 6.23. Production match showing gas/condensate rate and cumulative production in Eagle Ford shale play is shown in Figure 6.24

Table 6.9: Input data used for Eagle Ford shale play simulation (dry gas).

Depth (ft)	10,875
Thickness (ft)	283
Reservoir pressure (psi)	8,350
Desorption pressure (psi)	200
Diffusion coefficient (ft2/day)	0.006
Lateral length (ft)	4,000
Fracture half-length (ft)	100
Number of stages	10
Simulated volume (Bcf)	2.0

Due to the divergence between oil and gas prices on a Btu equivalent basis, the recent trend of exploiting liquid rich shale such as the Eagle Ford, Woodford, Marcellus etc., is understandable. Producing from the condensate window however has its own complexities. For beginners, condensate begins to drop out of the gas when the pressure falls below dew point pressure. To gas and condensate production the condensate drop out in the reservoir is detrimental, and condensate has to build up to a critical saturation before it starts to flow. The condensates until it flow exerts an additional resistance to gas flow which finally results in lower gas as well as condensate recovery. Due to the increased pressure drop, there is a higher possibility of condensate drop out near the matrix fracture interface when wells in conventional reservoirs are hydraulically fractured (as in the case for shale gas reservoirs). To forecast recovery, the dry gas model described and validated in the previous sections is therefore inadequate. Special gas inputs for gas condensate are required to complete the model data since the model was increased to handle liquid production. In addition, PVT and relative permeability values for the gas condensate system are needed in addition to the data provided for the dry gas. The mathematical model is refurbished to include two-phase (gas condensate) mass balance equation and appropriate deliverability equation for condensate is incorporated. The model which

reports condensate rate and saturation also solves for rate and pressure (as before). To match past production history or forecast production, the model can still be used.

Table 6.10: Input data used for Eagle Ford shale play simulation (gas condensate).

Depth (ft)	8,608
Thickness (ft)	224
Reservoir pressure (psi)	6,568
Desorption pressure (psi)	5,700
Diffusion coefficient (ft2/day)	0.040
Lateral length (ft)	4,000
Fracture half-length (ft)	100
Number of stages	12
Simulated volume (Bcf)	17.0
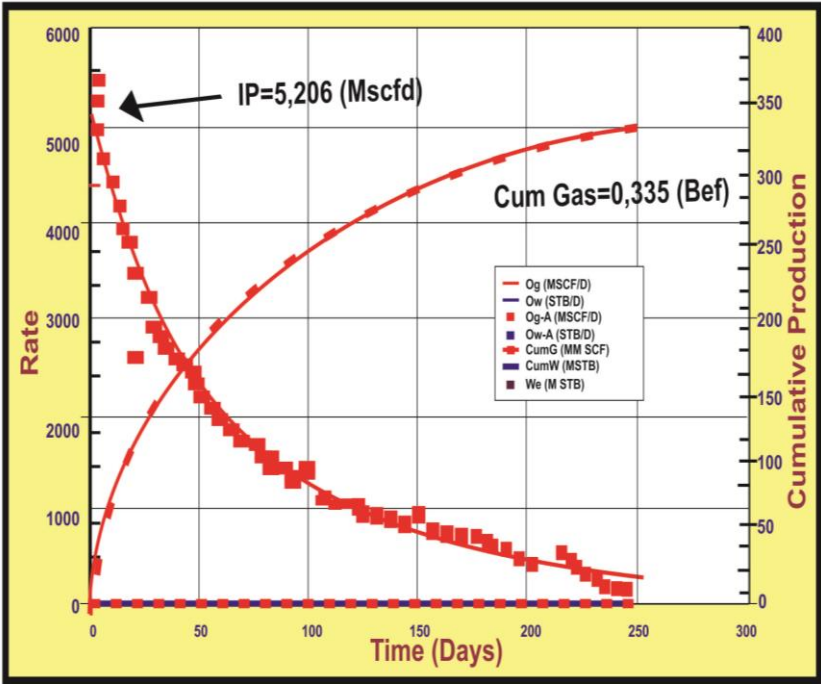
Figure 6. 23: Production match showing gas rate and cumulative production in Eagle Ford shale play [113].

From the Eagle Ford shale play, a representative well with limited production known to be producing from the condensate window was selected to demonstrate the significance of the two-phase model. The production data match and the associated data are presented in Figure 6.22 and Table 6.10 respectively. The behavior of the pressure and condensate saturation build up associated are exhibited in Figure 6.25.

The used data for the history matching and the data reported for the well are similar [120].

From the Eagle Ford shale play, a representative well with limited production known to be producing from the condensate window was selected to demonstrate the significance of the two-phase model. The production data match and the associated data are presented in Figure 6.22 and Table 6.10 respectively. The behavior of the pressure and condensate saturation build up associated are exhibited in Figure 6.25. The used data for the history matching and the data reported for the well are similar [120].
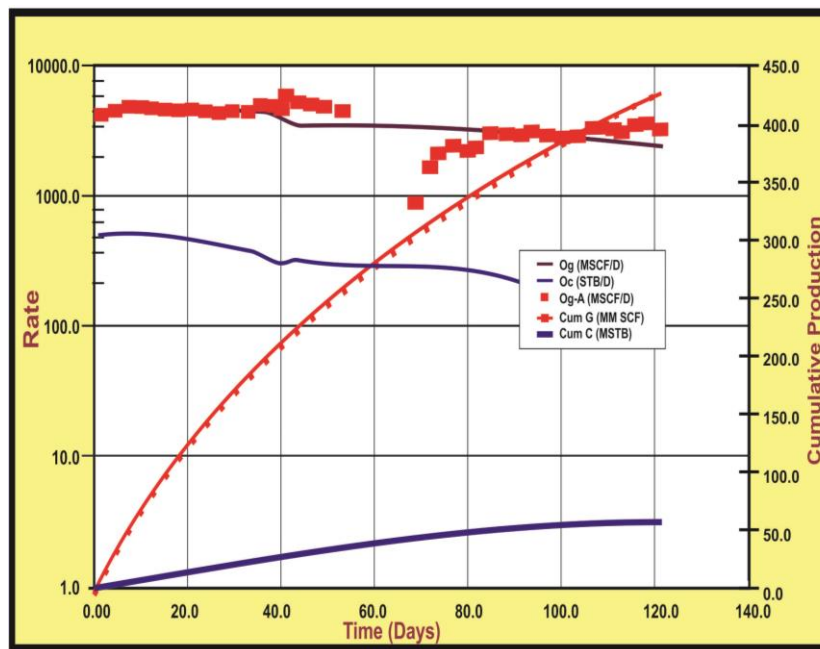
Figure 6.24: Production match showing gas/condensate rate and cumulative production in Eagle Ford shale play [113].

Another important feature for SGPM is that, several wells can be investigated as separate cases within a project. Their production attributes such as cumulative production, initial pressure, final pressure, maximum gas rate, 3-months cumulative production etc. can be viewed in a 3-dimensional plot as shown in Figure 6.26 once acceptable history matches or forecast is executed on each of them, to examine the spatial relationship. This feature can identify possible sweet spot in the shale play.
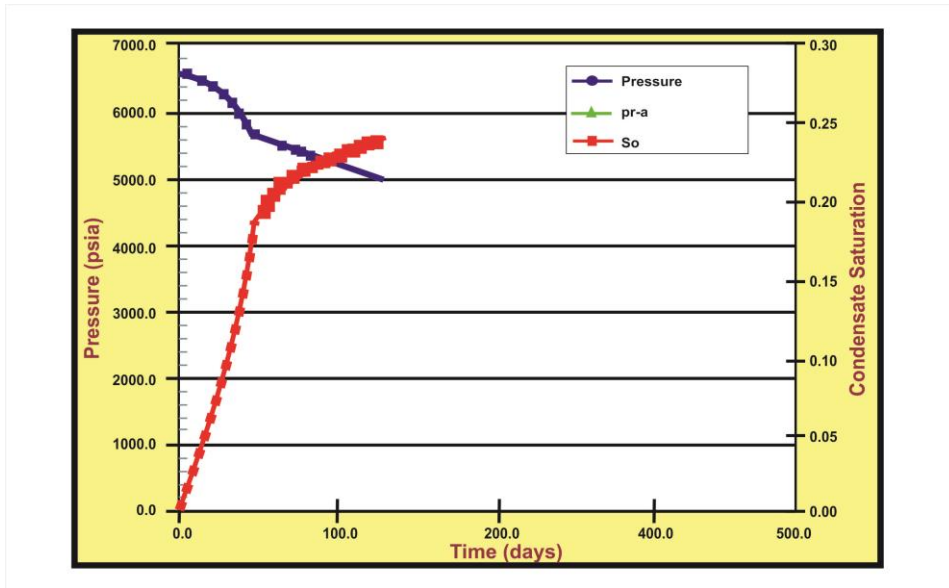
Figure 6.25: Pressure and saturation build up for Eagle Ford shale play [113].
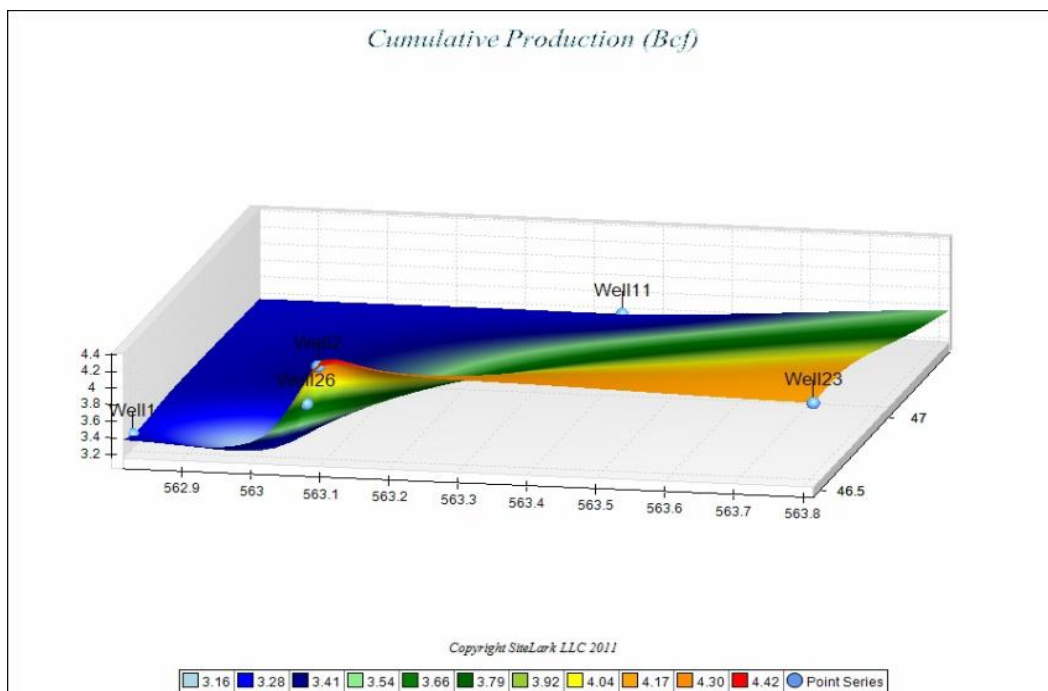
Figure 6.26: A 3-D plot showing spatial relationship for cumulative production of wells in close proximity to one another [113].

Nobakht et al. evaluate methods that are currently used to analyze linear flow in shale gas reservoirs, and the method that is accurate for shale gas reservoirs was established [121]. They started with a brief review of recently studies that addressed linear flow under constant flowing pressure and constant gas rate production, then

238

methods for calculating fracture half-length or contacted matrix surface area were compared and finally, a method for the analysis of linear flow for real data where both gas rate or flowing pressure is not constant was presented and validated using three numerical simulation cases.

Due to the fact that linear flow to fracture is the dominant flow regime that last for a long time in horizontal wells with multiple fractures which is the most effective method to exploit extremely low permeability reservoirs, there has been extensive studies conducted on analyzing this linear flow in these extremely low permeability reservoirs. The square root-time plot which is a plot of rate-normalized pressure versus square root of time is the most commonly method used for linear flow analysis. Nobakht and Clarkson proved that the assertion documented in literature that, linear flow appears as a straight line on the square root-time plot is not true [122]. A number of numerically-simulated cases in which the linear flow forms a straight line on the square root-time plot in the early time were presented. But the data deviates from the straight line as time goes on. It was also showed in contrast to the constant gas rate production that, the square root-time plot is a straight line for constant flowing pressure production.

At a constant flowing pressure, linear flow theory [123] shows that a plot of $\frac{1}{q}$ versus $\sqrt{t}$ on Cartesian coordinates is a straight line. In the literature, the slope of this line is used to calculate, $x_f\sqrt{k}$. Where x_f is the fracture half-length and k is the permeability, for gas

$$x_f\sqrt{k} \;=\; \frac{315.4T}{h\sqrt{(\Phi\mu_g C_t)_i}} \; \text{X} \; \frac{1}{P_{Pi} - P_{Pwf}} \; \text{X} \; \frac{1}{m_{CP}} \tag{6.9}$$

Where, T is the reservoir temperature (°R), Φ is the reservoir porosity (fraction), μ_g is the gas viscosity (cp), C_t is the total compressibility (psi^{-1}), P_{Pi} is the Pseudo-pressure at initial pressure (psi^2/cp), P_{Pwf} is the Pseudo-pressure at flowing pressure (psi^2/cp) and m_{CP} is slope of $\frac{1}{q}$ versus $\sqrt{t}$.

When analyzing tight gas reservoir the use of equation (6.9) however overestimates the value of $x_f\sqrt{k}$ since the equation (6.9) and the square root-time plot do not account for changing gas compressibility with pressure.

It was proposed [124], [125] to multiply $x_f\sqrt{k}$ obtained from equation (6.9) by empirically- obtained correction factor, f_{CP}, under constant flowing pressure condition.

$$f_{CP} = 1 - 0.0852D_D - 0.0857D_D^2 \tag{6.10}$$

Where D_D is drawdown parameter and is related to Pseudo-Pressure at initial pressure, P_{Pi}, and Pseudo-Pressure at flowing pressure, P_{Pwf}, using equation (6.11):

$$D_D = \frac{P_{Pi} - P_{Pwf}}{P_{Pi}} \tag{6.11}$$

Nobakht and Clarkson during constant flowing pressure production, studied linear flow in detail [122] and showed that the overestimation of $x_f\sqrt{k}$ with equation (6.9) is as a result of the square root-time plot not accounting for gas compressibility changes with pressure which is incorporated into Pseudo-time, t_a,

$$t_a = (\mu_g C_t)_i \int_0^t \frac{dt}{\bar{\mu}_g \bar{C}_t} \tag{6.12}$$

where, $\bar{\mu}_g$ and $\bar{C}_t$ are gas viscosity and total compressibility at the average reservoir pressure. Also inaccuracy arises when the average reservoir pressure in equation (6.12) is used to estimate $x_f\sqrt{k}$. It was proposed that, this can be corrected by using corrected Pseudo-time [121] where the viscosity of the gas and total compressibility in equation (6.12) are evaluated at average pressure in the affected region. Nobakht and Clarkson demonstrated by using the material balance equation in the region of influence [122], that the average pressure in the region of influence is independent of time at constant flowing pressure linear flow in the reservoir geometry (Figure 6.27), and this resulted in the formulation of new Pseudo-time having a linear relationship with time:

$$t_{a,CP} = \frac{(\mu_g C_t)_i}{\bar{\mu}_g \bar{C}_t} t \tag{6.13}$$

Here $t_{a,CP}$ is the corrected Pseudo-time for linear flow at constant flowing pressure.
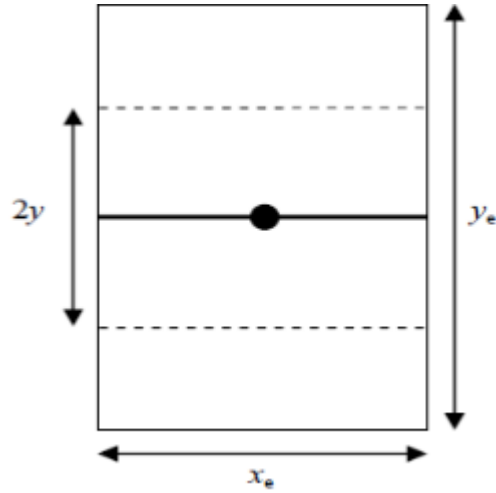
Figure 6.27: A hydraulically fractured well in the center of a rectangular reservoir [121].

It was concluded that to eliminate the overestimation of $x_f \sqrt{k}$ the slope of inverse gas rate versus square root of corrected Pseudo-time plot should be used in equation (6.9) when analyzing linear flow at constant flowing pressure. Since a plot of inverse gas rate versus square root-time is a straight line for linear flow at constant flowing pressure and the plot of inverse gas rate versus square root of corrected Pseudo-time plot is a straight line, the corrected Pseudo-time has a linear relationship with time. For analyzing linear flow at constant flowing pressure, the following procedure was proposed the:

(1) Plot $\frac{1}{q}$ versus $\sqrt{t}$ on Cartesian coordinates. The data should form a straight line during linear flow. Determine the slope of the line, m_{CP}.

(2) Calculate $x_f \sqrt{k}$ using equation (6.9).

(3) Calculate the average pressure in the region of influence, $\bar{P}$, from the following equation:

$$\frac{\bar{P}}{\bar{Z}^{**}} = \frac{P_i}{Z_i^{**}}\left[1 - 0.220\frac{(Z\mu_g C_t)_i(P_{Pi}-P_{Pwf})}{S_{gi}P_i}\sqrt{\frac{\bar{\mu}_g \bar{C}_t}{(\mu_g C_t)_i}}\right] \tag{6.14}$$

Where $\bar{Z}^{**}$ and Z_i^{**} are modfied Z-factor introduced by Moghadam et al. [127] at average pressure in the region of influence and initial pressure respectively, Z is the gas compressibility factor, P_i is the initial pressure and S_{gi} is initial gas saturation.

This equation is valid during transient linear flow and not after the onset of boundary-dominated flow.

(4) Using the average pressure in the region of influence calculated in the previous step, calculate the correction factor, $(f_{CP})_m$:

$$(f_{CP})_m = \sqrt{\frac{(\mu_g C_t)_i}{\bar{\mu}_g \bar{C}_t}}$$ (6.15)

(5) Multiply $x_f \sqrt{k}$ calculated in step 2 by the correction factor calculated in step 4. Again linear flow of gas under constant production rate was studied in detail [122] and it was demonstrated that the average pressure in the region of influence, unlike the constant flowing pressure case, is time-dependent for linear flow at constant production rate in the reservoir geometry (Figure 6.27). Ideal gas with constant viscosity and total compressibility dominated by gas compressibility was assumed, and equation (6.12) was used to   showed that the corrected Pseudo-time for constant rate of production, $t_{a,CR}$, becomes:

$$t_{a,CR} = t - \frac{2,000 q B_{gi} \sqrt{(\Phi \mu_g C_t)_i}}{3 \times 4 \times 0.113 h \Phi S_{gi} x_f \sqrt{K}} t \sqrt{t}$$ (6.16)

At early times under the assumption made, this equation show that $t_{a,CR} \approx t$ and it means during early time, the square root-time plot is a straight line. At late times where $t_{a,CR} < t$ the plot of square root-time deviates from the early-time straight line eventually and the time that transition begins depends on rate of gas production, hence the shape of the plot of square root-time depends on rate of gas production. The square root-time plot for three different rates for the reservoir geometry (Figure 6.27) is shown in Figure 6.28 with the following parameters: P_i=10,000psi, T= 120°F, K= 0.01md, h= 100ft, Φ= 10%, S$_g$= 100%, γ_g= 0.65, x_f= 250ft, x_e= 500ft, y_e= 5,000ft and c_f= 0.

Instead of using square root-time, it was suggested to use the square root of corrected Pseudo-time in the square root-time plot [122]. The data used to generate Figure 6.28 was plotted against square root corrected Pseudo-time in Figure 6.29, and it can be seen that the rate dependence of the square root-time plot is almost eliminated by using the corrected Pseudo-time. To analyze the linear flow under constant gas rate

of production with regards to constant pressure, the following procedure was proposed:
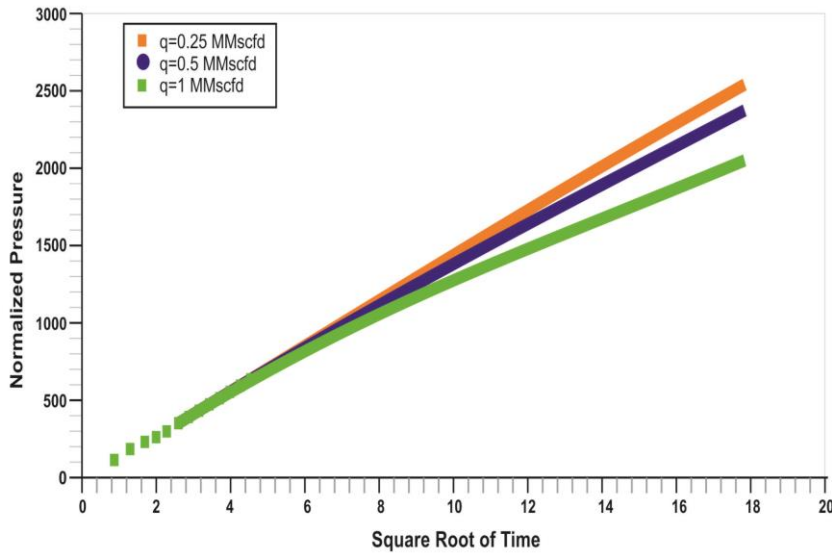
Figure 6.28: Plot for constant rate linear flow rate-dependence in the reservoir geometry shown in Figure 6.27 [121].

(1) Plot $P_{Pi} - P_{Pwf}$ versus $\sqrt{t}$ on Cartesian coordinates, place a line through early-time data points and determine the slope of the line, m_{CR}.

(2) Using the slope determine in step 1, calculate $x_f \sqrt{k}$ using equation (6.17):

$$x_f \sqrt{k} \quad = \frac{200.8Tq}{h\sqrt{(\Phi\mu_g C_t)_i}} \times \frac{1}{m_{CP}} \tag{6.17}$$

(3) Calculate the average pressure in the region of influence at different times using equation (6.18):

$$\frac{\bar{P}}{\bar{Z}^{**}} \quad = \frac{P_i}{Z_i^{**}} \left(1 - \frac{1,000qB_{gi}\sqrt{(\Phi\mu_g C_t)_i}}{4 \times 0.113h\Phi S_{gi}x_f\sqrt{K}} \sqrt{t} \right) \tag{6.18}$$

(4) Calculate the corrected Pseudo-time for constant rate production, $t_{a,CP}$, form equation (6.12) and by using average pressure in the region of influence calculated in step 3. Note that equation (6.16) is not used in this step for calculating $t_{a,CR}$ as this equation is developed assuming that gas is ideal with constant viscosity and the total compressibility is dominated by gas compressibility.

(5) Plot $P_{Pi} - P_{Pwf}$ versus $\sqrt{t_{a,CR}}$ on Cartesian coordinates. Place a line through early-time data points and determine the slope of the line, m_{CR}.

(6) Using the slope determine in step 5, calculate $x_f \sqrt{k}$ using equation (6.17).

(7) Continue step 3-6 until $x_f \sqrt{k}$ converges.
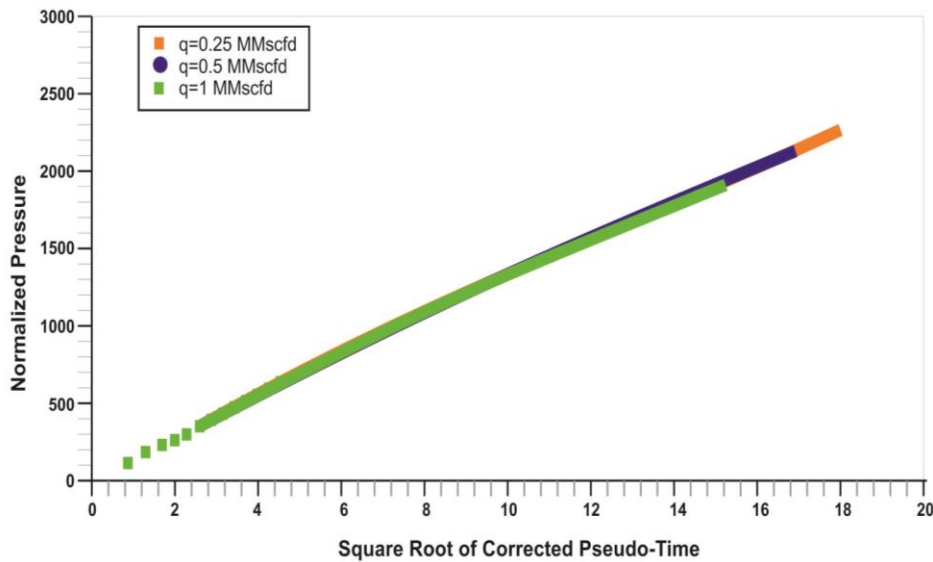
Figure 6. 29: Instead of square root of time data in figure 6.28 plotted against square root of corrected Pseudo-time [121].

It is well known from laboratory that gas diffusion and gas slippage can occur in shale ultra-low permeability On top of the viscous flow expressed by Darcy's law gas slippage causes additional flux and this leads to the higher apparent gas permeability than the liquid-equivalent permeability of the same porous medium. All the methods of analysis that do not account for slippage flow (or other forms of non-Darcy's flow) for analyzing linear flow in reservoirs of extremely low permeability are therefore not rigorous. This was found to be one of the limitations of current methods of analysis used in the industry to analyze production data from shale and tight gas reservoirs. The methods of analyzing production data were then modified by changing Pseudo-Pressure and Pseudo-time definition to incorporate slippage effects:

$$P^*_{Pi} - P^*{}_{Pwf} = 2 \int_{P_{Pwf}}^{P_i} \frac{k_r}{z\mu_g} P dP \qquad (6.19)$$

$$t_a^* = \left(\mu_g C_t\right)_i \int_0^t \frac{\overline{k}_r \, dp}{\overline{\mu}_g \overline{C}_t}.$$ (6.20)

Where k_r is permeability ratio defined as the ratio of apparent permeability, k_a, to the liquid-equivalent permeability, k_∞:

$$k_r = \frac{k_a}{k_\infty}.$$ (6.21)

The analytical method which was developed by Nobakht and Clarkson [122] does not account for desorption and the effects of gas slippage. Nobakht and Clarkson [122] published, an extended work using the following suggested procedures to analyze linear flow properly in the presence of slippage and desorption. by considering the presence of linear flow at constant flowing pressure.

(1) Plot $\frac{1}{q}$ versus $\sqrt{t}$ on Cartesian coordinates. The data should form a straight line during linear flow. Determine the slope of the line, m_{CP}.

(2) Calculate $x_f \sqrt{k}$ using the following equation:

$$x_f \sqrt{k_\infty} = \frac{315.4T}{h \sqrt{\left(\Phi \mu_g C_t\right)_i}} \times \frac{1}{P_{Pi}^* - P_{Pwf}^*} \times \frac{1}{m_{CP}}.$$ (6.22)

Where k_∞ is the liquid-equivalent permeability and P_{Pi}^* and P_{Pwf}^* are the modified Pseudo-pressure to account slippage at initial pressure and flowing pressure respectively.

(3) Calculate the average pressure in the region of influence, $\overline{P}$, from the following equation:

$$\frac{\overline{P}}{\overline{Z}^{**}} = \frac{P_i}{Z_i^{**}} \left[1 - 0.220 \frac{\left(Z^* \mu_g C_t\right)_i \left(P_{Pi}^* - P_{Pwf}^*\right)}{S_{gi} P_i} \sqrt{\frac{\overline{\mu}_g \overline{C}_t}{k_{ri} \overline{k}_r (\mu_g C_t)_i}} \right]$$ (6.23)

Where Z^* is gas compressibility factor, adjusted to account for desorption effects and $\overline{k}_r$ and k_{ri} are permeability ratios at average pressure in the region of influence and initial pressure respectively. Assuming oil, water and formation compressibility's are negligible, water influx is negligible and $S_g = 100\%$, Z^* becomes:

$$Z^* = \frac{Z}{1 + \frac{0.031214 Z T P_{sc} V_L \rho_B}{Z_{sc} T_{sc} (P_L + P) \Phi}}$$ (6.24)

Where ρ_B is shale bulk density, V_L is Langmuir volume, P_L is Langmuir pressure and P_{sc}, Z_{sc} and T_{sc} are pressure, gas compressibility factor and temperature at standard conditions respectively. The presence of desorption does not affect the Pseudo-pressure calculation. However, the total compressibility used in calculating the corrected Pseudo-time and equation (6.23), should account for desorption. Assuming oil, water and formation compressibility's are negligible, water influx is negligible and $S_g = 100\%$, the total compressibility at any pressure, P, in the presence of desorption becomes

$$C_t = C_g + \frac{\rho_B B_g V_L P_L}{32.0368(P_L + P)^2 \Phi}. \tag{6.25}$$

(4) Using the average pressure in the region of influence calculated in previous step, calculate the correction factor, $(f_{CP}^*)_m$:

$$(f_{CP}^*)_m = \sqrt{\frac{\bar{k}_r (\mu_g C_t)_i}{\bar{\mu}_g C_t}} \tag{6.26}$$

(5) Multiply $x_f \sqrt{k}$ calculated in step 2 by the correction factor calculated in step 4.

In the absence of slippage where $k_r = 1$ and in the absence of desorption $Z^* = Z$, equations (6.13) and (6.14) are identical derivation presented). It was discussed that the calculated correction factor from equation (6.16) is independent of permeability if $k_r = 1$, however in the presence of slippage, the correction factor depends on the liquid-equivalent permeability. The above methods presented are for analyzing linear flow either at constant flowing pressure or constant gas production rate. When working with real production data however, there is neither constant flowing pressure nor constant flowing pressure production, and with time both of them changes. Equations based on constant flowing pressure solution in the literature from the last decade are being used for calculating $x_f \sqrt{k}$ for real production data. But there has not been any work to discuss if using constant flowing pressure equation will be better than using constant production rate equations or the opposite.

6.1.3 Comparison among different methods for calculating $x_f \sqrt{k}$ –constant flowing pressure

Slippage and desorption are absence: A comparison among the calculated fracture half-lengths from the following three methods is presented in this section.

Method 1: Using equation (6.9) to calculate $x_f \sqrt{k}$.

Method 2: Using Ibrahim and Wattenbarger method [124], [125]. In this method, the correction factor defined in equation (6.10) is used.

Method 3: Using Nobakht and Clarkson method. In this method, the correction factor defined in equation (6.15) is used.

A number of test cases were built using numerical simulations of a year production profile to compare these three methods. Among all the cases, the common parameters are as follows;

T= 120 $^{\circ}$F, h= 100ft, Φ= 10%, S_g= 100%, γ_g= 0.65, x_f= 250ft, x_e= 500ft, y_e= 5,000ft and c_f= 0. Permeability, initial pressure and flowing pressure inputs data are given in Table 36 for numerical simulation cases. In this Table 6.11, the blank cells indicate that the value for that parameter is the same as that of Case 1.

Table 6.11: input parameters used for numerical simulation for different cases used to compare calculated fracture half-lengths using equation (6.9).

case	P_i (psi)	P_{Pwf} (psi)	K (md)
1	1,000	5,000	0.01
2			0.1
3			0.001
4		3,000	
5		3,000	0.1
6		2,000	
7		4,000	
8		6,000	
9		7,000	
10		8,000	
11	2,000	200	
12	2,000	500	
13	2,000	1,000	
14	2,000	1,500	
15	2,000	1,750	

The blank cells in the table indicate that the value for that parameter is the same as that of case 1. The fracture half-length is obtained for each case from the extracted value of $x_f \sqrt{k}$ from each methods and the input permeability for that case. Shown in Figure 6.30 are the calculated fracture half-lengths from these methods. It can be seen that the calculated fracture half-lengths obtained using equation (6.9) are higher than the $x_f = 250$ft expected (the input parameter to numerical simulation). The calculated fracture half-lengths improved when method 2 correction was applied. Using this method however overestimates the fracture half-length for some cases and underestimates for other cases. It was shown from Figure 6.30 that the calculated fracture half-length obtained using Nobakht and Clarkson method agreed with the expected value very well.

A comparison among the calculated fracture half-lengths for the following three methods is presented as follows;

Method 1: Using equation (6.9) to calculate $x_f \sqrt{k}$.

Mehod 2: Using Ibrahim and Wattenbarger method. In this method, the correction factor defined in equation (6.10) is used.

Method 3: Using Nobakht et al. method. In this method, the correction factor defined in equation (6.26) is used.

Using numerical simulation of a year production profile, a number of test cases were built to compare these methods stated above. Among all these test cases, the common parameters are as follows;

T= 120 °F, h= 100ft, Φ= 10%, S_g= 100%, γ_g= 0.65, x_f= 250ft, x_e= 500ft, y_e= 5,000ft, P_i= 2,000 psi and c_f= 0. In the presence of desorption, the other parameters required are; P_L= 540 psi, V_L= 89scf/ton and ρ_B= 2.47 g/cm^3. The flowing pressure and permeability input data are given in table 6.12 for numerical simulation cases. The apparent permeability was calculated using the dynamic slippage concept developed [128].
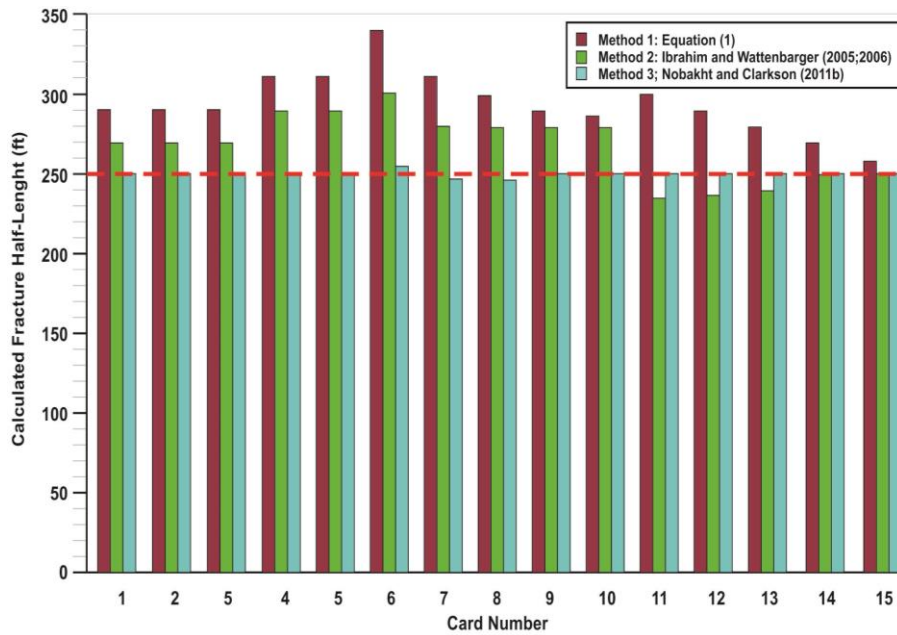
Figure 6.30: Comparison among calculated fracture half-lengths using different methods for cases 1-15 in Table 6.11. On the plot the dashed horizontal line shows the expected value of xf = 250 ft [121].

Table 6. 12: Input parameters used for numerical simulation for different cases used to compare calculated fracture half-length using equation (6.9).

Case	P_{Pwf} (psi)	K (md)	Slippage	Adsorption
1	200	0.001	Yes	No
2	200	0.0001	Yes	No
3	500	0.001	Yes	No
4	500	0.0001	Yes	No
5	200	0.001	Yes	Yes
6	200	0.0001	Yes	Yes

Figure 6.31 shows the calculated fracture half-lengths obtained from these methods. It can be seen that the calculated fracture half-lengths obtained using equation (6.9) are higher than the $x_f = 250$ft expected (the input parameter to numerical simulation). This due to the fact that slippage and desorption as well as changing gas compressibility with pressure are not been accounted for. Extra energy for production is been provided by these three phenomena and the larger fracture half-length will be required to match production if the analysis method does not account for these effects. The calculated fracture half-length has been improved by applying Ibrahim and Wattenbarger correction (method 2) [124], [125]. However unlike the case where slippage and adsorption are absent, it does not work well since the

249

empirical method was developed in the absence of slippage and desorption. From Figure 6.31 it is clear that Nobakht et al. method among the three methods is the best. Hence a fracture half-length that best match the expected value has been provided by this method. The dashed horizontal line shown in Figure 6.31 below is the expected value of $x_f = 250$ ft
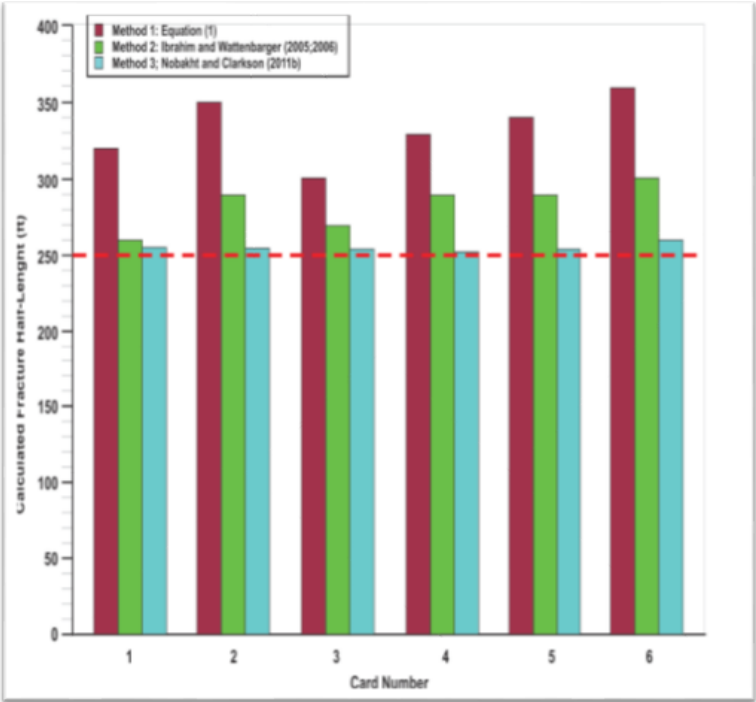
Figure 6.31: Comparison among calculated fracture half-lengths using different methods for cases 1-6 in Table 6.12 [121].

Calculation of $x_f\sqrt{k}$ for variable rate/variable flowing pressure data: Neither the flowing pressure nor the gas rate is usually constant when working with real production data. Hence during the analysis of real production data with variable rate and variable flowing pressure, the solutions for constant flowing pressure or constant gas production rate are approximations [129]. Linear flow analysis is made more difficult because the equation for $x_f\sqrt{k}$ calculations is different for constant flowing pressure (equation (6.27)) and constant rate of gas production (equation (6.28)).

$$x_f\sqrt{k} = \frac{315.4T}{h\sqrt{(\emptyset\mu_g C_t)_i}} \times \frac{1}{m'} \qquad (6.27)$$

$$x_f\sqrt{k} = \frac{200.8T}{h\sqrt{(\emptyset\mu_g C_t)_i}} \times \frac{1}{m'}. \qquad (6.28)$$

Here m' is the slope of the square root-time plot. In the literature equation (6.27) is most often used to calculate $x_f\sqrt{k}$ when analyzing real production data, because most researchers feel that the assumption of constant flowing pressure is more realistic.

Superposition times (linear, bilinear, boundary dominated and radial flow) historically are used to account for changing rate with time. The linear superposition time, t_{SL}, for linear flow case is defined as [121].

$$t_{SL} = \sum_{j=1}^{n} \frac{(q_j - q_{j-1})}{q_n} \sqrt{(t_n - t_{j-1})}$$

(6.29)

Normalized plot of pressure versus linear superposition time is then used for analyzing linear flow for constant rate, constant flowing pressure and variable rate/flowing pressure production. A straight line is obtained from the linear flow section of the data on this plot and the slope line, m'_s, is then used to calculate $x_f\sqrt{k}$

$$x_f\sqrt{k} = \frac{200.8T}{h\sqrt{(\emptyset \mu_g C_t)_i}} \times \frac{1}{m'_s}.$$

(6.30)

The corresponding constant rate equivalent is obtained by converting the variable data using the superposition functions. This is why equations (6.30) and (6.28) are the same for constant rate except m'_s and m'. Hence there is no confusion with this formulation whether to use constant pressure or constant rate equation to for calculating $x_f\sqrt{k}$, which very important when analyzing real production data. Due to the pressure-dependent gas properties, rather than the time, the calculation of superposition time should really be done in terms of (corrected) Pseudo-time, t_a:

$$t_{a,SL} = \sum_{j=1}^{n} \frac{(q_j - q_{j-1})}{q_n} \sqrt{(t_{a,n} - t_{a,j-1})}$$

(6.31)

$t_{a,SL}$ here is linear superposition Pseudo-time. The plot of normalized pressure versus linear superposition Pseudo-time slope can be used in equation (6.30) to calculate $x_f\sqrt{k}$. Calculation of the Pseudo-time (corrected) to be applied in equation (6.31) depends on the average pressure $\bar{P}$, in the region of influence at different times. The $\bar{P}$ can be calculated using the equation that follows [127]:

$$\frac{\bar{P}}{\bar{Z}^{**}} = \frac{P_i}{Z_i^{**}}\left(1 - \frac{G_P}{G}\right) \qquad (6.32)$$

Z_i^{**} and $\bar{Z}^{**}$ are modified Z-factor at initial pressure and average pressure in the region of influence respectively introduced [127]. G_P is the cumulative production and G is the gas in place in the region of influence, and can be calculated using equation (6.33) for constant flowing pressure and equation (6.34) for constant rate production.

$$G = \frac{4 \times 0.159 h \emptyset S_{gi} x_f \sqrt{k}}{B_{gi}\sqrt{(\emptyset \mu_g C_t)_i}} \sqrt{t} \qquad (6.33)$$

$$G = \frac{4 \times 0.113 h \emptyset S_{gi} x_f \sqrt{k}}{B_{gi}\sqrt{(\emptyset \mu_g C_t)_i}} \sqrt{t} \qquad (6.34)$$

For variable rate/variable flowing pressure case, the issue with calculating linear superposition Pseudo-time is estimation of gas-in-place in the region of influence at different times, since the gas-in-place in this region different for constant flowing pressure (equation (6.33)) and constant gas production rate (equation (6.34)). The following was proposed to address this issue:

(i) Plot $\frac{P_{Pi} - P_{Pwf}}{q}$ (or $\frac{P_{Pi}^* - P_{Pwf}^*}{q}$ if slippage is considered in the analysis) versus square root of time. Place a line through the early-time data points and determine the slope, m'.

(ii) Using the slope determine in step (i), calculate $x_f \sqrt{k}$ using equation (6.27) (that is, constant flowing pressure equation).

(iii) using the slope determine in step (i), calculate $x_f \sqrt{k}$ using equation (6.28) (that is, constant rate equation).

(iv) Plot $\frac{P_{Pi} - P_{Pwf}}{q}$ (or $\frac{P_{Pi}^* - P_{Pwf}^*}{q}$ if slippage is considered in the analysis) versus linear superposition time on a Cartesian coordinates. Place a line through the early-time data points and determine the slope of the line, m'_s.

(v) Using the slope determine in step (iv), calculate $x_f \sqrt{k}$ using equation (6.30)

(vi) If $x_f\sqrt{k}$ from step (v) is closer to that from step (ii) compare to that from step (iii), calculate G using equation (6.33). Otherwise, calculate G using equation (6.34).

To analyze linear flow for variable rate/variable flowing pressure data, the following was proposed:

1. (iv) Plot $\frac{P_{Pi}-P_{Pwf}}{q}$ (or $\frac{P_{Pi}^*-P_{Pwf}^*}{q}$ if slippage is considered in the analysis) versus linear superposition time on a Cartesian coordinates. Place a line through the early-time data points and determine the slope of the line, m_s'.

2. Using the slope determine in step 1, calculate $x_f\sqrt{k}$ using equation (6.30).

3. Calculate the average pressure in the region of influence at different times using equation (6.32) and G as described in steps (i) to (vi) above.

4. Calculate the corrected pseudo-time from equation (6.12) (or equation (6.20) if slippage is considered in the analysis) and by using the average pressure in the region of influence calculated in step 3.

5. Plot $\frac{P_{Pi}-P_{Pwf}}{q}$ (or $\frac{P_{Pi}^*-P_{Pwf}^*}{q}$ if slippage is considered in the analysis) versus linear superposition Pseudo-time (calculated using equation (6.31)) on Cartesian coordinates. Place a line through the early-time data points and determine the slope, m_s'.

6. Using the slope determined in step 5, calculate $x_f\sqrt{k}$ using equation (6.30).

7. Continue steps 3-6 until $x_f\sqrt{k}$ converges.

For example, Figure 6.32 shows the flowing pressure and gas rate data for this case. The input flowing pressure was used to calculate the rate using the reservoir geometry in figure 6.27 with T= 120 °F, h= 300ft, Φ= 6%, S_g= 100%, γ_g= 0.65, x_f= 320ft, x_e= 640ft, y_e= 3,500ft, P_i= 2,000 psi and c_f= 0. Using k= 0.015md, the calculated fracture half-length using equations (6.27) and (6.28) are x_f= 411 ft and x_f= 261 ft respectively, and the calculated fracture half-length using equation (6.30) is x_f= 368 ft. These values show that, it is appropriate to deal with case as a constant flowing pressure. Hence equation (6.33) can be used in step 3 to calculate gas-in-place in the region of influence at different times.
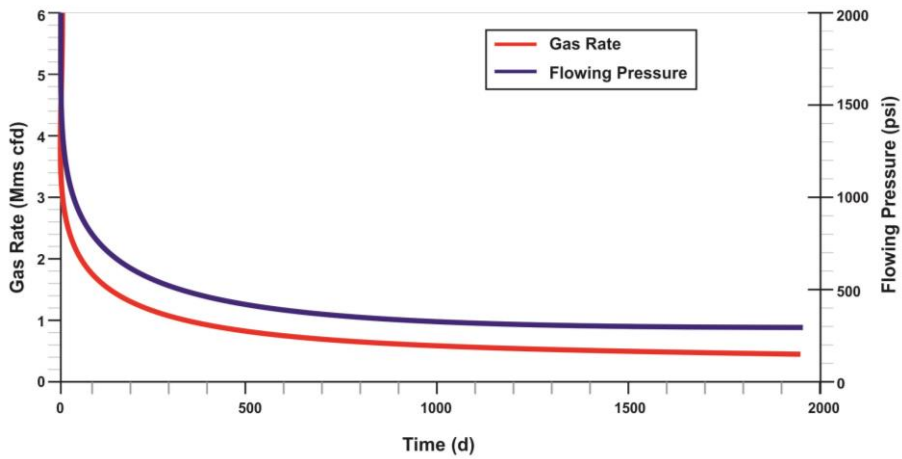
Figure 6. 32: Plot for example's normalized pressure versus linear superposition Pseudo-time in "calculation of a product of half fracture lenght and square root of permeability for real production data analysis" section [121].

A plot of normalized pressure versus linear superposition Pseudo-time after $x_f\sqrt{k}$ converges using $k=0.015$md and $x_f=319$ ft which is in better agreement with the expected value of $x_f=320$ ft is shown in Figure 6.33.
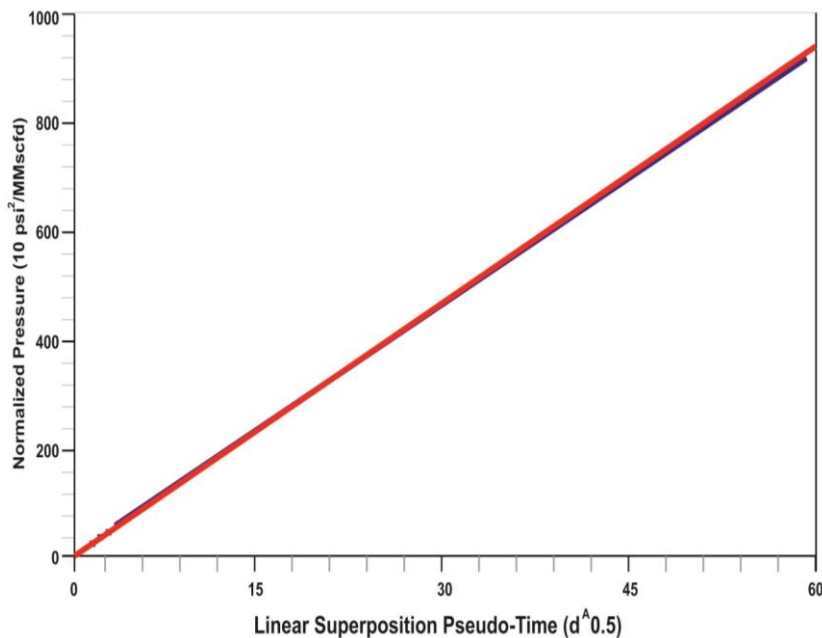
Figure 6. 33: Normalized pressure vs. linear superposition Pseudo-time plot for example in calculation of a product of half fracture lenght and square root of permeability for real production data analysis section [121]**.**

254

A linear dual porosity type curve analysis technology was used in the Eagle Ford shale in South Texas to analyze the production behavior and estimate the essential parameters for this reservoir, since there are no published reports for production data analysis in the Eagle Ford shale where development began in 2008 [130]. The type curves employed was constructed based on transient production rate with constant well pressure and double porosity in a closed boundary Stimulated Reservoir Volume (SRV) approach. Bello and Nobakht approach was employed to account for apparent skin in order to analyze the early-time production data.

For production forecasting and reserves estimation, the decline curve analysis (DCA) has been used as an effective method in shale gas reservoirs. Usually production in shale reservoirs are from stimulated reservoir volume in horizontal well stimulated by hydraulic fracturing and the shale gas reservoirs have very different petrophysical properties from the conventional, hence the analysis of production data is different from the first developed conventional DCA methods [131], and the modified versions by others including Fetkovich (1987), Agarwal et al. (1999) and Palacio and Blasingame (1993). Due to the differences in petrophysical properties, more complex fracture network occur in naturally fractured shale gas reservoirs compared to the traditional bi-wing fracture

The flow in shale gas reservoirs does not follow the radial behavior similar to the conventional gas reservoirs because of the ultra-low matrix permeability and high fracture conductivity, but it however follows a linear flow instead. The methods that were proposed for shale gas production data analysis by Lewis and Huges and other authors who used type curves technique to analyze shale gas production [132]. Hazlet et al. whose type curves were constructed based on Warren-Root models, were all based on radial flow [133]. To analyze the shale gas well performance using conventional type curves technique may result in "false" radial flow when the fracture conductivity is finite.

In this study the same dual porosity linear flow type curves presented were used to analyze the Eagle Ford shale gas production data. Also different flow regimes have been observed and the properties of the reservoir such as matrix permeability and completion efficiency or SRV were evaluated. Based on different assumptions, the estimated ultimate recovery (EUR) and future gas rate were predicted.

Basic theory and methodology for a long-term transient linear flow regimes are usually observed in most shale gas production data. A dual porosity transient linear flow type curves developed for multi-stage hydraulic fractured horizontal well for shale gas in which four flow regimes exist are;

(1)   Regime 1: Early linear flow in fracture system.
(2)   Regime 2: Bilinear flow caused by both fracture and matrix system.
(3)   Regime 3: Linear flow in matrix system.
(4)   Regime 4: Boundary dominated flow.

Based on the following equations, a combination of area with permeability can be calculated.

Early linear flow:

$$A_{cw}\sqrt{k_f} = \frac{1262T}{\sqrt{\omega(\phi\mu C_t)_{f+m}}} \cdot \frac{1}{m_1} \tag{6.35}$$

Bilinear flow:

$$A_{cw}\sqrt{k_f} = \frac{4070T}{[\sigma k_m(\phi\mu C_t)_{f+m}]^{0.25}} \cdot \frac{1}{m_2} \tag{6.36}$$

Matrix linear flow:

$$A_{cm}\sqrt{k_m} = \frac{1262T}{\sqrt{(\phi\mu C_t)_{f+m}}} \cdot \frac{1}{m_3} \tag{6.37}$$

Where m_1 and m_3 are slopes of the straight line on the plot of $\left[m(P_i) - m(P_{wf})\right]/q_g$

versus $\sqrt{t}$, and m_2 is the slope of the straight line of the plot of $\left[m(P_i) - m(P_{wf})\right]/q_g$ versus $t^{0.25}$.

Where, A_{cw} = the well face cross-sectional are to flow (ft^2),

k_f = the fracture permeability (md),

T = the absolute temperature (^{O}R),

ω = dimensionless storativity ratio, C_t = the total compressibility at initial reservoir pressure (psi^{-1}), μ = the viscosity (cp), $f + m$ = the total system (ffracture +matrix), m = the matrix, f = fracture, k_m = the matrix permeability (md), ϕ = the porosity, σ = the shape factor (ft^2), $m(P)$ = Pseudo-pressure for gas (psi^2/cp), P_{wf} = the wellbore flowing pressure (psi), q_g = the gas rate (Mscf/day), t = time (days) and P_i = the initial reservoir pressure (psi).

The apparent skin effects can be included in the available two approaches that follow. Flow convergence around a horizontal well is because of apparent skin and the bottom-hole pressure calculation caused an extra pressure drop or in early linear flow or bilinear flow, pressure drop within finite conductivity fractures. The two approaches mentioned above are,

The effect of skin on the linear flow reservoir response by Bello's approach was demonstrated to gradually diminish with time The straight line that passes through the origin becomes a curve with a nonzero intercept on the specified plot $\left[m(P_i) - m(P_{wf})\right]\big/q_g$ versus $\sqrt{t}$ when the skin is considered. The empirical equation (Bello and Wattenbarger, 2009) that follows was derived.

$$\frac{m(P_i) - m(P_{wf})}{q_g} = m_3\sqrt{t} + \frac{b}{1 + \frac{0.45m_3\sqrt{t}}{b}} \tag{6.38}$$

B is the intercept of field data on the $\left[m(P_i) - m(P_{wf})\right]\big/q_g$ versus $t^{0.5}$ plot (psi^2/cp/Mscf/day).S

Nobakht's approach stated that the effect of skin produces a straight line with intercept.as shown in equation (6.39) below,

$$\frac{m(P_i) - m(P_{wf})}{q_g} = m_3\sqrt{t} + b \tag{6.39}$$

Eagle ford reservoir and well description: Stegent et al. (2010) state that the depth of the Eagle Ford shale ranges from 2,500 feet to 14,000 feet with thickness ranging from 50 feet to more than 300 feet, the Total Organic Content (TOC) ranges from 2% to 9% and the pressure gradients are between 0.4 psi/ft to 0.8 psi/ft. from core analysis, it was observed that the gas saturation ranges from 83% to 85% and the permeability varies from 1 nano-Darcy to 800 nano-Darcy [134]. The first wells for exploration which was drilled in 2008 in the Eagle Ford shale was drilled in LaSalle County in the gas window of the play. In this Eagle Ford shale, oil is been produce at the top, high liquid or condensate been produce in the middle and dry gas predominantly been produce at the bottom of the map shown in Figure 6.34.

Well A completed with a ten stages proppant fracture stimulation treatment is a horizontal dry gas producer in a 4,000 feet lateral. In this well, each stage which is 400 feet was perforated with four, two-foot cluster spaced apart in a distance of 75 feet. Only 20 transverse fractures are effective on production according to the result of radioactive log and production log. Simulated reservoir volume was estimated by the fracturing modeling to be 169 MMft^3 and the height of the pay zone is 283 feet. In table 38, the summary of the reservoir and fluid properties data are shown below. The daily rate of gas production and original bottom-hole flowing pressure (BHFP) is presented for 250 days in Figures 6.35 and 6.36 respectively [120]. BHFP was smoothed using an exponential smoothing algorithm to minimize the effects of data fluctuation. In the smoothing the equation used is as follows;

$$x_{smth}(t) = \alpha \cdot x(t) + (1 - \alpha) \cdot x_{smth}(t - 1) \qquad (6.40)$$

Here α which is the dampening factor has a value of 0.25. After 50 days from the graph in Figure 6.36, the BHFP can be assumed to be constant hence the type curves with constant BHFP can be used for the data analysis.
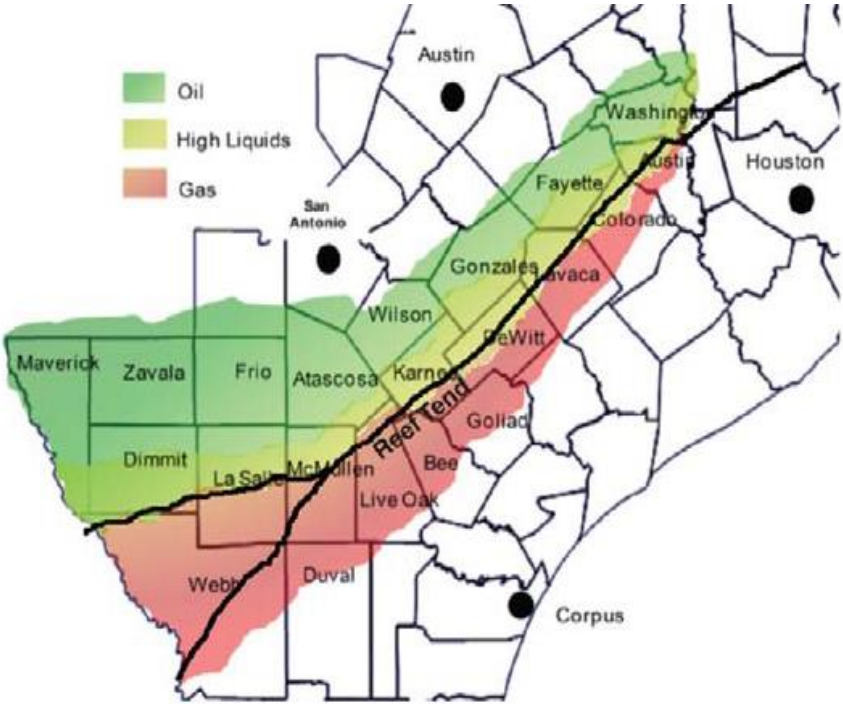
Figure 6.34: Lateral extent of Eagle Ford shale in South Texas [130].
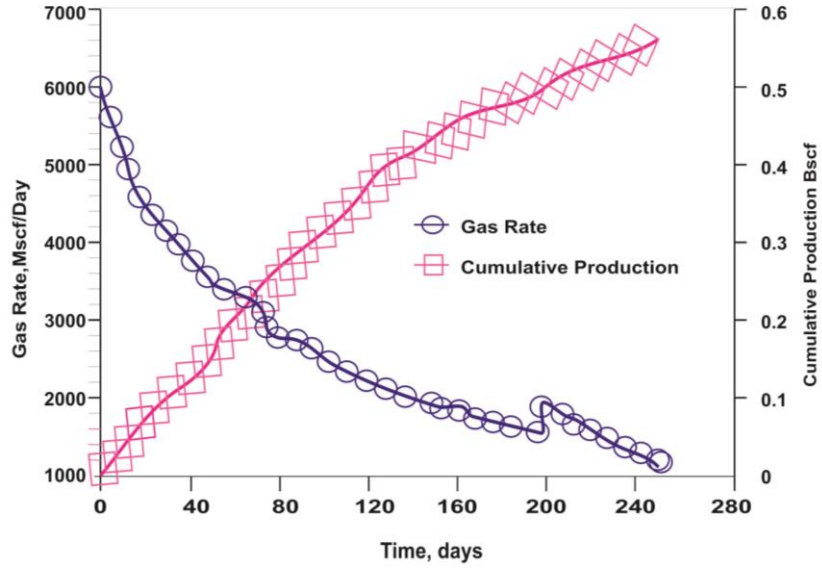
Figure 6.35: cumulative production and gas rate [120].
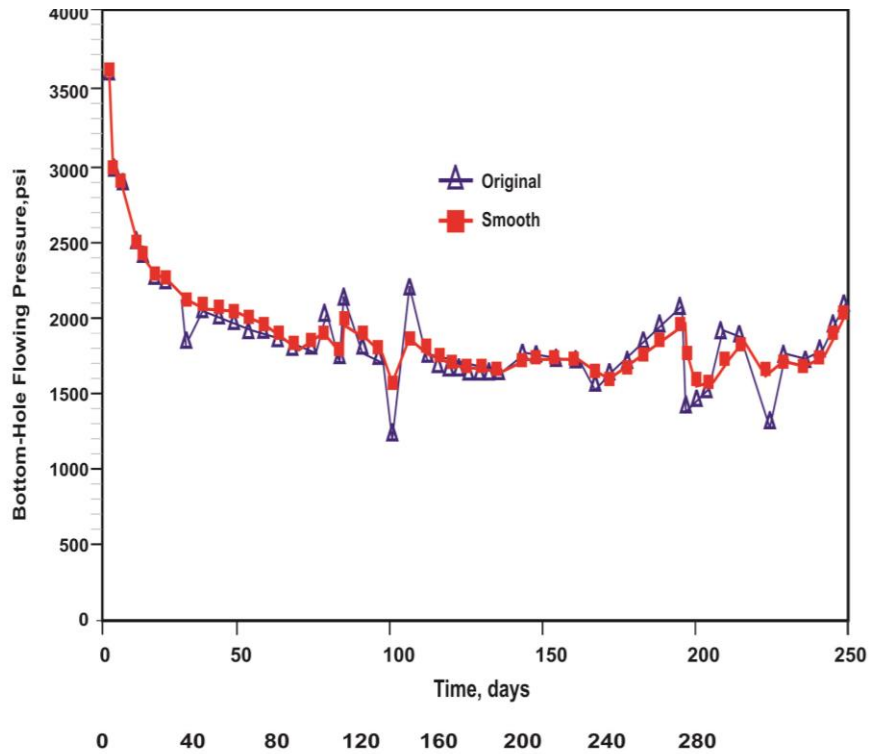
Figure 6.36: Normalized Pseudo-pressure versus square root of time [120].

6.2 Flow Regimes Identifications

Three regimes identified based on Figures 6.37 and 6.38 are: (1) bilinear flow or apparent skin effect, (2) matrix linear flow and (3) boundary dominated flow. The

normalized log-log plot of $q\big/\left[m(P_i) - m(P_{wf})\right]$ versus time is shown in Figure 6.37.

The data exhibits a negative slope of $1\big/4$ the very early times indicating either bilinear flow or apparent skin effects and the data also exhibits negative slope of one-half in the later times indicating matrix linear flow. Figure 6.38 is a normalized Pseudo-pressure plot of $\left[m(P_i) - m(P_{wf})\right]\big/q$ versus $\sqrt{t}$ where a deviation of early time data from straight line was observed, and it also has an intercept on the normalized Pseudo-pressure axis. This behavior indicates a non-linear flow like skin effects, and the straight line shown by this data in the early time indicates typical characteristics of linear flow. The data begin to deviate in every late time from the straight line at approximately 225 days and this is an indication of the boundary effects. The boundary effects cannot be indicated on the log-log plot since the time period within which the boundary effects occur is very short.
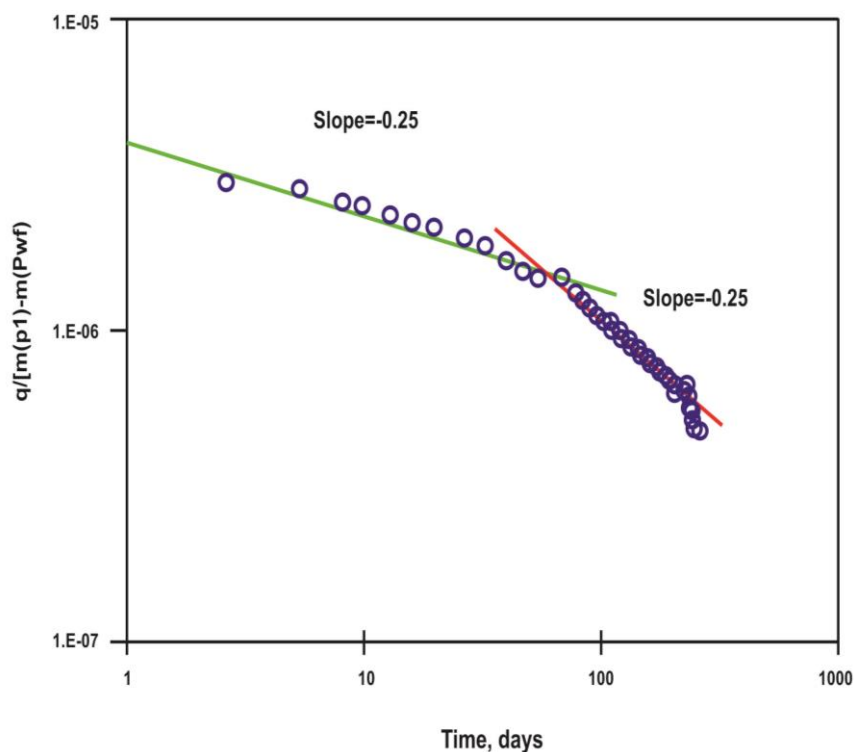
Figure 6. 37: Normalized rate versus time [130].
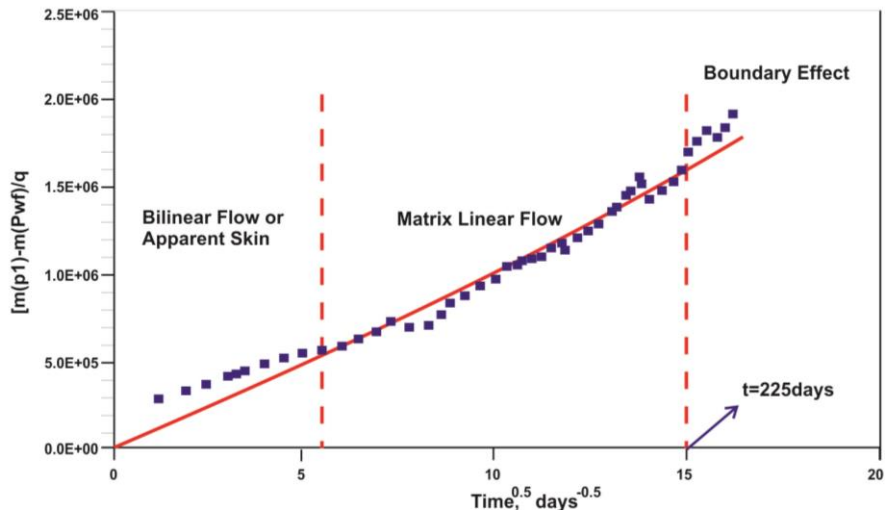
Figure 6.38: Normalized Pseudo-pressure versus square root of time [130].

6.2.1 Linear flow parameters analysis

From the following simple calculation in Figure 6.39, the half-width of the drainage area (rectangular geometry) can be calculated. Bi-wing hydraulic fracture geometry and slab matrix bulk are assumed. The half-width is equal to SRV divided by $2X_e h$.

$$y_e = \frac{SRV}{2X_e h} = \frac{169 \times 10^6}{2 \times 4{,}000 \times 283} \approx 75 \; ft.$$

Here, y_e is the drainage area half-width for rectangular geometry equivalent to fracture half-length (ft), X_e is the drainage area length for rectangular geometry (ft) and h is the reservoir thickness (ft).

It observed that if SRV is not known y_e can be estimated from Original Gas-In-Place (OGIP). From the well length 4,000 divided by the number of effective fracture number (20), average fracture spacing (L) was calculated as shown below.

$$\mathrm{L} = \frac{4{,}000}{20} = 200 \text{ ft.}$$

Then the well-face cross-sectional area to flow was calculated as follows;

$$A_{cw} = 2 \cdot X_e \cdot h = 2 \times 4{,}000 \times 283 = 2.264 \times 10^6 \text{ ft}^2$$

In a double porosity slab model, the matrix-fracture surface area was calculated from equation below:

$$A_{cm} = 2 \times 2y_e \times h \times 20 = 1.698 \times 10^6 \text{ ft}^2$$

Two possibilities were analyzed based on the flow regimes identification.

261
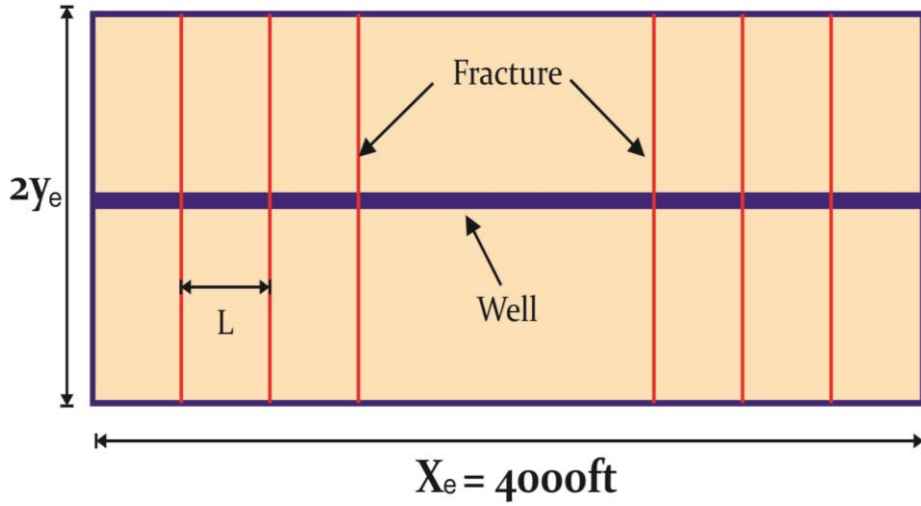
Figure 6.39: Reservoir geometry for dual porosity slab model [130].

6.2.2 Bilnear flow followed by matrix linear flow

A plot of "$[m(P_i) - m(P_{wf})]/q$" versus $\sqrt{t}$ and $t^{0.25}$ are shown in Figures 6.40 and 6.41, respectively, to obtain $m_2 = 283,333$ and m3 = 111,250.

Based on the following calculations, $A_{cm}\sqrt{k_m}$ was then determined:

$$A_{cm}\sqrt{k_m} = \frac{1262T}{\sqrt{(\emptyset\mu C_t)_{f+m}}} \cdot \frac{1}{m_3} = \frac{1262 \times 745}{\sqrt{0.0576 \times 0.00006 \times 0.03334}} \cdot \frac{1}{111,250}$$
$$= 2.49 \times 10^4 ft^2 \cdot md^{0.5}$$

$(\emptyset\mu C_t)_m$ was assumed to be equal to $(\emptyset\mu C_t)_{f+m}$ since the fracture porosity can be negligible compared to matrix porosity.

The gas desorption is negligible as a result of the high reservoir average pressure in the early production. Again the total compressibility was assumed to be C_g as the rock compressibility was ignored. The permeability of the matrix was evaluated from the calculation that follows:

$$k_m = \left[\frac{A_{cm}\sqrt{k_m}}{A_{cm}}\right]^2 = \left(\frac{2.49\times10^4}{1.698\times10^6}\right)^2 = 2.15 \times 10^{-4} \text{ md}$$

The fracture permeability k_f was determined from the following equation:

$$A_{cw}\sqrt{k_f} = \frac{4070T}{[\sigma k_m(\emptyset\mu C_t)_{f+m}]^{0.25}} \cdot \frac{1}{m_2} = \frac{4070\times745}{[3.0\times10^{-4}\times2.15\times10^{-4}\times0.00006\times0.03334]^{0.25}} \times$$
$$\frac{1}{283333} = 6.48 \times 10^4 \text{ ft}^2 \cdot md^{0.5}$$

For slab model, matrix block shape factor is;

$$\sigma = \frac{12}{L^2} = 3.0 \times 10^{-4} \text{ ft}^{-2}$$

$$k_f = \left[\frac{A_{cw}\sqrt{k_f}}{A_{cw}}\right]^2 = \left[\frac{6.48\times10^4}{2.264\times10^6}\right]^2 = 8.2 \times 10^{-4} \text{ md}$$

This fracture permeability is low due to the fact that the well-face cross-sectional area has been used.
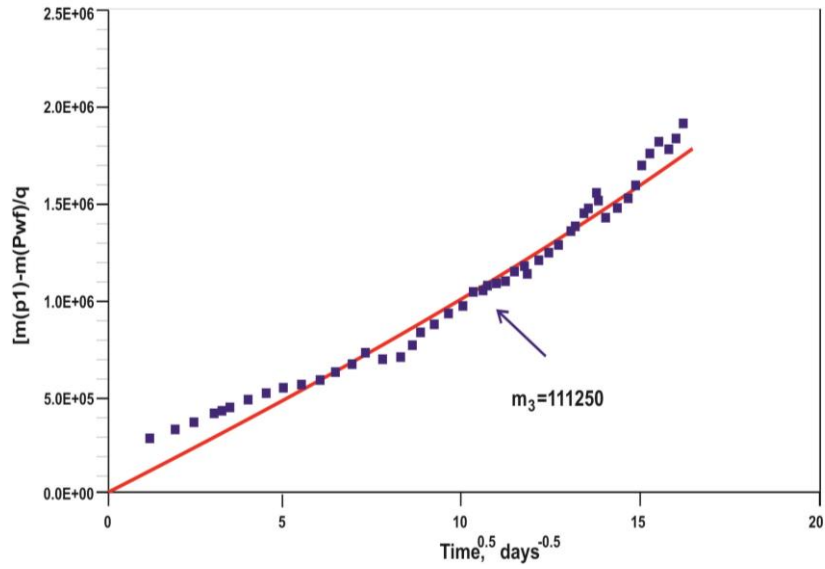
Figure 6.40: Specialized plot analysis [130].

$$\left[m(P_i) - m(P_{wf})\right]/q \text{ vs, } \sqrt{t}$$
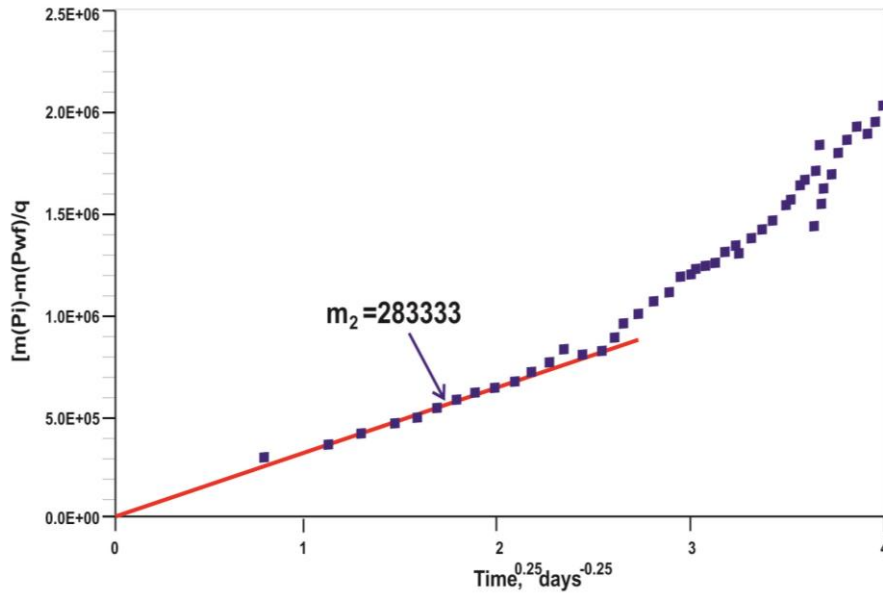
Figure 6.41: Specialized plot analysis [130].

$$\left\lfloor m(P_i) - m(P_{wf}) \right\rfloor\Big/_{q} \text{ Versus } t^{0.25}$$

6.2.3 Matrix linear flow with apparent skin

From figure 6.40, two parameters of $m_3 = 111{,}250$ and intercept of $b = 2.1 \times 10^5$ were obtained in Bello's approach, and substituted into equation (6.38). Accounting for apparent skin, the initial relationship of production rate versus time is given as:

$$\frac{m(P_i) - m(P_{wf})}{q} = 111{,}250\sqrt{t} + \frac{2.15 \times 10^5}{1 + \frac{0.45 \times 111{,}250\sqrt{t}}{2.15 \times 10^5}} \qquad (6.41)$$

The above equation was used to match the production data and fortunately by initial guess (Figures 6.42 and 6.43), acceptable results were obtained. In the case where the matching is not good, an assumed m_3 and b are needed as matching parameters to reach reasonable results. The matrix permeability was estimated to be 2.15×10^{-4} md based on $m_3 = 111{,}250$.
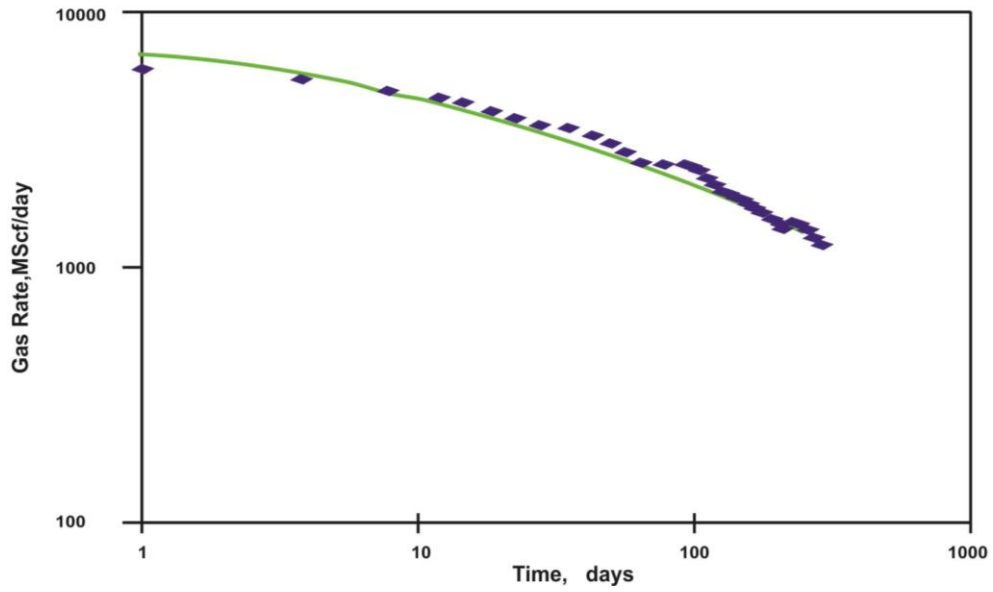
Figure 6.42: Fitting the results with equation (6.41) log-log plot [130].
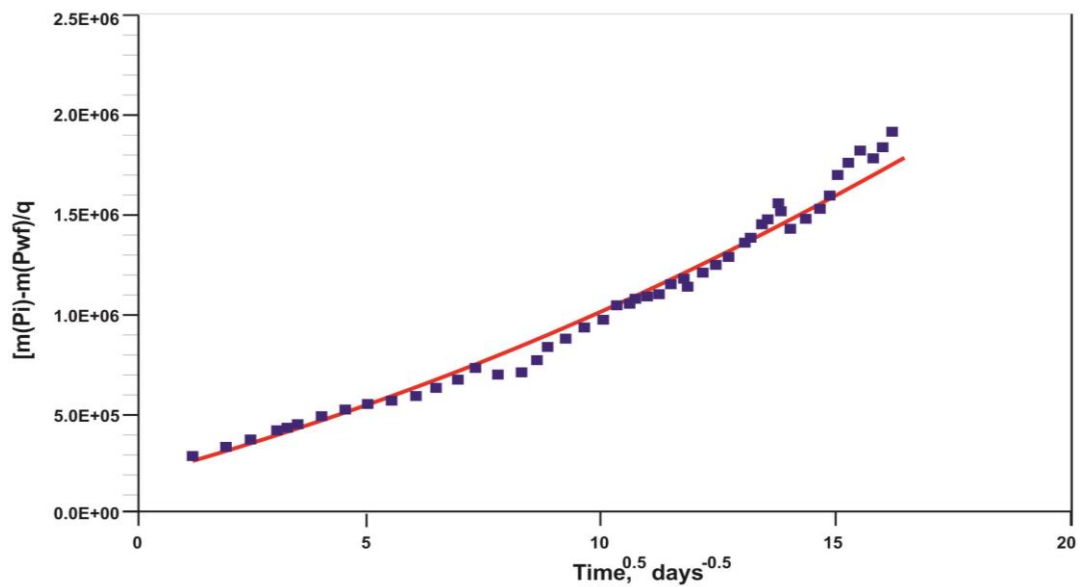
Figure 6.43: Fitting the results with equation (6.41), Square root of time plot [130].

A straight line has being drawn through the data point from a plot of $\left[m(P_i) - m(P_{wf})\right]\big/q_g$ versus $\sqrt{t}$, and the intercept of b $= 1.5 \times 10^5$ was obtained in Figure 6.44 using Nobakht's approach.
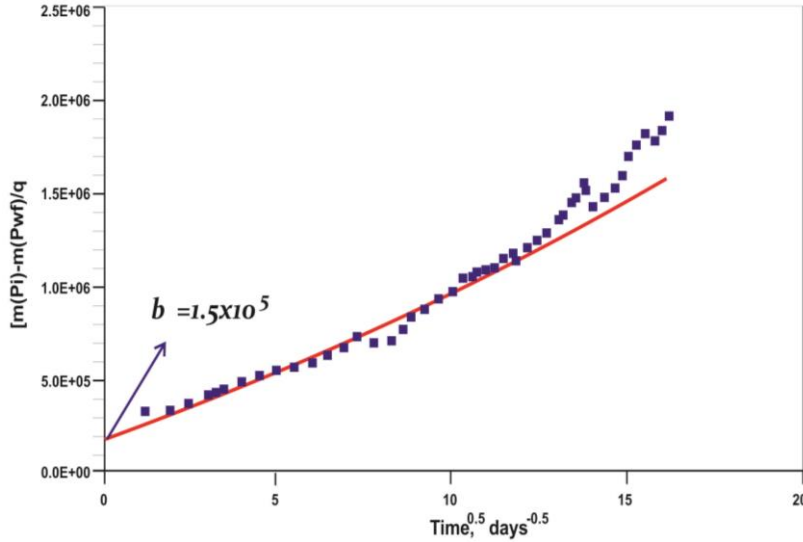
Figure 6.44: Specialized plot to obtain intercept b for Nobakht's approach [130].

The modified normalized pressure calculation then was done as follows:

$$\left[\frac{m(P_i)-m(P_{wf})}{q}\right]_m = \frac{m(P_i)-m(P_{wf})}{q} - b \qquad (\mathbf{6.42})$$

Figure 6.45 shows a log-log plot of $\left\{[m(P_i)-m(P_{wf})]\Big/q\right\}_m$ versus time where a

slope of one-half was indicated even in the early time. Figure 6.46 shows a plot of

$\left\{[m(P_i)-m(P_{wf})]\Big/q\right\}_m$ versus $\sqrt{t}$ where a slope of $m_3 = 93750$ was obtained.

Hence $A_{cm}\sqrt{k_m}$ can be calculated as follows;

$$A_{cm}\sqrt{k_m} = \frac{1262T}{\sqrt{(\emptyset\mu C_t)_{f+m}}} \cdot \frac{1}{m} \approx \frac{1262 \times 745}{\sqrt{0.0576 \times 0.00006 \times 0.03334}} \cdot \frac{1}{93750}$$

$$= 2.95 \times 10^4$$

Then the estimated matrix permeability was calculated as shown below.

$$k_m = \left[\frac{A_{cm}\sqrt{k_m}}{A_{cm}}\right]^2 = \left[\frac{2.95 \times 10^4}{1.698 \times 10^6}\right]^2 = 3.02 \times 10^{-4} \text{ md.}$$

It was also found out from Figure 6.46 that the time at the end of the straight line has been changed to 132 days.
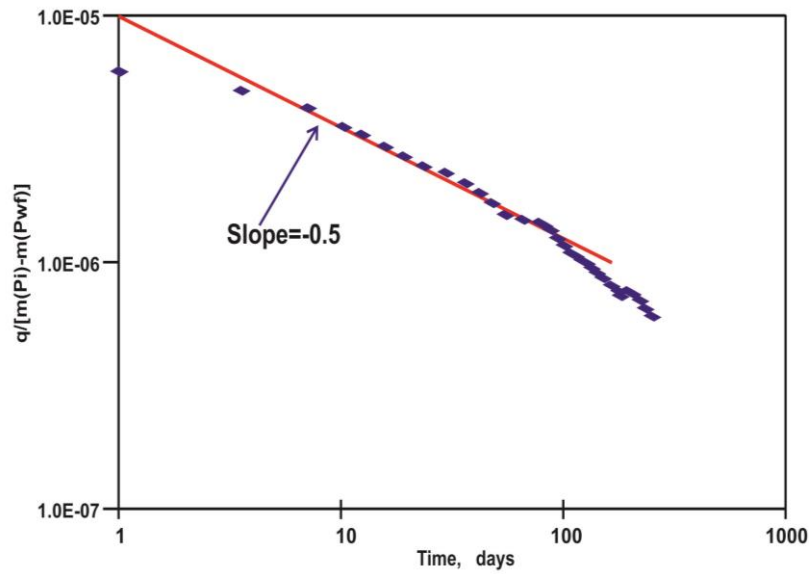
Figure 6.45: Modified normalized rate versus time on log-log plot [130].
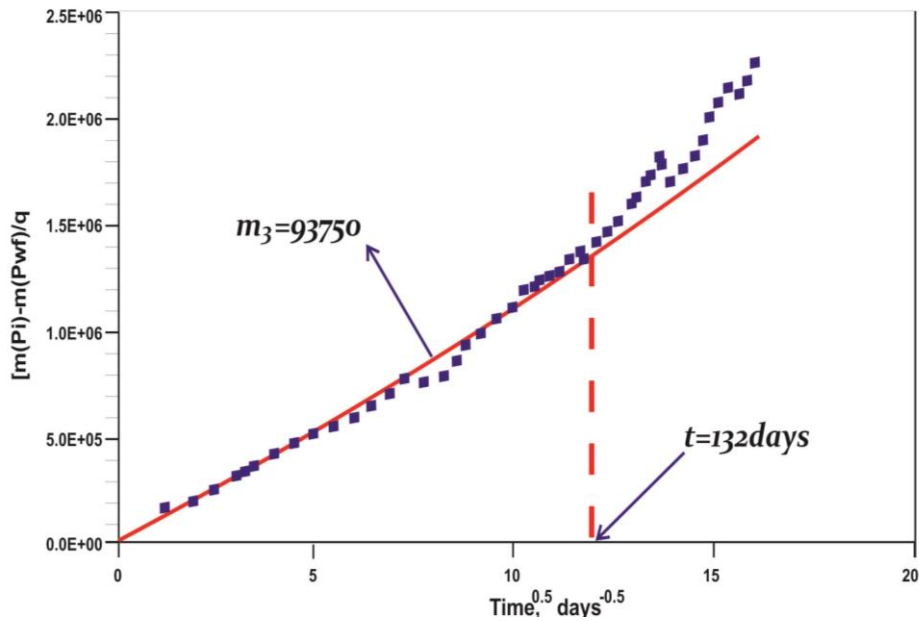
Figure 6. 46: Modified $\lfloor m(P\_i)-m(P\_wf)\rfloor/q$ vs, $\sqrt{t}$ [130].

The approach for estimating OGIP by Wattenbarger et al. which is based on the assumption that boundary dominated flow begins when pressure at the matrix block center starts to decline, has been previously presented [123]. Equation (6.43) is the formula used in this approach;

267

$$\text{OGIP} = \frac{200.6 T S_{gi}}{(\mu C_t B_g)_i} \cdot \frac{\sqrt{t_{esl}}}{m_3} \tag{6.43}$$

In this study the above equation becomes;

$$\text{OGIP} = \frac{200.6 \times 745}{0.03334 \times 0.00006 \times 0.0032} \cdot \frac{\sqrt{t_{esl}}}{m_3}$$

In Bello's approach: $m_3 = 111,250$ and $t_{esl} = 225$ days, hence OGIP = 3.15 Bscf

In Nobakht's approach: $m_3 = 93750$ and $t_{esl} = 132$ days, hence OGIP = 2.87 Bscf

The SRV can be obtained, if OGIP is known, by using the following equation:

$$\text{SRV} = \frac{OGIP \cdot B_{gi}}{\emptyset S_{gi}} \tag{6.44}$$

Therefore from Bello's approach, SRV = 175 MMft^3 and from Nobakht's approach, the SRV = 159 MMft^3. Comparing the SRV values obtained by Bello and Nobakht to the previous SRV value of 169 MMft^3, it can be seen that Bello's approach overestimate 6 MMft^3 in SRV and Nobakht approach underestimates 10 MMft^3. But both approach yield reasonable results.

6.3 Numerical Simulation And Discussion

A numerical simulation was designed to validate the results obtained from type curves matching. A single porosity single phase model was developed. Twenty transverse fractures have been defined evenly in this model as a very high permeability path along the horizontal wellbore as shown in Figure 6.47.
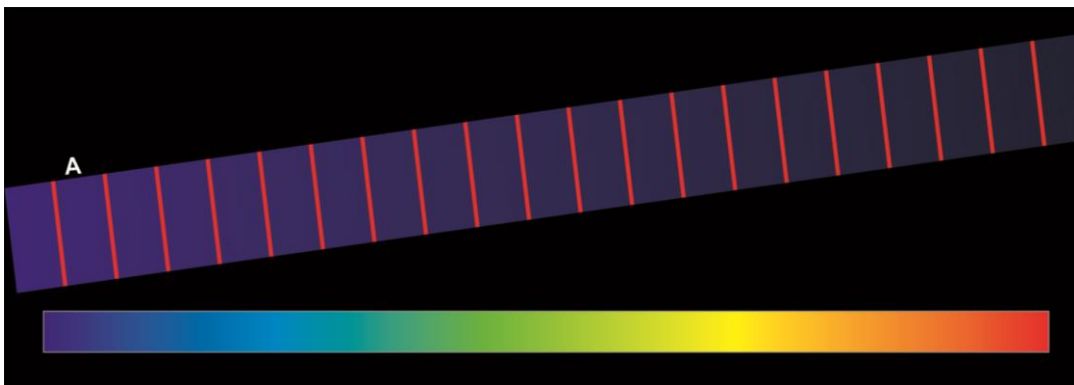
Figure 6.47: Simulation model for well A, 20 transverse fractures [130].

The well was placed at the center of the reservoir which area was assumed to be equal to the SRV area. Table 6.13 show the other parameters used in the numerical simulation. The matching of the simulated data with actual production history shown in Figure 6.48 was good except some points in the initial data which is affected by fracture system. The matrix permeability used in the matching was 1.25×10^{-4} md. Comparing this value to that of Bello's and Nokbakht's, it can be seen that the matrix permeability from the type curve is higher especially 172% of Bello's and 242% of Nobakht's as shown in Table 6.14. It was stated that the overestimation of $A_{cm}\sqrt{k_m}$ and OGIP could be as result of the effects of drawdown on transient linear flow [125], and the following empirical equation was developed to estimate the correction factor.

$$f_{cp} = 1 - 0.0852 D_D - 0.0857 D_D^2 \qquad (6.45)$$

Here D_D is the drawdown parameter which is defined by the following equation:

$$D_D = \frac{m(P_i) - m(P_{wf})}{m(P_i)} \qquad (6.46)$$

An average bottom-hole pressure of 1,500 psi was used and $D_D = 0.941$ obtained. A correction factor of 0.844 was then determined as follows:

$$f_{cp} = 1 - 0.0852 \times 0.941 - 0.0857 \times (0.941)^2 = 0.844$$

The matrix permeability, SRV and OGIP were modified by using the correction factor and the results were presented in Table 6.14. It was observed that the modified matrix permeability was still higher than the permeability obtained from the simulation, and the differences was believed to be related to the assumption of dual porosity flow behavior in the type curve analysis where a single porosity model was used in the reservoir simulation. The single porosity model was used because good results could not be obtained by using the matrix shape factor of $\sigma = 3.0 \times 10^{-4}$ ft^{-2} in the double porosity simulation. Also, only the effect of convergence skin was considered in Bello's approach, however, the in the horizontal wellbore the pressure drop was not considered. The permeability from simulation in overall was in the range of acceptable agreement with the type curve analysis. Bello's approach was closer to the numerical simulation result since the effect of skin indicates a deviated curve from the straight line with an intercept (Figure 6.44). This assertion can be seen in Table 6.13.

Table 6. 13: Parameters estimation and modification.

| approach | OGIP, Bscf | | SRV, MMf^t | | Matrix permeability, 10^{-4} md | | |
	original	Modified	original	Modified	original	Modified	Numerical simulation
Bello's	3.15	2.66	175	148	2.15	1.81	1.25
Nobakht's	2.87	2.42	159	134	3.02	2.55	
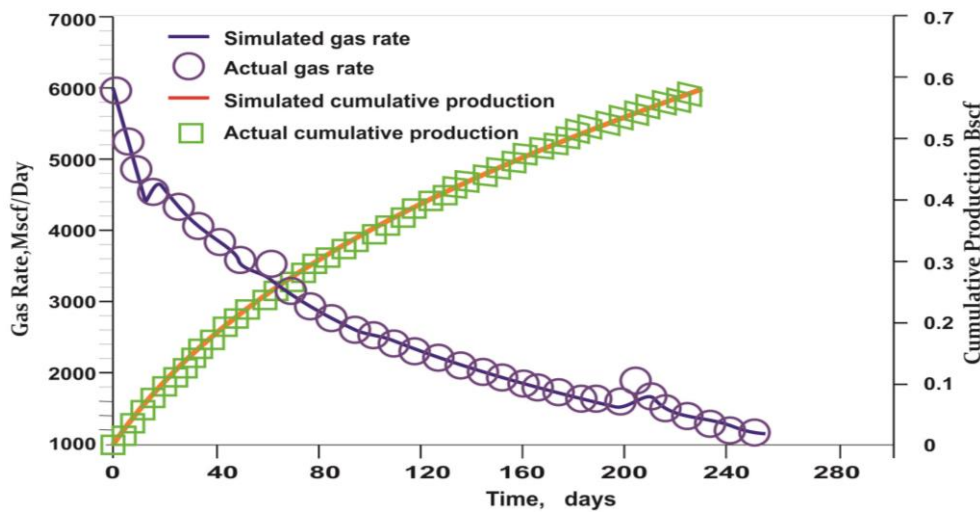
Figure 6.48: Well A history matching [130].

It is necessary to state that the modified SRV are lower than the reported SRV from hydraulic fracture modeling especially 79% for Nobakht's case and 86% for Bello's case (Table 6.13). These results however are in the acceptable estimation range. In the calculations, the adsorbed gas has not been included and as results the modified OGIP is either 2.66Bscf or 2.42 Bscf which represents the total free gas in the region of SRV.

The shale gas production can be predicted using dual porosity linear flow model, many parameters however are required and this may lead to uncertainties of the results. Material balance and Pseudo-steady flow equations were combined and used for forecasting production for boundary dominated flow in this case. The material balance equation for volumetric gas reservoirs accounting for gas desorption (King, 1990) is given as:

$$\frac{\bar{P}}{\bar{Z}^*} = \frac{P_i}{Z_i^*}\left(1 - \frac{G_P}{G}\right)$$ (**6.47**)

$$\bar{Z}^* = \frac{Z}{1 + \frac{zRTC_E}{\emptyset\bar{P}}}$$ (**6.48**)

Here, C_E is equilibrium isotherm (lb-mole/ft^3). The water and rock compressibility was assumed to be negligible. Equation for Pseudo-steady flow for gas reservoir is given as:

$$q_g = J_{cp}\left[m(P_i) - m(P_{wf})\right]$$ (**6.49**)

Here, J_{cp} is the production index for constant bottom-hole pressure (Mscf/day/psi^2/cp). The average J_{cp} which depends on average pressure or OGIP was calculated using the least production data for well A. then for two different OGIP values of Bello's and Nobakht's cases two results can be obtained.

The production forecasting at constant bottom-hole pressure of 1,500 psi for 15 years for well A is shown in Figure 6.49. A little higher production rate in Bello's approach than Nobakht's case was obtained as a result of larger OGIP. After 15 years, the gas rate decline with time and the decline rate gradually is close to a constant value. Due to the fact that the contribution of un-stimulated zone production was not considered, the production forecasting in this calculation is underestimated. Two adsorption isotherm (Figure 6.50) were used in order to investigate the effect of desorption on production forecasting where isotherm 2 has the value of 1,500 psi. The production of 15 years at constant bottom-hole pressure of 500 psi for different adsorption isotherms are shown in Figures 6.51 and 6.52. It was observed that more adsorbed gas is released by the higher Langmuir pressure and this resulted in higher gas production. The effect of desorption using isotherm 1 however is not significant because of the relative high average reservoir pressure which is not allowing desorption of gas in this case. However, it is always needed for long-term production forecasting to account for desorption. Gas desorption as seen in Table 6.14, can make the EUR to be higher up to 27%.

A genesis of the decline curves with the use of a simple hydrodynamic analogy was provided [135]. Also some physical factors critical to well productivity were examined. Based on several studies on production decline curves. They observed that an exponential or hyperbolic curve adequately fits production decline data for the

Devonian shale wells. An attempt have also been made to characterize the production decline based on open flow, rock pressure, and specific shale production mechanisms.

From the Devonian shale wells, productions is generally characterized by low production rates and large production timespans. Rather common are wells with continued production over 25 years, and some wells with continue production over 50 years are still producing. With production rates however being relatively low, an average well might produce around 300 MMcf in about 20 years or even more. Increasing production rates per well basis, not only adds to gas supplies but also enhances the economic viability of producing more in less time.
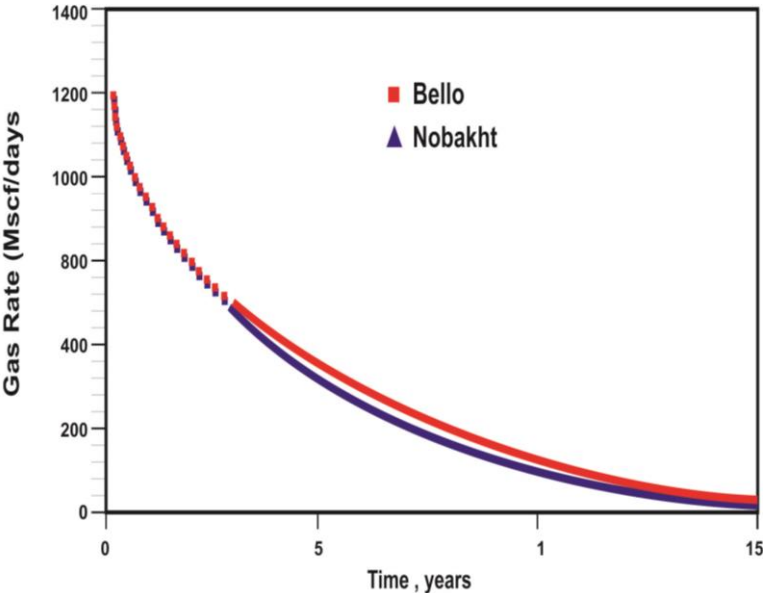
Figure 6.49: 15 years production forecasting, no desorption [130].
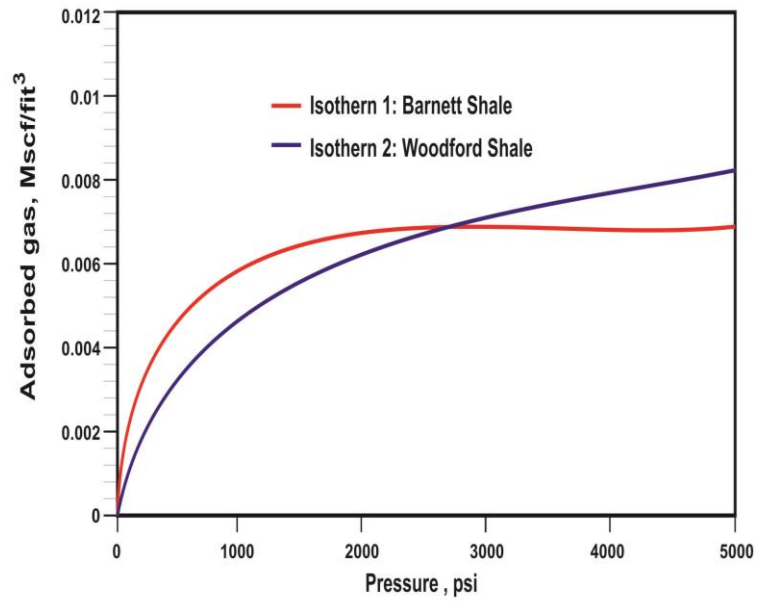
Figure 6.50: Adsorption isotherm Barnett shale [130].
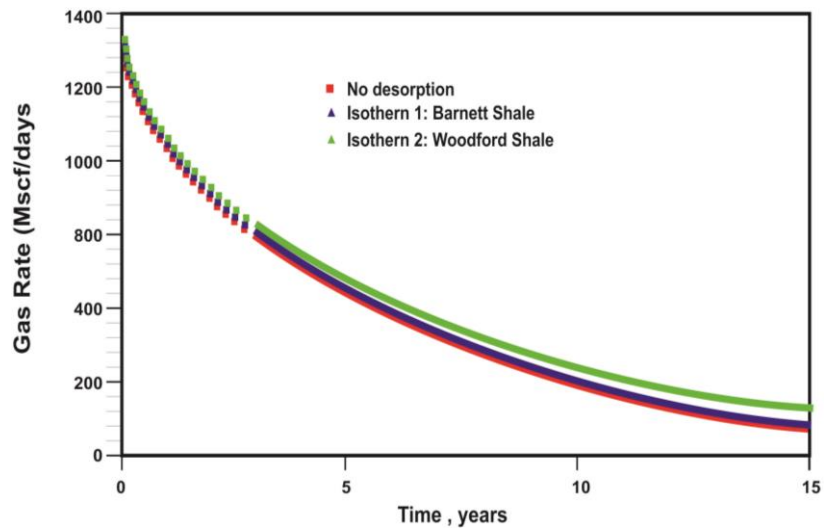
Figure 6.51: Production forecasting for different adsorption isotherms [130].
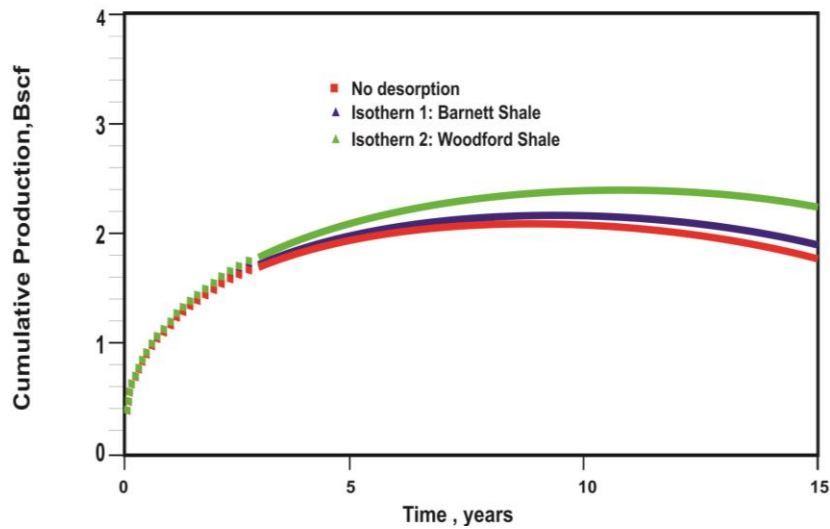
Figure 6.52: Production forecasting for different adsorption isotherms [130].

Table 6.14: EUR comparison.

	EUR at 30 years,Bscf	
	Bello	Nobakht
No desorption	2.38	2.22
Isotherm 1	2.58	2.42
Isotherm 2	23.00	2.82

During the initial stage, it is mostly desirable to estimate well productivity based on measurable variables. Though initial open flow and rock pressures might be used, they do not necessarily signal long-term well performance. This observations are shown in Table 6.15 below.

Table 6.15: Observations of some wells.

Observation wells	IOF	IRP (PSI)	Cum. Prod (MMcf)	Time (years)	Location
1	4500	1610	1165	18	Kanawha, WV
2	257	525	1772	18	Martin, KY
3 (cf 4)	133	410	25	12	Pike, KY
4	67	210	115	12	Wayne, WV
5	340	675	78	16	Lawrence, OH
6 (cf 2)	3209	715	123	19	Meigs, OH
7	1205	200	2001	34	Floyd, KY
8 (cf 7)	1838	655	120	33	Pike, KY
9 (cf 8)	52	308	127	11	Wayne, WV
10	50	762	95	18	Meigs, OH

11	7587	325	367	24	Lincoln, WV
12 (cf 11)	2659	225	1025	20	Lincoln, WV
13	179	470	1400	18	Mingo, WV
14 (cf 13,16)	1485	517	497	19	Mingo, WV
15 (cf 4)	71	720	47	20	Meigs, OH
16	2718	260	608	25	Mingo, WV
17 (cf 16)	12899	355	382	25	Lincoln, WV

From these observations, it is reveal that productivity may be sensitive to physical factors other than open flow and rock pressure, which perhaps cannot be measured directly. It will be necessary to analyze the generating mechanism of production decline curves for possible clues, because relatively low open flow and rock pressure do not necessarily imply low productivity. Graduating production decline data by various curves fit only, is not itself sufficient to understand the mechanism. Some insights have to be obtain possibly from hydrodynamic analogy.

6.4 The Hydrodynamic Analogy

A detailed treatment of geological reservoirs is not intended. Precise reservoir configuration involving fracture geometry (shape, size and spatial orientation), structural, lithologic and other geologic fractures are not addressed. The broad division between the gas-generating shale matrix (lower permeability and porosity) from gas-filled fractures, fissures, sandstones, siltstones and other sources (higher permeability and porosity) is however addressed.

The total reservoir schematically, is partitioned into domains R_1 and R_2 as shown in Figure 6.53 below. Basic attributes of R_1 and R_2 are contained in the set $\{K, \emptyset, P, V\}$ where K = permeability, $\emptyset$ = porosity, P = pressure, V = volume of gas. It will be assumed that flow occurs, and has taken place over geologic time, from domain R_1 to R_2. Flow to the wellbore is from R_2. The hydrodynamic analogy is that, of two circular cylinders containing liquid that are interconnected with inlets (source) and outlets (sinks), as shown in Figure 6.54 below.
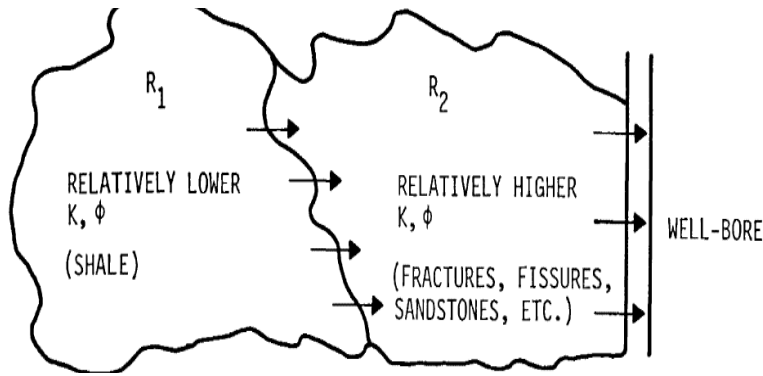
Figure 6.53: Reservoir partition [135].
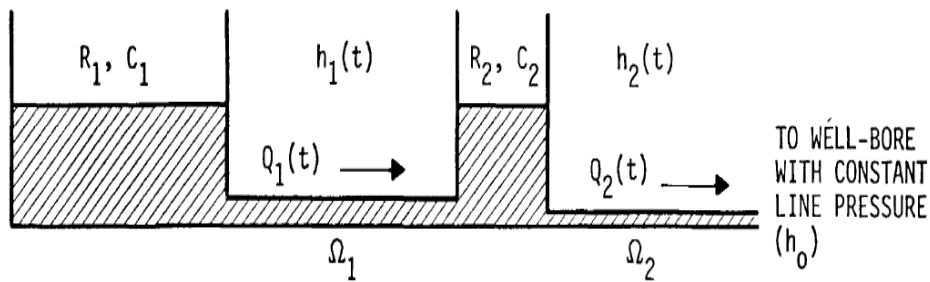
Figure 6.54: Hydrodynamic system [135].

Form R_1 Q_1 is outflow (sink) but inflow (source) to R_2; C (capacitance) is uniform cross-sectional area; $h_1(t)$ is pressure at time t at the boundary and it is proportional to the height of liquid; Ω_1 is resistance to flow at the dividing R_1 fromR_2, and it is a measure of permeability in the region of the boundary. Similar interpretation hold for the R_2 reservoir.

Theoretically, a first-order equivalent relationship between pressure-volume (PV) initial conditions in the actual cylinder "reservoir" could be established.

For R_1:

$$(\pi r_1^2)\, d_1 = V_1$$

That is; $C_1 d_1 = V_1$

$$d_1 \sim P_1$$

For R_2:

$$(\pi r_2^2)\, d_2 = V_2$$

That is; $C_2 d_2 = V_2$

$$d_2 \sim P_2$$

Where d_1 and d_2 are respective liquid heights.

From the above, C_1 and C_2 could be uniquely determined from initial conditions since $d_1 = d_2 \sim p$, the equilibrium pressure at the boundary at time $t = 0$. The pressure in the hydrodynamic system are a function of depth would vary with depth even at time $t = 0$.

The two important assumptions regarding flow are;

(1) Ω_1, Ω_2 (the resistance to boundary flow) will be independent, that is Ω (x, y, z, t) = Ω, at the boundary. This equivalent to permeability K (x, y, z, t) = K being a constant on the boundary. The resistance with reference to Figure 6.54 are at the intersections of R_1 and R_2, and R_2 is the wellbore.

(2)   There are no independent source and sinks within R_1 and R_2 apart from mass transfer resulting from flow in the system. For example, kerogen source will be ignored on the assumption that, gas released by these sources over geologic times is almost complete and further gas release and rates of release are negligible in comparison to the total volume of gas in matrix and fracture pores and interstice.

The equivalence between the hydrodynamic and reservoir systems are summarized in Table 6.16 below.

Table 6.16: Factor equivalence.

Hydrodynamic system	Shale reservoir
Capacitance, C	Porosity, $\emptyset$; C = C($\emptyset$)
Pressure h(x, y, z. t) = h(t) at the boundary	Pressure, P(x, y, z, t)
Resistance, Ω(x, y, z, t) = Ω at the boundary	Permeability, K(x, y, z,) = K(1/Ω)
Bulk flow rate, Q(t, Ω, ∇h)	Darcy's flow rate, q(x, y, z, t, K, ∇h, v,)

6.4.1 Production decline curve derivation

The following simple relationships are obtained with reference to the hydrodynamic system (Figure 6.53), and the nomenclature given in Table 6.16.

For "reservoir" R_1;

(Continuity equation)

$$C1 \frac{dh_1\,(t)}{d_t} = Q_1\,(t) \tag{6.50}$$

(Flow equation)

$$Q_1\,(t) = \frac{h_1\,(t) - h_2(t)}{\Omega_1} \tag{6.51}$$

For "Reservoir" R_2;

(Continuity equation)

$$C2 \frac{dh_2\,(t)}{d_t} = -\,Q_2\,(t) + Q_1(t) \tag{6.52}$$

(Flow equation)

$$Q_2\,(t) = \frac{h_2\,(t) - h_0}{\Omega_2} \tag{6.53}$$

Where h_0 is a constant line pressure.

Substituting for h2 (t) in equation 6.52 with equation 6.53 gives:

$$C_2\Omega_2 \frac{dQ_2(t)}{dt} + Q_2(t) = Q_1(t)$$

$$\rightarrow \frac{dQ_2(t)}{dt} + \lambda Q_2(t) = \lambda Q_1(t)(\lambda = {}^{1}/_{C_2\Omega_2})$$

$$\rightarrow Q_2(t) = e^{-\lambda t}\left[C + \lambda \int e^{\lambda t}\,Q_1(t)\,dt\right] \tag{6.54}$$

Where C is a constant of integration.

Initial conditions: At t= 0, Q_1 (t) = Q_1 (0) = 0, that is when the height of liquid initially in both cylinders is the same, there is no pressure gradient and flow is possible from R_1 to R_2.

$\rightarrow C = Q_2(t)$. Initial open flow.

Equation 6.54 therefore becomes;

$$Q_2(t) = Q_2(0)e^{-\lambda t} + \lambda e^{-\lambda t}\int_0^t e^{\lambda \theta}\,Q_1\,(\theta)d\theta \tag{6.55}$$

An important special case:

$Q_1\,(\theta) = Q_1$, Which is the rate of change of velocity ${dQ_1\,(t)}/{dt} = 0$ at the boundary of R_1 and R_2, is a constant. This means that the rate of movement of shale gas molecules at and near the boundary (e.g. fracture faces) is infinitesimal from the equivalent reservoir standpoint, to be considered as constant. In this case, $Q_1(\theta) = Q_1$, equation (6.55) becomes;

$$Q_2(t) = Q_2(0)e^{-\lambda t} + Q_1\lambda e^{-\lambda t} \int_0^t e^{\lambda\theta} \, d\theta \qquad (6.56)$$

$$Q_2(t) = Q_2(0)e^{-\lambda t} + Q_1\left(1 - e^{-\lambda t}\right) \qquad (6.57)$$

If $t \gg T$, $Q_2(t) \rightarrow Q_1$

The decline curve for production generated by this equation is shown in Figure 6.55 below. Q_1, The constant rate of flow from R1 to R2 will be maintained as long as the flow from the "source-strength", the shale matrix to the more permeable fractures, fissures, and sandstones is sustained in a steady manner. The derived decline curve in Figure 6.55 is supported by the empirical evidence resulting from Devonian shale production data.
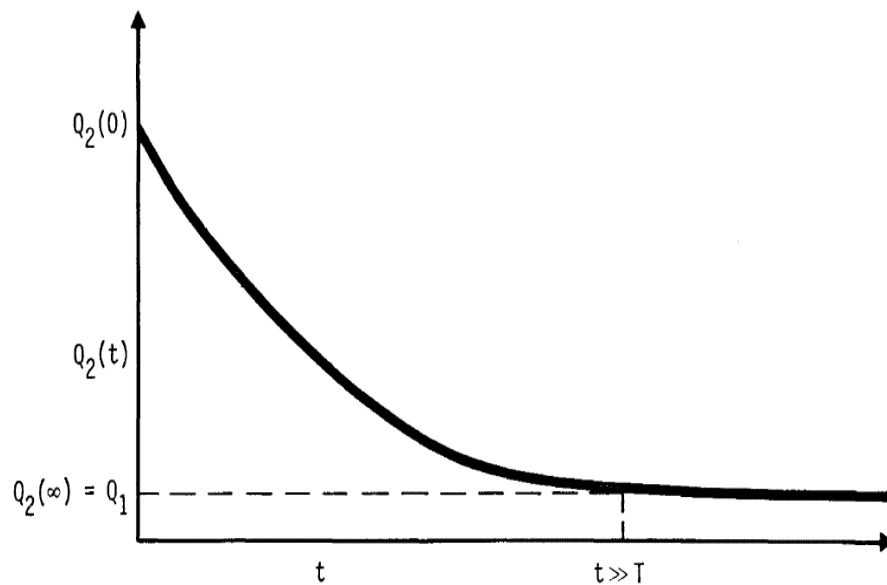
Figure 6.55: Theoretical decline curve [135].

For $Q_1 \rightarrow 0$ or small, an exponential curve dominated by the first term on the right hand side of equation (6.57) would provide a better fit than in the case when Q_1 is large, where hyperbolic curve is the better fit. Figures 6.56 through 6.59 shows some of the history matches of these cases. Production has cease in any case since the resource if not infinite. In many decline curves, the tail end is significantly larger than the body, and this indicates the dominating influence of Q_1 (dual porosity). If $Q_1 \rightarrow 0$ and λ is small (larger capacitance and small permeability), the decline curve is exponential (characterized by single porosity) without much discernible effects of Q_1, the flow of matrix shale gas.
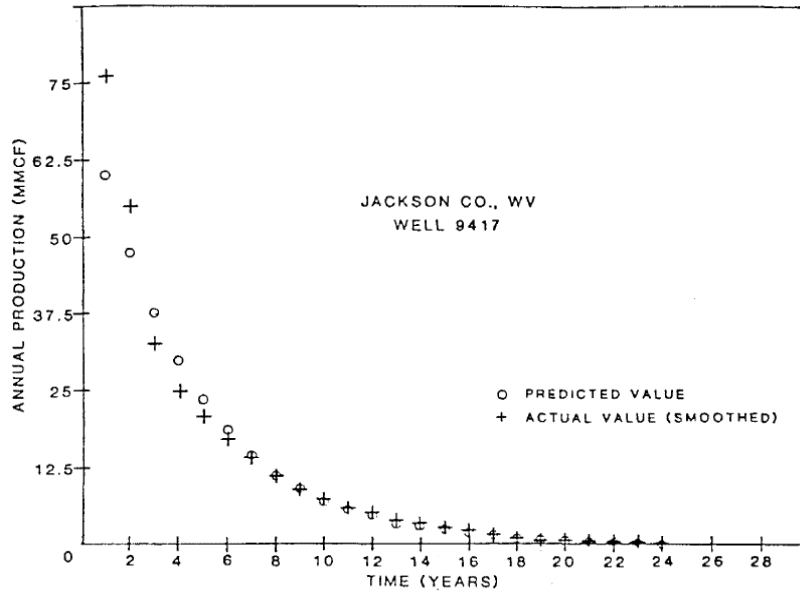
Figure 6.56: Production rate history match for well 9417 [135].
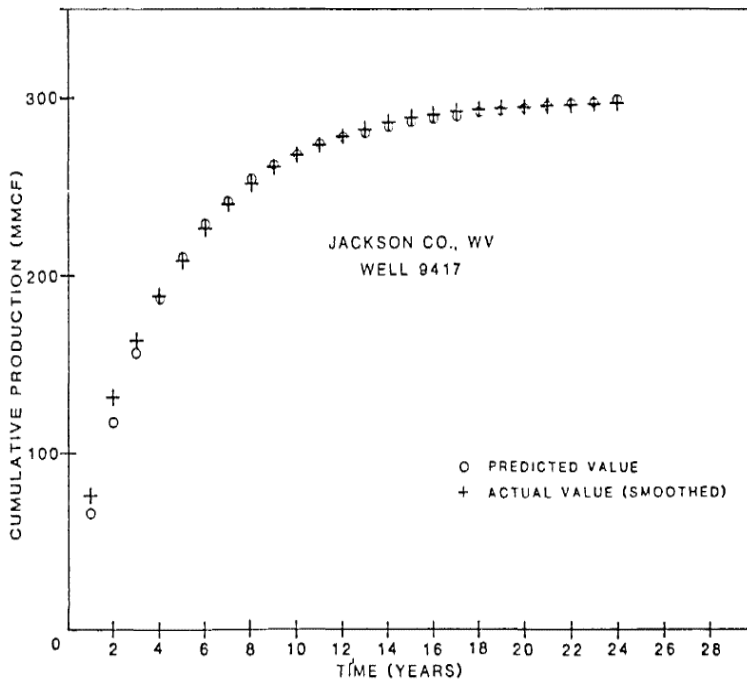
Figure 6.57: Cumulative production history match for well 9417 [135].

280
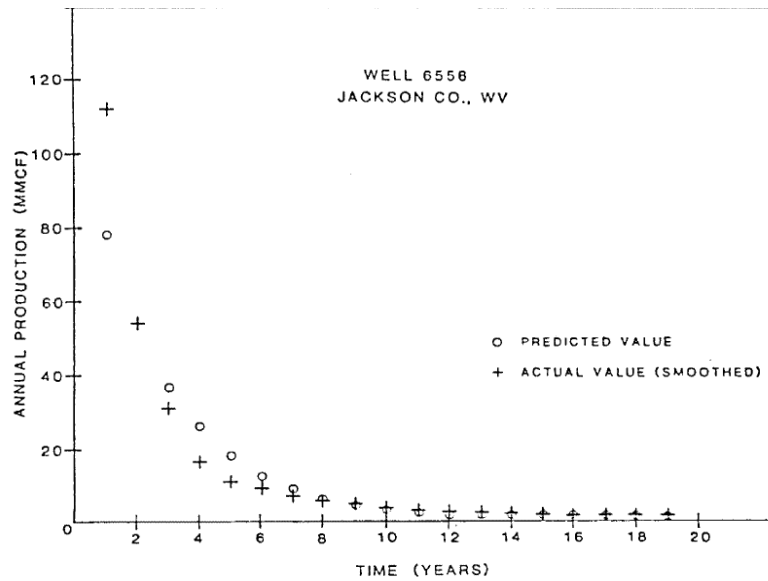
Figure 6.58: Production rate history match for well 6556 [135].
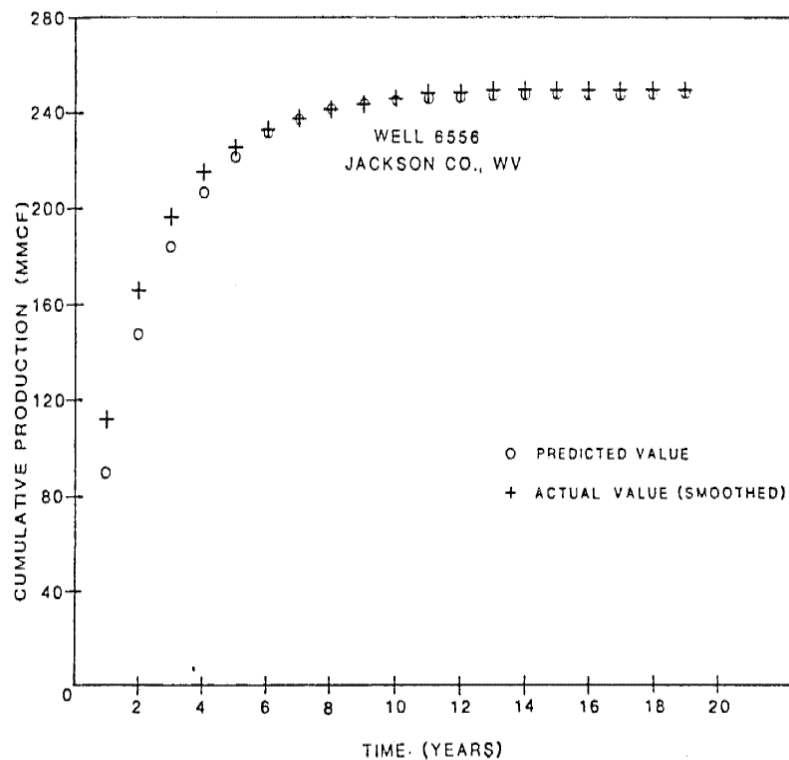
Figure 6.59: Cumulative production history match for well 6556 [135].

From the production data and other observation, it is seen that Devonian shale wells with relatively low initial open flow and rock pressures have been allowed to produce over long timespans. These wells in many instances have actually produced more in the long-run than wells with higher initial open flow and rock pressures. A

gas operator as a result, is not always in a position to estimate long-term well productivity merely on the basis of initial open flow and rock pressures.

This practical observation can be explained by the flow rate derivation. Consider the flow rate equation once again.

$$Q_2(t) = Q_2(0)e^{-\lambda t} + Q_1\left(1 - e^{-\lambda t}\right), \qquad \lambda = \frac{1}{C_2 \Omega_2}.$$

That is,

$$Q_2(t) = [Q_2(0) - Q_1]e^{-\lambda t} + Q_1$$

Let two different wells have the following characteristics:

Well X:

$$(Q_2(t), Q_2(0), Q_1, \lambda)$$

And let;

$$Q_2(0) > Q_2'(0)$$

$\lambda > \lambda'$

And $Q_1 < Q_1'$

Well X':

$(Q_2'(t), Q_2'(0), Q_1', \lambda')$

The production decline curves for wells X and X' under these conditions, with well X' having greater productivity are shown in Figure 6.60 below. Observation wells 4 and 5 in Table 6.16 for example reflect the decline curves in Figure 6.60.
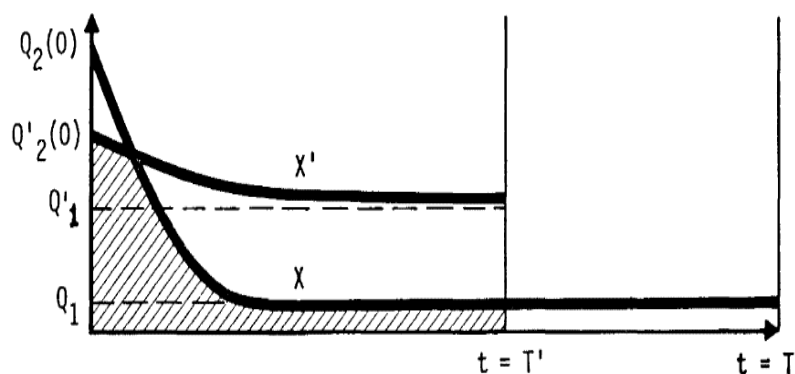
Figure 6.60: Comparison of wells X and X' [135].

The two most important factors of the flow rate equation which will enhance production in general sense are Q_1 (the steady flow of matrix gas across the boundary to fractures, fissures, sandstones, etc.) and λ, the rate of decline. The larger Q_1 and

fracture capacitance C_2 (smaller λ) for a given fracture permeability are, the higher the cumulative production will be.

The factor Q_1 may be regarded as the total flux across the boundary surface per unit time. The factor Q_1 may be expressed as:

$$Q_1 = \iint_s \underline{q} \cdot \underline{n} \, ds$$

where q = K∇P (Darcy's law), and Gauss's theorem:

$$\iiint_v \nabla \cdot \underline{\underline{q}} \, d\tau = \iint_s \underline{\underline{q}} \cdot \underline{\underline{n}} \, ds$$

That is, the divergence (source-strength) of $\underline{q}$ within the volume of shale is equal to $\underline{q}$ integrated over the total surface (fracture faces and interfaces) which is Q_1. Though $\underline{q}$ (from Darcy's law) may be small, Q_1 could be very large depending on S (the total surface area). Similar statement should hold for Q_2.

Brown M. et al. presents an analytical trilinear-flow solution [136] to simulate the pressure transient and production behaviors of fractured horizontal wells in unconventional shale reservoirs [137]. Though the model is simple, it is versatile enough to incorporate the fundamental petrophysical characteristics of shale reservoir including the intrinsic properties of the matrix and natural fractures. Various reservoir components including special characteristics of fluid exchange may be considered.

The advantages of the trainer solution are, computational convenience makes it a practical alternative to more rigorous but computationally intensive and time consuming solutions, and is convenience in deriving asymptotic approximations that provides insight about potential flow regimes and conditions leading to these flow regimes. Linear and bilinear flow regimes which have been noted for fractured horizontal wells in the literature on the basis of their diagnostic features, are not been associated with particular reservoir characteristics and flow relationships. The tri-linear flow solution also provides a suitable algorithm for the regression analysis of pressure transient tests in shale reservoirs.

Horizontal wells production from unconventional shale reservoirs involves flow in shale matrix, in the reservoir fracture network (called natural fractures in this study),

and in hydraulic fractures (assumed as biwing transverse fractures in this study). It is although possible to develop detailed analytical [138], [139], and numerical models [140] to represent transient flow of fluid toward a multiple-fractured horizontal well in tight, unconventional reservoirs such as shale, the disadvantages of these models includes increased computational requirements, the implicit functional relationships of key parameters, and the inconvenience in their use in alternative applications. Some simplifications are possible how ever if the natural fracture network is a results of shear slippage because of hydraulic fracturing and localized around the horizontal well.

Hydraulically fractured horizontal well in shale reservoirs have their matrix permeability's in the range of micro-Darcie's or below, and the contribution to the reservoir beyond the stimulated reservoir volume (SRV) is usually negligible [140], [141]. The key characteristics of flow convergence toward a multiply-fractured horizontal well within the SRV, may be preserved in the tri-linear flow model presented [137] despite the complex interplay of flow among matrix, natural fractures, and hydraulic fractures. The model is not applicable if the regions beyond the well tips dominates the well response. However this condition is not likely exist unless the shale matrix permeability is well above the micro-Darcy range or the bottom-hole pressure or rate is unrealistically low.

The tri-linear model other than that, can be used whenever the use of an analytical model is warranted by the complexity of the problem and the availability of data. Analytical models are preferred for pressure transient purposes if they can represent sufficient details of fluid and reservoir characteristics.

As shown in Figure 6.61 below, the tri-linear flow model couples with linear flows in three contiguous flow regions. The outer reservoir above the tip of the hydraulic fractures (denoted by the subscript O), the inner reservoir between hydraulic fractures (denoted by the subscript I), and the hydraulic fracture (denoted by the subscript F). Each of these regions can have a distinct properties. The hydraulic fractures may have finite conductivity, and the inner reservoir may be naturally fractured or homogeneous.
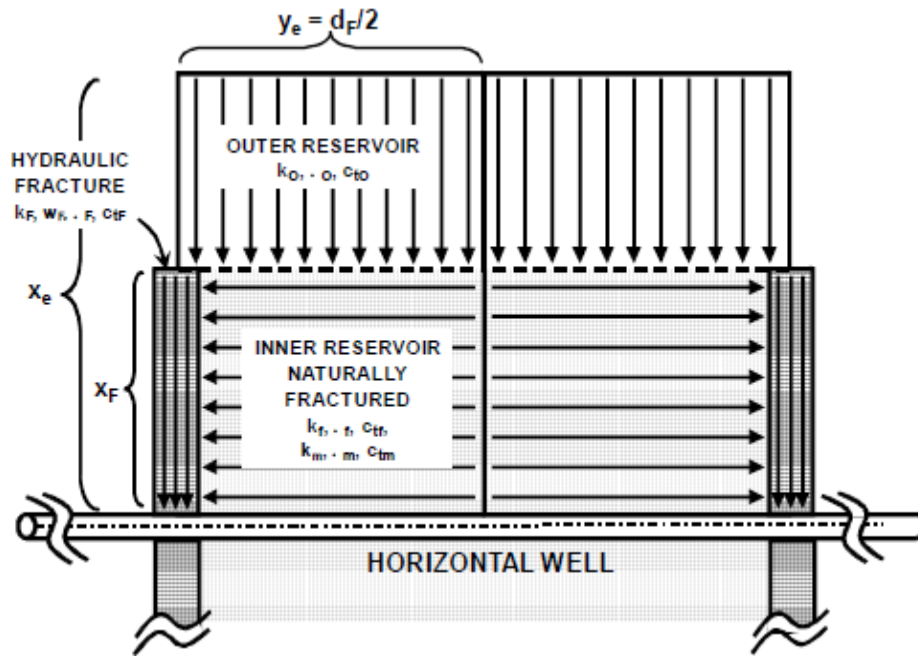
Figure 6.61: Schematic of the tri-linear flow model representing three contiguous flow regimes for multiple fractured horizontal well [135].

Some idealizations and simplifications are made to derive a practical model. This model is derived for single-phase flow of a constant compressibility fluid. Single-phase gas flow is handled through pseudo-pressure transformation. Flow from reservoir into horizontal well is only by virtue of hydraulic fractures; that is, production directly from the surface of horizontal well is assumed be negligible (as the surface area of the horizontal well is negligible with respect to the total surface area of the hydraulic fractures). Along the horizontal well, hydraulic fractures are assumed to have identical properties and are equally spaced by a distance, d_F. This assumption can be overruled by an approach similar to that Raghavan et al used [139]. Creating equally spaced hydraulic fractures of similar properties however, is a common field practice and, unless there is significant contrast in individual-fracture properties, the use of the average fracture properties should be sufficiently accurate.

Around the horizontal well, the SRV is envisioned like a naturally fractured porous medium and idealized as a dual-porosity region. Two common models of dual-porosity idealization are used in this study. The model that considers pseudo-steady fluid transfer from matrix to fracture [142] is referred as the Pseudo-steady model. The model that incorporates transient fluid transfer from matrix to fracture [143], [144], [145] is referred to the transient model. Matrix and fracture media are denoted

by the subscript m and f respectively for the dual porosity reservoir. Though the choice of the particular dual porosity model does not affect the general solution for the tri-linear flow model, it does affect the definition of the key parameters.

Each hydraulic fracture is considered to be a finite conductivity porous media. One dimensional linear flow is assumed in hydraulic fractures because the wellbore storage normally masks the very-early-time radial flow convergence towards the well within the hydraulic fractures [146], [147], [148], [149], the effect of radial flow convergence at the fracture/horizontal well intersection however, is taken into account by a flow-choking skin. The effect of the wellbore storage in incorporated into the model by convolution.

Flow in the inner reservoir between hydraulic fractures and flow in the outer reservoir beyond the tips of the hydraulic fractures additionally, are both assumed to be linear. In the inner reservoir, linear flow is assumed as a result of either a non-perforated horizontal well between fractures or that, the hydraulic fractures dominate production. The bisector of the distance between two hydraulic fractures as shown in figure, is a no-flow boundary because of the assumption of identical hydraulic fractures.

The outer reservoir does not contribute to production significantly for most common application in unconventional shale gas reservoirs. However, its contribution if it contributes, is akin to linear flow towards a finite conductivity fracture. As explained [139], [138], a multiple fractured horizontal well behaves like a single fracture between the two outer most fractures along the horizontal well at long times. The flow from the outer reservoir therefore is mainly in the direction perpendicular to flow in the inner reservoir. Minimum allowable flow rates are reached under this flow regime unless the horizontal well is short.

The single porosity results of the tri-linear flow model are the same as early-time solution [138]. The tri-linear flow was verified by comparing the results with the semi-analytical solution [140].

In this studies, the pressure transient response of a horizontal well with n_F identical transverse hydraulic fractures under the conditions assumed can be modeled by considering one of the fracture producing from a rectangular reservoir section at a

rate equal to $q_F = q/n_F$, where q is the total flow rate of the horizontal well shown in Figure 6.62.
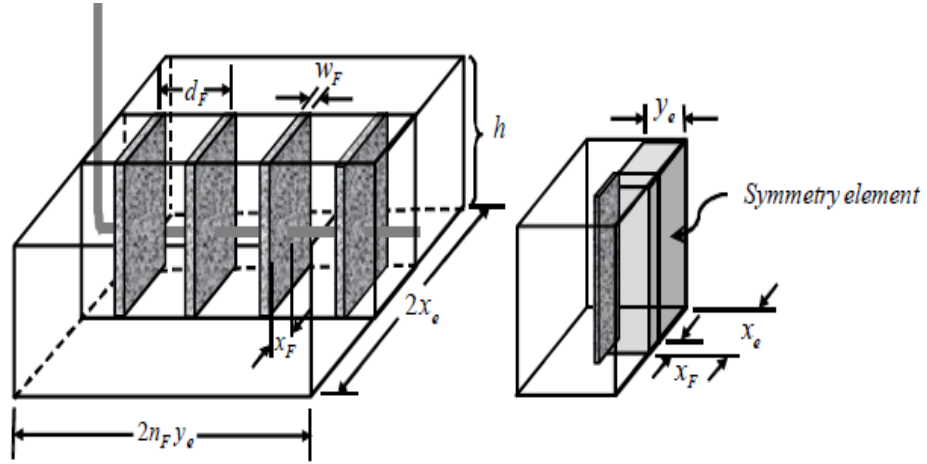
Figure 6.62: Multiple fractured horizontal well and the symmetry element used in the derivation of the tri-linear flow model [135].

The fracture is located centrally in the closed rectangular drainage area of size $2x_e \times 2y_e$, which is equal to $1/n_F$ of the total drainage area of the horizontal well as shown in figures 6.61 and 6.62. In the formation, the fracture has a half length of x_F and a width of w_F and penetrates the entire thickness, h.

The tri-linear solution is derived in terms of dimensionless variables for convenience. The definitions of the parameters used in pseudo-steady and transient dual-porosity models are first explained here. The definitions of the dimensionless variables used in the tri-linear flow model are then presented.

Dual-porosity parameters: A naturally fractured reservoir may be characterized in terms of intrinsic or bulk (equivalent) properties in dual-porosity idealization. If X_ξ denotes an intrinsic property of the medium where ξ = m (matrix) or f (fracture), then the bulk properties of the medium ξ are defined by;

$$\bar{X}_\xi = r_\xi X_\xi \qquad (6.58)$$

In the equation 6.58 above, $r_\xi = V_\xi/V_b$ where V_ξ is the bulk volume of the medium, ξ and V_b is the bulk volume of the total system ($V_b = V_m + V_f$). It is customary to introduce the pseudo-steady dual-porosity model [142] in terms of bulk properties.

Into the pseudo-steady dual-porosity medium, characteristics of the matrix and fracture media are incorporated by the storativity and flow-capacity ratios defined respectively as follows;

$$\omega = \frac{(\widetilde{\emptyset}\widetilde{C_t})_f}{(\widetilde{\emptyset}\widetilde{C_t})_f + (\widetilde{\emptyset}\widetilde{C_t})_m} \qquad (6.59)$$

And

$$\lambda = \sigma l^2 \frac{\widetilde{k_m}}{\widetilde{k_f}} \qquad (6.60)$$

l in equation 6.60 is a reference length that is chosen in this study as the half-length of the hydraulic fracture; $l = x_F$ (in comparing the results of this study with other model, adjustment should be made to the values of λ to compensate for different choice of reference length).

In equation 6.60, the definition of the matrix shape factor σ is an important issue to discuss, but this discussion is outside the scope of this study. The following first approximation for shape factor of rectangular matrix blocks was proposed by Kazemi et al. [95];

$$\sigma = 4\left(\frac{1}{L_x^2} + \frac{1}{L_y^2} + \frac{1}{L_z^2}\right), \qquad (6.61)$$

Where; L_x, L_y and L_z are the dimensions of the matrix block. Square matrix block of side-length L is assumed for this study and used $\sigma = \frac{12}{L^2}$ to compute the shape factor.

The transient dual-porosity model [143], [144], [145] may be introduced in terms of either intrinsic or bulk properties of the fractures and matrix media.

The transient dual-porosity model represent the naturally fractured reservoir as a stack of alternating matrix and fracture slabs. If h_f and h_m denote the thickness of each fracture and matrix slab respectively and n_f and n_m are the number of fracture and matrix slabs respectively, then the total fracture and matrix thickness are $h_{ft} = n_f h_f$ and $h_{mt} = n_m h_m$ respectively. The formation thickness thus; h $= h_{ft} + h_{mt}$.

Serra et al. [145] define the storativity and flow-capacity ratios for the transient dual-porosity model respectively by;

$$\omega = \frac{(\emptyset C_t)_m}{(\emptyset C_t)_f} \qquad (6.62)$$

And

$$\lambda = 12 \left(\frac{l^2}{h_m^2}\right)\left(\frac{k_m h_{mt}}{k_f h_{ft}}\right) = 12 \left(\frac{l^2}{h_m^2}\right)\left(\frac{k_m h_f}{k_f h_f}\right) \qquad \textbf{(6.63)}$$

It should be noted that, choosing the matrix slab thickness h_m, in the transient model equal to the side-length of the square matrix blocks L, in the pseudo-steady model, yield the same value of the flow-capacity ratio for both dual-porosity models. In the comparison of the results, this equivalence will be used from both dual-porosity models.

The dimensionless pressure and time was defined respectively as follows;

$$P_D = \frac{k_I h_I}{141.2 \, q_F B \mu} (P_i - P) \qquad \textbf{(6.64)}$$

And

$$t_D = \frac{\eta_l}{x_F^2} t, \qquad \textbf{(6.65)}$$

Where

$$\eta_l = 2.637 \times 10^{-4} \frac{k_I}{(\emptyset C_t)_I \mu} \qquad \textbf{(6.66)}$$

The usual approach for the analysis of gas wells was followed and incorporate the liquid-flow of Al-Hussainy et al. analogy [96] through the pseudo-pressure transformation.

$$m(p) = 2 \int_{p_b}^{p} \frac{\acute{p}}{\mu z} \, d\acute{p} \qquad \textbf{(6.67)}$$

The transformations [151], [152] may be used to analyze buildup test. But such transformations should not be used for drawdown test.

The subscript I used in equations 6.64 and 6.65 and in the rest of the definition given here, refers to the property of the inner reservoir. The definitions are based on the homogeneous matrix properties for a homogeneous (single-porosity) inner reservoir. When the inner reservoir is naturally fractured and the transient dual-porosity model is used, $k_p, h_p \text{ and } (\emptyset C_t)_I$ refers, respectively, to the intrinsic fracture permeability ($k_I = k_f$), total fracture thickness ($h_I = h_{ft} = n_f h_f$), and the intrinsic fracture storativity [$(\emptyset C_t)_I = (\emptyset C_t)_f$]. In the case of the pseudo-steady dual-porosity model, k_I is the bulk fracture permeability ($k_I = \tilde{k}_f$), h_I is the formation thickness ($h_I = h$), and $(\emptyset C_t)_I$ is the total system storativity [$(\emptyset C_t)_I = \left(\tilde{\emptyset}\tilde{C}_t\right)_f + \left(\tilde{\emptyset}\tilde{C}_t\right)_m$]. It should be

noted that the definition of the dimensionless pressure is the same for both dual-porosity models because $k_f h_{ft} = k_f \left(h_{ft}/h \right) h = \tilde{k}_f h$.

The dimensionless distance in x- and y-direction are defined, respectively, by;

$$x_D = \frac{x}{x_F} \tag{6.68}$$

And

$$y_D = \frac{y}{x_F} \tag{6.69}$$

The dimensionless distance to the reservoir boundaries are given by x_{eD} and y_{eD}.

In this our model, the following definitions of dimensionless fracture and reservoir conductivities respectively will be used.

$$C_{FD} = \frac{k_F w_F}{\tilde{k}_I x_F} \tag{6.70}$$

And

$$C_{RD} = \frac{\tilde{k}_I w_F}{k_o y_e} \tag{6.71}$$

Note, regardless of the choice of the dual-porosity model, C_{FD} and C_{RD} are defined on the basis of the bulk permeability of the inner reservoir, k_I. The following diffusivity ratios are also defined:

$$\eta_{FD} = \frac{\eta_F}{\eta_I} \tag{6.72}$$

And

$$\eta_{OD} = \frac{\eta_o}{\eta_I} \tag{6.73}$$

Where η_I is the diffusivity of the inner reservoir defined in equation 6.66 and η_F and η_o are the diffusivities of the hydraulic fracture and outer reservoir given respectively and are defined by;

$$\eta_F = 2.637 \times 10^{-4} \frac{k_F}{(\phi C_t)_F \mu} \tag{6.74}$$

And

$$\eta_O = 2.637 \times 10^{-4} \frac{k_O}{(\phi C_t)_O \mu} \tag{6.75}$$

During the test for gas flow, η_F and η_O are evaluated at the highest pressure [150]. The outer reservoir properties for horizontal wells producing from shale may be

taken to be the same as the properties of the inner reservoir matrix as a first approximation.

The Mathematical model for analytical derivation of the tri-linear flow model in this study follows the same lines as Cinco-Ley and Meng, who presented the finite conductivity fracture solution in a dual-porosity reservoir [153]. One-quarter of the hydraulic fracture, as noted in the definitions section of this study, in a rectangular drainage region (Figures6.61 and 6.62) is considered.

The solution for outer reservoir, inner reservoir, and the hydraulic fracture is derived, and then couples the solutions by using the flux- and pressure-continuity conditions on the interface between the regions. Because we consider the possibility that the inner reservoir may be naturally fractured, it is more convenient to derive the solution in the Laplace transform-domain. The algorithm proposed by Stehfest is used in this study to numerically invert the results computed in the Laplace transform-domain into the time domain [154].

Outer reservoir solution: The diffusivity equation and associated boundary conditions for the outer reservoir, assuming one-dimensional flow in the x-direction, are given by

$$\frac{\partial^2 \bar{P}_{OD}}{\partial x_D} - \frac{S}{\eta_{OD}} \bar{P}_{OD} = 0 \qquad (6.76)$$

$$\left(\frac{\partial \bar{P}_{OD}}{\partial x_D}\right)_{x_D = x_{eD}} = 0 \qquad (6.77)$$

And

$$\bar{P}_{OD}|_{x_D=1} = \bar{P}_{ID}|_{x_D=1} \qquad (6.78)$$

Where the over-bar symbol represents dimensionless pressure in the Laplace-transform domain and s is the Laplace-transform parameter with respect to dimensionless time, t_D. In equation 6.76 through 6.77, the solution of the boundary-value problem can be obtained in the Laplace-transform domain as follows:

$$\bar{P}_{OD} = \bar{P}_{ID}|_{x_D=1} \frac{\cosh\left[\sqrt{S/\eta_{OD}} (X_{eD} - X_D)\right]}{\cosh\left[\sqrt{S/\eta_{OD}} (X_{eD} - 1)\right]} \qquad (6.79)$$

The outer reservoir solution in equation 6.79, P_{OD}, is given in terms of the inner reservoir pressure at the interface of the inner and outer reservoir, $\bar{P}_{ID}|_{X_D-1}$.

Inner reservoir solution: In the inner reservoir, flow is assumed to be in one-dimension and in the y-direction perpendicular to the hydraulic fracture plane. The partial differential equation associated is given by

$$\frac{\partial^2 \bar{P}_{ID}}{\partial y_D^2} + \left(\frac{1}{y_{eD} C_{RD}}\right) \frac{\partial \bar{P}_{OD}}{\partial x_D}\bigg|_{X_D=1} - u\bar{P}_{ID} = 0 \qquad (6.80)$$

Where;

$$u = sf(s) \qquad (6.81)$$

and

$$f(s) = \begin{cases} 1 \\ \frac{s\omega(1-\omega)+\lambda}{s(1-\omega)+\lambda} \\ 1 + \sqrt{\lambda\omega/(3s)} \, \tanh\left(\sqrt{3\omega s/\lambda}\right) \end{cases} \qquad (6.82)$$

Where f (s) = 1 is for homogeneous inner region

F (s) = $\frac{s\omega(1-\omega)+\lambda}{s(1-\omega)+\lambda}$ is for pseudo-steady dual-porosity inner reservoir, and

F (s) = $1 + \sqrt{\lambda\omega/(3s)} \, \tanh\left(\sqrt{3\omega s/\lambda}\right)$ is for transient dual-porosity inner reservoir

Substituting from equation 6.79,

$$\frac{\partial \bar{P}_{OD}}{\partial x_D}\bigg|_{X_D=1} = -\beta_O \bar{P}_{ID}|_{X_D=1} \qquad (6.83)$$

Where

$$\beta_O = \sqrt{S/\eta_{OD}} \, \tanh\left[\sqrt{S/\eta_{OD}}\,(x_{eD}-1)\right] \qquad (6.84)$$

And assuming, $P_{ID} \neq f(x_D)$, equation 6.80 becomes

$$\frac{\partial^2 \bar{P}_{ID}}{\partial y^2} - \alpha_O \bar{P}_{ID} = 0 \qquad (6.85)$$

Where

$$\alpha = \frac{\beta_O}{C_{RD} y_{eD}} + u \qquad (6.86)$$

The boundary conditions for the inner reservoir are given by

$$\left(\frac{\partial \bar{P}_{ID}}{\partial y_D}\right)_{y_D=y_{eD}} = 0 \qquad (6.87)$$

And

$$\bar{P}_{ID}|_{y_{D=} w_{D}/_2} = \bar{P}_{FD}|_{y_{D=} w_{D}/_2}. \qquad (6.88)$$

Therefore, the solution of equation 6.85 with the boundary conditions given by equations 6.87 and 6.88, is

$$\bar{P}_{ID} = \left(\bar{P}_{FD}|_{y_{D=} w_{D}/_2}\right) \frac{\cosh\left[\sqrt{\alpha_o}(y_{eD}-y_D)\right]}{\cosh\left[\alpha_o\left(y_{eD}-\frac{w_D}{2}\right)\right]} \qquad (6.89)$$

And depends on the hydraulic fracture solution, $\bar{P}_{FD}|_{y_D = {}^{w_D}/_2}$.

Hydraulic-fracture solution: In the hydraulic fracture, the partial differential equation describing one-dimensional flow is given by

$$\frac{\partial^2 \bar{P}_{FD}}{\partial x_D^2} + \frac{2}{C_{FD}} \frac{\partial \bar{P}_{ID}}{\partial y_D}\Bigg|_{y_D = {}^{w_D}/_2} - \frac{s}{\eta_{FD}} \bar{P}_{FD} = 0. \tag{6.90}$$

From equation 6.89, we substitute

$$\frac{\partial \bar{P}_{ID}}{\partial y_D}\Bigg|_{y_D = {}^{w_D}/_2} = -\beta_F \bar{P}_{FD}|_{y_D = {}^{w_D}/_2} \tag{6.91}$$

And equation 6.90 can be written as follows:

$$\frac{\partial^2 \bar{P}_{FD}}{\partial x_D^2} - \alpha_F \bar{P}_{FD} = 0 \tag{6.92}$$

In equations 6.91 and 6.92,

$$\beta_F = \sqrt{\alpha_o} \tanh\left[\sqrt{\alpha_o}\left(y_{eD} - \frac{w_D}{2}\right)\right] \tag{6.93}$$

And

$$\alpha_o = \frac{2\beta_F}{C_{FD}} + \frac{s}{\eta_{FD}}. \tag{6.94}$$

The hydraulic fracture problem boundary conditions are given by

$$\frac{\partial \bar{P}_{FD}}{\partial x_D}\Bigg|_{x_D = 1} = 0. \tag{6.95}$$

And

$$\frac{\partial \bar{P}_{FD}}{\partial x_D}\Bigg|_{x_D = 0} = -\frac{\pi}{C_{FD}s}. \tag{6.96}$$

Then, for the hydraulic fracture, the dimensionless pressure solution is obtained as

$$\bar{P}_{FD} = \frac{\pi}{C_{FD}s\sqrt{\alpha_o}} \frac{\cosh[\sqrt{\alpha_F}(1 - x_D)]}{\sinh(\sqrt{\alpha_F})} \tag{6.97}$$

From equation 6.97, the dimensionless wellbore pressure is obtained and is given by

$$\bar{P}_{wD} = \bar{P}_{FD}(x_D = 0) = \frac{\pi}{C_{FD}s\sqrt{\alpha_F}\tanh(\sqrt{\alpha_F})} \tag{6.98}$$

One-dimensional linear flow within the hydraulic fracture is assumed in the preceding derivations; that is, the radial flow convergence towards the wellbore

within the hydraulic fracture is ignored. The following equations were provided [147] to compute the skin factor caused by flow choking within the fracture:

$$S_c = \frac{k_I h_I}{k_F w_F} \left[\ln \left(\frac{h}{2r_w} \right) - \frac{\pi}{2} \right]$$ (6.99)

The following solution was obtained after adding the choking skin to equation 6.98. This solution is a good approximation for dimensionless wellbore pressure after end of the radial flow in the hydraulic fracture:

$$\bar{P}_{wD} = \frac{\pi}{C_{FD} s \sqrt{\alpha} \tanh(\sqrt{\alpha})} + \frac{S_c}{s}.$$ (6.100)

The effect of wellbore storage should be taken into account at early times in order to develop a more practical solution. By substituting $\bar{P}_{wD}$ from equation 43 into the following convolution expression in the Laplace domain, the effect of wellbore storage can be incorporated into the solution:

$$\bar{P}_{wD,storage} = \frac{\bar{P}_{wD}}{1 + C_D s^2 \bar{P}_{wD}}$$ (6.101)

Where the dimensionless wellbore storage coefficient C_D is given by

$$C_D = \frac{5.615 C}{2\pi (\emptyset C h_I)_I x_F^2}$$ (6.102)

The definition of C_D depends on the dual-porosity model selected to represent the inner reservoir and, for the same value of the wellbore storage coefficient C, a different dimensionless wellbore storage coefficient C_D is obtained for pseudo-steady and transient dual-porosity models.

The solution given by equation 6.100 or equation 6.101 was also used to compute dimensionless buildup pressure from the following superposition equation:

$$L[P_{sD}(\Delta t_D)] = L[P_{wD}(t_{pD})] - L[P_{wD}(t_{pD} + \Delta t_D)] + L[P_{wD}(\Delta t_D)]$$ (6.103)

Where

$$P_{SD} = \frac{k_I h_I}{141.2 q_F B \mu} (P_{ws} - P_{wf,s})$$ (6.104)

In equation 6.103, t_{pD} is the dimensionless producing time, Δt_D is the dimensionless shut-in time, and $L[P_D(t_D)]$ denotes the Laplace-transform of $P_D(t_D)$ with respect to

t_D. In equation 6.104, P_{ws} is the bottom-hole shut-in pressure and $P_{wf,s}$ is the bottom-hole pressure at the instant of shut-in.

For multiple-fractured horizontal wells in homogeneous reservoirs, analytical pressure-transient solutions developed [138], [139] by using the ideas of Bennett et al. who developed solutions for fractured vertical wells in layered reservoirs[155]. Substituting f (s) = 1 and u = s in equation 6.100 for a homogeneous reservoir, the tri-linear flow model yields the same asymptotic solutions at early times as the other methods [138], [139]. This provides analytical verification of our tri-linear flow model.

The tri-linear flow solution is also verified by comparing the results with the semi-analytical solution [140]. The semi-analytical solution models hydraulic fracture a porous media and considers radial flow convergence towards the wellbore within the hydraulic fractures. The semi-analytical solution therefore, is expected to capture the characteristics of early time flow regimes in hydraulic fractures (fracture radial- and radial/linear flow regimes). The accuracy of the computations at very early time however, is hindered by gridding and discretization of the boundaries. The tri-linear flow model similarly incorporates the effects of flow choking in hydraulic fractures through a skin factor, and therefore becomes accurate after the end of early time radial flow in hydraulic fractures. Difference are expected in the results of the two models at early times considering the limitations of these semi-analytical and tri-linear models.

The early time flow regimes are masked and the limitations of the models at early times becomes insignificant for practical purposes when the effects of wellbore storage in taken into account. The comparison of the results from tri-linear and semi-analytical models without the effects of wellbore storage will be presented first in the following. The effects of wellbore storage on early time results will be demonstrated.

The results of the tri-linear and semi-analytical [140] models without the effects of wellbore storage ($C_D = 0$) is shown in Figure 6.55 below. Pseudo-steady dual-porosity behavior has been assumed for the inner reservoir. Because the tri-linear model assumed that the reservoir is limited to the stimulated reservoir volume, the tri-linear model responses in Figure 6.63 show a unit slope behavior caused by the closed outer boundary at late time. At late times, the semi-analytical model responses

fall slightly below the tri-linear model responses because of the weak support of the outer reservoir beyond SRV.

At early times, the differences in the results of the two models shown in figure 6.63 are also to be expected and may be explained a follows. The semi-analytical model displays the characteristics of radial/linear flow [148], [149], [156] by a constant derivative trend at early times. On the other hand, the derivative responses of the tri-linear flow model displays the characteristics of linear flow in hydraulic fractures. The tri-linear model matches the pressure responses of the semi-analytical model except at very early times, indicating that the effects of the early time fracture radial flow is incorporated into the pressure responses of the tri-linear flow model accurately enough by assuming a choking skin defined in equation 6.99.

Figure 6.64 is considered the same way as in Figure 6.63 but the results of the wellbore storage coefficient of C = 0.0105 bbl/psi is added. Most of the hydraulic fracture flow regimes are masked because of the relatively small wellbore storage effect. However, the discussion is intended for rigor and completeness; otherwise, for a reasonable wellbore storage effect, the differences displayed between the early time responses of the tri-linear and semi-analytical models should disappear within a few seconds for most practical applications (for the particular case in Figure 6.64, $t_D = 10^{-3}$ corresponds approximately to 30 seconds). It should be noted that the apparent wellbore storage effect on the early time behavior of the semi-analytical model is a numerical artifact.

Impact of choice in dual-porosity models at intermediate times, although the transient and pseudo-steady dual-porosity models are known to have differences, the ramifications of the choice in dual-porosity models are sometimes overlooked (especially when using standard numerical packages). Assuming there is no wellbore storage, in Figure 6.65, the tri-linear flow results for the pseudo-steady and transient dual-porosity models are compared.

The pseudo-steady dual-porosity responses as a function of t_D and the transient dual-porosity responses as a function of ${t_D}/{(1 - \omega)}$ is plotted to make comparison at the same real time (definitions of dimensionless time for the pseudo-steady and transient dual-porosity models used total-system properties and intrinsic fracture respectively). Though the responses for $t_D \leq 10^{-4}$ are not of practical interest, they are included in

Figure 6.65 to display the expected dual-porosity characteristics at early time, intermediate time and late time.
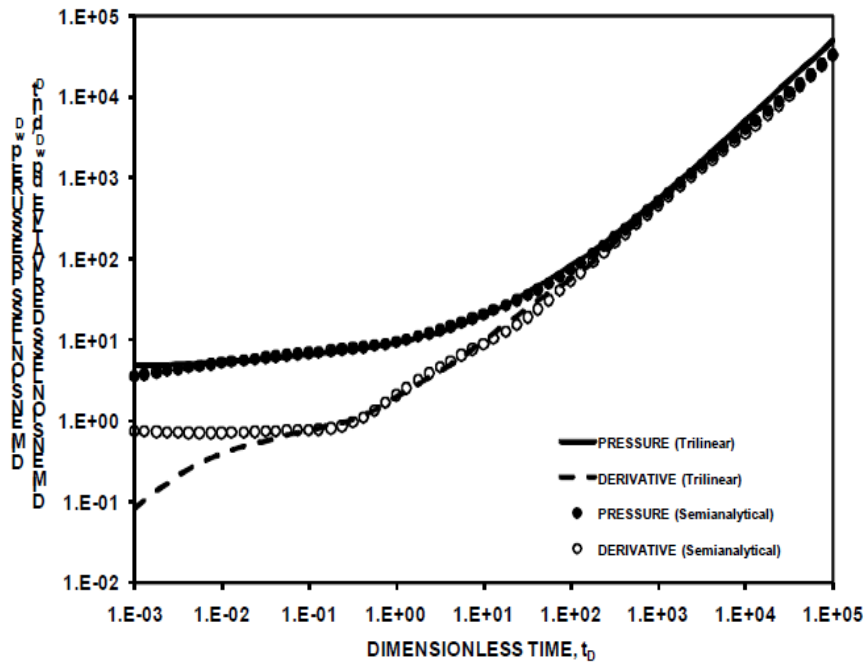
Figure 6.63: Comparison of the tri-linear and semi-analytical models results without wellbore storage [135].
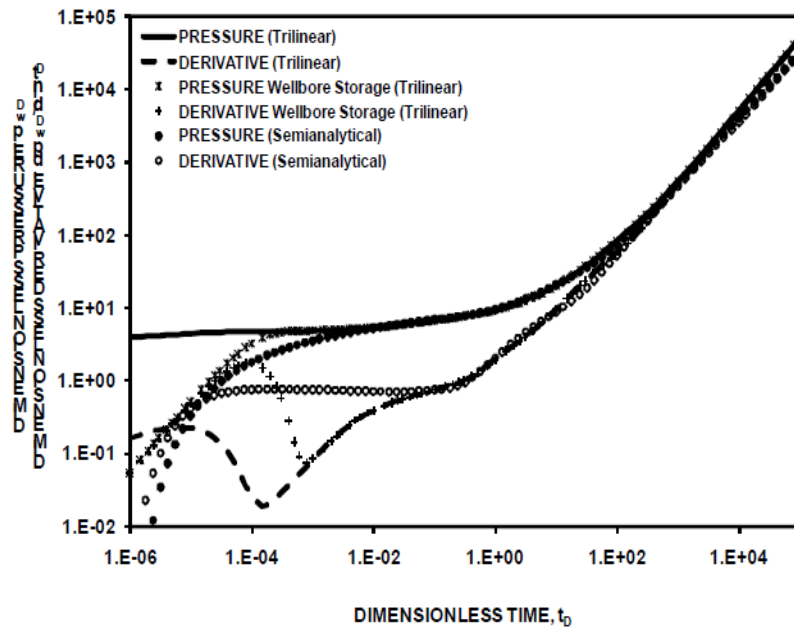
Figure 6.64: Comparison of the tri-linear and semi-analytical models results with wellbore storage [135].

In the derivative responses of the dual-porosity models, the appearance of dip requires two conditions: there should be considerable flow from matrix to fracture

network and the pseudo-steady (stabilized) flow in the matrix. As soon as the fluid transfer from matrix to fracture begins, the pseudo-steady dual-porosity idealization assumes instantaneous stabilization of flow in the matrix. On the other hand, the transient dual-porosity idealization takes into account the transient flow conditions before pseudo-steady (stabilized) flow is established in the matrix. The duration of the transient flow period is determined by the permeability, size, and the geometry of the matrix blocks.

An extended period of transient fluid transfer from matrix to fracture is possible if the matrix is tight and the fracture density is small. The dip in the derivative responses under these conditions is either delayed (if pseudo-steady state is established in the matrix before pseudo-steady state develops in the total system), or masked by the reservoir boundary effects (in this case, the matrix and fracture system reached pseudo-steady state concurrently). In the case of small matrix blocks and relatively high permeabilities, which are more common in conventional tight gas reservoirs, the transient flow period in the matrix is shorter and the differences between the results of the two dual-porosity idealization may be insignificant for practical purposes.
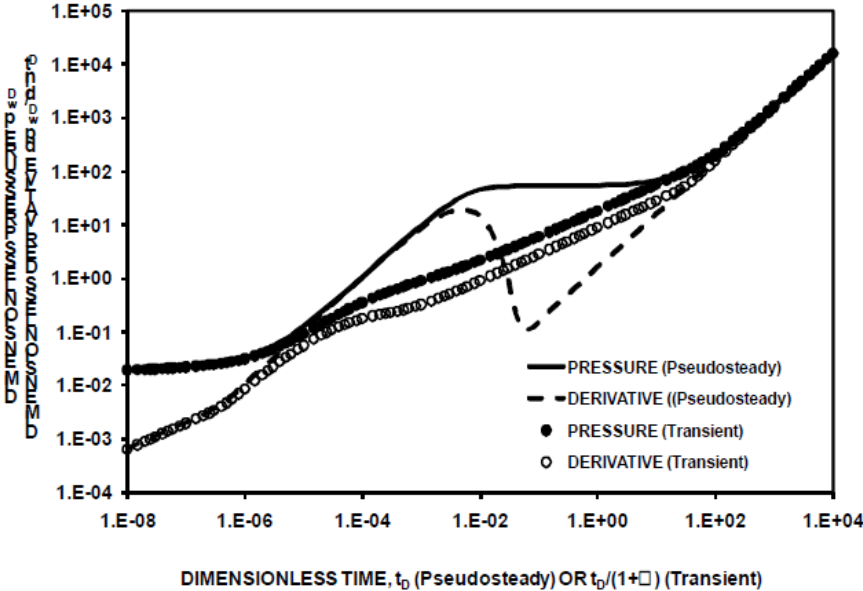
Figure 6.65: Comparison of the pseudo-steady and transient dual-porosity models for naturally fractured inner reservoir [135].

298

Also in Figure 6.65, for the transient dual-porosity case considered, the matrix does not reach pseudo-steady state before pseudo-steady state is established in the total system (the unit-slope derivative behavior at late time). The characteristic dip in the derivative responses therefore is not shown (masked by the reservoir depletion under pseudo-steady state). The same data used in Figure 6.65 is used in Figure 6.66, a wellbore storage coefficient of C = 0.0105 bbl/psi is considered. The pseudo-steady and transient dual-porosity models responses are considerably different. The results shown in Figure 6.66 more importantly, indicate that some characteristics of the pressure derivative responses may be attributed to inaccurate flow regimes because of the inappropriate choice of the dual-porosity model.
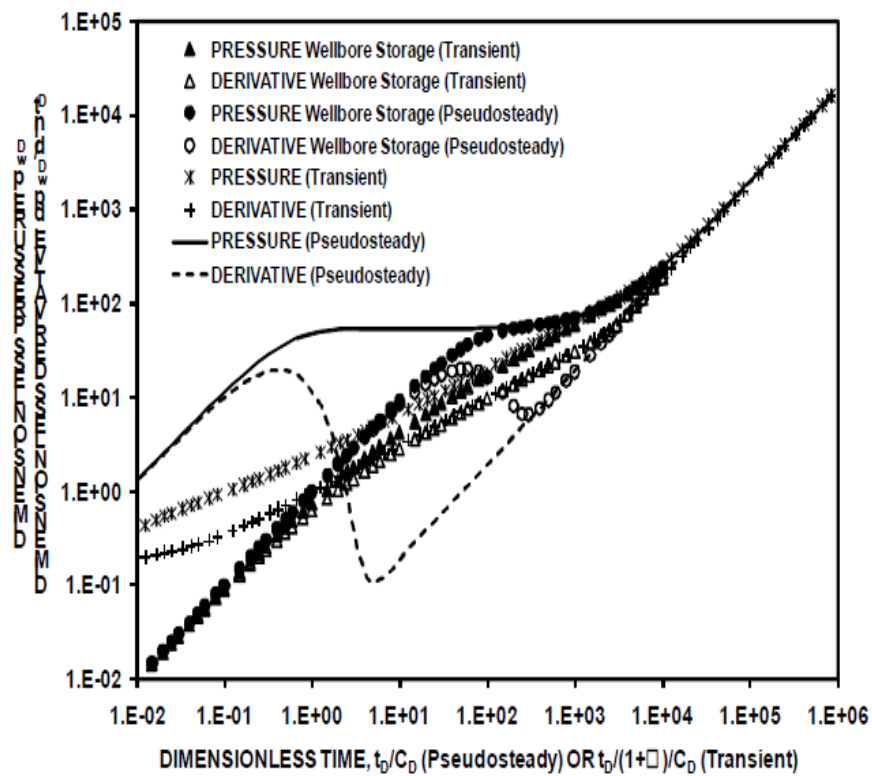
Figure 6.66: Effects of wellbore storage on pseudo-steady and transient dual-porosity models for naturally fractured inner reservoir [135].

6.4.2 Asymptotic approximation and flow regimes

For the tri-linear flow solution, asymptotic approximations may be obtained by considering the limiting form of equation 6.100 for large and small values of the Laplace transform parameter s (the limiting forms for large and small values of s represent the early time and late time behavior of the solution respectively). Depending on the relative values of s, ω, and λ, approximate forms of f(s) given in

299

equation 6.82 are substituted into equation 6.100. For pseudo-steady and transient dual-porosity models, suitable approximation of f(s) are given respectively by

$$f(s) = \begin{cases} 1, & as\ s \to 0 \\ \lambda/[s(1-\omega)], & for\ intermediate\ values\ of\ s \\ \omega, & as\ s \to \infty \end{cases} \quad (\textbf{6.105})$$

And

$$f(s) = \begin{cases} 1+\omega \\ \sqrt{\lambda\omega/(3s)} \\ 1 \end{cases} \quad (\textbf{6.106})$$

The conditions in equation 6.105 is the same as in equation 6.106.

Also, $\tanh(\alpha)$ may be replaced by the following approximations in deriving asymptotic approximations to equation 6.100 similarly:

$$\tanh(\alpha) = \begin{cases} \alpha & as\ \alpha \to 0 \\ \alpha - \alpha^3/3 & for\ intermediate\ values\ of\ \alpha \\ 1 & as\ \alpha \to \infty \end{cases} \quad (\textbf{6.107})$$

For the tri-linear flow solution, it is possible to derive several asymptotic approximations by considering the relationship in equations 6.105 through 6.107. The existence and applicability of the asymptotic relationships with respect to field data depend on the complex interplay of a large number of parameters controlling the pressure transient responses. The asymptotic can be derived analytically, graphically or empirically. The objective here is merely to draw attention to the multiple intermediate time approximations that are possible with the same diagnostic slope values on a log-log plots of pressure and derivative responses. The use of the analysis techniques based on the slope characteristics of straight lines is not warranted because not only the slope, but also the value of the straight line should be matched with an asymptotic relationship. Though non-uniqueness is an issue because of the large number of regression parameters, matching the entire data span with a model responses (regression analysis) usually converges to a better solution (or diverges altogether). The results may be refined by straight line analysis, after an initial match is obtained, using the asymptotic solutions.

6.5 Economics Evaluation of shale plays

The shale plays have a great future, always have had a great future, but the present is impossible to predict. Rising gas and oil prices and improvement in technology have made the development of shale plays economically [159].

In the USA oil and gas industry, shale gas plays are the current rage. Major shale gas plays are unfolding at present time in Barnett, Woodford, New Albany, and Fayetteville shales and othe basins are being targeted as well [160]. The most mature of these plays is the Barnett shale near Fort Worth Texas with more than 6000 wells on production. There is enough production history now to begin to develop an idea of how commercial these plays can be. There has been a number of changes in drilling and completion practices over the years. Major advances in technology including horizontal wells drilling, fracturing and re-fracturing existing wells, and using slick water (gelled water) for frac jobs. The economics of the Barnett shale play is examined as it is actually developed [160].

The economics are run on each individual well basis and sum up for each area. The base case economic parameters are chosen to represent an approximation of current conditions. These cases are run on a before-income-tax basis and the net cash flow are discounted back to time zero (the date of first production for each of the individual area) at 10 percent per annum [160]. Base case run were made for each area. Also for each area, sensitivity runs were made for individual varrying prices, capital costs, and operating costs 25 percent higher than the base case values. Additional sensitivity run was made by removing the top 5 percent of the wells in each area from the analysis. A total number of 24 different runs were made and the results of sensitivity case on discounted profit to investment ratio are shown in Table 6.17 and the cost of the base case economic parameters are shown in Table 6.18 [160].

At today's cost and prices it takes an ultimate recovery of about 550 to 900 MMcf to pay out for a well and the top 5 percent of the wells based on ultimate recovery have a significant effect on the economic viability of the project in any given area.

Table 6.17: Sensitivity case on discounted profit to investment ratio [160].

	Low Area			Medium Area			High Area		
	-25%	Base	+25%	-25%	Base	+25%	-25%	Base	+25%
Price	0.36	0.54	0.72	0.62	0.90	1.18	0.89	1.24	1.59
Capex	0.91	0.54	0.35	1.55	0.90	0.59	1.79	1.24	0.93
Opex	0.58	0.54	0.49	0.96	0.90	0.85	1.29	1.24	1.20

Table 6.18: The cost of the base case economic parameters [160].

Capital costs		
Vertical well drill & completion	2,400,000	
Vertical well refrac	600,000	
Horizontal well drill & completion	3,400,000	
Horizontal well refrac	1,000,000	
Operating cost	6,000	$/well/month
As of date	Varies by area	
Disc rate	10%	Per annum
Working interest	100%	
Net revenue interest	85%	
Severance tax rate	7.5%	
Ad valorem tax rate	3.0%	
BTU	1000	BTU/SCF
Shrinkage	0	
Net back wellhead gas price	$7	Per MMBTU

The minimum economic price for shale oil varies depending on the technology and resource quality [159]. In another study, it was propposed that, for a mature 100,000bbl/d capacity plant, the average minimum economic prices are $38 per bbl for true in-situ, $47 per bbl for surface mining, $57 per bbl for underground mining, and $62 per bbl for modified in-situ [159].

7. CONCLUSIONS

A great of information has been reviewed and summarized for the entire exploration and research activities for shale gas and shale oil. Shale formations are found in many countries of the world, hence improvement in technology and techniques to produce from the shale will help ease the energy crisis.

For a shale play to be economically viable, the total organic content (TOC) must be in the range of 2% to 14%. This condition must be met before further analysis on the shale play should be conducted.

The techniques were employed in different shales and it was observed that shale plays behave differently even in the same locality. It was also observed that, as research continues, the shale plays are more understood and productivity is therefore enhanced. However, research is ongoing in most of the shale plays.

The most important factor to determine during the analysis of the shale play is the brittleness or ductility of the shale. These can be determine by using Young's modulus and Poisson's ratio. Since the shale play cannot be produced economically without fracturing, factors to determine the possible regions for fracturing is the backbone of the shale play if economic production is required.

For the costs and prices during this thesis work is conducted, an ultimate recovery of about 550 to 900 million standard cubic feet of gas has to be produced to pay out for one well. In oil production from shales, for a mature field with 100 000 barrels per day oil production the minimum oil price should be at least 43 USD per barrel.

REFERENCES

[1] **Caldwell, P.**, (2010). Broxburn Shale, The Rise and fall of an Industry" The Grimsay Press, an imprint of Zeticula, 57 St. Vincent Crescent, Glassgow, G3 8NQ, Scotland, pp. 1-12.

[2] **King, G. E.**, (2012). Hydraulic Fracturing 101: What Every Representative, Environmentalist, Regulator, Reporter, Investor, University Researcher, Neighbor and Engineer Should Know About Estimation Frac Risk and Improving Frac Performance in Unconventional Gas and Oil Wells, paper SPE 152596, presented at the SPE Hydraulic Fracturing Technol. Conf., Woodlands, Texas, USA, 6-8, February.

[3] **EIA,** (2011). Review of Emerging Resources: U.S. Shale Gas and Shale Oil Plays, an overview based on the report prepared by INTEK, Inc., for the U.S. Energy Information Administration (EIA), the U.S. Department of Energy, Washington D.C., USA, July.

[4] **Filer**, **J. K.**, (1987). Geology of Devonian Shale Oil and Gas in Pleasants, Wood, and Ritchie Counties, West Virginia, SPE Formation and Evaluation, December. Page 419-420.

[5] **Ghods, P. and Zhang**, **D.**, (2012). Automatic Estimation of Fracture Properties in Multi-stage Fracture Shale Gas Horizontal Wells for Reservoir Modelling, Paper SPE 153913, Presented at the SPE Western Regional Meeting, Bakersfield, California, USA, 19-23 March.

[6] **Andrews**, **A.**, (2002). Oil Shale: History Incentives and Policy, Congressional Research Service Report, RL 33359, Diane Publishing Co., April 13.

[7] **Loucks**, **R. A.**, (2005). Shale Oil, Tapping the Treasure, Xlibris LLC, Bloomington, Indiana, USA, www.Xlibris.com, pp. 15-27.

[8] **Andrews**, **A.**, (2002). Oil Shale: History Incentives and Policy, Congressional Research Service Report, RL 33359, Diane Publishing Co., April 13, pp. CRS-12.

[9] **Ibid.**, (2002). pp. CRS-13.

[10] **Chen, J-H., Mehmani, A., Li, B., Georgi, D., and Jin, G.,** (2013). Estimation of Total Hydrocarbon in the Presence of Capillary Condensation for Unconventional Shale Reservoirs, paper SPE 164468, Presented at SPE Middle East Oil and Gas Show and Conf., Manama, Bahrain, 10-13 March.

[11] **Strickland, R.**, **Purvis**, **D.**, **and Blasingame**, **T.**, (2011). Practical Aspects of Reserves Determination for Shale Gas, paper SPE 144357, presented at the SPE North America Unconventional Gas Conf. and Exhb., Woodlands, Texas, USA, 12-16 June.

[12] **Shumaker**, **R. C.**, (1982). A Deltaic Geologic Study of Three Fractured Devonian Shale Gas Fields in the Appalachian Basin, paper SPE/DOE 10791, presented at the SPE/DOE Unconventional Gas Recovery Symp. of the Society of Petroleum Engineers, Pittsburgh, PA, 16-18 May.

[13] **Cluff**, **R. M. and Dickerson, D. R.**, (1982). Natural Gas Potentials of the New Albany Shale Group (Devonian-Mississippian) in South-eastern Illinois, Soc. of Pet. Eng. Jou. April. pp 292.

[14] **Evans, C. R.**, **McIvor**, **D. K.**, **and Magara**, **K.**, (1975). Organic Matter, Compaction History and Hydrocarbon Occurrence-Makenzie Delta, Canada, paper WPC-16114, presented at 9th World Petroleum Congress, 11-16 May, Tokyo, Japan. Pp.149-157.

[15] **Yousif S. and Nouman G.**, (1995). Geological Model of the Jurassic Section in the State of Kuwait, paper SPE 29796, presented at the SPE Middle East Oil Show, Bahrain, 11-14 March.

[16] **Sadooni, F. N**, (1997). Stratigraphy and Petroleum Prospects of Upper Jurassic Carbonates in Iraq, Petroleum Geoscience, 3, pp. 233-243.

[17] **Goff, J. C.**, (2005). Origin and Potential of Unconventional Jurassic Oil Reservoirs on the Northern Arabian Plate, paper SPE 93505, presented at the 14th SPE Middle East Oil and Gas Show and Conf., Bahrain, 12-15 March.

[18] **Ucan, S.**, **Olmos, S.**, **Rios S.**, **and Marin**, **H.**, (2007). Oil Invasion in Gas Zone and Sweep Efficiency Due to Stratigraphic Barrier in Active Waterdrive System, Hollin Formation, Ecuador, paper SPE 108123, presented at 10th SPE Latin America and Caribbean Petroleum Eng. Conf., Buenos Aires, Argentina, 15-18 April.

[19] **Chelini, V., Muttoni, A., Mele, M., Rossi, E., Galimberti, R. F., and Ortenzi A.**, (2010). Gas Shale Reservoir Characterization: A North Africa Case, paper SPE 134292, SPE Annual Tech. Conf. and Exhb., Florence, Italy, 19-22 September.

[20] **Nawel R., Mohamed A. B., Saidi M. and Ibrahim B.,** (2012). Geochemical Correlation and Migration Studies of the South Eastern Part of Tunisia, paper SPE 150832, presented at the North Africa Tech. Conf. and Exh., Cairo, Egypt, 20-22 February.

[21] **Fox J. N., Martiniuk C. D.**, (1994). Reservoir Characteristics and Petroleum Potential of the Bakken Formation, South Western Manitoba, *Jou. Canadian Pet. Tech.,* Vol. 33, No. 8, October.

[22] **Zargari**, **S. and Mohaghegh**, **S. D.**, (2010). Field Development Strategies for Bakken Shale Formation, paper SPE 139032, presented at the SPE Eastern Regional Meeting, Morgantown, West Virginia, USA, 12-14 October.

[23] **A Report on Shale Gas Potential in Turkey**, (2011). XIII. Turkey, World Shale Gas Resources: An Initial Assessment, Published by Advanced Resources International,Inc. February 17.

[24] **Alvaro A., Mehrnoosh S. and Heidari Z.**, (2012). Petrophysical Rock Typing in Organi-Rich Source Rocks Using Well Logs, presented at the Unconventional Resource Technol. Conf., Denver, Colorado, U.S.A, 12-14 August.

[25] **Andrew C. P., Conoco P., Heidari Z., and Torres-Verdin**, (2012). Rock Classification from Conventional Well Logs in Hydrocarbon-Bearing Shale, paper SPE 159255, presented at the SPE Ann. Tech. Conf. and Exh., San Antonio, Texas, USA, 8-10 October.

[26] **Heidari, Z., Torres-Verdín, C., and Preeg, W.E.**, (2011). Quantitative Method for Estimating Total Organic Carbon and Porosity, and for Diagnosing Mineral Constituents from Well Logs in Shale-Gas Formations. Colorado Springs: The Society of Petrophysicists and Well Log Analysts.

[27] **DeCoster, J.**, (1998). Overview of Factor Analysis. August. http://www.stat-help.com/notes.html (accessed December 2014).

[28] **Sagar K., Chandra S. Rai and Carl H. S. M.**, (2010). Rock Typing in Gas Shales, paper SPE 134539, presented at the SPE Ann. Tech. Conf. and Exh., Florence, Italy, 19-22 September.

[29] **Sagar V. K., Chandra S. R. and Carl H. S. M**, (2010). Petrophysical Characterization of Barnett Shale, paper SPE 131770, presented at the SPE Unconventional Gas Conf., Pittsburgh, Pennsylvania. USA, 23-25 February.

[30] **Singh P.**, (2008). Lithofacies and Sequence Stratigraphic Framework of the Barnett Shale, NorthEast Texas. Phd. Dissertation, Univ. of Oklahoma, Norman, Oklahoma.

[31] **Karastathis A.**, (2007). Petrophysical Measurements on Tight Gas Shale. Masters Thesis, Univ. of Oklahoma, Norman, Oklahoma.

[32] **Sondhi N. and Solano L. P.**, (2009). Application of Thermogravimetric-Fourier Transform Infrared Spectroscopy Analysis in Determining Heating Protocol for Porosity Measurements in Shales. Poster presentation at SPWLA Ann. Meeting, Houston.

[33] **Vanorsdale C.R., and Boring P. A.**, (1987). Evaluation of Initial Data to Estimate Devonian Shale Gas Reserves, paper SPE 16862, presented at the 62nd Ann. Tech. Conf. and Exh. of Soc. of Pet Eng, Dallas, TX, USA, 27-30 September.

[34] **Ambrose, R. J., Hartman, R. C., Diaz-Campos, M., Akkutlu, I. Y., and Sondergeld**, C. H., (2010). Shale Gas-in-Place Calculations Part I: New Pore-Scale Considerations, paper SPE 131772, SPE Unconventional Gas Conf., Pittsburgh, Pennsylvania, USA, February 23-25.

[35] **Dubinin, M. M.**, (1960). The Potential Theory of Adsorption of Gases and Vapors for Adsorbents with Energetically Nonuniform Surfaces. *Chemical Review* 60 (2): 235–241.

[36] **Haydel, J.J. and Kobayashi, R.**, (1967). Adsorption Equilibria in the Methane-Propane-Silica Gel System at High Pressures. *Ind. Eng. Chem. Fundamen.* 6 (4): 564–554.

[37] **Menon, P.G.**, (1968). Adsorption at high pressures, Chem. Rev. 68 (3): pp 277–294.

[38] **Ozawa S., Kusumi, S. and Ogino Y.**, (1976). Physical adsorption of gases at high pressure. IV. An improvement of the Dubinin—Astakhov adsorption equation. *Jou. of Colloid Interface Sci.* **56** (1): 83–91.

[39] **Tsai M.C., Chen W.N., Cen P.L., Yang R.T., Kornosky R.M., Holcombe N.T. and Strakey J.P.**, (1985). Adsorption of gas mixture on activated carbon. *Carbon* **23** (2): 167–73

[40] **Ming L., Anzhong G., Xuesheng L. and Rongshun, W.**, (2003). Determination of the adsorbate density from supercritical gas adsorption equilibrium data. *Carbon* **41** (3): 585–588.

[41] **Nath S.K, Escobedo F.A. and de Pablo J.J.**, (1998). On the simulation of vapor-liquid equilibria for alkanes. *Jou. Phys. Chem.* **108** (23): 9905–9911.

[42] **Todorov I.T. and Smith W.**, (2008). The DLPOLY_3 User Manual. Cheshire, UK: Science & Technology Facilities Council (STFC).

[43] **Krishna R.** (2009). Describing the Diffusion of Guest Molecules inside Porous Structures. *Jou. Phys. Chem. C* **113** (46): pp19756–19781.

[44] **Shapiro A. A., Stenby E.H.**, (1997, Kelvin equation for a non-ideal multicomponent mixture, Fluid Phase Equilibria, 134,), pp87-101

[45] **Katz D.L. and Saltman W.**, (1939), Surface Tension of Hydrocarbons, Ind. Eng. Chem., 31, p91-94

[46] **Weinang C.F., Katz D.L.,** (1943), Surface Tension of Methane-Propane Mixtures, Ind. Eng. Chem., 35, p239

[47] **Ray J. A., Robert C. Hartman, and Akkutlu I. Y.**, (2011). Multi-component Sorbed-phase Consideration for Shale Gas-in-place Calculations, paper SPE 141416, presented at the SPE Production and Operations Symposium, Oklahoma, USA, 27-29 March.

[48] **Aytac E.**, (2010). Lower Palezoic Oil Potential of Southeast Turkey, District X and XI, presented at Petform Panels, Ankara, January 11.

[49] **Atilla, A.**, (2010). Potential Shale Gas Resources inTurkey: Evaluating Ecological Prospects, Geochemical Properties, Surface Access & Infrastructure, presented at the Global Shale Gas Summit, Warsaw, Poland, July 19.

[50] **Gurgey K.**, **Phillip R. P.**, **Clayton C.**, **Emiroglu**, **H.**, **and Siyako**, **M.**, (2005). Geochemical and Isotopic Approach to Maturity/

Source/Mixing Estimations for Natural Gas and Associated Condensates in the Thrace Basin, NW Turkey, Applied Geochemistry 20, No. 11, pp. 2017-2037.

[51] **Gurgey, K.**, (2009). Geochemical Overview and Undiscovered Gas Resources Genertaed from Hamitabat Petroleum System in the Thrace Basin, Turkey, Marine and Pet. Geo. 26, No. 7, pp. 1240-1254.

[52] **Karahanoglu N., Eder A., and Illeez H. I.,** (1995). Mathematical Approach to Hydrocarbon Generation History and Source Rock Potential in the Thrace Basin, Turkey, Marine and Pet. Geo. 12, No. 6, pp. 587-596.

[53] **Hosgormez, H., and Yalcin**, **M. N.,** (2005). Gas-Source Rock Correlation in Thrace Basin, Turkey, Marine and Pet. Geo., 22, No. 8, pp. 901-916.

[54] **Atilla**, **A.**, (2010). Potential Unconventional Reservoirs in Different Basins of Turkey, presented at the AAPG European Region Ann. Conf., Kiev, Ukraine, October 17.

[55] **Sari A. and Kars A. S.**, (2008). Source Rock Characterization of the Tertiary Units in Havsa-Edirne Area: Thrace Basin, Turkey, Energy Source, Part A: Recovery, Utilization and Environmental Effects 30, N0. 10 (2008): 891.

[56] **Anurag Y., Ahmad S. Q. and Khan S.**, (2014). Integrated Well Construction Approach for Exploratory Shale Gas Horizontals, paper SPE 167743, presented at the SPE/EAGE European Unconventional Conf. and Exh., Viena, Austria, 25-27 February.

[57] **Yost II A. B., Overbey W.K., Carden R.S. G., Shursen M.,** (1987). Drilling a 2,000-ft Horizontal Well in the Devonian Shale, paper SPE 16681, presented at the 62nd Ann. Tech. Conf. and Exh. of Soc. of Petroleum Engineers, Dallas, TX, 27-30 September.

[58] **Pitcher J., Jackson T.**, (2012). Geosteering in Unconventional Shale: Current Practice and Developing Methodologies, paper SPE 152580, SPE/EAGE European Unconventional Resources Conf. and Exh., Vienna, Austria, 20-22 March.

[59]   **Pitcher J. and Buller D.**, (2011). Shale Assets: Applying the Right Technology for Improving Results, paper presented at the AAGP Int. Convention and Exh., Milan, Italy, 23-26 October.

[60] **Al-Hajari A., Soremi A., Ma S., Juliah A., Thompson T., Saghiyyah G., Lotfy A., Bayrakdar M., Bittar M., and Chemali R.**, (2009). Proactive Geosteering in Thin Reservoir Bounded by Anhydrite in Saudi Arabia, paper IPTC 13304, Presented at IPTC, Doha, Qatar, 7-9 December.

[61] **Schmidt K., Poole M., and Hildred G.**, (2010). A Triumvirate of Targeting – A Three Pronged Approach to Keeping a Horizontal Well in the Desired Eagle Ford Reservoir Interval, American

Association of Petroleum Geologists, Int. Ann. Conf. and Exh., 12-15 September.

[62] **Marsala A.F., Loermans T., Shen S. Christian S. and Richard Z.**, (2011). Real-Yime Mineralogy, Lithology and Chemostratigraphy While Drilling using Portable Energy-Dispersive X-ray Fluorescence, paper SPE 143468, presented at the SPE EUROPEC/EAGE Ann. Conf. and Exh., Vienna, Austria, 23-26 May.

[63] **Passey Q.R., Bohacs K. M., Esch W.L., Klimentidis R., and Sinha S.**, (2010). From Oil-Prone Rock to Gas Producing Shale Reservoir – Geologic and Petrophysical Characterization of Unconventional Shale Gas Reservoir, paper SPE 131350, presented at the CPS/SPE International Oil and Gas Conf. and Exh., Beijing, China, 8-10 June.

[64] **Grady D.E., and Kipp M. E.,** (1979). Oil Shale and Fragmentation at Higher Loading, presented at the 20th U.S Symposium on Rock Mech., Austin, Texas, 4-6 June.

[65] **Rinehart, J. S.,** (1965). Dynamic Fracture Strengths of Rocks, Proc. Seventh Syrup. Rock Mech., Pennsylvania State University,

[66] **Grady D. E., and Hollenbach R. E.**, (1977). Rate Controlling Processes in the Brittle Failure of Rock, Sandia Laboratories Report SAND76-0659, Albuquerque, NM.

[67] **Forrestal M. J., Grady D. E. andSchuler K. W.**, (1978). An Experimental Method to Estimate the Dynamic Fracture Strength of Oil Shale in the 103 to 104 s -1 Strain Rate Regime, *Int. Jou. Rock Mech. Min. Sci.*, 15, 263-265.

[68] **Felix, M. R.,** (1976). Determination of Stress Levels for Dynamic Fracture of Oil Shale, Experimental Mechanics, 17, 381-384.

[69] **McHugh S. L., Seamen L., Murri W. J., Tokheim R. E., and Curran D. R.,** (1977). Fracture and Fragmentation of Oil Shale, Stanford Research Institute Final Report, December

[70] **Walsh, J. B.**, (1965). The Effect of Cracks on the Compressibility of Rock, *Jou. Geophys*. Res., 70,381-389.

[71] **Freund, L. B**., (1973). Crack Propagation in an Elastic Solid Subject to General Loading-III. Stress Wave Loading, *Jou. Mech. Phy. Solids*, 21, 47-61.

[72] **Grady, D. E. and Kipp M. E.,** (1979). Explosive Fracture of Rock: Application to Oil Shale, Submitted for publication to *Int. Jou. Rock Mech. Min. Sci.*

[73] **Jaeger, J. C. and Cook N. C. W.**, (1969). Fundamentals of Rock Mechanics, New York, Chapman and Hall.

[74] **Schmidt, R. A.,** (1977). Fracture Mechanics of Oil Shale, Proc. 18th Symp. Rock Mech., Keystone, CO.

[75] **Komar C.A.**, (1978). Development of a Rationale for Stimulation Design in the Devonian Shale, paper SPE 7166, presented at the 1978 Regional Gas Technology Symposium of the Society of Petroleum Engineers of AIME, Omaha, Nebraska, 7-9 June.

[76] **Mutalik P.N. and Bob G**, (2008). Case History of Sequential and Simultaneous Fracturing of the Barnett Shale in Parker County, paper SPE 116124, presented at the 2008 SPE Ann. Tech.. Conf. and Exh., Denver, Colorado, USA, 21-24 September.

[77] **Leonard R., Woodroof R., Bullard K., Middlebrook M. and Wilson R.,** (2007). Barnett Shale Completions: A Method for Assessing New Completion Strategies, paper SPE 110809, presented at the 2007 SPE Ann. Tech. Conf. and Exh., Anaheim, California, USA, 11-14 November.

[78] **Babatunde A., Kirby W., Kevin W. and Sink J.,** (2011). Channel Hydraulic Fracturing and its Applicability in the Marcellus Shale, paper SPE 149426, presented at the SPE Eastern Regional Meeting, Columbus, Ohio, USA, August.

[79] **Hagedorn A. R. and Brown K. E**.,(1965). Experimental Study of Pressure Gradients Occurring During Continuous Two-Phase Flow in Small Diameter Vertical Conduits. *Jou. Pet. Technol*., p.475, April.

[80] **Poe B. D., Conger J. G., Farkas R., Jones B., Lee K. K., and Boney, C.L.** (1999). Advanced Fractured Well Diagnostics for Production Data Analysis. paper SPE 56750 presented at SPE Ann. Tech. Conf. and Exh.

[81] **Donald L. T, Eldridge M. M. and John B. R.,** (2014). Super Fracking, AIP Publication, Physics Today 67(8), 34(2014); 10.1063/PT.3.2480, August.

[82] **Behl R. J.,** (1999). Am. Spec. Pap. 338, 301.

[83] **Hornafius J. S., Quigley D., and Luyendyk B. P.,** (1999). *Jou*. Geophysics Resources, (Oceans) 104, 20703.

[84] **Montgomery C. T. and Smith M. B.,** (2010). *Jou., Pet. Technol*. 62(12), 26.

[85] **Busetti S., Mish K., and Reches Z.,** (2012). Am . Association, petroleum Geology, Bull. 96, 1687.

[86] **Maxwell S.,** (2011). Leading Edge 30, 340.

[87] **Gale J. F. W., Reed R. M. and Holder J.,** (2007). Am. Association, Petroleum geology, Bull. 91, 603.

[88] **Bowker K. A.,** (2007). Am. Association of Petroleum geology, Bull. 91, 523

[89] **US Energy Information Administration,** (2011). Review of Emerging Resources: US Shale Gas and Shale Oil Plays, July.

[90] **Norris J. Q., Turcotte D. L., and Rundle J. B.,** (2014). Pyhsics Review, Ed. 89, 022119.

[91] **Richman R., Mullen M., Petre E., Bill G. and Kundart D.,** (2008). A Practical Use of Shale Petrophysics for Stimulation Design Optimization, SPE Paper 115258, SPE Ann. Tech. Conf. and Exh., Denver, Colorado, 21-24 September.

[92] **Mullen M., Roundtree R., Barree R. and Turk G.,** (2007). A Composite Determination of Mechanical Rock Properties for Stimulation Design (What to do when you do not have a sonic log), SPE paper 108139, presented at the SPE Rock Mountain Oil and Gas Technol. Symposium, Denver, Colorado, 16-18 April.

[93] **Russum D.,** (2007). Status of Unconventional Gas in North America, Presented at the CSUG/PTAC 7th Ann. Unconventional Gas Symposium. p 40.

[94] **Wang F.,** (2008). Production Fairway: Speed Rails in Gas Shale, Presented at the 7th Ann. Gas Shale Summit, Dallas, Texas, 6-7 May..

[95] **Barree, R.** Introduction to Gohfer and Stimulation Design, Internal Publication, Barree Associates.

[96] **Dan B., Hughes S., Market J., Petre E., Halliburton, and Spain D. and Odumosu T.,** (2010). Petrophysical Evaluation for Enhancing Hydraulic Stimulation in Horizontal Shale Gas Wells, paper SPE 132990, SPE Ann. Tech. Conf. and Exh., Florence, Italy, 19-22 September.

[97] **Parcker M., Buller D., Petre E. and Dreher D.,** (2009). Haynesville Shale Petrophysical Evaluation, paper SPE 122937, presented at the SPE Rocky Mountain Petroleum Technol. Conf., Denver, Colorado, U.S.A14-16 April.

[98] **Ramurthy M., Barree R. D., Broacha E., Longwell J. D., Kundert D.P. and Tamaya C.,** (2009). Effects of High Process Zone Stress in Shale Stimulation Treatment, paper SPE 123581, presented at the SPE Rocky Mountain Petroleum Tech. Conf., Denver, Colorado, USA, 14-16 April.

[99] **Dix M.C., Pearce T.J. and Jones S.,** (2006). Modeling of Carbonate-Evaporate Lithology and Mineralogy from Whole-Rock Elemental Analysis: A Tool for Improving Petrophysical Evaluation and Chemostartigraphic Correlation, Presented at the AAPG Ann. Meeting, Houston, Texas, USA, 9-12 April.

[100] **Galford J., Quirein J., Shannon S., Traux J. and Witkowsky J.,** (2009). A New Neutron-Induced Gamma-ray Spectroscopy Tool for Geochemical Logging, paper SPE 123992, presented at the SPE Ann. Tech. Conf. and Exh., New Orleans, Louisiana, USA, 4-7 October.

[101] **Chen D., Quirein J., Hamid S., Smith H. Jr. and Grable J.,** (2004). Neutral Network Ensemble Selection using Multi-Objective Genetic Algorithm in Processing Pulsed Neutron Data, SPWLA paper E, presented at the SPWLA 45th Ann. Logging Symposium, Noordwijk, The Netherlands, 6-9 June.

[102] **Jacobson L. A., Ethridge R. and Sampson G.**, (1998). A New Small-Diameter, High-Performance Reservoir Monitoring Tool, paper K, presented at the SPWLA 39th Ann. Logging Symposium, Keystone, Colorado, USA, 26-29 May.

[103] **Buller D., Suparman F. N. U., Kwong S., Spain D. and Miller M.**, (2010). A Novel Approach to Shale Gas Evaluation using a Cased-hole Pulsed Neutron Tool, SPWLA Paper 87257, Presented at the SPWLA 51st Annual Logging Symposium, Perth, Australia, 19-23 June.

[104] **Warpinski N.R., Mayerhofer M. J., Vincent M. C., Cipolla C. L. and Lolon E. P.**, (2008). Stimulating Unconventional Reservoir Maximizing Network Growth While Optimizing Fracture Conductivity, paper SPE 114173, Presented at the SPE Unconventional Reservoirs Conf., Keystone, Colorado, USA, 10-12 February.

[105] **Cipolla C. L., Warpinski N.R., Mayerhofer M. J., Lolon E. P. and Vincent M. C.**, (2008). The Relationship between Fracture Complexity, Reservoir Properties, and Fracture Treatment Design, paper SPE 115769, presented at SPE Ann. Tech. Conf. and Exh., Denver, Colorado, USA, 21-24 September.

[106] **Weaver J., Rickman R. and Luo H.**, (2008). Fracture Conductivity Loss Due to Geochemical Interactions between Man-Made Proppants and Formations, paper SPE 118174, presented at the SPE Eastern Region/AAPG Eastern Section Joint Meeting, Pittsburgh, Pennsylvania, USA, 11-15 October.

[107] **Neil M., Dan B., and King K. C.,** (2011). Statistical Analysis of the Effect of Completion Methodology on Production in the Haynesville Shale, Paper SPE 144120, SPE North American Unconventional Gas Conf. and Exh., The Woodlands, Texas, USA, 14-16 June.

[108] **Lolon E., Mayerhofer M., Gracia I., Durey D., Byrd A. and Rhodes R.**, (2008). Integrated Fracture and Production Modeling Study in the Lower Cottom Valley Sands, Northern Louisiana, paper SPE 115467, presented SPE Ann. Tech. Conf. and Exh., Denver, Colorado, USA, 21-24 September.

[109] **Weaver J., and Nguyen p.**, (2010). Hydrophobic Filming Reduces Frac Gel and Mineral Scale Damage, paper SPE 138314, presented at the SPE Eastern Regional Meeting, Morgantown, West Virginia, USA, 12-14 October.

[110] **Stegent N., Ingram S., and Callard J.**, (2011). Hydraulic Fracture Stimulation Design Considerations and Production Analysis, paper SPE 139981, presented at SPE Hydraulic Fracturing Technol. Conf. and Exh., The Woodlands, Texas, USA, 24-26 January.

[111] **Krunal J., and John L.**, (2013). Comparison of Various Deterministic Forecasting Techniques in Shale Gas Reservoirs, Paper SPE

163870, Presented at the SPE Hydraulic Fracturing Technol. Conf., Woodlands, Texas, USA, 4-6 February.

[112] **Doung A. N.,** (2010). An Unconventional Rate Decline Approach for Tight and Fracture Dominated Gas Wells, paper SPE 137748, presented at the Canadian Unconventional Resources and International Petroleum conf., Calgary, Aberta, Canada,

[113] **Deepankar B.,** (2011). Shale Gas Predictive Model (SGPM)- An Alternative Approach to Predict Shale Gas Production, paper SPE 148491, presented at the SPE Eastern Regional Meeting, Columbus, Ohio, USA, 17-19 August.

[114] **Andrade J., Civan F., Devegowda D. and Sigal R.F.,** (2011). Design and Examination of Requirements for a Rigorous Shale-Gas Reservoir Simulator Compared to Current Shale-Gas Simulators, paper SPE 144401, the 2011 Americas Unconventional Gas Conf., the Woodlands, TX, 14-16 June

[115] **Cipolla C. L., Elyeler L., Jim E., and Vinit S. T.,** (2009), Modeling Well performance in Shale-Gas Reservoirs, paper SPE 125532, the SPE/WAGE Reservoir Characterization and Simulation Conf., Abu Dhabi, UAE, 19 – 21 October.

[116] **Can B. and Kabir C.S.,** (2011) Probabilistic Performance Forecasting for Unconventional Reservoirs with Stretched-Exponential Model, paper SPE 143666 prepared for presentation at the Americas Unconventional Gas Conf., the Woodlands, TX, 14-16 June.

[117] **King G. E.,** (1993). Material Balance Techniques for Coal Seam and Devonian Shale Gas Reservoirs with Limited Water Influx, *SPERE*, Feb

[118] **Raghavan R. and Joshi S.D.,** (1993), Productivity of Multiple Drainholes or Fractures Horizontal Wells, *SPEFE*, Mar

[119] **Arthur D.J.,** (2008), Hydraulically Fracturing Considerations for Natural Gas Wells of the Marcellus Shale, paper presented at the Ann. Forum of the Groundwater Protection Council, Cincinnati, Ohio, USA, 21-24,Sept.

[120] **Bazan L.W.,** (2010), Improving Production in the Eagle Ford Shale with Fracture Modeling, Increased Conductivity and Optimized Stage and Cluster Spacing Along Horizontal Wellbore, paper SPE 138425 presented at the SPE Tight Gas Completions Conf., San Antonio, 2-3, November

[121] **Nobakht M. and Clarkson C.R.,** (2011). Analysis of Production Data in Shale Gas Reservoir: Rigorous Corrections for Fluid and Flow Properties, paper SPE 149404, presented at the SPE Eastern Regional Meeting, Columbus, Ohio, USA, 17-19 August.

[122] **Clarkson C.R., Nobakht M., Kaviani D. and Ertekin T.,** (2011). Production Analysis of Tight Gas and Shale Gas Reservoirs Using the Dynamic-Slippage Concept. paper SPE 144317 presented at the

North American Unconventional Gas Conf., The Woodlands,Texas, Texas, 12–16 June

[123] **El-Banbi A. H. and Wattenbarger R. A.**, (1998), Analysis of Linear Flow in Gas Well Production. paper SPE 39972 presented at SPE Gas Technol. Symposium, Calgary, Alberta, 15–18 March.

[124] **Ibrahim M. and Wattenbarger R. A.**, (2005). Rate Dependence of Transient Linear Flow in Tight Gas Wells. Paper CIPC 2005-057 presented at Canadian International Petroleum Conf., Calgary, Alberta, 7–9 June

[125] **Ibrahim M. and Wattenbarger R. A.**, (2006). Analysis of Rate Dependence in Transient Linear Flow in Tight Gas Wells. Paper SPE 100836 presented at the Abu Dhabi International Petroleum Exh. and Conf., Abu Dhabi, UAE, 5–8 November

[126] **Anderson D.M. and Mattar L.**, (2005). An Improved Pseudo-Time for Gas Reservoirs with Significant Transient Flow. Paper CIPC 2005-114 presented at Canadian International Petroleum Conf., Calgary, Alberta, 7–9 June.

[127] **Moghadam S., Jeje O. and Mattar L.**, (2011). Advanced Gas Material Balance in Simplified Format. *Jou. Can Pet Tech* **50** (1): 90–98. SPE-139428-PA.

[128] **Ertekin T., King G.R. and Schwerer F. C.**, (1986). Dynamic Gas Slippage: A Unique Dual-Mechanism Approach to the Flow of Gas in Tight Formations. paper SPE 12045-PA, *SPE Form Eval* **1** (1): 43–52.

[129] **Samandarli O., Al-Ahmadi H. and Wattenbarger R. A.**, (2011). A New Method for History Matching and Forecasting Shale Gas Reservoir Production Performance with a Dual Porosity Model, paper SPE 144335 presented at the North American Unconventional Gas Conf., The Woodlands, Texas, Texas, 12–16 June**.**

[130] **BingXiang Xu, Manouchehr H., Dennis C., Xiangfang Li**, (2012). Production Data Analysis in Eagle Ford Shale Gas Reservoir, paper SPE 153072, presented at the SPE/EAGE European Unconventional Resources Conf. and Exh., Vienna, Austria, 20-22, March.

[131] **Arps J.J.**, (1945). Analysis of Decline Curves. *Trans.,* AIME, 160: 228-247.

[132] **Lee W.J. and Gatens Ill J.M.**, (1985). Analysis of Eastern Devonian Gas Shales Production Data, paper SPE 14506, presented at the SPE 1985, Eastern Regional Meeting, Morgsntown, West Virginia, 6-8 November

[133] **Hazlett W. G., Lee W. J. and Narahara G. M.**, (1986). Production Data Analysis Type Curves for the Devonian Shales. paper SPE 15934, presented at the SPE Eastern Regional Meeting, Columbus, Ohio, 12-14 November.

[134] **Inamdar A., Malpani R., and Atwood K.,** (2010). Evaluation of Stimulation Techniques Using Microseismic Mapping in the Eagle Ford Shale,. Paper SPE 136873, presented at the SPE Tight Gas Completions Conf. San Antonio, Texas, USA, 2–3 November.

[135] **Christopher V. P.,** (1982). A Hydrodynamic Analogy of Production Decline for Devonian Shale Wells, paper SPE/DOE 10837, presented at SPE/DOE Unconventional Gas Recovery Symposium of the Society of Petroleum Engineers, Pittsburgh, PA, 16-18 May.

[136] **Brown M., and Ozkan E., Raghavan R. S, and Kazemi H.,** (2011). Practical Solutions for Pressure Transient Responses of Fractured Horizontal Wells in Unconventional Shale Reservoirs, paper SPE 125043, SPE Ann. Tech. Conf. and Exh., New Orleans, 4-7 October.

[137] **Ozkan E., Brown M. L., Raghavan R. S. and Kazemi, H.,** (2009). Comparison of Fractured Horizontal Well Performance in Conventional and Unconventional Reservoirs, paper SPE 121290, presented at the SPE Western Regional Meeting, San Jose, California, USA, 24-26 March.

[138] **Chen C. C. and Raghavan, R. S,** (1997). A Multiply-Fractured Horizontal Well in a Rectangular Drainage Region, Paper SPE 37072-PA, *SPE Jou.*2 (4): 455-465.

[139] **Raghavan, R.S., Chen C.C., and Agarwal B.,** (1997). An Analysis of Horizontal Wells Intercepted by Multiple Fractures, *SPE Jou.* 2 (3): 235-245. paper SPE 27652-PA.

[140] **Medeiros F., Ozkan E., and Kazemi H.,** (2008). Productivity and Drainage Area of Fracture Horizontal Wells in Tight Gas Reservoirs, SPE Res Eval and Eng 11 (5): 902-911. paper SPE 108110-PA.

[141] **Mayerhofer M. J., Lolon E.P., Warpinski N.R., Cipolla C.L., Walser D., and Rightmire C. M.,** (2010). What is Stimulated Reservoir Volume?, SPE Prod and Oper 25 (1): 89-98, paper SPE 119890-PA

[142] **Warren J. E., and Root P.J.,** (1963). The Behavior of Naturally Fractured Reservoir, *SPE Jou.* 3 (3): 245-255, paper SPE 426-PA

[143] **Kazemi H.,** (1969). Pressure Transient Analysis of Naturally Fractured Reservoir with Uniform Fracture Distribution, *SPE Jou.* 9 (4):451-462. paper SPE 2156-PA.

[144] **De Swaan O. A.,** (1976). Analytical Solution for Determining Naturally Fractured Reservoir Properties by Well Testing, *SPE Jou.* 16 (3): 117-122, paper SPE 5346-PA.

[145] **Serra K.V., Reynolds A.C., and Raghavan R. S.,** (1983). New Pressure Transient Analysis Method for Naturally Fractured Reservoir, *Jou. pet technol* 35 (12): 2271-2283, paper SPE 10780-PA.

[146] **Soliman M.Y., Hunt J. L., and El Rabaa A. M.**, (1990). Fracturing Aspects of Horizontal Wells, *Jou. Pet Technol* 42 (8): 966-973, Paper SPE 18542-PA.

[147] **Murkherjee H. and Economides M.J.**, (1991). A Parametric Comparison of Horizontal and Vertical Wells Performance, SPE Form Eval 6 (2): 209-216, paper SPE 18303-PA.

[148] **Larsen L. and Hegre T. M.**, (1991). Pressure Transient Behavior of Horizontal Wells with Finite Conductivity Vertical Fractures, paper SPE 22076, presented at the International Arctic Technol. Conf., Anchorage, 29-31 May.

[149] **Larsen L. and Hegre T. M.**, (1994). Pressure Transient Analysis of Multi-Fractured Horizontal Wells, paper SPE 28389, presented at the SPE Ann. Tech. Conf. and Exh., New Orleans, 25-28 September.

[150] **Al-Hussainy R., Ramey H .J. Jr., and Crawford P.B.**, (1966). The Flow of Real Gases through Porous Media, *Jou. Pet Technol* 18 (5): 624-636, Paper SPE 1243-PA.

[151] **Agarwal R.A.**, (1979). Real Gas Pseudo Time – A New Function for Pressure Buildup Analysis of MHF Gas Wells, paper SPE 8279, presented at the SPE ann. Tech. Conf. and Exh., Las Vegas, Neveda, USA, 23-26 September.

[152] **Scott J. O.**, (1979). Application of a New Method for Determining Flow Characteristics of Fractured Gas Wells in Tight Sands, paper SPE 7931, presented at the Symposium on Low Permeability Gas Reservoirs, Denver, 20-22 May.

[153] **Cinco-Ley H. and Meng H. Z.**, (1988). Pressure Transient Analysis of Wells with Finite Conductivity Vertical Fractures in Double Porosity Reservoirs, paper SPE 18172, presented at the SPE Annual Tech. Conf. and Exh., Houston.

[154] **Stehfest H.**, (1970). Algorithm 368: Numerical Inversion of Laplace Transforms, Conunun. ACM 13 (1): 47-49,

[155] **Bennett C. O., Camacho-V., R. G., Reynolds A.C. and Raghavan, R. S.**, (1985). Approximate Solution for Fractured Wells Producing Layered Reservoirs, SPE *Jou.* 25 (5): 729-742, Paper SPE 11599-PA.

[156] **Al-Kobaisi M., Ozkan E., and Kazemi H.**, (2006). A Hybrid Numerical/Analytical Model of a Finite Conductivity Vertical Fracture Intercepted by a Horizontal Well, SPE res Eval and Eng 24 (10): 345-355, Paper SPE 92040-PA.

[157] **Valko P. P. and Lee W.J.**, (2010). A Better Way to Forecast Production from Unconventional Gas Wells, Paper SPE 134231, Presented at the SPE Ann. Tech. Conf. and Exh., Florence, Italy

[158] **Buller D., Hughes S., Market J., Petre E., Spain D. and Odumosu T.**, (2010). Petrophysical Evaluation for Enhancing Hydraulic Stimulation in Horizontal Shale Gas Wells, paper SPE

132990, presented at the SPE Ann. Tech. Conf. and Exh., Florence, Italy, 19-22 September.

[159] **Khosrow B., Damar A., Mohan H. and Marshall C.,** (2008). Economics Development in the United States, paper SPE 116560, SPE Ann. Tech. Conf. and Exh., Denver, Colorado, USA, 21-24 September.

[160] **John D. W.,** (2008). Economics Evalaution os Shale Gas Reservoirs, paper SPE 119899, 2008 SPE Shale Gas Production Conf. Forth Worth, Texas, USA, 16-18 November.

.

CURRICULUM VITAE

Name Surname: Osman Mohammed

Place and Date of Birth: 13th January 1980**,** Tamale, Ghana.

Address: H/No. K. R. S 11, Kalariga, Tamale, Ghana

E-Mail: sumani_osman@yahoo.com

B.Sc.: Applied Chemistry with Enviromental Science (University for Development Studies, Tamale, Ghana).

Professional Experience and Rewards:
Medical Laboratory Technologist, Korle-Bu Teaching Hospital, Accra, Ghana.
Senior Research Assistant, University of Ghana Medical School, Korle-Bu, Accra, Ghana.